Mécanismes de decohérence dans les conducteurs mésoscopiques / Decoherence mechanisms in mesocopic conductors

Anne Anthore

▶ **To cite this version:**

Anne Anthore. Mécanismes de decohérence dans les conducteurs mésoscopiques / Decoherence mechanisms in mesocopic conductors. Condensed Matter [cond-mat]. Université Pierre et Marie Curie - Paris VI, 2003. English. NNT : . tel-00003518

HAL Id: tel-00003518

https://theses.hal.science/tel-00003518v1

Submitted on 9 Oct 2003

HAL is a multi-disciplinary open access archive for the deposit and dissemination of scientific research documents, whether they are published or not. The documents may come from teaching and research institutions in France or abroad, or from public or private research centers.

L'archive ouverte pluridisciplinaire **HAL**, est destinée au dépôt et à la diffusion de documents scientifiques de niveau recherche, publiés ou non, émanant des établissements d'enseignement et de recherche français ou étrangers, des laboratoires publics ou privés.

THESE DE DOCTORAT DE L' UNIVERSITE PARIS 6

Spécialité :
Physique des Solides

Présentée par Anne ANTHORE
Pour obtenir le grade de DOCTEUR DE L' UNIVERSITE PARIS 6

Sujet de la thèse :

MECANISMES DE DECOHERENCE DANS LES CONDUCTEURS MESOSCOPIQUES

soutenue le 26 septembre 2003
devant le jury composé de:

R. Combescot
H. Courtois (rapporteur)
D. Estève (directeur de thèse)
F. Hekking
G. Montambaux
C. Van Haesendonck (rapporteur)

Remerciements

Au terme de ces trois années, je tiens à remercier toutes les personnes du groupe Quantronique grâce à qui cette thèse a pu voir le jour dans une ambiance très agréable. Tout d' abord, merci à Daniel Estève, mon directeur de thèse, qui prend très au sérieux l' aspect formateur d' une thèse sans se prendre au sérieux, qui est toujours disponible pour discuter malgré ses nombreuses occupations et grâce à qui j' ai beaucoup appris. Je remercie Hugues Pothier, mon directeur de thèse bis, car aucun des résultats de cette thèse n' aurait existé sans son aide précieuse en fabrication, pour les mesures et pour l' interprétation des données ni sans ses moqueries motivantes. Merci à Frédéric Pierre, mon prédécesseur sur ce sujet dans le groupe, qui m' a initiée pendant mon stage de DEA à la fabrication, au C++ et au reggae (même si je n' ai pas été aussi réceptive dans tous les domaines), qui a continué à développer le merveilleux programme SimulK pendant son post-doc et qui a réalisé et interprété les mesures de localisation faible sur les échantillons que je fabriquais. Merci à Cristian Urbina pour ses conseils avisés de lecture à la fois en physique et dans d'autres domaines, à Philippe Joyez pour son aide discrète mais toujours très efficace et à Denis Vion pour ses conseils en fabrication et Mathematica. Je remercie Pief Orfila pour ses compétences techniques, ses explications toujours claires sur le fonctionnement des machines allant des plus simples aux plus compliquées, les parties de badminton et les tours de vélo. J' ai aussi bénéficié des compétences techniques de Pascal Sénat qui vient de rejoindre le groupe et supplée Pief très efficacement. J' ai beaucoup apprécié la gentillesse et les qualités de pédagogue de Norman Birge pendant le dernier mois de cette thèse et j' ai profité des larges connaissances de Michel Devoret pendant ma première année. Je remercie enfin tous les post-docs et thésards que j' ai côtoyés pendant mon passage dans le groupe et qui respectaient (tout autant que les permanents), à mon grand plaisir, la tradition de fabrication et dégustation de gâteaux :

Audrey Cottet, Martin Chauvin, Grégoire Ithier, Benjamin Huard, Hélène Le Sueur, Marcelo Goffman, Abdel Aassime, Peter Vom Stein et Eddy Collin.

Je n'oublie pas d'avoir une pensée pour toutes les personnes extérieures au groupe, que je rencontrais fréquemment : notamment, les "chimistes" du SCM Mathieu Lambert, Roland Lefèvre et Stéphane Auvray qui partageaient les moyens de fabrication et rendaient l'attente des machines plus distrayante et Valentin Rodriguez, Franck Selva, Fabien Portier et Sophie Djordjevic que j'ai eu l'occasion de mieux connaître lors de repas thésards.

Je remercie Odile Kaitasov, Sébastien Gautrot et Jacques Chaumont du laboratoire CSNSM de Paris XI pour la réalisation des implantations d'impuretés magnétiques. J'ai également tiré profit de discussions fructueuses avec Georg Göppert, Hermann Grabert, Takis Kontos et Marco Aprili.

Je remercie Pierre Janvier pour son accueil au magasin, Sandrine Thunin et Madame Marciano pour leur disponibilité et leur aide dans toutes les démarches administratives, les techniciens rencontrés au grand et au petit atelier pour leurs conseils d'utilisation des machines.

Je suis reconnaissante à Hervé Courtois et Chris Van Haesendonck d'avoir accepté d'être rapporteurs de ce travail et à Roland Combescot, Frank Hekking et Gilles Montambaux d'avoir participé au jury.

Enfin, je tiens à exprimer toute ma gratitude à mon grand-père, mes parents pour leur soutien permanent depuis le début, et à mes frères sans qui mon sens de la répartie n'aurait pas été assez affûté pour contrer les moqueries d'Hugues. Je pense également à ma famille plus lointaine et mes amis qui, par leur présence, rendent la vie plus facile : à bientôt en Finlande ! Le bon déroulement de ce travail est en grande partie dû à Ronald qui a eu confiance en moi et qui continue à m'accorder sa confiance : merci.

Table of contents

PART 2: MAGNETIC IMPURITIES IN METALS

Decoherence mechanisms in mesoscopic conductors

In mesoscopic electronic systems, quantum coherence is not characterized by a unique parameter such as a length scale, but depends on the physical property that is concerned, on the energy range which is probed, and often on other circuit dependent parameters. For instance, the conductance of a nanostructure in which electrons behave as independent carriers is affected by quantum interference effects up to a length scale that depends on temperature and on the applied voltage. In some systems, this length scale can even overcome the circuit size, as demonstrated by recent interference experiments in a multi-path circuit carved in a 2D electron gas [1]. Understanding the limitations to quantum coherence in the independent electron transport regime is presently a fundamental issue, which also has practical implications since the loss of quantum coherence hinders the development of quantum devices fully exploiting quantum interference effects. The issue of quantum coherence becomes more complex in presence of interactions between electrons, because the Fermi liquid can adopt a many-body quantum state. Other phenomena than those limiting the intrinsic electronic quantum coherence come then into play. The goal of this thesis work is to probe quantum coherence in diffusive metallic conductors both in the independent electron regime and in presence of pairing interactions, which induce superconducting order. The experiments are based on tunnel spectroscopy, a technique described in the inset.

Tunnel Spectroscopy of Mesoscopic Systems

Tunneling of electrons between metallic electrodes gives spectroscopic information on the density and filling of the states in the electrodes [2]. In this thesis, the focus is on metallic wires, and the generic sample geometry that we have used is shown below:

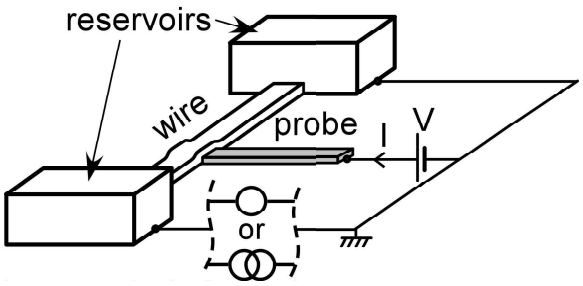

The metallic wire under investigation is connected to large pads, and it can be current biased or driven out-of-equilibrium by a voltage. A probe electrode forms a tunnel junction with the wire. Assuming that the density of states and the filling factors of the probe electrode are known, the density or filling of the states in the wire at the position of the junction can be inferred from the differential conductance $dI/dV(V)$ of the tunnel junction.

The physical quantity that is probed is given below as a function of the nature of the probe electrode and of the wire (superconducting (S), normal (N), or any (X)).

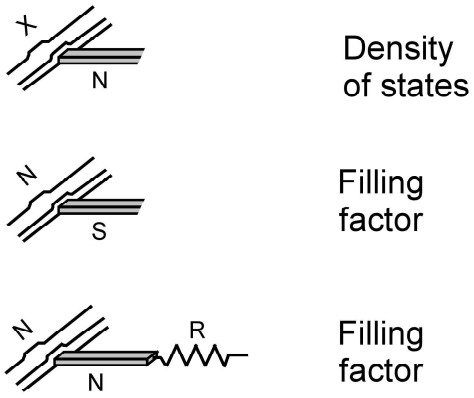

In the following, a short overview of the main results of this thesis is given.

1.1 Electron-electron interaction and Kondo effect

In metals, electron energy levels in the conduction band are associated with extended wave functions. In the normal state, electrons fill these states according to the Pauli exclusion principle, up to the Fermi energy. Coulomb interaction modifies this simple independent electron picture of a Fermi liquid, but the electronic excitations are still almost independent fermionic particles as proven by Landau [3] and are thus called “quasiparticles”. The issue of quantum coherence of these quasiparticles has been a main concern during the last twenty years. In the case of thin films, electronic waves are scattered by structural defects and by film boundaries, and Landau quasiparticles undergo a diffusion-like motion. In this diffusive regime, a quasiparticle is predicted to remain coherent over a length scale that depends on its energy and on the energy distribution functions of all the quasiparticles. For a quasiparticle at the Fermi level, in absence of other limiting mechanisms than Coulomb interaction, this length scale is predicted to grow indefinitely as temperature tends to zero. Yet a controversy stands about the explanation of the commonly observed saturation of the coherence length at low temperature [4]. It was even claimed that this saturation is a universal feature due to “zero point fluctuations” [5]. This assessment was later ruled out by counterexamples: the saturation of τ_ϕ is not systematic in samples with similar electrical and geometrical parameters [6]. The saturation was also attributed to the presence in the samples of magnetic impurities with small Kondo temperature. Indeed, the scattering rate from magnetic impurities increases when temperature is lowered, till the Kondo temperature is reached. In contrast, the scattering rate due to Coulomb interactions decreases. These two scattering mechanisms can thus result in a plateau in the temperature dependence of the phase coherence time above the Kondo temperature. If the Kondo temperature is at the edge of the explored temperature range, this plateau looks like a saturation.

Prior to this thesis work, energy exchange in mesoscopic wires had been measured in the Quantronics group in order to precisely understand the inelastic scattering mechanisms

limiting phase coherence. In these experiments, the rates of energy exchange were found higher than predicted by the theory of Coulomb electron-electron interactions, with furthermore an unexpected energy dependence, and sample to sample variations [6]. In the meanwhile, Kaminski and Glazmann [7] proposed that magnetic impurities could also be responsible for this abnormal energy exchange. Indeed, even if their spin states are degenerate, scattering from magnetic impurities can mediate energy exchange between electrons at second and higher orders in the coupling between electrons and magnetic impurities (see Figure 1). Due to Kondo effect, the coupling constant between electrons and magnetic impurities is renormalized and reaches a maximum at the Kondo temperature. Kondo-Impurity Mediated (KIM in the following) interaction between electrons can then dominate Coulomb interaction. It was calculated that the crossover to a KIM interaction dominated regime takes place at a very small amount of magnetic impurities, of the order of a part per million (ppm).

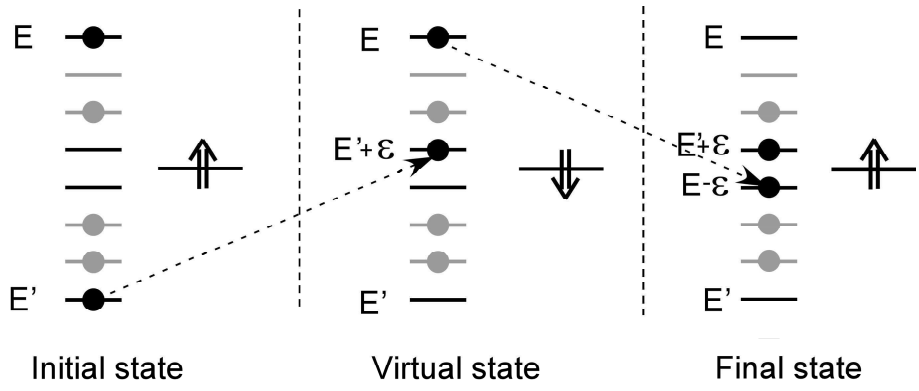

Figure 1: Two-step inelastic scattering process involving two electrons (black disks) and a single magnetic impurity (double arrow). In each panel, the left ladder represents the electrons energy spectrum. The gray disks and lines represent the non-involved electrons and states. The isolated state on the right side represents the energy level of the degenerate spin states of the magnetic impurity. In a first step, an electron of energy E' interacts with the magnetic impurity, gaining an energy ε and making the impurity spin flip. In a second step, an electron of energy E interacts with the magnetic impurity, loosing the energy ε and making the impurity spin flip back to its initial state. In this second order process, two electrons have exchanged the energy ε via a magnetic impurity.

To test if magnetic impurities are responsible for the saturation of the phase coherence length at low temperature and play a role in energy exchange, we performed two complementary sets of experiments. First, we measured the phase coherence time in samples in which a known concentration of magnetic impurities was implanted [8]. Second, in samples displaying

anomalous energy exchange, we measured energy exchange between electrons in presence of a magnetic field [9], which is expected to modify the KIM interaction rate.

1.1.1 Limitation of phase coherence by spin-flip scattering from magnetic impurities

In this first experiment, we measured the temperature dependence of τ_ϕ in wires made of silver, in which manganese impurities at controlled concentrations were implanted. The Kondo temperature of manganese in silver is $T_K \simeq 40$ mK [10].

The phase coherence time was deduced from the weak localization corrections to the magnetoresistance of long wires. The temperature dependence of the electronic phase coherence time for four different samples is shown in Figure 2. The first one, called Ag6N, was made from a 99.9999 % purity source. The second one, called Ag5N, was made from a 99.999 % purity source. The third and the fourth ones, called $Ag5N_{cMn0.3}$ and $Ag5N_{cMn1}$, were co-evaporated with Ag5N, then implanted with 0.3 ppm and 1 ppm of Mn. The measurements down to 40 mK were performed at Michigan State University by F. Pierre and N. O. Birge. It was found that the purer the sample, the higher the phase coherence time at low temperature. The temperature dependence of τ_ϕ is fit with a function taking into account Coulomb electron-electron interaction, electron-phonon interaction and spin-flip scattering. The concentration of magnetic impurities was a fit parameter and was found in close agreement with the nominal purity of sources and the concentrations of implanted Mn atoms.

1.1.2 Energy exchange mediated by magnetic impurities

In order to investigate KIM interaction, we measured energy exchange between electrons in a metallic wire in presence of a magnetic field B that splits the Zeeman energy levels of magnetic impurities. If the magnetic field is large enough, the magnetic impurities are frozen in their ground state and a drastic reduction of the rate of KIM energy exchange is expected. To access the energy exchange between electrons, we prepare an out-of-equilibrium situation by placing the wire between two metal contacts biased at different potentials. Since

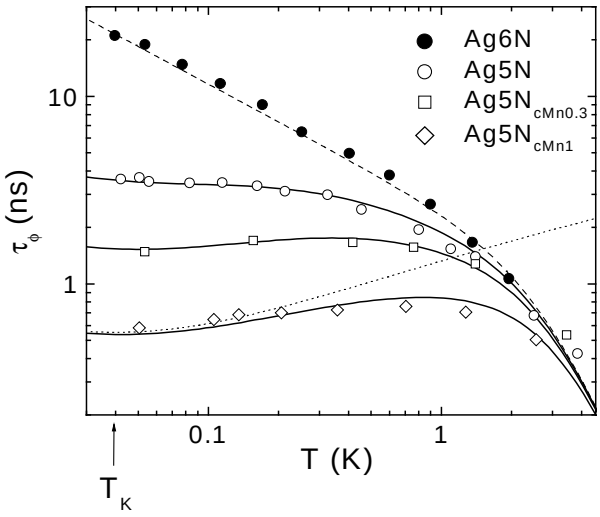

Figure 2: Phase coherence time as function of temperature in several silver wires. Sample Ag6N is made of the purest (6N) source. Samples Ag5N, $Ag5N_{cMn0.3}$, and $Ag5N_{cMn1}$ were co-evaporated using a 5N silver source. Afterward, 0.3 ppm and 1 ppm of manganese was added by ion implantation in samples $Ag5N_{cMn0.3}$ and $Ag5N_{cMn1}$, respectively. Continuous lines are fits of $\tau_\phi(T)$ taking into account the contributions of electron-electron interaction and electron-phonon interaction (dashed line), and spin-flip collisions using the concentration c_{imp} of magnetic impurities as a fit parameter (dotted line is for $c_{imp} = 1\,\text{ppm}$). Best fits are obtained using $c_{imp} = 0.13,\ 0.39$ and 0.96 ppm respectively for samples Ag5N, $Ag5N_{cMn0.3}$, and $Ag5N_{cMn1}$.

energy exchange between electrons tends to establish a local equilibrium, the electron energy distribution function along the wire is therefore sensitive to interactions if the time an electron spends in the wire is of the same order as the typical interaction time. To obtain the energy distribution function at zero magnetic field, we use the non-linearity of the differential conductance of a superconducting-normal tunnel junction, as in previous experiments in the group. To access the energy distribution function in presence of a magnetic field, we take advantage of the Coulomb blockade of tunneling through a tunnel junction in series with a resistance (the superconducting probe was designed long and narrow so that it presents a resistance of the order of $1\ \text{k}\Omega$ in its normal state) [11]. The differential conductance of such a junction presents a broad single dip when electron interactions are strong and lead to electronic thermalization, and a double dip when only little interaction occurs while electrons travel through the wire (see Figure 3).

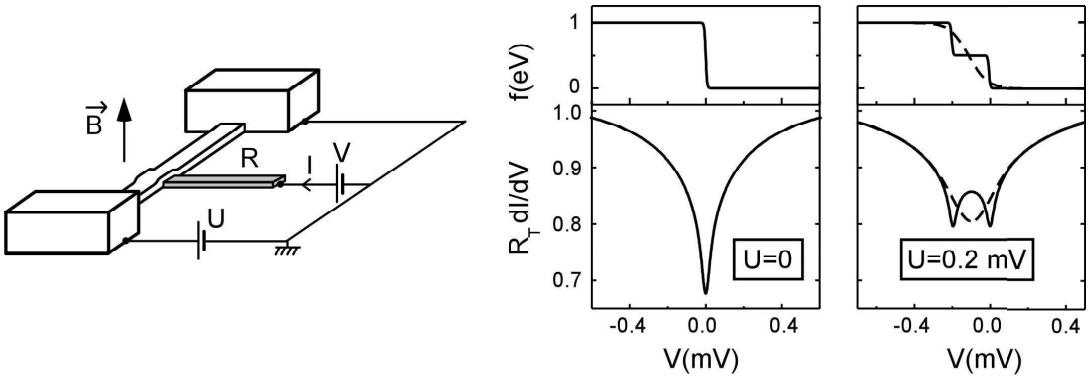

Figure 3: Left: Schematic of the circuit: A normal wire is connected to large reservoirs biased at different potentials. A normal resistive probe electrode forms a tunnel junction with the wire in its middle. Right: At equilibrium ($U = 0$), the energy distribution function in the wire is a Fermi function and the differential conductance $dI/dV(V)$ of the junction displays a dip at zero bias, due to Coulomb blockade of tunneling (left). When the electrons of the wire are driven out-of-equilibrium by a finite voltage U (right), their energy distribution function $f(E)$ depends on the interaction rate between electrons. In the absence of interactions, $f(E)$ is a two-step function and $dI/dV(V)$ presents two dips (solid lines). With strong interactions, $f(E)$ is rounded, and $dI/dV(V)$ presents a broad dip (dashed lines).

We performed measurements on two samples made from the same source of 6N- and 5N-silver as the samples used to determine the phase coherence time dependence on temperature. The results are presented in Figure 4. In $Ag_{6N}I20$, made from the 6N-silver source, sharp distributions are found at $B = 0$, and no magnetic field effect on the differential conductance is found. In contrast, in $Ag_{5N}IV20$, made from the 5N-silver source, rounded distributions are found at low magnetic field. As B is increased, the single dip in the differential conductance splits into two dips at a field value that scales with U. Hence extra interactions, present in this sample at $B = 0$, are suppressed by the magnetic field, in agreement with the expected behavior of KIM interaction. The effect of KIM interaction was calculated using a recent theoretical work that takes into account Kondo effect [12], the concentration of magnetic impurities c_{imp} being a fit parameter. Data of $Ag_{5N}IV20$ are fit with $c_{imp} = 17$ ppm, a value two orders of magnitude larger than the one deduced from the phase coherence time measurement on the sample obtained from the same silver source.

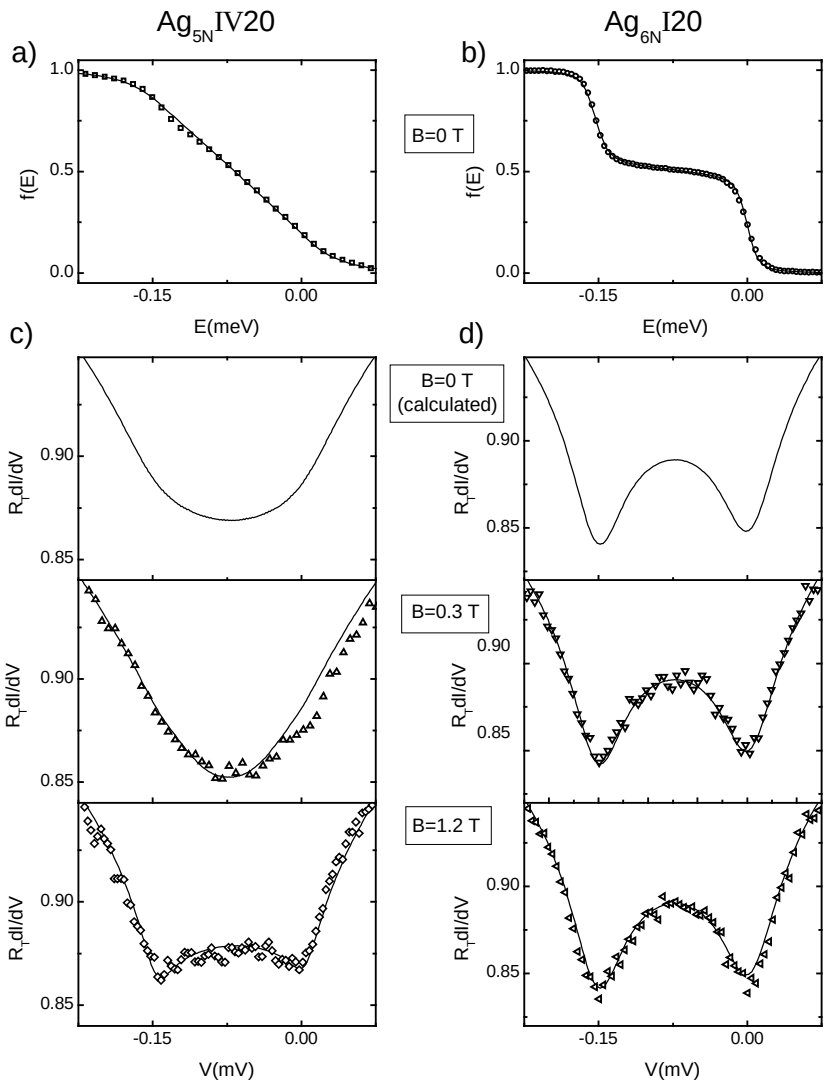

Figure 4: a) and b) Symbols: Distribution functions $f(E)$ at zero magnetic field and $U = 0.15\,\mathrm{mV}$ in two silver wires with same electronic diffusion time. The distribution functions were obtained by deconvolution of the differential conductance $dI/dV(V)$ of a tunnel junction formed between the middle of the wires and probe electrodes in the superconducting state [6]. c) and d): Top panels: Calculated Coulomb blockade signal $dI/dV(V)$ at the junction ends using the measured $f(E)$ at $B = 0$. Other panels: Symbols: Measured $dI/dV(V)$ at $U = 0.15$ mV, with $B = 0.3$ T and 1.2 T, the probe electrode being in the resistive state. Solid lines: Fits with theory based on Kondo effect.

Such a comparison between phase coherence time and energy exchange measurements [13] was also performed on copper wires, in which the phase coherence time is always found to saturate below $100\,\mathrm{mK}$. The concentration of magnetic impurities deduced from τ_ϕ measurements was about 0.3 ppm. Energy exchange measurements on a copper wire showed

a magnetic field dependence, and the concentration of magnetic impurities deduced from the fit was 4.8 ppm. Therefore a large discrepancy between both fit concentrations also appears for copper, suggesting that the description of scattering from magnetic impurities is inadequate or that pollution arises during the fabrication process of samples for energy exchange measurements.

The implantation of magnetic impurities at a known concentration in a very pure sample like $Ag_{6N}I20$ would be a quantitative test of this theory. Experimentally, the implantation cannot be performed after fabrication because ion implantation destroys the tunnel junction. Another fabrication process is being developed in order to circumvent this difficulty.

1.1.3 Conclusion

This set of experiments sheds light on low temperature decoherence by showing that a minute concentration of magnetic impurities can result in an almost constant phase coherence time on a broad temperature range, and in a sizeable increase of energy exchange. Since the nominal purity of commercial sources is warranted to one ppm at best, a minute concentration of magnetic impurities cannot be excluded. Moreover, pollution of the sample at this level can never be absolutely excluded. Unfortunately, *a posteriori* analysis measurements on our thin films are not sensitive enough to detect impurities at the ppm level. It could even be argued that the phase coherence time measurements are probably the most accurate method to detect so small concentrations of low-T_K magnetic impurities, particularly in thin metallic films.

1.2 Mesoscopic superconductivity

In presence of attractive interactions between quasiparticles, another quantum coherence phenomenon, namely superconductivity, sets in at low enough temperature: the Fermi liquid adopts a many-body quantum state with pair correlations, and an order parameter characterized by a phase. A fundamental characteristic of the superconducting state is that a

supercurrent, *i.e.* a current at zero voltage, can flow. Although the superconducting state is rather robust against decoherence in the underlying Fermi liquid of quasiparticles, specific depairing mechanisms tend to weaken and eventually suppress the pairing order. This is the case when a magnetic field is applied or a current flows through the superconductor, as shown in the first experiment presented in this part. Conversely, in a proximity effect situation, in which a superconductor and a normal electrode are placed in contact, the extension of the induced pairing order in the normal part depends on the coherence length of individual quasiparticles. In diffusive conductors at equilibrium, both the depairing in a superconductor and the propagation of pair correlations in a normal metal can be described with the Usadel equations, derived from the formalism of non-equilibrium superconductivity [14]. This formalism can also describe out-of-equilibrium proximity effect situations as long as the superconductors are all at the same potential. In the second experiment presented in this part, we address a situation beyond this limit: a normal wire connected to two superconductors biased at different potentials.

1.2.1 Density of states in a superconductor carrying a supercurrent

We have carried out an experiment to test the predicted equivalence of the depairing induced by a magnetic field or by a supercurrent in a superconducting wire [15]. Indeed both effects enter as a single "depairing energy" in the Usadel equations. To deal with a simple case, the superconductor was chosen wire-shaped with thickness and width smaller than the London length, so that the current flow was homogeneous and the magnetic field penetrated completely. Moreover, the width and thickness were of the same order as the coherence length $L_\Delta = \sqrt{\hbar D / \Delta}$ so that pair correlations did not vary in the transverse directions. We measured the single particle density of states, which is a good marker of pair-correlations, in presence of a supercurrent, or of a magnetic field. The density of states was inferred from the differential conductance $dI/dV\left(V\right)$ of a tunnel junction formed between the superconducting wire and a probe electrode made of normal metal. In absence of magnetic field and supercurrent, the conductance displays a gap Δ_0 and a sharp peak in agreement with the predictions of the BCS

theory. In Figure 5, measured differential conductance curves are presented for different values of supercurrent and magnetic field. In both cases, good agreement is found with theory using the concept of depairing energy.

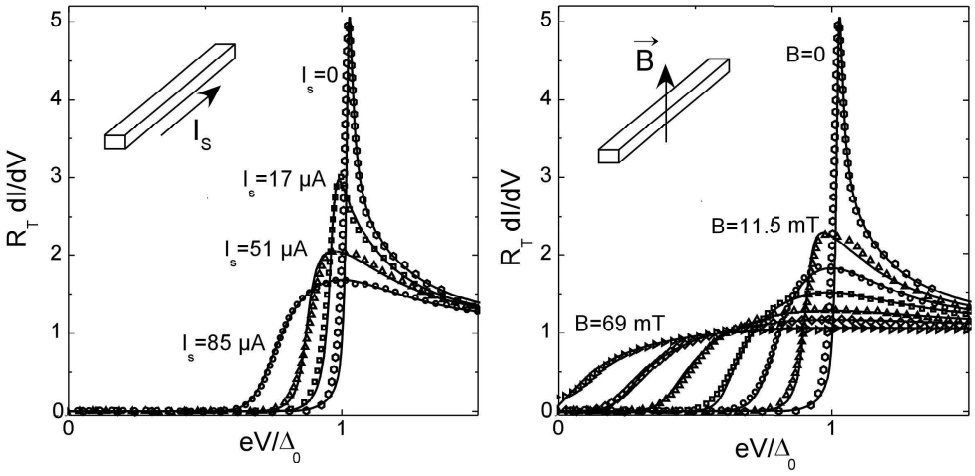

Figure 5: Open Symbols: Normalized differential conductance of a tunnel junction of resistance R_T between a normal probe and a superconducting wire when the wire sustains a supercurrent I_S (left panel) or is exposed to a magnetic field B (right panel). To a good approximation, the differential conductance is proportional to the density of states in the superconducting wire. In absence of supercurrent and magnetic field, the density of states is zero below the gap energy Δ_0. Solid lines: Fits using non-equilibrium superconductivity theory using only the depairing energy as a fit parameter.

1.2.2 Out-of-equilibrium proximity effect

We investigated proximity effect in a normal (N) diffusive silver wire connected to two aluminum superconducting (S) contacts biased at different potentials [16]. The aim of this experiment was to probe proximity effect in a simple out-of-equilibrium situation.

The equilibrium transport properties in such a set-up have been previously investigated by Dubos *et al.* [17]. The observed supercurrent was quantitatively explained by Usadel equations. When superconductors are biased at different potentials, their phase difference depends on time, and this theory cannot be directly used. Yet, in our experiment, it appears that some out-of-equilibrium properties can be accounted for by a simplified picture of

proximity effect, which neglects the modifications of the density of states but takes into account the Andreev reflections at the NS contacts, which are responsible for the conversion of the quasiparticle current in the normal conductor into a supercurrent. In the normal wire, the current is exclusively carried by electrons and holes. In the superconductor, the current is carried by the pairs in the superconducting condensate, and single particle excitations are not possible below the gap energy Δ. At an NS interface, an electron in the normal metal with energy smaller than Δ is reflected into a hole while a Cooper pair enters the superconductor. In an SNS configuration, these Andreev reflections manifest themselves directly in the shape of the energy distribution of electrons in the normal wire. Indeed, as shown in Figure 6, low energy electrons and holes bounce back and forth between the superconductors, gaining energy at each traversal until they can enter a superconductor. As a consequence, the energy distribution function in the wire presents multiple steps.

In the experiments, the out-of-equilibrium distribution functions were obtained by numerical deconvolution of the differential conductance of a tunnel junction formed between the normal wire and a superconducting probe [2]. The position of the steps in the measured distribution functions is well accounted for by the picture of Andreev reflections occurring at the NS interfaces (see Figure 6). Yet, these steps are rounded, revealing a redistribution of energy among the electrons. To account for this rounding, electron-electron interaction and electron-phonon interaction need to be included in the calculation, within the framework of the stationary Boltzmann equation [6], Andreev reflections at the NS interface entering as boundary conditions. As shown in Figure 7, this approach leads to a precise description of the measured distribution functions in wires that are long enough.

Even if this simple approach accounts successfully for the energy distribution functions in the normal wire, it fails in explaining the current-voltage characteristic of the SNS system, which presents a structure that was also observed by Hoss *et al.* [18]. In contrast, the Boltzmann equation approach predicts a linear current-voltage characteristic. It appears hence that the modification of the density of states near the NS interfaces due to proximity effect, which leads to a renormalization of the diffusion coefficient, cannot be neglected to understand the current-voltage characteristic. It is only because the length scale on which the density of states

is modified is small compared to the wire length that this effect could be neglected in the calculation of the distribution functions.

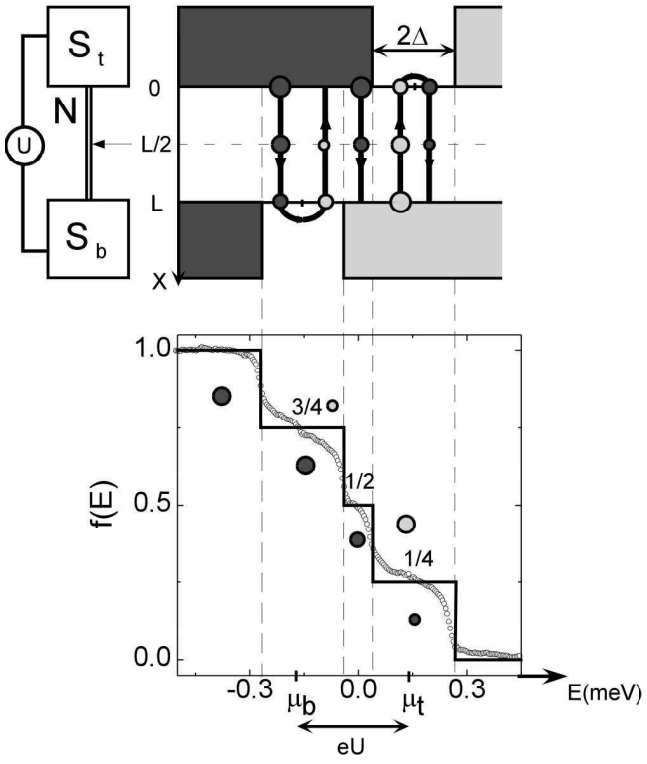

Figure 6: Left: Layout of the experiment: A voltage U is applied between two superconductors (S) connected through a normal wire (N) of length L. A superconducting probe, represented by an arrow, forms a tunnel junction with the central part of the wire. Right: Top: Representation in the energy (horizontal axis) and position (vertical axis) space of the quasiparticle paths responsible for the current transport. The excitation spectra of the top and bottom superconductors have a gap 2Δ centered on their electrochemical potentials μ_t and μ_b ($\mu_t - \mu_b = eU$), with electron states occupied at negative energies (dark areas) and empty at positive energies (light gray areas). Quasiparticle paths consist of electrons (dark disk) and holes (light gray disk) trajectories at symmetric energies about μ_t and μ_b, connected by Andreev reflection. The area of the disk is proportional to the occupation factor of the quasiparticle state, which varies linearly along the path from 1 to 0. The bottom plot shows the energy distribution measured at the center of a 5-μm long silver wire connected to two aluminum superconducting pads (symbols), and the prediction (solid line) of the theory without interactions between quasiparticles.

Hence, we find that even if some manifestations of out-of-equilibrium proximity effect can be understood by *ad-hoc* adaptations of existing theories, a theory that includes interactions between electrons and that treats non-stationary cases is missing.

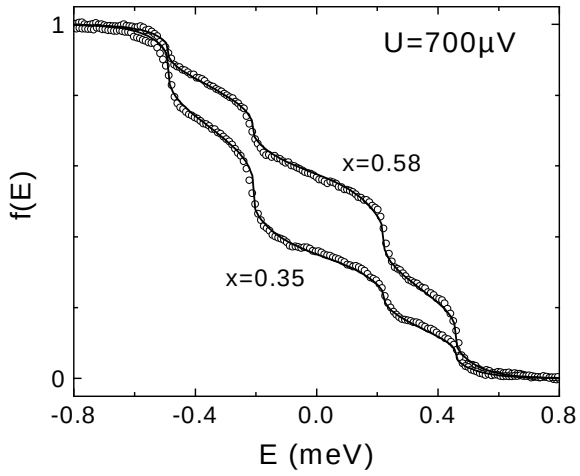

Figure 7: Symbols: Distribution functions measured at two positions in a 5 μm-long silver wire, connected at both ends ($x = 0$ and $x = 1$) to superconducting electrodes biased at the potential 0 and 700 μV. Solid lines: Solution of the Boltzmann equation accounting for the Andreev reflections at the reservoirs and electron-electron interactions within the wire.

References of chapter 1

[1] Yang Yi, Yunchul Chung, D. Sprinzak, M. Heiblum, D. Mahalu, and Hadas Shtrikman, Nature **422**, 415 (2003).

[2] J. M. Rowell, in *Tunneling Phenomena in Solids*, edited by E. Burstein and S. Lundqvist (Plenum, New York, 1969), p. 385; T. Claeson, *ibid.*, p 443.

[3] D. Pines, and P. Nozières, *The Theory of Quantum Liquids* (W. A. Benjamin, New York, 1966).

[4] P. Mohanty, E. M. Q. Jariwala, and R. A. Webb, Phys. Rev. Lett. **78**, 3366 (1997).

[5] D. S. Golubev and A. D. Zaikin, Phys. Rev. Lett. **81**, 1074 (1998).

[6] F. Pierre, Ann. Phys. (Paris) **26**, No 4 (2001).

[7] A. Kaminski and L. I. Glazman, Phys. Rev. Lett. **86**, 2400 (2001).

[8] F. Pierre, A. B. Gougam, A. Anthore, H. Pothier, D. Esteve, and N.O. Birge, Phys. Rev. B **68**, 085413 (2003).

[9] A. Anthore, F. Pierre, H. Pothier, and D. Esteve, Phys. Rev. Lett. **90**, 076806 (2003).

[10] D. K. Wohlleben and B. R. Coles, in *Magnetism*, edited by H. Suhl (Academic, New York, 1973), Vol. 5.

[11] For a review, see G.L. Ingold and Yu. Nazarov, in *Single Charge Tunneling*, edited by H. Grabert and M.H. Devoret (Plenum Press, New York, 1992).

[12] G. Göppert, Y.M. Galperin, B.L. Altshuler, and H. Grabert, Phys. Rev. B **66**, 195328 (2002).

[13] A. Anthore, F. Pierre, H. Pothier, D. Esteve and M.H. Devoret, (cond-mat/ 0109297) *Electronic Correlations: From Meso- to Nano-physics*, edited by T. Martin, G. Montambaux, and J. Trân Thanh Vân (EDP Sciences, New York, 2001).

[14] For a review, see W. Belzig, F. K. Wilhelm, C. Bruder, G. Schon, and A. D. Zaikin, Superlattices and Microstructures, vol. 25 No 5/6 (1999) (cond-mat/9812297).

[15] A. Anthore, H. Pothier, and D. Esteve, Phys. Rev. Lett. **90**, 127001 (2003).

[16] F. Pierre, A. Anthore, H. Pothier, C. Urbina and D. Esteve, Phys. Rev. Lett. **86**, 1078 (2001).

[17] P. Dubos, H. Courtois, O. Buisson and B. Pannetier, Phys. Rev. Lett. 87, 206801 (2001).

[18] T. Hoss, C. Strunk, T. Nussbaumer, R. Huber, U. Staufer, and C. Schönenberger, Phys. Rev. B **62**, 4079-4085 (2000).

PART 1

EXPERIMENTAL TECHNIQUES

Chapter 2 Tunnel spectroscopy of mesoscopic systems

Tunneling of electrons between metallic electrodes provides spectroscopic information on the densities and filling of the states of the electrodes [1]. Tunnel spectroscopy is thus a powerful technique to probe mesoscopic effects, and has been used extensively in this thesis. In the following, the principles of tunnel spectroscopy are described.

2.1 Tunnel junctions

2.1.1 Description

A tunnel junction consists of two conductors separated by a thin insulating layer (see Figure 1).

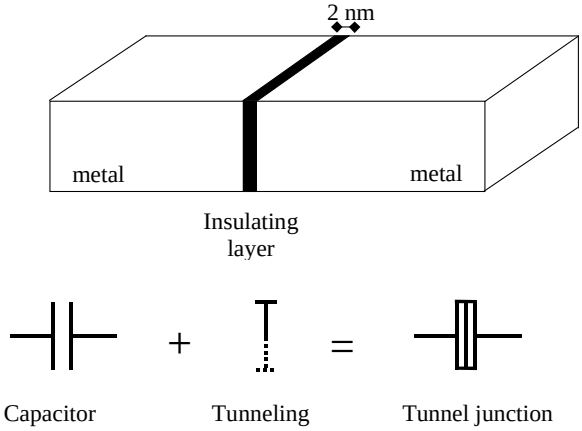

Figure 1: Top: Tunnel junction between metallic electrodes. The thin insulating layer is a barrier that conducting electrons cannot cross according to classical physics. However, if the insulating layer is thin enough, quantum tunneling of electrons through the barrier leads to a measurable conductance. Bottom: Model of a tunnel junction: The junction is decomposed into a tunnel element of resistance R_T in parallel with a capacitance C.

Although electrons cannot propagate in the insulator, the barrier is thin enough to allow electron transfer by quantum tunneling, which leads to a measurable conductance. A tunnel junction is decomposed into the parallel combination of a tunnel element of resistance R_T and a capacitance C, which accounts for the possible charging of the metallic electrodes on both sides of the insulating layer.

2.1.2 Current through an N-X tunnel junction

The expression of the current through a tunnel junction with at least one electrode in the normal state (N), embedded in an electromagnetic environment, involves the distribution functions (f_L and f_R) and the density of states (DOS) of both electrodes (n_L and n_R in units of the density of states at the Fermi level ν_F of the considered metal), and the probability $P(\varepsilon,T)$ that a part ε of the available energy is released to the electromagnetic environment of the junction when a tunnel event occurs [2]:

$$I(V)=\frac{1}{eR_T}\int_{-\infty}^{+\infty}dE\; n_L(E)\int_{-\infty}^{+\infty}d\varepsilon\; P(\varepsilon,T)\;\Big(f_L(E)n_R(E-eV-\varepsilon)\big(1-f_R(E-eV-\varepsilon)\big) -\big(1-f_L(E)\big)n_R(E-eV+\varepsilon)f_R(E-eV+\varepsilon)\Big), \quad (1)$$

where e is the absolute value of the electronic charge (see Figure 2).

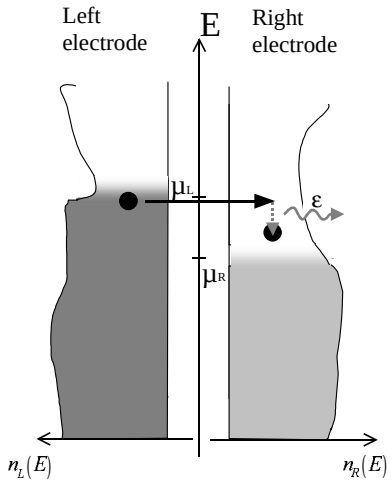

Figure 2: Tunneling process through a junction when the junction is voltage biased: $eV=\mu_L-\mu_R$. The current through the junction depends on the density of states in the electrodes n_L and n_R, the filling of these states f_L and f_R, and the probability $P(\varepsilon,T)$ that the energy ε is released to the electromagnetic environment.

When the tunnel junction is formed between a superconducting electrode S and a normal metal N with negligible resistance, Eq. (1) simplifies considerably:

$$I(V) = \frac{1}{eR_T} \int_{-\infty}^{+\infty} dE\, n_S(E - eV)\left(f_N(E) - \Theta(E - eV)\right), \qquad (2)$$

with the function $\Theta(E) = 1$ if $E < 0$ and $\Theta(E) = 0$ if $E \geq 0$.

2.2 Principle of tunnel spectroscopy

To perform tunnel spectroscopy, we take advantage of simple configurations with normal and superconducting electrodes, embedded or not in a resistive environment, for which the current-voltage characteristic is non-linear. Then, if only one quantity in Eq. (1) is unknown, spectroscopic information on the density or filling of the states is obtained from the measurement of the differential conductance dI/dV of the junction. The different configurations used in this thesis are presented in Figure 3.

- An NS tunnel junction allows to perform the tunnel spectroscopy of the density of states in the superconducting part (case 1), or of the energy distribution function in the normal part (case 2).
- When an NN junction is embedded in a resistive environment, the quasiparticle energy distribution in one of the normal electrodes can be inferred from the differential conductance of the tunnel junction. This set-up allows to measure the quasiparticle energy distribution in presence of a magnetic field.

In set-ups aiming at the measurement of the energy distribution of quasiparticles $f(E)$, the differential conductance is not directly proportional to $f(E)$ but to a convolution of $f(E)$ with a known function that depends on the physical process involved. The procedure to infer $f(E)$ from the differential conductance is detailed in the following.

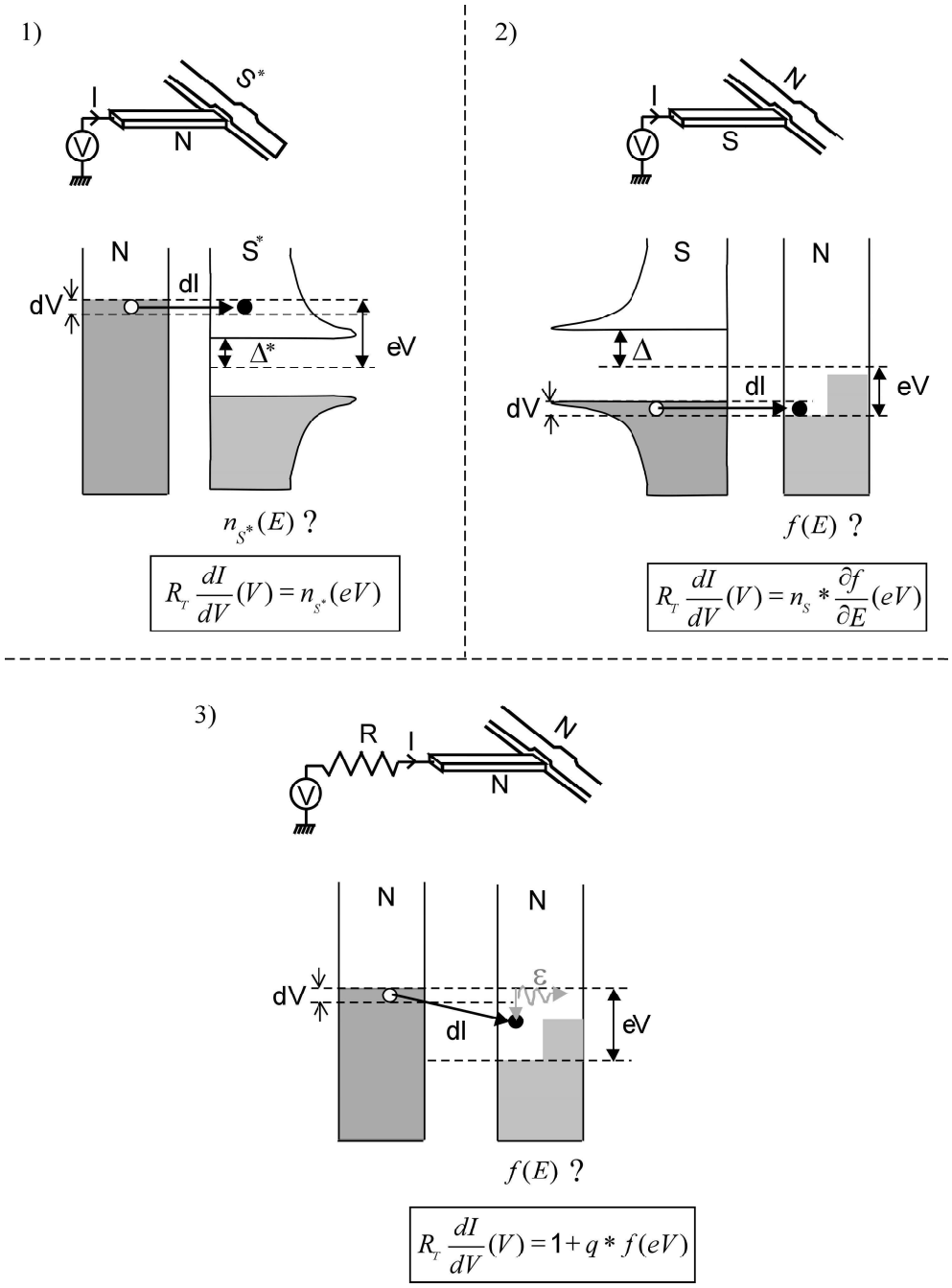

Figure 3: 1), 2) and 3): Top: A tunnel junction is formed between a probe electrode (left) in which the density of states and the filling factor are well known and an electrode (right) in which either the density of states $n(E)$, or the filling factor $f(E)$ are to be probed. Bottom: Representation of the electronic states and their filling for both electrodes. In each case, the unknown quantity in the right electrode, and its relation with the differential conductance of the junction are given.

2.3 Tunnel spectroscopy of the quasiparticle energy distribution function in a normal metal

2.3.1 Relation between the tunnel junction differential conductance and the distribution function

When performing the tunnel spectroscopy of the distribution function, the differential conductance can be written in the generic form:

$$R_T \frac{dI}{dV}(V) = 1 + q * f(eV), \tag{3}$$

where $q(E)$ is a function dependent on the junction and on the environment characteristics.

2.3.1.1 Case of a superconducting-normal junction

When the probe electrode is superconducting, $q(E)$ is the derivative of the density of states n_S in the superconducting electrode. In our experiments, this density of states n_S is well described by the BCS function:

$$n_S(E) = \frac{|E|}{\sqrt{E^2 - \Delta^2}}. \tag{4}$$

2.3.1.2 Case of a normal-normal junction: dynamical Coulomb blockade of tunneling

When both electrodes are normal, *i.e.* $n_L(E) = n_R(E) = 1$, but in presence of a resistive environment for the junction, a convolution product is also found as a result of Coulomb blockade. The current through the junction can be written from Eq. (1):

$$I(V) = \frac{1}{eR_T}\int_{-\infty}^{+\infty} dE \int_{-\infty}^{+\infty} d\varepsilon\ P(\varepsilon,T)\ \Big(f_L(E)\big(1 - f_R(E + eV - \varepsilon)\big) - \big(1 - f_L(E)\big) f_R(E + eV + \varepsilon)\Big). \tag{5}$$

The differential conductance can be written as (using the normalization $\int_{-\infty}^{+\infty} d\varepsilon\, P(\varepsilon,T) = 1$):

$$\frac{dI}{dV}(V) = \frac{1}{R_T}\left(1 + \int_{-\infty}^{+\infty} d\varepsilon\ P(\varepsilon,T) \int_{-\infty}^{+\infty} dE\ f_L(E) \frac{\partial\big(f_R(E + eV + \varepsilon) - f_R(E + eV - \varepsilon)\big)}{\partial E}\right), \tag{6}$$

which can be recast in the form (3) with:

$$q(E) = \int_{-\infty}^{+\infty} d\varepsilon \; P(\varepsilon, T) \frac{\partial \left(f_R(E+\varepsilon) - f_R(E-\varepsilon) \right)}{\partial E}.$$

The determination of $P(\varepsilon, T)$ is based on the Coulomb blockade theory (see Appendix). The function $q(E)$ depends then on the impedance of the environment, the capacitance of the junction and the electronic temperature in the probe electrode. Practically, the quasiparticle energy distribution function in the normal probe electrode f_R is assumed to be a Fermi function at a temperature close to the fridge temperature.

2.3.2 Experimental procedure

To characterize the function $q(E)$ entering in the expression of the differential conductance (Eq. (3)), the differential conductance $dI/dV(V)$ is first measured with both electrodes at equilibrium. The distribution functions are in this situation Fermi functions at a temperature close to the refrigerator temperature. The characteristics of the probe electrode are then determined from a fit of $dI/dV(V)$ with Eq. (3). When the probe electrode is superconducting, the parameters to be determined are the tunnel resistance of the junction R_T and the gap Δ of the BCS density of states (Eq. (4)). When the probe electrode is normal, the parameters to be determined are the tunnel resistance of the junction R_T, the resistance R_p and the temperature T of the probe electrode, and the capacitance of the junction C. Examples of fits are shown in the top of Figure 4 for both cases.

After this calibration step, the differential conductance obtained with a modified $f(E)$ in the wire is measured (see Figure 4). When the probe electrode is superconducting, the data are deconvolved using Eq. (3) to obtain the corresponding $f(E)$ [3] (see Chapter 7). The deconvolution procedure uses a steepest descent method [4]. When the probe electrode is normal, the deconvolution procedure could not be applied in our experiments. The reason is that the Coulomb singularity is not as sharp as the BCS singularity so that the signal to noise ratio is too small to avoid additional numerical noise during the deconvolution procedure. We have then chosen to fit the measured differential conductance with Eq. (3) using the function

$q(E)$ as determined in the calibration step and a function $f(E)$ calculated with a model in which few fit parameters enter (see Chapter 7).

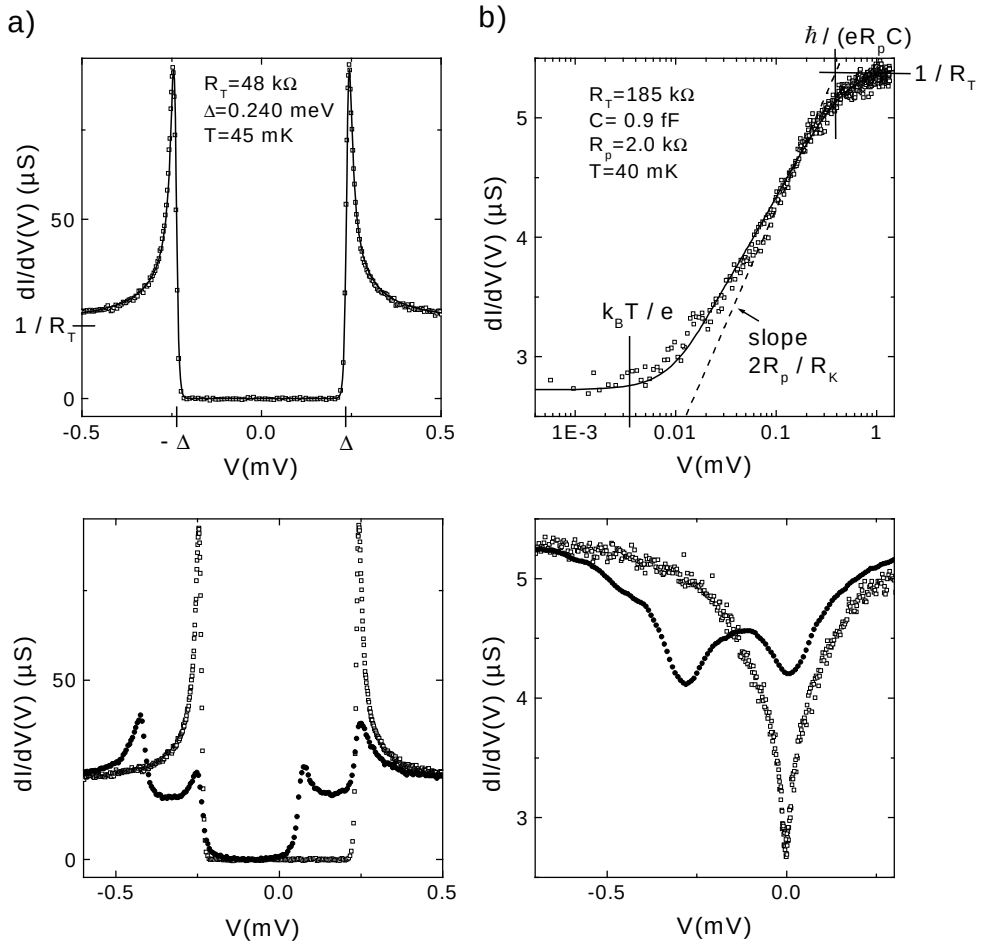

Figure 4: Top: a) Symbols: Measured differential conductance of an NS junction. Line: Fit using Eqs. (3) with $R_T = 48\ \mathrm{k\Omega}$, $\Delta = 0.240\,\mathrm{meV}$, and a distribution function $f(E)$ equal to a Fermi function at $45\ \mathrm{mK}$. b) Symbols: Differential conductance of a normal-normal tunnel junction, embedded in a resistive environment. Solid line: Fit using Eq. (6) with the parameters: $R_T = 185\ \mathrm{k\Omega}$, $C = 0.9\,\mathrm{fF}$, $R_p = 2\ \mathrm{k\Omega}$ and $T = 40$ mK. Bottom: a) and b) Open symbols: Same curves as in top panel. Full symbols: Example of measured differential conductance when the quasiparticle energy distribution function is modified in the normal electrode to be probed.

Appendix: Dynamical Coulomb blockade

A review on dynamical Coulomb blockade can be found in [2]. In this appendix, we just present the equations used to calculate the function $q(E)$ to be convolved with the energy distribution function in the case of a normal resistive probe electrode (see Section 2.3.1.2).

When a tunnel junction is embedded in an electromagnetic environment, the probability $P(\varepsilon,T)$ that a part ε of the available energy in a tunnel event is released to the environment is determined by the environment impedance $Z(\omega)$ [2]:

$$\begin{aligned} P(\varepsilon,T) &= \int_{-\infty}^{+\infty} \frac{dt}{2\pi\hbar} \exp\left(J(t,T) + i\varepsilon t/\hbar\right) \\ J(t,T) &= \int_{-\infty}^{+\infty} \frac{d\omega}{\omega} 2\,\mathrm{Re}\left(\frac{Z(\omega)}{R_K}\right) \frac{e^{-i\omega t}-1}{1-e^{-\frac{\hbar\omega}{k_B T}}}, \end{aligned} \tag{7}$$

with $R_K = h/e^2 \simeq 25.813\ \mathrm{k\Omega}$ the resistance quantum.

In the case of a resistive environment, the circuit can be modeled as shown in Figure 5.

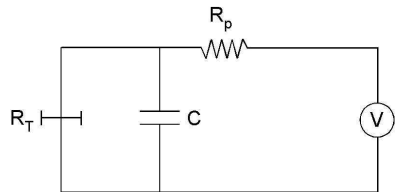

Figure 5: Electrical circuit representing a tunnel junction in a resistive environment: the junction between the wire and the probe is decomposed into a tunnel element of resistance R_T in parallel with a capacitance C, whereas the probe electrode is represented as a resistance R_p. The environment impedance $Z(\omega)$ is the parallel combination of R_p and C.

The environmental impedance $Z(\omega)$ consists of the parallel combination of the junction capacitance C with the probe resistance R_p:

$$Z(\omega) = R_p / \left(1 + iR_p C\omega\right).$$

For this impedance, $J(t)$ has an analytical expression from which $P(\varepsilon,T)$ can be calculated [5]:

$$J(t)=\frac{\pi R_p}{R_K}\left(\left(1-e^{-\omega_c|t|}\right)\left(\cot\frac{\hbar\omega_c}{2k_BT}-i\right)-\frac{2|t|}{\hbar k_BT}+2\sum_{n=1}^{+\infty}\frac{\omega_c^2\left(1-e^{-\omega_n|t|}\right)}{2\pi n\left(\omega_n^2-\omega_c^2\right)}\right), \tag{8}$$

where $\omega_n=2\pi n\,k_BT/\hbar$ are the Matsubara frequencies and $\omega_C=1/\left(R_pC\right)$ is the cutoff frequency of $Z(\omega)$. The probability $P(\varepsilon,T)$ is represented in Figure 6 in a case similar to the experiments ($C=0.9$ fF , $R_p=2.0$ kΩ and $T=40$ mK).

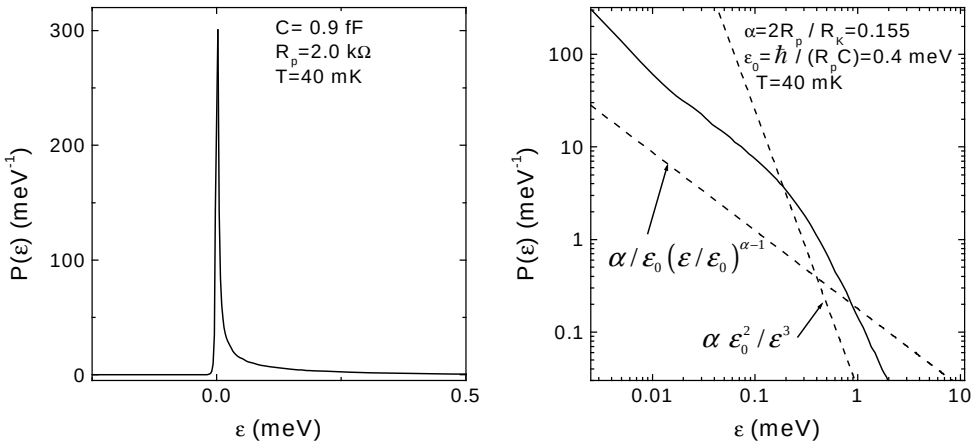

Figure 6: Left: Probability $P(\varepsilon)$ that a part ε of the energy is released to the electromagnetic environment when a tunnel event occurs, calculated at $T=40$ mK for a junction with capacitance 0.9 fF , embedded in a resistive environment of $R_p=2.0$ kΩ . Right: Log-log plot of $P(\varepsilon)$ in the same conditions for $\varepsilon>0$ (solid line) and of the asymptotic limit at $T=0$ (dashed lines). For low energies, $P(\varepsilon)\approx\alpha/\varepsilon_0\left(\varepsilon/\varepsilon_0\right)^{\alpha-1}$ and for large energies, $P(\varepsilon)=\alpha\,\varepsilon_0^2/\varepsilon^3$ with $\alpha=2R_p/R_K$ and $\varepsilon_0=\hbar/\left(R_pC\right)$. The effect of temperature is to increase $P(\varepsilon)$ and to allow the environment to emit energy, resulting in the non-zero value of $P(\varepsilon)$ at negative energies.

References of chapter 2

[1] J. M. Rowell, in *Tunneling Phenomena in Solids*, edited by E. Burstein and S. Lundqvist (Plenum, New York, 1969), p. 385; T. Claeson, *ibid.*, p 443.

[2] G.-L. Ingold and Yu. Nazarov in *Single Charge Tunneling*, edited by H. Grabert and M. H. Devoret (Plenum Press, New York, 1992)

[3] S. Guéron, PhD thesis: *"Quasiparticles in a diffusive conductor: Interaction and pairing"*, University Paris VI, october 1997; F. Pierre, Ann. Phys. (Paris) **26,** No 4 (2001).

[4] *Numerical Recipes*, Cambridge University Press (Cambridge, 1987), Chapter 10.

[5] P. Joyez and D. Esteve, Phys. Rev. B **56**, 1848 (1997); Phys. Rev. B **58**, 15912 (1998).

Chapter 3 Sample processing

3.1 Sample fabrication

In the following, we describe the different steps of sample fabrication. The samples are made using electron-beam lithography and standard deposition techniques. Most of them are fabricated in a single pump-down, using deposition at several angles through a suspended shadow mask.

A typical fabrication scheme is outlined in Figure 1.

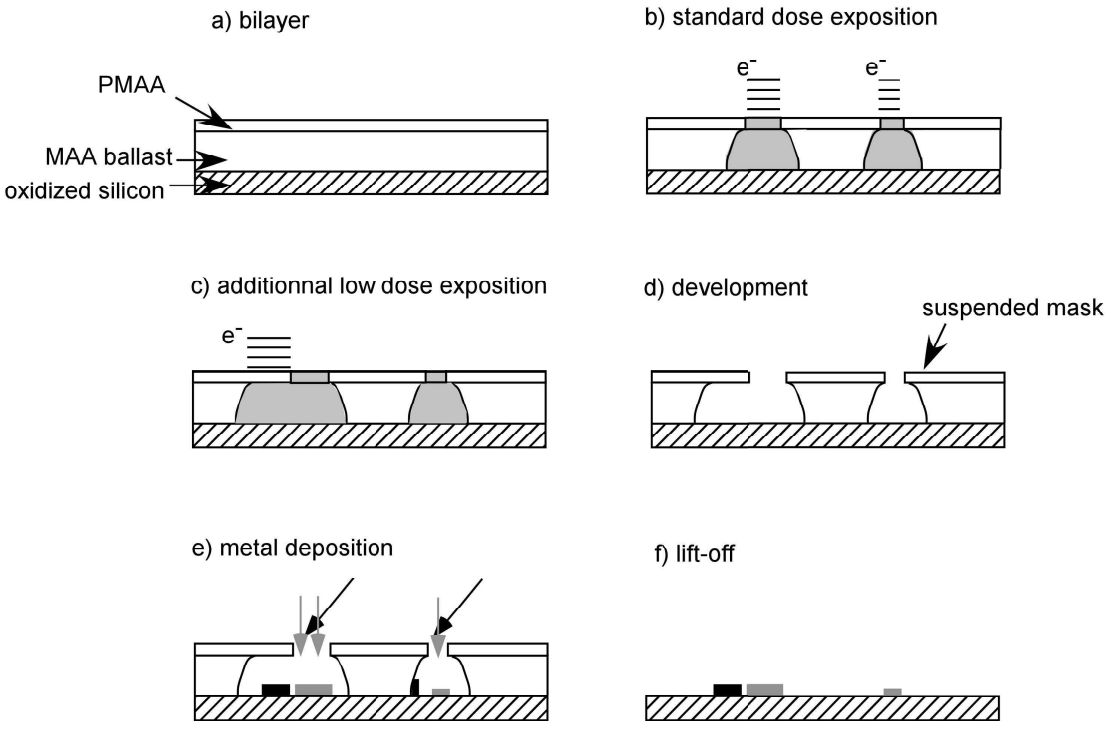

Figure 1: Typical fabrication scheme: a) Substrate coated with a bilayer of resists; b) and c) e-beam exposure; d) suspended mask after development; e) metal deposition through the suspended mask. f) structure after the final lift-off step.

3.1.1 Wafer preparation

3.1.1.1 Monolayer coating

This process is used for the lithography of large numbers of samples at once. An oxidized silicon wafer is coated with UVIII^{TM} [1], a highly electrosensitive polymer (12 $\mu C/cm^2$). After having spun a primer at 2000 rpm/min for 1 min, UVIII^{TM} is spun at 2000 rpm/min for 2 min and prebaked at 135 °C on a hot plate for about 1 min; the obtained thickness is 500 nm.

3.1.1.2 Bilayer coating

This process is used when a suspended mask over a ballast layer is required. The process begins with the coating of an oxidized silicon wafer with two layers of electrosensitive polymers. The ballast layer sustains the second layer, which constitutes the mask. The bottom layer is a copolymer whose chains are more easily broken by exposure to the electron beam than those of the top polymer, so that an undercut is obtained. We have used the following coating procedure:

Bottom layer: Copolymer polymethyl-meta-acrylate/meta-acrylate acid (PMMA/MAA) diluted in mass at 10 % in ethyl-lactate. The molecular mass of the MAA is 8.5 K. Spun at 4000 rpm/min for about 60 s and baked on a hot plate at 180 °C for 10 min, the thickness is about 500 nm.

Top layer: PMMA of molecular mass 950 K diluted at 3 % in anisole. Spun at 8000 rpm/min for about 60 s and baked on a hot plate at 180 °C for 30 min, the obtained thickness is about 100 nm.

The coated wafer is then cut into $6 \times 6\ mm^2$ chips, which are processed individually.

3.1.2 Sample processing

3.1.2.1 Wafer processing

3.1.2.1.1 Electron beam exposure

The patterning is done by steering the beam of a Philips XL30 SFEG scanning electron microscope. The exposure pattern, dose and blanking of the beam are controlled by the Elphy-quantum software from Raith. We currently use a beam acceleration voltage of 25 kV. The sample holder is shifted between each pattern.

3.1.2.1.2 Development

Monolayers of UVIII^{TM} resist are post-baked on a hot plate at 140°C for 1 min, developed in MEGAPOSIT$^{®}$ MF CD-26 for 60 s and rinsed in pure water.

3.1.2.2 Single chip processing

3.1.2.2.1 Exposure to electron beam

The patterning of each chip is done with the beam of a JEOL 840A scanning electron microscope. The exposure pattern, dose and blanking of the beam are controlled by the Proxy-writer software from Raith. We use a beam acceleration voltage of 35 kV, for which the standard exposure dose for PMMA is about 200 $\mu C/cm^2$.

3.1.2.2.2 Development

Bilayers are developed in a solution of MIBK diluted in isopropanol (MIBK: 1 IPA: 3) while being sonicated for 45 s, then rinsed in IPA. A suspended mask is then obtained.

3.1.3 Metal deposition and oxidation

Metal deposition and tunnel junction fabrication proceed in an electron gun evaporator. The sample is positioned on a tiltable sample holder. Junctions between different materials are obtained by deposition through several slits in the suspended mask, as shown in

Figure 2. The first image of one slit overlaps with a part of the image of another slit. Tunnel barriers are formed by oxidizing aluminum with an oxygen-argon mixture (20-80 %). After deposition, the mask and resist are lifted off in acetone at 65 °C. The fine details on UVIII^{TM} wafers are lifted off in ethanol at room temperature, with a few seconds sonication at the end.

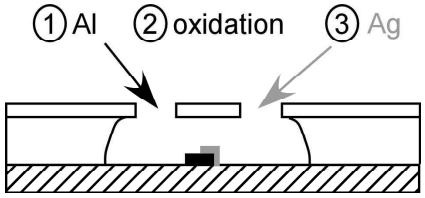

Figure 2: Fabrication of a superconducting/normal tunnel junction in a two-angle deposition process. In our experiments, the superconductor is aluminum, the insulating layer is aluminum oxide, and the normal metal is silver, copper or gold.

3.2 Example: Sample used for energy exchange measurements in presence of an applied magnetic field

As explained in Chapter 2, information on energy relaxation in a magnetic field was inferred from the differential conductance of a tunnel junction formed between a wire and a resistive probe. The wire itself was connected to two much thicker pads, which played the role of reservoirs. Two different fabrication processes have been developed. In the first one, we processed chip by chip: the whole design was defined in a single lithography step, followed by a three-angle evaporation. In the second one, two lithography steps were used: the first one to form the wire and its reservoirs, the second one to form the probe electrode. This more complex process allows the implantation of magnetic impurities before junction fabrications, which avoids the destruction of the barrier by the ion beam.

3.2.1 One-step processing

A typical mask used is shown in Figure 3. The zones defining the wire, the reservoirs and the shifted long probe finger are exposed with the nominal dose. The area around the long

probe finger is exposed with a low dose so that an undercut is created below the PMMA mask. Therefore, the image of the probe at an angle falls on the substrate and below the wire. The additional low dose exposure in other regions just helps the formation of this undercut. The probe finger is obtained by depositing 17 nm of aluminum at +55 ° angle, oxidized afterwards; the wire is obtained by depositing 45 nm of metal (silver, copper, gold or aluminum) at 0° angle, and the reservoirs are obtained by depositing 430 nm of gold (or aluminum) at –50 °. Since there is no undercut around the wire, its Al image lies on the side of the ballast and is removed by the lift-off. The unwanted aluminum projection of the wire, which would have been connected in parallel with the tested wire, is thus avoided. The gold images of the fine wires in the third step are avoided because the slits defining the wires clog before the end of evaporation.

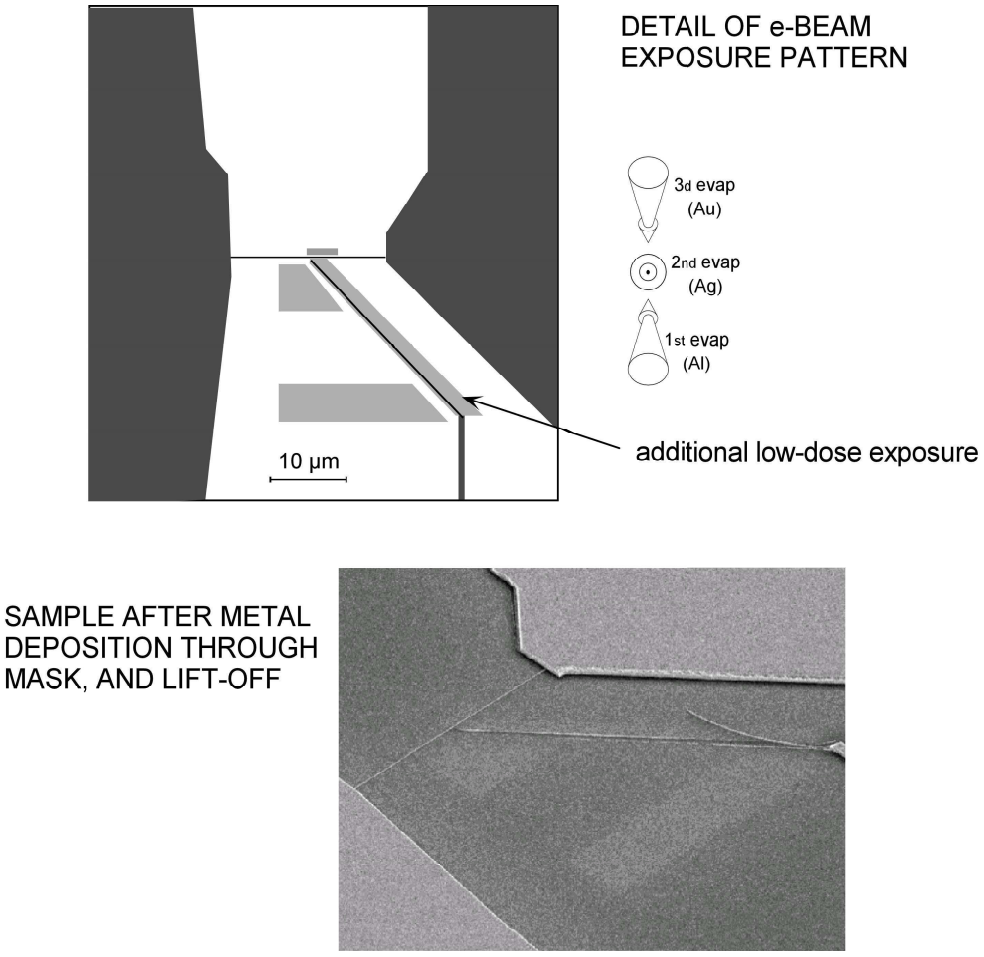

Figure 3: One-step fabrication of a sample for the energy exchange measurement in a magnetic field. Top: exposure pattern of the center of the chip, with dose encoded in levels of gray. The arrows indicate schematically the order and angle of deposition of the different metals. Bottom: Actual sample, seen at an angle.

3.2.2 Two-step processing

This process is used to perform experiments with controlled impurity concentrations, obtained by ion implantation. The previous process cannot be used because the tunnel junctions are too fragile: in a few hours they evolve from a few kiloohms resistance to an open circuit. Moreover, the tunnel barriers turn to short-circuit during ion implantation. These difficulties are circumvented with the two-step process. In a first step, a complete wafer, coated with UVIII^{TM}, is e-beam exposed, defining 64 patterns (see Figure 4). These patterns consist of 120 nm-wide wires of different length (5, 10, 20, and 40) connected to two large pads, together with a third pad used in the second step (see Figure 5) and 895-µm long wires to allow weak localization measurements. Then, 45 nm and 100 nm of silver are deposited at angles 0° and 50°, respectively. After lift-off, the wafer is split in two parts so that part of the wires can be implanted with manganese ions. Afterwards, the wafer is coated with MAA-PMMA[1] to realize the second lithography step. The coated wafer is then cut into small chips, which are processed individually. In the second step, we pattern the measure probe, realigned on the first pattern of silver. To obtain good quality junctions, the silver is cleaned by ion milling before deposition (in 10^{-4} mb of Ar, $V = 500$ V , $I = 5$ mA for 5 s). Afterwards 3 nm of aluminum is deposited at 30° angle and oxidized at 1 torr for 10 min to form the tunnel junction. Finally, 12 nm of aluminum is deposited at 30° to form the resistive probe in a magnetic field.

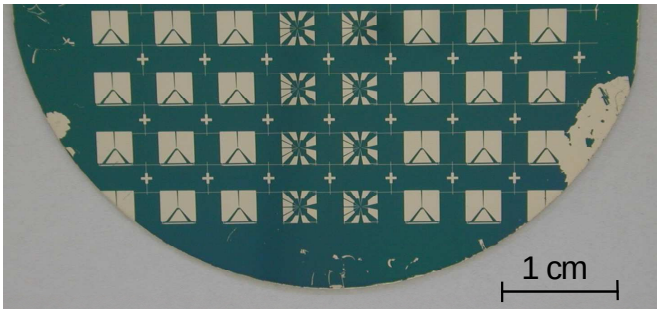

Figure 4: Part of the wafer processed to be ion-implanted. In the middle, eight samples are dedicated to weak localization measurements. The other ones are processed individually in a second lithography step.

[1] The bilayer of MAA-PMMA is only baked at 140°C instead of 180°C. We prefer to heat our samples as little as possible because the silver films deposited in a first step degrade with temperature.

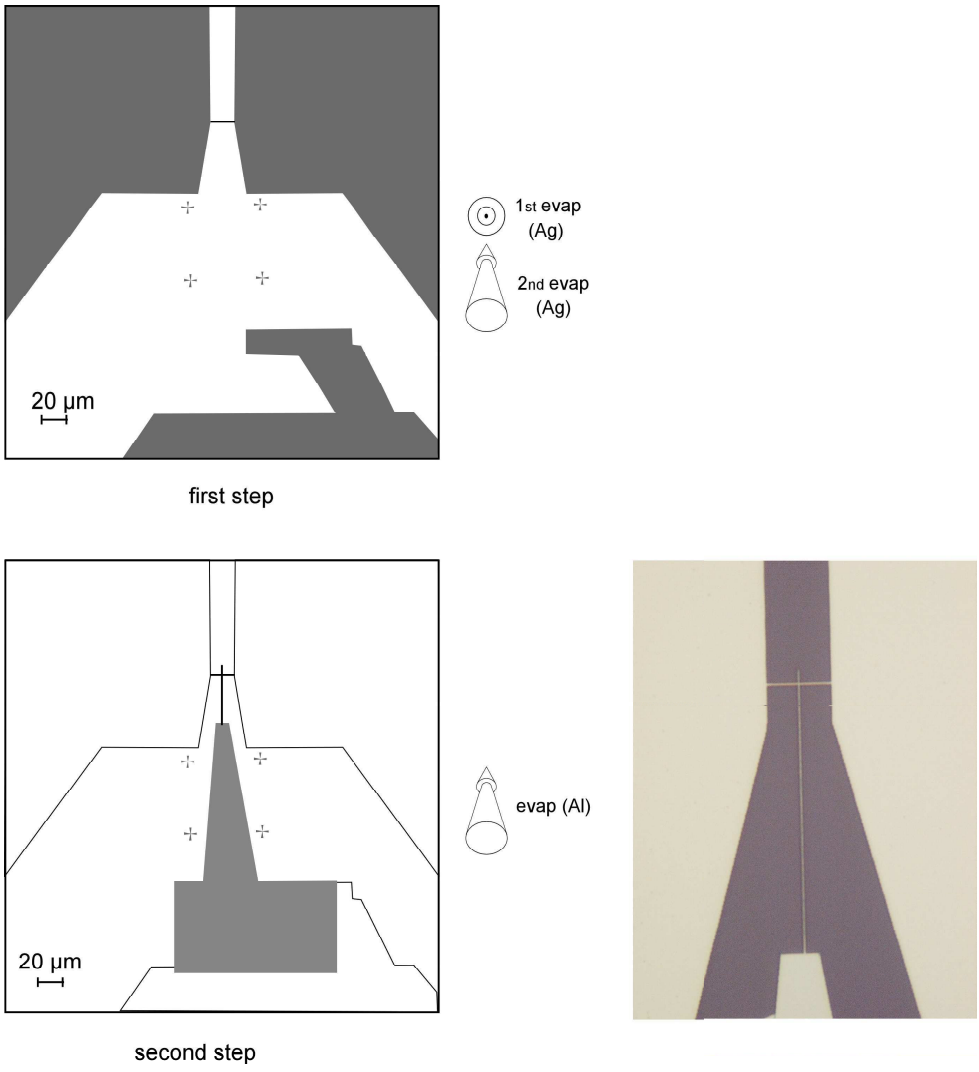

Figure 5**:** Two-step fabrication of a sample for the energy exchange measurement in a magnetic field. Exposure pattern of the center of the chip for both steps. The arrows indicate schematically the order and angle of deposition of the different metals. Right: Optical image of the center of the final chip.

3.3 Implantation of magnetic impurities in thin films

The implantation of manganese in silver wires, for the experiments on electron-electron interaction, was realized at the CSNSM at Orsay University by O. Kaitasov, S. Gautrot, and J. Chaumont in the medium energy implantor IRMA [2]. A $MnCl_2$ source is first

vaporized in vacuum ($1.8\,10^{-6}$ mb). A plasma is formed by electronic arc discharge to obtain charged manganese ions $^{55}Mn^{+}$. These ions are first accelerated at 40 keV and separated electromagnetically from other isotopes and elements obtained from the impurities (mainly FeCl) in the source. They are once again accelerated at 30 keV, a value calculated to obtain a Gaussian impurity concentration in the thickness of the silver film. The ion beam is focused thanks to an electrostatic quadripolar triplet lensing system. The ion beam, of section 1 cm^2, is swept on the sample holder so that the dose is homogeneous. During the implantation process, the current flowing from the sample holder to ground is monitored to control the total amount of ions received. Secondary electrons are repelled towards the sample by a negative polarized grid. Typically, the measured current was of 10 nA on a surface of 56.5 cm^2. In 195 s, a 1 ppm concentration of Mn impurities is implanted in 0.045 µm thick silver films. This corresponds to 5300 ions in the volume of a $0.045\times0.1\times20$ μm^3 wire.

References of chapter 3

[1] UVIII^{TM} is a positive resist from Shipley supplier with organic compounds diluted in ethyllactate.

[2] J. Chaumont, F. Lalu, M. Salomé, and A.M. Lamoise, Nucl. Instr. and Meth. **189**, 193 (1981).

Chapter 4 Measurements at low temperature

Once processed, the chip is glued with silver paint on a sample holder fitted with connectors. The circuit pads are bonded to the pins of the connector with 25 µm-diameter aluminum wires. The sample holder is thermally anchored to the mixing chamber of a dilution refrigerator through a copper braid (see Figure 1).

Electrical connections to the sample are made through filtered coaxial lines (see Figure 2). Microfabricated distributed RC filters shaped as meander lines [1] are used as well as lossy coaxial cables. The voltage drop across the sample is measured in series with the last filter stage, using a twisted-pair connection and a low-noise, battery-powered room-temperature pre-amplifier (NF LI-75A). The current in the sample is produced by applying a voltage to a bias line consisting of a voltage divider in series with a resistance. The current is calculated from the input voltage, the measured voltage across the sample and the resistance values of filters and lines. To measure differential conductance curves, a small AC modulation is added to the DC voltage and a lock-in detection is performed. The bias and output voltages are recorded on a computer through IEEE connections.

It is possible to measure in a single cool-down several circuits with a single bias line and a single twisted pair thanks to a 12-position rotary switch connected to the bias and measuring lines at the output of the last filter. Six resistors of known values, connected in-between, mark the positions. Positions are switched by a motor thermally anchored to the still of the dilution refrigerator.

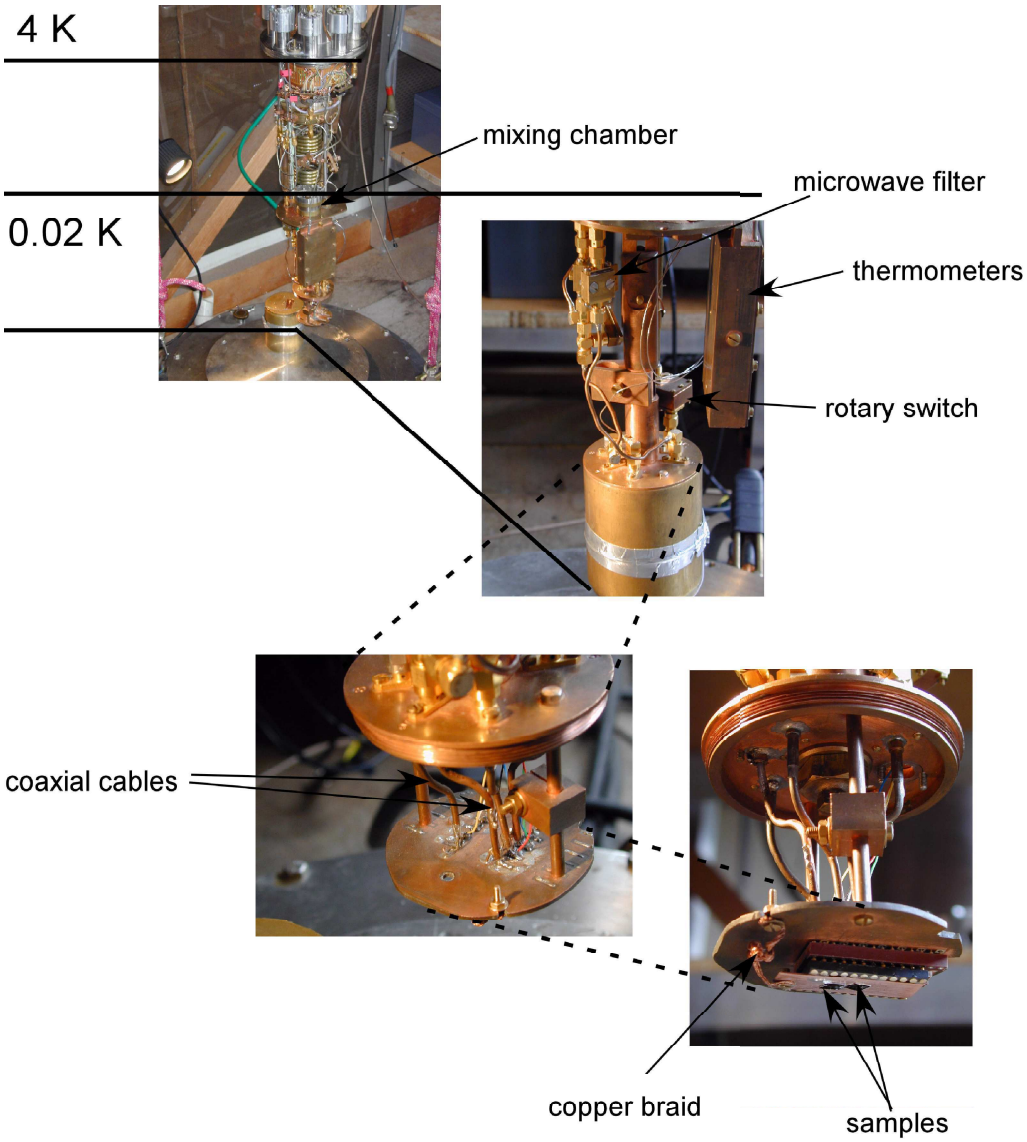

Figure 1: : Photographs of the insert in the dilution refrigerator and details of the sample holder.

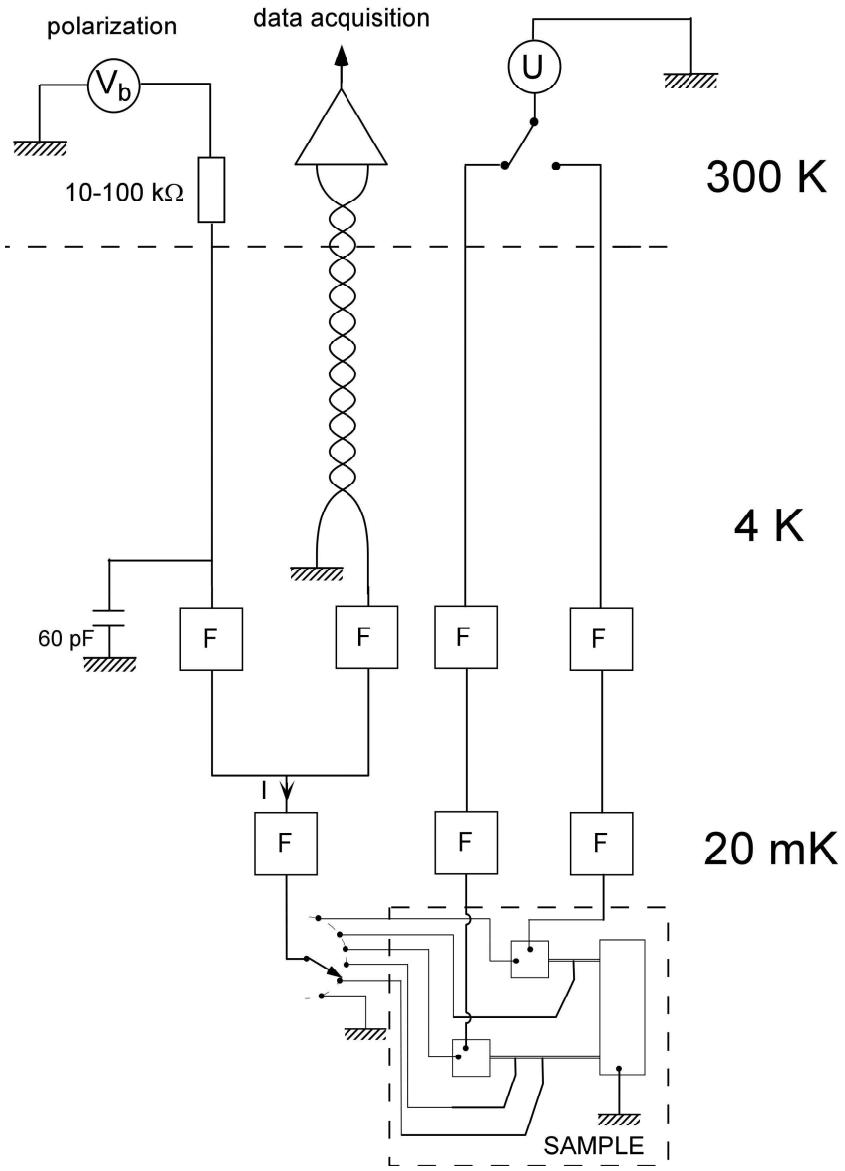

Figure 2: Schematic of the electrical wiring in the dilution refrigerator for the experiment measuring the distribution function in a normal wire connected to superconducting pads. Current is injected to the sample by the source V_b through the biasing line. Voltage across the sample in series with a filter F is measured with an amplifier at room temperature connected by a shielded twisted pair.

Reference of chapter 4

[1] D. Vion, P. F. Orfila, P. Joyez, D. Esteve, and M. H. Devoret, J. Appl. Phys. **77**, 2519 (1994).

PART 2

MAGNETIC IMPURITIES IN METALS

Chapter 5 Introduction to Kondo effect

Kondo effect arises from the interaction between single magnetic atoms and the electrons of a metal. It results in the renormalization of the coupling between electrons and magnetic atoms and an enhanced scattering of electrons from magnetic atoms, observed in the temperature dependence of the resistivity.

It was proposed that Kondo effect explains previous energy exchange and phase coherence time measurements in metals that were not accounted for by the theory of electron-electron interaction. In this chapter, we describe the consequences of Kondo effect, in the limit of non-interacting magnetic impurities, on resistance, phase coherence and energy exchange.

5.1 Kondo effect and low temperature resistance

The theory of Kondo effect was first developed to account for the temperature dependence of the resistivity of metals containing magnetic impurities. In such materials, it was found that the resistivity presents a minimum at finite temperature, with a logarithmic increase when the temperature is lowered further, instead of decreasing as predicted from theories of electron-electron and electron-phonon interactions.

The electrical resistance is determined by the amount of back-scattering of electrons from phonons, defects, or impurities that hinders the electronic motion through the crystal. The coupling between a magnetic impurity of spin S and electrons was described by Kondo with the Hamiltonian:

$$\mathrm{H}_c = J_0 \sum_{k,k'} \left(\left(c^+_{k\uparrow} c_{k\uparrow} - c^+_{k\downarrow} c_{k'\downarrow} \right) S^z + c^+_{k\downarrow} c_{k'\uparrow} S^+ + c^+_{k\uparrow} c_{k'\downarrow} S^- \right), \quad (1)$$

where $c_{k\uparrow}$ and $c^+_{k\uparrow}$ are respectively the annihilation and creation operators of an electron of

momentum k and spin up, S^z, S^+ and S^- are the magnetic impurity spin operators, and J_0 is the coupling constant between electrons and magnetic impurities. In 1964, Kondo found out that when calculating the scattering of electrons by magnetic impurities using perturbation theory, the second order term is of the same order as the first order term [1]. Afterwards, it was calculated that the series of perturbations with this Hamiltonian diverges for energies equal to the Kondo temperature, defined as $k_B T_K = \mathrm{D}\,\mathrm{e}^{-1/(\nu_F J_0)}$, with k_B the Boltzmann constant, D the energy bandwidth of conduction electrons in the host metal, and ν_F their density of states at the Fermi level (see appendix). The divergence arises from the non-commutation of spin operators. For scalar interactions like Coulomb interaction, the perturbation theory is still valid. For temperature larger than T_K, the resistance is found proportional to $-c_{imp} \ln\left(k_B T / \mathrm{D}\right)$, where c_{imp} is the impurity concentration.

In 1974, Wilson solved the Kondo problem within the renormalization theory and ruled out the zero-temperature divergence of the resistance [2]. Physically, at temperatures much smaller than the Kondo temperature, the spin of the magnetic impurity is totally screened by the conduction electrons. For conducting electrons, the screened impurity appears then as a potential scattering center.

5.2 Kondo effect and phase coherence time

Scattering from magnetic impurities results in spin-flip for electrons. Within the Suhl-Nagaoka approximation for the Kondo effect, the temperature-dependent spin-flip scattering rate is approximated by [3]:

$$\frac{1}{\tau^{sf}} = \frac{c_{imp}}{\pi \hbar \nu_F} \frac{\pi^2 S(S+1)}{\pi^2 S(S+1) + \ln^2\left(T / T_K\right)}, \tag{2}$$

with S the spin, and T the Kondo temperature of the magnetic impurities. This formula was first derived to determine the spin-flip scattering rate in superconductors [4]. The phase decoherence rate due to spin-flip scattering can be identified to the spin-flip scattering rate in a superconductor only for $T \gg T_K$. Yet, in previous experiments of phase coherence time measurements using electronic weak localization, it was found that this formula describes

correctly experimental results down to T_K [4,5].

The relation between the spin-flip scattering rate $1/\tau^{sf}$ and the decoherence rate $1/\tau_\phi^{sf}$ depends on the comparison between the spin-flip scattering time of conduction electrons τ^{sf} and the spin relaxation time τ (Korringa time) of the magnetic impurity [6]. Due to dynamical effect, the decoherence rate can be enhanced. The decoherence rate due to magnetic impurity is written:

$$\begin{aligned} \frac{1}{\tau_\phi^{sf}} &= \frac{1}{\tau^{sf}} \text{ if } \tau^{sf} > \tau_K \\ \frac{1}{\tau_\phi^{sf}} &= \frac{2}{\tau^{sf}} \text{ if } \tau^{sf} < \tau_K . \end{aligned} \tag{3}$$

In practice, $\tau^{sf} > \tau_K$ as long as

$$T \le \frac{c_{imp}}{\nu_F k_B} .$$

In gold, silver, or copper, this criterion reads $T < 40\,\text{mK} \times c_{imp}[\text{ppm}]$, in which c_{imp} is now given in parts per million atoms (ppm).

5.3 Kondo effect and energy exchange between electrons

In the past, theories of Kondo effect focused on the renormalization of the scattering rate of electrons from magnetic impurities and, as far as mesoscopic physics is concerned, on the corresponding spin-flip rate. When considering the scattering of a single electron from a magnetic impurity (processes presented in the appendix), the electron energy is conserved as long as the spin states of the impurities are degenerate, *i.e.* at zero magnetic field. In contrast, processes involving two electrons only conserve the sum of the energies and energy exchange is possible even at zero magnetic field (see Figure 1). This mechanism of energy exchange between electrons mediated by magnetic impurities has been proposed only recently by Kaminsky and Glazman [7]. We call this type of interaction Kondo-Impurity-Mediated interaction (KIM interaction).

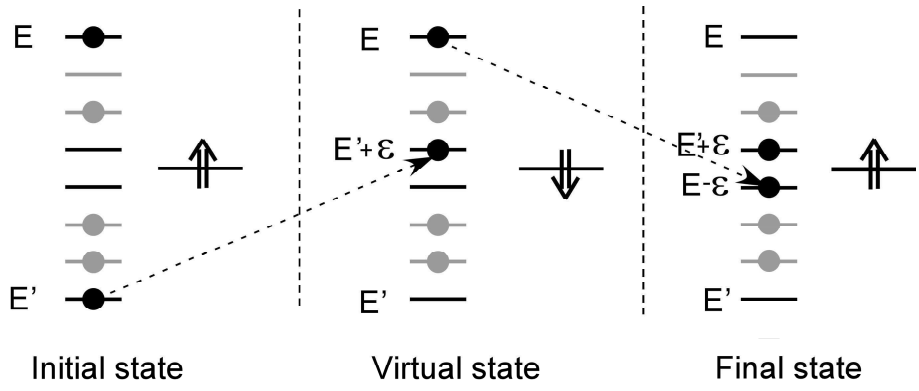

Figure 1: Scattering process involving two electrons and a single magnetic impurity, at lowest order. In each panel, the left ladder represents the energy spectrum of the electrons and the line on the right side represent the energy level of the degenerate spin-up and spin-down of the magnetic impurity.

At second order in perturbation, the scattering of two electrons from a given magnetic impurity is equivalent to an effective electron-electron interaction with a matrix element $M(\varepsilon)$ proportional to the inverse of the exchanged energy ε. According to the Fermi Golden Rule, the exchange of energy ε by the KIM interactions leads to the rate $\gamma(E,\varepsilon)$ of change of the population of an electronic state at energy E and of occupation number $f(E)$:

$$\gamma(E,\varepsilon) = \mathrm{K}(\varepsilon)\ \left(f(E+\varepsilon)\ (1-f(E)) - f(E)\ (1-f(E-\varepsilon))\right)\int dE' f(E')\ (1-f(E'+\varepsilon)), \quad (4)$$

with

$$\mathrm{K}(\varepsilon) \propto \left|M(\varepsilon)\right|^2 = \pi^2 \frac{c_{imp}}{\nu_F h} S(S+1) \frac{(\nu_F J)^4}{\varepsilon^2} = \kappa_{imp-e}/\varepsilon^2 ,$$

where J is the renormalized coupling constant between electrons and magnetic impurities by Kondo effect. This result obtained by Kaminski and Glazman is in agreement with the phenomenological result $\mathrm{K} \propto 1/\varepsilon^2$ inferred from previous experiments [8,5], which was not accounted for by theory of electron-electron interaction. The renormalization of the coupling constant must be performed using processes involving two electrons and a single magnetic impurity which were neglected in the calculation of the resistance because they enter at second order. Examples of diagrams to be included in the calculation are shown on Figure 2. However as pointed out by Kaminski and Glazman, Kondo effect is expected to modify the coupling constant in a way depending on ε, T_K and $f(E)$. A complication arises in the

renormalization calculation when the electronic energy distribution function is out-of-equilibrium and when the spin-states of magnetic impurities are no more degenerated. Yet the complete calculation has been performed using poor-man scaling, by Göppert *et al.* in [9] and will be presented in the Chapter 7 of this thesis.

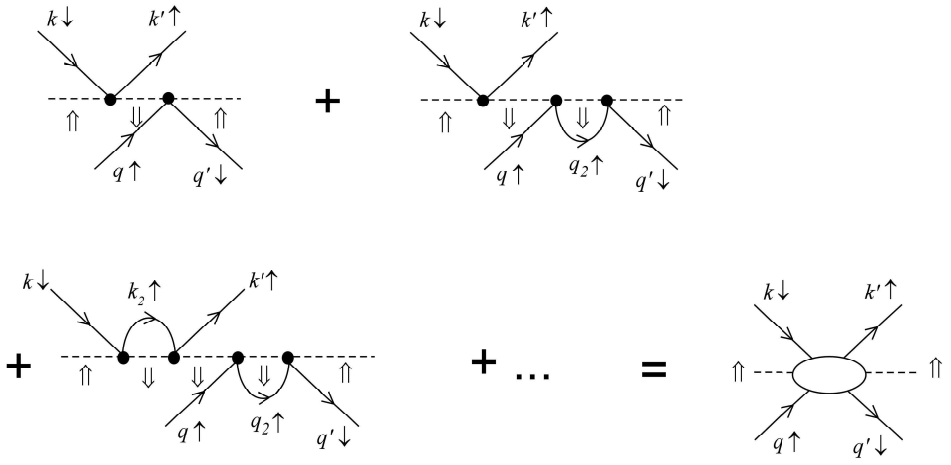

Figure 2 : “First” and “second” order inelastic processes involving two electrons and one magnetic impurity and equivalent diagram with a bubble to summarize the different coupling.

Appendix: Perturbative approach of the Kondo effect

The Kondo Hamiltonian H_c describing the coupling between a magnetic impurity of spin S and electrons is written in the second quantification formalism:

$$\mathrm{H}_c = J_0 \sum_{k,k'} \left(\left(c^+_{k\uparrow} c_{k'\uparrow} - c^+_{k\downarrow} c_{k'\downarrow} \right) S^z + c^+_{k\downarrow} c_{k'\uparrow} S^+ + c^+_{k\uparrow} c_{k'\downarrow} S^- \right), \tag{5}$$

where $c_{k\uparrow}$ ($c^+_{k\uparrow}$) annihilates (creates) an electron of momentum k and spin up and S^z, S^+ and S^- are the magnetic impurity spin operators. In the Kondo model, magnetic impurities are assumed to be so diluted that they are independent; the RKKY model does not apply here [10].

The calculation presented here aims at showing how the minimum in the resistance was first explained by Kondo (for more details, see [11]). For simplicity, we have chosen $S = 1/2$. As a convention in the following, only the electronic states of interest that are occupied are specified in the notation of the initial and final states. When considering the elastic processes that let the spins of electrons down and the magnetic impurity spin-up (see Figure 3), the electron energy $\varepsilon_k = \hbar k^2/(2m) = \hbar k'^2/(2m)$ being conserved, one finds for the first order process:

$$t_1 = \left\langle k\downarrow, \Uparrow \left| H_c \right| k'\downarrow, \Uparrow \right\rangle = \frac{J_0}{2}. \tag{6}$$

As shown on Figure 3, four terms, numbered from 1) to 4) are included in the calculation of the second order term in perturbation.

$$\begin{aligned} t_2 = & \sum_{k_2} \frac{\left\langle k'\downarrow, \Uparrow \left| \mathrm{H}_c \right| k_2\uparrow, \Downarrow \right\rangle \left\langle k_2\uparrow, \Downarrow \left| \mathrm{H}_c \right| k\downarrow, \Uparrow \right\rangle}{\varepsilon_k - \varepsilon_2} \\ & + \sum_{k_2} \frac{\left\langle k_2\uparrow, \Downarrow \left| \mathrm{H}_c \right| k'\downarrow, \Uparrow \right\rangle \left\langle k\downarrow, \Uparrow \left| \mathrm{H}_c \right| k_2\uparrow, \Downarrow \right\rangle}{\varepsilon_k - \varepsilon_2} \\ & + \sum_{k_2} \frac{\left\langle k'\downarrow, \Uparrow \left| \mathrm{H}_c \right| k_2\downarrow, \Uparrow \right\rangle \left\langle k_2\downarrow, \Uparrow \left| \mathrm{H}_c \right| k\downarrow, \Uparrow \right\rangle}{\varepsilon_k - \varepsilon_2} \\ & + \sum_{k_2} \frac{\left\langle k_2\downarrow, \Uparrow \left| \mathrm{H}_c \right| k'\downarrow, \Uparrow \right\rangle \left\langle k\downarrow, \Uparrow \left| \mathrm{H}_c \right| k_2\downarrow, \Uparrow \right\rangle}{\varepsilon_k - \varepsilon_2}. \end{aligned} \tag{7}$$

This leads to:

$$\begin{aligned} t_2 = & \sum_{\varepsilon_2} \frac{J_0^2}{\varepsilon_k - \varepsilon_2} \left\langle k' \downarrow \left| c_{k'\downarrow}^{+} c_{k_2\uparrow} c_{k_2\uparrow}^{+} c_{k\downarrow} \right| k \downarrow \right\rangle \left\langle \Uparrow \left| S^{+} S^{-} \right| \Uparrow \right\rangle \\ & + \sum_{\varepsilon_2} \frac{J_0^2}{\varepsilon_k - \varepsilon_2} \left\langle k' \downarrow \left| c_{k_2\uparrow}^{+} c_{k\downarrow} c_{k'\downarrow}^{+} c_{k_2\uparrow} \right| k \downarrow \right\rangle \left\langle \Uparrow \left| S^{-} S^{+} \right| \Uparrow \right\rangle \\ & + \sum_{\varepsilon_2} \frac{J_0^2}{\varepsilon_k - \varepsilon_2} \left\langle k' \downarrow \left| c_{k'\downarrow}^{+} c_{k_2\uparrow} c_{k_2\uparrow}^{+} c_{k\downarrow} \right| k \downarrow \right\rangle \left\langle \Uparrow \left| S_z^2 \right| \Uparrow \right\rangle \\ & + \sum_{\varepsilon_2} \frac{J_0^2}{\varepsilon_k - \varepsilon_2} \left\langle k' \downarrow \left| c_{k_2\uparrow}^{+} c_{k\downarrow} c_{k'\downarrow}^{+} c_{k_2\uparrow} \right| k \downarrow \right\rangle \left\langle \Uparrow \left| S_z^2 \right| \Uparrow \right\rangle . \end{aligned} \tag{8}$$

Using the anticommutation rules for the fermion operators and knowing that $\left\langle \Uparrow \left| S^{-} S^{+} \right| \Uparrow \right\rangle = 0$, Eq. (8) becomes:

$$\begin{aligned} t_2 = & \left\langle k' \downarrow \left| -\sum_{\varepsilon_2} \frac{J_0^2}{\varepsilon_k - \varepsilon_2} c_{k'\downarrow}^{+} c_{k\downarrow} \left(1 - c_{k_2\uparrow}^{+} c_{k_2\uparrow} \right) \right| k \downarrow \right\rangle \left\langle \Uparrow \left| S^{+} S^{-} \right| \Uparrow \right\rangle \\ & + 0 \\ & + \left\langle k' \downarrow \left| -\sum_{\varepsilon_2} \frac{J_0^2}{\varepsilon_k - \varepsilon_2} c_{k'\downarrow}^{+} c_{k\downarrow} \left(1 - c_{k_2\uparrow}^{+} c_{k_2\uparrow} \right) \right| k \downarrow \right\rangle \left\langle \Uparrow \left| S_z^2 \right| \Uparrow \right\rangle \\ & + \left\langle k' \downarrow \left| -\sum_{\varepsilon_2} \frac{J_0^2}{\varepsilon_k - \varepsilon_2} c_{k'\downarrow}^{+} c_{k\downarrow} c_{k_2\uparrow}^{+} c_{k_2\uparrow} \right| k \downarrow \right\rangle \left\langle \Uparrow \left| S_z^2 \right| \Uparrow \right\rangle . \end{aligned} \tag{9}$$

To take into account the many-body case, one can simply state that $c_{k_2}^{+} c_{k_2} = f\left(\varepsilon_2\right)$, with $f\left(\varepsilon_2\right)$ the occupation factor of the state k_2. Equation (9) is written:

$$\begin{aligned} t_2 = & \left\langle k' \downarrow \left| -\sum_{\varepsilon_2} \frac{J_0^2}{\varepsilon_k - \varepsilon_2} c_{k'\downarrow}^{+} c_{k\downarrow} \left(1 - f\left(\varepsilon_2\right) \right) \right| k \downarrow \right\rangle \left\langle \Uparrow \left| S^{+} S^{-} \right| \Uparrow \right\rangle \\ & + \left\langle k' \downarrow \left| -\sum_{\varepsilon_2} \frac{J_0^2}{\varepsilon_k - \varepsilon_2} c_{k'\downarrow}^{+} c_{k\downarrow} \right| k \downarrow \right\rangle \left\langle \Uparrow \left| S_z^2 \right| \Uparrow \right\rangle . \end{aligned} \tag{10}$$

Besides, since $\left\langle \Uparrow \left| S_z^2 \right| \Uparrow \right\rangle = 1/4$, Eq. (9) can be written:

$$t_2 = -\frac{5 J_0^2 \nu_F}{4} \sum_{\varepsilon_2} \frac{1}{\varepsilon_k - \varepsilon_2} + J_0^2 \nu_F \sum_{\varepsilon_2} \frac{f\left(\varepsilon_2\right)}{\varepsilon_k - \varepsilon_2} . \tag{11}$$

The first term in t_2 leads to small correction to the scattering rate, whereas the second one due to the introduction of a cut-off in energy by $f\left(\varepsilon_2\right)$ leads to the logarithmic contribution:

$$J_0^2 \nu_F \int_0^{\mathrm{D}} d\varepsilon_2 \ \frac{1}{\varepsilon_{\mathrm{k}} - \varepsilon_2} = J_0^2 \nu_F \ln \frac{\mathrm{D}}{\varepsilon}.$$

where D is the bandwidth of the conduction electrons and ν_F their density of states at the Fermi level per unit of volume. For energies such as $\varepsilon < \mathrm{D} e^{-1/(\nu_F J)}$, this second order term is larger than the first order one. Note that if we chose the magnetic impurity spin-down, the second term in Eq. (8) would have lead to the logarithmic correction whereas the first one would have been zero. The logarithmic correction arises from the non-commutativity of the spin-operators S^+ and S^-.

Starting from other spin configurations leads to the same result. When adding all the processes, one finds an effective coupling constant for electrons of energy ε:

$$\begin{aligned} J_{eff}(\varepsilon) &\simeq J_0 + J_0^2 \nu_F \ln \frac{\mathrm{D}}{\varepsilon} + \ldots \\ &\simeq \frac{J_0}{1 - J_0 \nu_F \ln \frac{\mathrm{D}}{\varepsilon}}, \end{aligned} \tag{12}$$

the last equality following from a summation using the renormalization group technique [12]. One finds

$$J_{eff}(\varepsilon) = \frac{1}{\nu_F \ln(\varepsilon / T_K)}.$$

For the characteristic energy, $\varepsilon = k_B T_K = \mathrm{D}\, \mathrm{e}^{-1/(J_0 \nu_F)}$, corresponding to the Kondo temperature, J_{eff} diverges. All the electronic transport properties are determined by this energy scale.

Starting from an independent electron model, the conductivity is determined by an average of the scattering times $\tau(\varepsilon)$, which are inferred from the values of t_2, near Fermi energy:

$$\sigma = \frac{e^2}{(12\pi^3)} \mathrm{v}_F{}^2 \nu_F \int d\varepsilon \frac{-\partial f}{\partial \varepsilon} \tau(\varepsilon) \simeq 1 + 2 J_0 \nu_F \left(\ln(\mathrm{D} / k_B T) + \text{constant} \right). \tag{13}$$

The resistivity varies logarithmically with temperature above T_K.

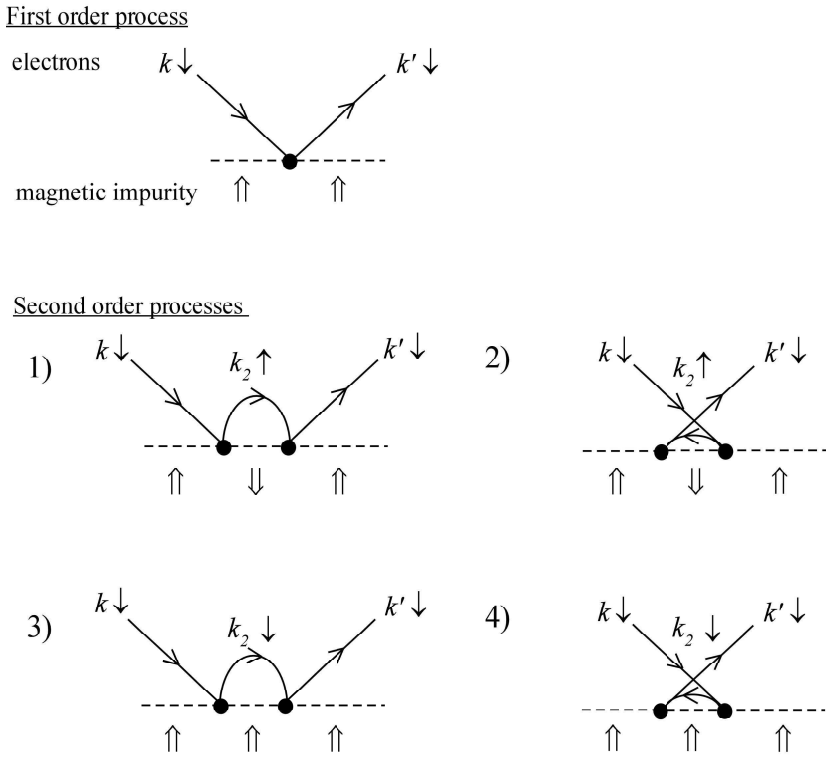

Figure 3: First and second order elastic processes involving one electron and one magnetic impurity in a case where initial and final electron spin states are identical.

References of chapter 5

[1] J. Kondo, Prog. Theor. Phys. **32**, 37 (1964).

[2] K. G. Wilson, Rev. Mod. Phys. **47**, 773 (1975).

[3] M.B. Maple, *Magnetism*, edited by H. Suhl (Academic, New York, 1973), vol.5.

[4] C. Van Haesendonck, J. Vranken, and Y. Bruynseraede, Phys. Rev. B **58**, 1968 (1987).

[5] F. Pierre, Annales de Physique, **26**, No 4 (2001).

[6] V.I. Falko, JETP Lett. **53**, 340 (1991).

[7] A. Kaminski and L. I. Glazman, Phys. Rev. Lett. **86**, 2400 (2001).

[8] S. Guéron, PhD thesis: "Quasiparticles in a diffusive conductor: Interaction and pairing", University Paris VI, october 1997 .

[9] G. Göppert and H. Grabert, Phys. Rev. B **64**, 033301 (2001); G. Göppert, Y. M. Galperin, B. L. Altshuler, and H. Grabert , Phys. Rev. B **66**, 195328 (2002).

[10] M.A. Ruderman and C. Kittel, Phys. Rev. **96**, 99 (1954); T. Kasuya, Prog. Theor. Phys. **16**, 45 (1956); K. Yosida, Phys. Rev. **106**, 893 (1957).

[11] A.C. Hewson, *The Kondo Problem to Heavy Fermions*, edited by D. Edwards and D. Melville (Cambridge University Press, 1993), p. 29.

[12] P.W. Anderson, J. Phys. C **3**, 2436 (1970).

Chapter 6 Phase coherence time and Kondo effect

In this chapter, the focus is on phase coherence at low temperature in metallic wires. There is currently an experimental and theoretical controversy concerning the very low temperature behavior of the phase coherence time. The standard theory of electron-electron scattering predicts that the phase coherence time increases as a power law as the temperature goes to zero. Yet, many experiments show a saturation of the phase coherence time at sub-kelvin temperatures. Do those experimental observations reveal a fundamental, intrinsic decoherence mechanism, or an extrinsic, sample-dependent source of decoherence?

The aim of the experiments presented in this chapter was to test if a very dilute amount of magnetic impurities with a rather small Kondo temperature could cause an apparent saturation of the electronic phase coherence time.

6.1 Magnetoresistance and phase coherence time

The phase coherence time τ_ϕ is one of the few parameters that determine the weak localization correction to the magnetoresistance of a wire, and it is the only one that depends on temperature. This is why measurements of the magnetoresistance versus temperature allow determination of τ_ϕ over a large range of magnitude.

6.1.1 Quantum coherence and transport properties

In diffusive thin films, electrons undergo a large amount of scattering events from sample boundaries, phonons, lattice defects, impurities and other electrons. Although the

mean free path between collisions is $l_e \approx 10$ nm, quantum coherence effects persist on a much larger scale than l_e (typically of the order of a micrometer) because scattering is mainly elastic. Elastic scattering can be pictured as resulting from static potential, on which the diffusive-like electronic quantum states are built, and determines the low-temperature resistivity. The phase coherence of the states leads to a small correction to the resistivity, which depends on the magnetic field. This so-called weak localization correction results from quantum interferences between electronic paths. The probability P to go from an initial point P_i to a final point P_f, is the modulus squared of the sum of the probability amplitudes A_α for all the paths connecting these two points:

$$\begin{aligned} P &= \left| \sum_\alpha A_\alpha \right|^2 \\ &= \sum_\alpha \left| A_\alpha \right|^2 + \sum_{\alpha,\beta} A_\alpha A_\beta^* . \end{aligned} \tag{1}$$

The first term in Eq. (1) is the sum of classical probabilities along the different paths, whereas the second term accounts for quantum interferences.

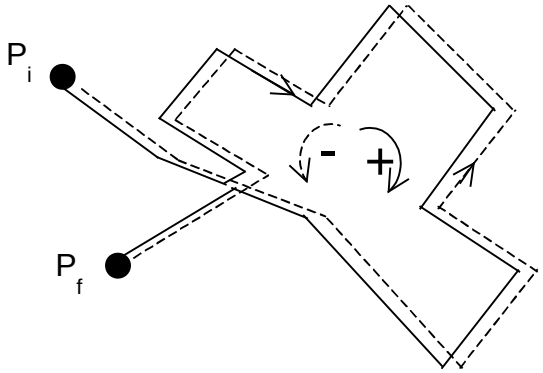

Figure 1: The weak localization corrections to the conductance of a diffusive metal result from the constructive (destructive if the spin-orbit coupling is strong) interference between the paths (+) and (-) following the same loop in opposite directions.

For arbitrary paths α and β, the interference term has a random phase, and the average contribution of such paths to P is zero. Yet, if α encloses a loop and β differs from α only by the direction in which the electrons travel on the loop (see Figure 1), α and β interfere constructively (destructively if spin-orbit coupling is strong):

$$\left|A_+ + A_-\right|^2 = 4\left|A_+\right|^2 . \quad (2)$$

This results in P in an increased (decreased) weight of the paths enclosing loops. Electron propagation along such paths is in average slower than on other paths. As a consequence, the electron mobility, thus the metal conductivity, decrease (increase) due to quantum coherence.

The amplitude of this effect, called weak (anti-)localization, depends on the electronic phase coherence time τ_ϕ because only loops of size smaller than the phase coherence length $L_\phi = \sqrt{D\tau_\phi}$ contribute to the weak localization correction to the conductance. Indeed, the addition of the amplitudes of paths α and β only makes sense if electron coherence is maintained while traveling around the loop.

6.1.2 Magnetic field effect

When a magnetic field is applied, time-reversal symmetry is broken. The two paths (+) and (-) of Figure 1 are then dephased by:

$$\delta = 2\frac{\phi_B}{\phi_0} . \quad (3)$$

where ϕ_B is the magnetic flux enclosed in the loop, and $\phi_0 = \hbar / e$ the flux quantum.

As a consequence, the magnetic field suppresses significantly the weak localization correction in a metallic wire of width w when $\delta \approx \sqrt{D\tau_\phi}\, w / L_H^2$ with $L_H = \sqrt{\phi_0 / B}$ the magnetic length (w is assumed to be smaller than L_ϕ)[1]. The weak localization correction to the resistance R of a metallic wire of length L reads [1,2]:

$$\frac{\Delta R}{R}(B) = \frac{2R}{R_K L}\left\{\frac{3}{2}\left(\frac{1}{L_\phi^2} + \frac{4}{3L_{so}^2} + \frac{1}{3}\left(\frac{wB}{\phi_0}\right)^2\right)^{-1/2} - \frac{1}{2}\left(\frac{1}{L_\phi^2} + \frac{1}{3}\left(\frac{wB}{\phi_0}\right)^2\right)^{-1/2}\right\}, \quad (4)$$

where $R_K = h / e^2$ is the resistance quantum and L_{so} is the spin-orbit diffusion length related to the intensity of the spin-orbit coupling, characteristic of a given metal. Expression (4) holds for metallic wires in the diffusive regime, far from the metal-insulator transition, and in the quasi one-dimensional regime: $l_e \ll w, t$ and $L_\phi, L_{so} \ll L$ with t the sample thickness. Typical

[1] This expression of δ holds when the magnetic field B is applied perpendicularly to the wire.

calculated magnetoresistances using Eq. (4) are shown on Figure 2 for a given spin-orbit length L_{so}, and two L_ϕ values $L_\phi = 6L_{so}$ (solid line) or $L_\phi = L_{so}$ (dashed line).

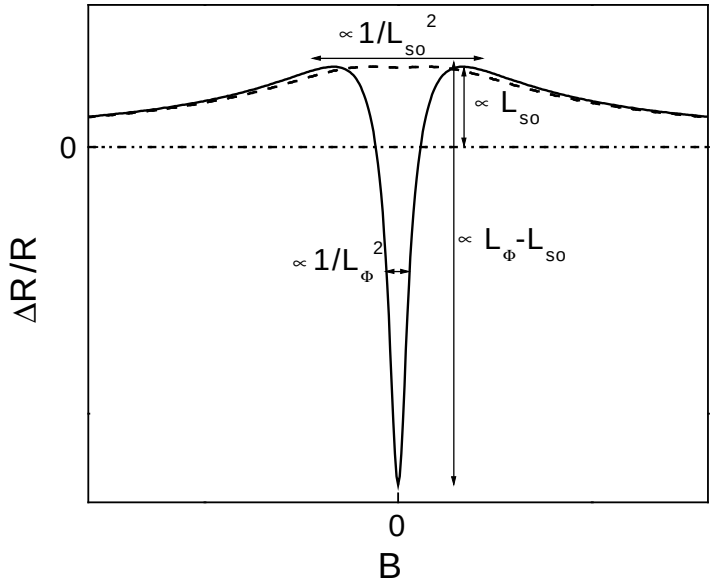

Figure 2: Generic magnetoresistance curves calculated with Eq. (4). The amplitudes and characteristic fields are given by the spin-orbit length L_{so} and the phase coherence length L_ϕ. Solid line: $L_\phi = 6L_{so}$, dashed line: Same L_{so} and $L_\phi = L_{so}$.

6.1.3 Finite length effect

The magnetoresistance was measured on wires long compared to L_ϕ, connected to large reservoirs at their ends. We evaluate here the effect of finite length. At zero magnetic field, in the strong spin-orbit coupling limit relevant to our experiments, the amplitude of the weak localization correction is proportional to the number of loops smaller than L_ϕ. The ratio $\Delta R / R$ is therefore proportional to L_ϕ:

$$\frac{\Delta R}{R}(0) = -\frac{2R}{R_K}\frac{L_\phi}{L}. \qquad (5)$$

Due to finite length of the wires, the loops starting from a point near the reservoir are cut because as soon as an electron enters in a reservoir, its probability to return in the wire is very small. As a consequence, the number of loops participating to the weak localization signal is

reduced. To evaluate this correction, we first write the classical probability $P(x,t)$ for an electron to be at position x at time t in a wire of length L, knowing that it was at position x_0 at $t=0$:

$$P(x,t)=\sum_n \sin\left(\frac{n\pi}{L}x_0\right)\sin\left(\frac{n\pi}{L}x\right)e^{-D\left(\frac{n\pi}{L}\right)^2 t}, \tag{6}$$

where D is the diffusion coefficient. Here, the absorption in the reservoirs is taken into account in the boundary conditions: $P(0,t)=P(L,t)=0$. The return probability at position x_0 in a time shorter than τ_ϕ is then:

$$P(x_0\to x_0)\propto \int dt\; e^{-\frac{t}{\tau_\phi}}\sum_n \sin\left(\frac{n\pi}{L}x_0\right)\sin\left(\frac{n\pi}{L}x\right)e^{-D\left(\frac{n\pi}{L}\right)^2 t}. \tag{7}$$

For the whole wire, the amount N of loops of size smaller than $L_\phi=\sqrt{D\tau_\phi}$ is for $L_\phi \ll L$ proportional to:

$$N=\int \frac{dx}{L}P(x_0\to x_0)\propto \tau_\phi\frac{(L-L_\phi)}{4L_\phi}\propto L_\phi\left(1-\frac{L_\phi}{L}\right). \tag{8}$$

Therefore, Eq. (5) must be replaced by

$$\frac{\Delta R}{R}(0)=-\frac{2R}{R_K}\frac{L_\phi}{L}\left(1-\frac{L_\phi}{L}\right). \tag{9}$$

Fits with Eq. (9) instead of Eq. (5) result in significant increase of the larger values of L_ϕ at the lowest temperature in samples in which L_ϕ becomes comparable to L. This finite size effect is illustrated on Figure 3, in the most spectacular case for our experiments. The measurements are on 200 µm-long silver sample Ag(6N)c where the finite size effect is rather large because L_ϕ reaches 20 µm at the lowest temperature.

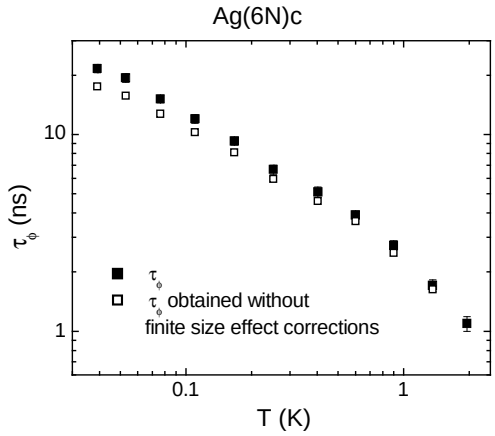

Figure 3: Phase coherence time τ_ϕ versus temperature in the sample Ag(6N)c (see paper below). Open symbols: Phase coherence time obtained by fitting the magnetoresistance data with Eq. (5). Full symbols: Phase coherence time obtained when taking into account effect of the finite length of the wire using Eq.(9).

6.2 Dephasing of electrons in mesoscopic metal wires

We reproduce here our article published in Phys. Rev. B **68**, 085413 (2003). The silver samples were obtained with the same 6N- and 5N- sources as the one used to make the samples for energy exchange measurements (see Chapter 7 and Chapter 8).

Dephasing of electrons in mesoscopic metal wires

F. Pierre,[1,2,3,*] A. B. Gougam,[1,†] A. Anthore,[2] H. Pothier,[2] D. Esteve,[2] and Norman O. Birge[1]
[1]*Department of Physics and Astronomy, Michigan State University, East Lansing, Michigan 48824-2320, USA*
[2]*Service de Physique de l'Etat Condensé, Direction des Sciences de la Matière, CEA-Saclay, 91191 Gif-sur-Yvette, France*
[3]*Department of Applied Physics, Yale University, New Haven, Connecticut 06520, USA*
(Received 11 February 2003; published 26 August 2003)

We have extracted the phase coherence time τ_ϕ of electronic quasiparticles from the low field magnetoresistance of weakly disordered wires made of silver, copper, and gold. In samples fabricated using our purest silver and gold sources, τ_ϕ increases as $T^{-2/3}$ when the temperature T is reduced, as predicted by the theory of electron–electron interactions in diffusive wires. In contrast, samples made of a silver source material of lesser purity or of copper exhibit an apparent saturation of τ_ϕ starting between 0.1 and 1 K down to our base temperature of 40 mK. By implanting manganese impurities in silver wires, we show that even a minute concentration of magnetic impurities having a small Kondo temperature can lead to a quasisaturation of τ_ϕ over a broad temperature range, while the resistance increase expected from the Kondo effect remains hidden by a large background. We also measured the conductance of Aharonov–Bohm rings fabricated using a very pure copper source and found that the amplitude of the h/e conductance oscillations increases strongly with magnetic field. This set of experiments suggests that the frequently observed ''saturation'' of τ_ϕ in weakly disordered metallic thin films can be attributed to spin–flip scattering from extremely dilute magnetic impurities, at a level undetectable by other means.

DOI: 10.1103/PhysRevB.68.085413 PACS number(s): 73.23.−b, 73.50.−h, 71.10.Ay, 72.70.+m

I. MOTIVATIONS

The time τ_ϕ during which the quantum coherence of an electron is maintained is of fundamental importance in mesoscopic physics. The observability of many phenomena specific to this field relies on a long enough phase coherence time.[1] Amongst these are the weak localization correction to the conductance (WL), the universal conductance fluctuations (UCF), the Aharonov-Bohm (AB) effect, persistent currents in rings, the proximity effect near the interface between a superconductor and a normal metal, and others. Hence it is crucial to find out what mechanisms limit the quantum coherence of electrons.

In metallic thin films, at low temperature, electrons experience mostly elastic collisions from sample boundaries, defects of the ion lattice and static impurities in the metal. These collisions do not destroy the quantum coherence of electrons. Instead they can be pictured as resulting from a static potential on which the diffusivelike electronic quantum states are built.

What limits the quantum coherence of electrons are inelastic collisions. These are collisions with other electrons through the screened Coulomb interaction, with phonons, and also with extrinsic sources such as magnetic impurities or two level systems in the metal. Whereas above about 1 K electron–phonon interactions are known to be the dominant source of decoherence,[2] electron–electron interactions are expected to be the leading inelastic process at lower temperatures in samples without extrinsic sources of decoherence.[3]

The theory of electron–electron interactions in the diffusive regime was worked out in the early 1980s (for a review, see Ref. 4). It predicts a power law divergence of τ_ϕ when the temperature T goes to zero. Effects of quantum interference are therefore expected to grow significantly upon cooling down the electrons. In mesoscopic wires, the predicted power law $\tau_\phi \propto T^{-2/3}$ was first observed in 1986 by Wind *et al.*[5] between 2 K and 5 K in aluminum and silver wires and then by Echternach *et al.*[6] down to 100 mK in a gold wire. However, in 1997, Mohanty, Jariwala, and Webb[7] published a series of measurements of τ_ϕ on gold wires with a broad range of diffusion coefficients. They observed that the phase coherence time tends to saturate at low temperature, typically below 0.5 K, in apparent contradiction with theoretical predictions. That same year, measurements of the energy exchange rate between electrons in copper wires[8] were found to be at odds, both qualitatively and quantitatively, with the prediction for electron–electron interactions. Both experiments suggested that electrons in mesoscopic metallic wires interact with each other differently and more strongly than predicted by theory.

To shed some light on this issue we present here several sets of experiments probing the phase coherence time at low temperature in mesoscopic metal wires.[9] We summarize our most important conclusions here. First, we measured $\tau_\phi(T)$ down to 40 mK in several wires made of copper, silver, and gold and fabricated from source materials of various purities. We found in the four very pure silver wires and in the very pure gold wire that $\tau_\phi(T)$ does not saturate in the investigated temperature range, but continues to increase as the temperature is lowered in agreement with the theoretical prediction. Since these samples have comparable resistances and geometries as some measured in Ref. 7, this observation casts doubt on the assertion[7] that saturation of τ_ϕ is a universal feature of weakly-disordered metals. Second, we tested the impact of very dilute magnetic impurities with a small Kondo temperature on the temperature dependence of τ_ϕ. We found that even at concentrations lower than one part per million (1 ppm), such impurities can cause $\tau_\phi(T)$ to display a plateau over a large temperature range. This could explain why saturation of τ_ϕ at low temperature is frequently

 ©2003 The American Physical Society

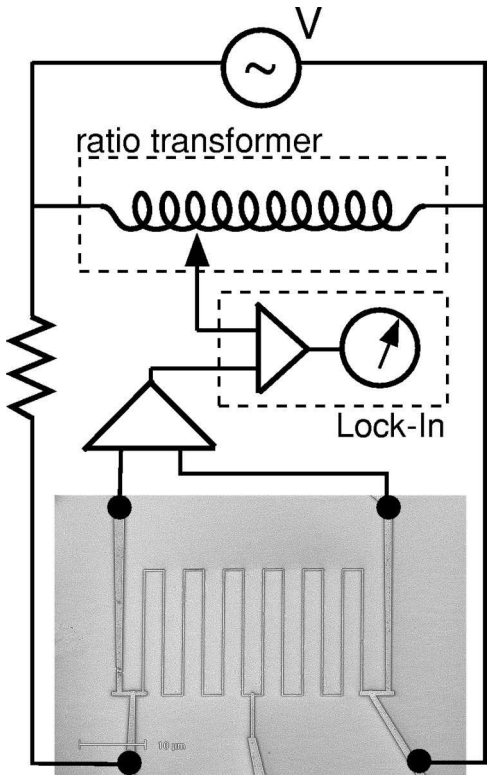

FIG. 1. Photograph of a silver sample taken with a scanning electron microscope, and schematic of measurement circuit. The wire resistance is obtained by a four-lead measurement in a bridge configuration: the current is injected by two arms through the bias resistor and the voltage is measured across two other arms in order to probe only the wire resistance; a ratio transformer is used to enhance sensitivity to small variations of the sample resistance.

observed. Finally, we probed the magnetic field dependence of the phase coherence time by measuring the magnetoresistance of copper Aharonov-Bohm rings showing a temperature-independent τ_ϕ at low temperature. The amplitude of the Aharonov-Bohm conductance oscillations increased strongly on a field scale proportional to the temperature, indicating that the phase coherence time at zero field was limited by spin-flip scattering from magnetic impurities.

II. EXPERIMENTAL TECHNIQUES

A. Sample fabrication

Figure 1 displays the photograph of a typical sample together with a schematic of the measurement setup.

All samples were fabricated using standard e-beam lithography techniques. A bilayer resist, consisting of a copolymer P(MMA/MAA) bottom layer and a PMMA top layer, was first spun onto an oxidized Si substrate wafer. This bilayer was then patterned by e-beam lithography to tailor a mask. The metal—gold, copper, or silver—was deposited directly through this mask in evaporators used only for nonmagnetic metals.[10]

Samples made at Saclay used a Si substrate thermally oxidized over 500 nm, and metal evaporation was performed in an electron gun evaporator. The silver source material was placed inside a carbon liner, whereas copper and gold were put directly in the buckets of the e-gun system. Metal evaporation took place at a base pressure of about 10^{-6} mbar with an evaporation rate of 0.2, 0.5, and 1 nm/s for silver, gold, and copper, respectively (see Ref. 11).

Samples made at Michigan State University (MSU) were evaporated on a Si substrate with only the native oxide in a thermal evaporator used only for silver, aluminum, gold, copper and titanium. The source material and boat were replaced before each evaporation and manipulated using plastic tweezers. The pressure during evaporation was about 10^{-6} mbar and the evaporation rate ranged between 0.2 and 0.5 nm/s.[12]

We measured the low field magnetoresistance of copper, gold, and silver wires fabricated using source materials of purity 99.999% (5N) and 99.9999% (6N). Electrical and geometrical characteristics of the samples are summarized in Table I.

TABLE I. Geometrical and electrical characteristics of the measured samples (Ref. 14). The diffusion coefficient D is obtained using Einstein's relation $1/\rho = \nu_F e^2 D$ with the density of states in copper, silver and gold respectively $\nu_F = 1.56\times10^{47}$, 1.03×10^{47}, and 1.14×10^{47} $J^{-1}\,m^{-3}$, and the resistivity ρ extracted from the resistance R, thickness t, length L, and width w of the long wire. Length and width were measured with a scanning electron microscope (SEM). The thickness of most samples was measured with an atomic force microscope (AFM); for others the value given by a calibrated thickness monitor in the evaporator was used. A rectangular cross section is assumed.

Sample	Made at	L (μm)	t (nm)	w (nm)	R (kΩ)	D (cm^2/s)
Ag(6N)a	Saclay	135	45	65	1.44	115
Ag(6N)b	Saclay	270	45	100	3.30	70
Ag(6N)c	Saclay	400	55	105	1.44	185
Ag(6N)d	MSU	285	35	90	1.99	165
Ag(5N)a	Saclay	135	65	108	0.68	105
Ag(5N)b	Saclay	270	65	90	1.31	135
$Ag(5N)c_{Mn0.3}$	Saclay	135	65	110	0.47	150
$Ag(5N)d_{Mn1}$	Saclay	270	65	95	1.22	135
Au(6N)	MSU	175	45	90	1.08	135
Cu(6N)a	MSU	285	45	155	0.70	145
Cu(6N)b	MSU	285	20	70	7.98	60
Cu(6N)c	MSU	285	35	75	4.37	65
Cu(6N)d	MSU	285	20	80	8.50	50
Cu(5N)a	Saclay	270	45	110	1.68	70
Cu(5N)b	Saclay	270	45	100	0.95	160

B. Experimental setup

The samples were immersed in the mixing chamber of a top loading dilution refrigerator. Electrical lines to the sample were filtered by commercial ''pi'' filters at the top of the cryostat and by discrete RC filters in the mixing chamber. Resistance measurements were performed using a standard ac four-terminal technique with a room temperature preamplifier of input voltage noise 1.5 nV/$\sqrt{\text{Hz}}$ and a lock-in am-

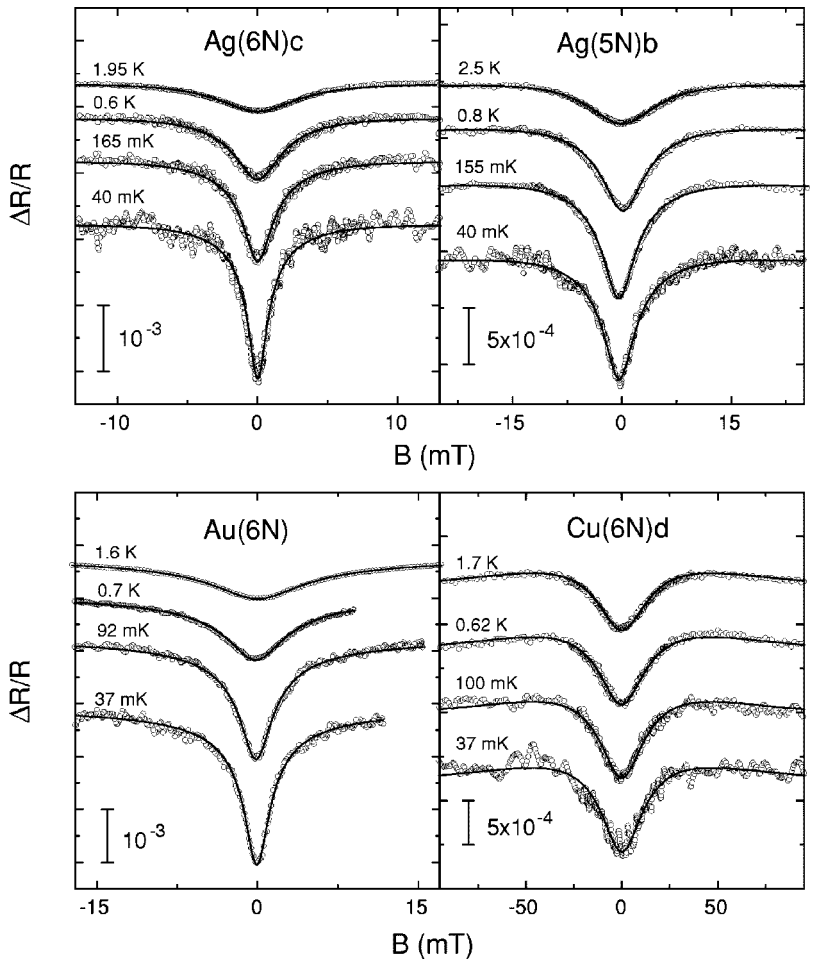

FIG. 2. Magnetoresistance data (symbols) and fits to Eq. (1) (solid lines). Top panels are measurements of two silver samples made of source materials of nominal purity 6N (99.9999%, top left panel) and 5N (99.999%, top right panel). Bottom panels display data measured on gold (bottom left panel) and copper (bottom right panel) samples made of 6N nominal purity source materials. The curves are offset vertically for clarity.

plifier operated at frequencies between 100 and 300 Hz (see Fig. 1). To avoid significant heating of electrons we used ac voltages $V_{\rm ac}$ across the samples such that $eV_{\rm ac} \lesssim k_B T$. This is particularly important at temperatures below 100 mK for which the length scale for electron–phonon interactions, responsible for cooling down the electronic fluid, can be as large as several millimeters (see Appendix A). A bridge circuit with a ratio transformer on one arm was used to enhance the measurement sensitivity to small changes in sample resistance. A magnetic field was applied perpendicular to the plane of the sample using a superconducting coil.

III. LOW FIELD MAGNETORESISTANCE MEASUREMENTS

The most accurate way to extract τ_ϕ at low magnetic field in metallic thin films is to measure the magnetoresistance and to fit it using weak localization theory.[13] Both the amplitude and width of the weak localization peak (dip when spin–orbit coupling is strong) in the resistance are sensitive to the phase coherence length.

Figure 2 displays the low field magnetoresistance of samples Ag(6N)c, Ag(5N)b, Au(6N), and Cu(6N)d at several temperatures. The positive magnetoresistance indicates that spin–orbit scattering is stronger than inelastic scattering ($\tau_{\rm so} < \tau_\phi$). Raw magnetoresistance measurements already reveal a qualitative difference between these samples: the dip in the magnetoresistance of samples Ag(6N)c and Au(6N) becomes deeper and narrower upon cooling down to base temperature whereas it stops changing at low temperature in samples Ag(5N)b and Cu(6N)d.

The magnetoresistance $\Delta R \equiv R(B) - R(\infty)$ is fit with the quasi-1D expression for the weak localization correction,

$$\frac{\Delta R}{R} = \frac{2R}{R_{\rm K} L}\left\{\frac{3}{2}\left[\frac{1}{L_\phi^2} + \frac{4}{3L_{\rm so}^2} + \frac{1}{3}\left(\frac{w}{L_H^2}\right)^2\right]^{-1/2} - \frac{1}{2}\left[\frac{1}{L_\phi^2} + \frac{1}{3}\left(\frac{w}{L_H^2}\right)^2\right]^{-1/2}\right\}, \quad (1)$$

where R is the resistance of a wire of length L and width w, $R_{\rm K} = h/e^2$ is the resistance quantum, $L_\phi = \sqrt{D\tau_\phi}$ is the phase coherence length, D is the diffusion coefficient of electrons, $L_H = \sqrt{\hbar/eB}$ is the magnetic length, B is the magnetic field applied perpendicularly to the sample plane, and $L_{\rm so} = \sqrt{D\tau_{\rm so}}$ is the spin–orbit length that characterizes the intensity of spin–orbit coupling. Expression (1) holds for metallic wires in the diffusive regime, far from the metal–insulator transition, and in the quasi-1D regime, $l_e \ll w, t \ll L_H, L_\phi, L_{\rm so} \ll L$, with t the sample thickness and l_e the elastic mean free path of electrons (see Refs. 15,16 and Appendix B).

TABLE II. Fit parameters of the magnetoresistance data to weak localization theory: maximum phase coherence time $\tau_\phi^{\max}$, obtained at the lowest temperature of $\sim$40 mK; spin–orbit length L_{so} and effective width w_{WL}. We also recall the width w obtained from SEM pictures. The upwards arrow $\nearrow$ indicates that τ_ϕ keeps increasing down to 40 mK. In the other samples, τ_ϕ is nearly constant at low temperature.

Sample	$\tau_\phi^{\max}$ (ns)	L_{so} (μm)	w_{WL} (w) (nm)
Ag(6N)a	9$\nearrow$	0.65	57 (65)
Ag(6N)b	12$\nearrow$	0.35	85 (100)
Ag(6N)c	22$\nearrow$	1.0	90 (105)
Ag(6N)d	12$\nearrow$	0.82	75 (90)
Ag(5N)a	2.9	0.65	108 (108)
Ag(5N)b	3.5	0.75	82 (90)
Au(6N)	11$\nearrow$	0.085	85 (90)
Cu(6N)a	0.45	0.67	155 (155)
Cu(6N)b	0.95	0.4	70 (70)
Cu(6N)c	0.2	0.35	75 (75)
Cu(6N)d	0.35	0.33	80 (80)
Cu(5N)a	1.8	0.52	110 (110)
Cu(5N)b	0.9	0.67	100 (100)

In the fit procedure, we use the measured sample resistance and length given in Table I. Our experimental setup being designed to measure resistance changes with an higher accuracy than absolute values, ΔR is known only up to a small additive constant that we adjusted to fit each magnetoresistance curve. The width was fixed at a value w_{WL} giving the best overall fits for the complete set of data at various temperatures. The difference between the width w measured from scanning electron microscope images and the best fit value w_{WL} (see Table II) was found to be always less than 15%.[17] The spin–orbit length L_{so} was obtained from fits of the magnetoresistance measured at the highest temperature. These parameters being determined, L_ϕ remains as the only fit parameter for each magnetoresistance curve. Examples of fits are displayed as solid lines in Fig. 2.

In order to get τ_ϕ from L_ϕ, the diffusion coefficient D was determined using the measured geometrical and electrical sample characteristics given in Table I. Figure 3 shows τ_ϕ as a function of temperature for samples Ag(6N)c, Ag(5N)b, Au(6N), and Cu(6N)b. This confirms quantitatively the differences between samples already mentioned from the raw magnetoresistance data. On the one hand, the samples Ag(6N)c and Au(6N), fabricated using our purest (6N) silver and gold sources, present a large phase coherence time that keeps increasing at low temperature. On the other hand, the copper sample Cu(6N)b and the sample Ag(5N)b, fabricated using a silver source of smaller nominal purity (5N), present a much smaller phase coherence time and exhibit a plateau in $\tau_\phi(T)$, in contradiction with the theoretical prediction for electron–electron interactions. This trend, illustrated in Fig. 3, has been confirmed by the measurements of several samples, as summarized in Table II.

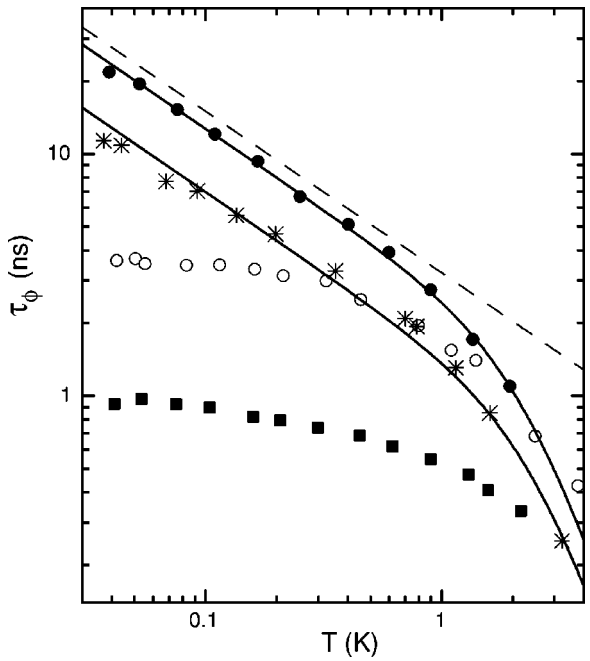

FIG. 3. Phase coherence time τ_ϕ versus temperature in wires made of copper Cu(6N)b (■), gold Au(6N) (*), and silver Ag(6N)c (●) and Ag(5N)b (○). The phase coherence time increases continuously with decreasing temperature in wires fabricated using our purest (6N) silver and gold sources as illustrated respectively with samples Ag(6N)c and Au(6N). Continuous lines are fits of the measured phase coherence time including inelastic collisions with electrons and phonons [Eq. (4)]. The dashed line is the prediction of electron–electron interactions only [Eq. (3)] for sample Ag(6N)c. In contrast, the phase coherence time increases much more slowly in samples made of copper (independently of the source material purity) and in samples made of silver using our source of lower (5N) nominal purity.

IV. COMPARISON WITH THEORETICAL PREDICTIONS AND DISCUSSION

A. Purest silver and gold samples

Theory predicts that, in samples without extrinsic sources of decoherence, $\tau_\phi(T)$ is limited by the contributions of electron–electron τ_{ee} and electron–phonon τ_{ph} interactions. In principle, decoherence by electron–electron scattering is not purely an exponential process, hence the decoherence rates from electron–electron and electron–phonon scattering do not simply add. In practice (see Appendix B), the exact formula for the magnetoresistance is indistinguishable from Eq. (1) with a total decoherence rate,

$$\frac{1}{\tau_\phi(T)} = \frac{1}{\tau_{ee}(T)} + \frac{1}{\tau_{ph}(T)}. \tag{2}$$

For our wires, whose width and thickness are smaller than L_ϕ, the quasi-1D prediction for electron–electron interactions applies[15]

$$\tau_{ee} = \hbar \left[\frac{(4/\pi)(R_K/R)\nu_F SL}{(k_B T)^2} \right]^{1/3} \equiv \frac{1}{A_{thy} T^{2/3}}, \tag{3}$$

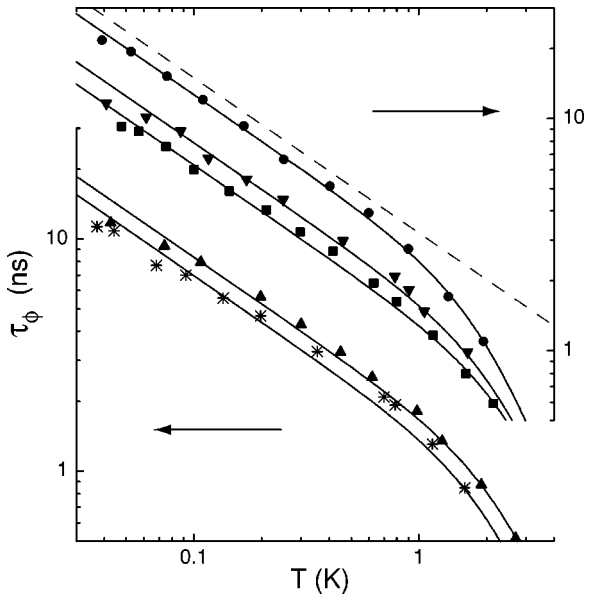

FIG. 4. Phase coherence time vs temperature in samples Ag(6N)a (■), Ag(6N)b (▼), Ag(6N)c (●), Ag(6N)d (▲), and Au(6N) (*), all made of 6N sources. Continuous lines are fits of the data to Eq. (4). For clarity, the graph has been split in two part, shifted vertically one with respect to the other. The quantitative prediction of Eq. (3) for electron–electron interactions in sample Ag(6N)c is shown as a dashed line.

where ν_F is the density of states per unit volume at the Fermi energy, and S is the cross section of the wire.

In order to test the theoretical predictions, the measured $\tau_\phi(T)$ curves were fit with the functional form,

$$\tau_\phi^{-1} = AT^{2/3} + BT^3, \tag{4}$$

where the second term describes electron–phonon scattering, dominant at higher temperatures.[2] Fits are shown as continuous lines in Fig. 4 (the fit parameters minimize the distance between the data points and the fit curve in a log–log plot). Equation (4) describes accurately the temperature dependence of $\tau_\phi(T)$ for samples Ag(6N)a, b, c and, with a slightly reduced fidelity, for samples Ag(6N)d and sample Au(6N). In all these samples, fabricated using 6N source materials of silver and gold, $\tau_\phi(T)$ follows very closely, below about 1 K, the $1/T^{2/3}$ dependence expected when the electron–electron interaction is the dominant inelastic process. Nevertheless, if the exponent of T is left as a fit parameter, better fits are obtained with smaller exponents ranging from 0.59 for samples Ag(6N)d and Au(6N) up to 0.64 for sample Ag(6N)c. This issue will be discussed in Sec. V B. The dashed line in Fig. 3 and Fig. 4 is the quantitative prediction of Eq. (3) for electron–electron interactions in sample Ag(6N)c. The dephasing times are close, though always slightly smaller, to the theoretical prediction of Eq. (3). Table III lists the best fit parameters A, B, together with the prediction $A_{\rm thy}$ of Eq. (3).

TABLE III. Theoretical predictions of Eq. (3) and fit parameters for $\tau_\phi(T)$ in the purest silver and gold samples using the functional form given by Eq. (4).

Sample	$A_{\rm thy}$ ($\rm ns^{-1}\,K^{-2/3}$)	A ($\rm ns^{-1}\,K^{-2/3}$)	B ($\rm ns^{-1}\,K^{-3}$)
Ag(6N)a	0.55	0.73	0.045
Ag(6N)b	0.51	0.59	0.05
Ag(6N)c	0.31	0.37	0.047
Ag(6N)d	0.47	0.56	0.044
Au(6N)	0.40	0.67	0.069

This data set casts doubt on the claim by Mohanty, Jariwala, and Webb[7] (MJW) that saturation of τ_ϕ is a universal phenomenon in mesoscopic wires. One can always argue that the saturation temperature for our silver samples is below 40 mK, hence unobservable in our experiments. However, the resistivity and dimensions of sample Ag(6N)a are similar to those of sample Au-3 in the MJW paper,[7] which exhibits saturation of τ_ϕ starting at about 100 mK, and has a maximum value of $\tau_\phi^{\rm max} = 2$ ns. In contrast, τ_ϕ reaches 9 ns in Ag(6N)a.

B. Silver 5N and copper samples

In silver samples made from a 5N purity source, the phase coherence time is systematically shorter than predicted by Eq. (3) and displays an unexpectedly flat temperature dependence below 400 mK. The same is true for all the copper samples we measured, independently of source purity.[18] These trends are illustrated for samples Ag(5N)b and Cu(6N)b in Fig. 3.

What can be responsible for this anomalous behavior? There have been several theoretical suggestions regarding sources of extra dephasing. Some of these, such as the presence of a parasitic high frequency electromagnetic radiation,[19] can be ruled out purely on experimental grounds. Indeed some samples do show a saturation of τ_ϕ, while others of similar resistance and geometry, measured in the same cryostat, do not. This indicates that, in our experiments at least, the observed excess dephasing is not an artifact of the measurement. The main suggestions to explain the anomalous behavior of τ_ϕ are dephasing by very dilute magnetic impurities,[11,20] dephasing by two-level systems associated with lattice defects,[21,22] and dephasing by electron–electron interactions through high energy electromagnetic modes.[23]

The correlation between source material purity and excess dephasing amongst silver samples fabricated using the exact same process but with either our 5N or 6N source material suggests that impurities are responsible for the anomalous temperature dependence of τ_ϕ. The fact that, among all the 6N silver samples, $\tau_\phi(T)$ deviates the most from the prediction of electron–electron interactions in Ag(6N)d, fabricated in MSU (see Fig. 4) would mean that the 6N silver source material used at MSU contains more ''dangerous'' impurities than the one at Saclay.

The phase coherence time in the copper samples is always almost independent of temperature below about 200 mK down to our base temperature of 40 mK (see Refs. 11,24,25). However, as opposed to silver samples, this unexpected be-

TABLE IV. Kondo temperature T_K (K) of common, low T_K, magnetic impurities in Ag, Au, and Cu (taken from Ref. 27).

Host \ Impurity	Cr	Fe	Mn
Ag	~0.02	~3	0.04
Au	~0.01	0.3	<0.01
Cu	1.0	25	0.01

havior is not correlated with the source material purity (5N or 6N). A likely explanation is provided by early measurements showing that the surface oxide of copper can cause dephasing.[26]

V. INFLUENCE ON τ_ϕ OF VERY DILUTE MAGNETIC IMPURITIES

Dephasing of conduction electrons by paramagnetic impurities has been known since 1980,[20] hence it may come as a surprise that this issue is still under debate today. In their Letter on the "saturation" of τ_ϕ at low temperature,[7] Mohanty, Jariwala, and Webb studied the effect of intentionally doping their gold wires with iron impurities. They found that τ_ϕ in those samples did not truly saturate, but rather reached a plateau around 1 K and increased again below about 0.3 K. In addition, the presence of the iron impurities could be detected by a logarithmic contribution to the temperature dependence of the resistance $R(T)$, known as the Kondo effect. They concluded from those data that magnetic impurities were not the cause of the saturation of τ_ϕ they observed in their nominally pure gold samples. However, it is well known that the spin-flip scattering rate peaks near the Kondo temperature T_K, then decreases at lower temperature. While MJW showed convincingly that "saturation" of τ_ϕ in gold could not be caused by iron impurities with $T_K \approx 0.3$ K, their data do not exclude an effect of impurities with a lower Kondo temperature, such as manganese or chromium (see Table IV).

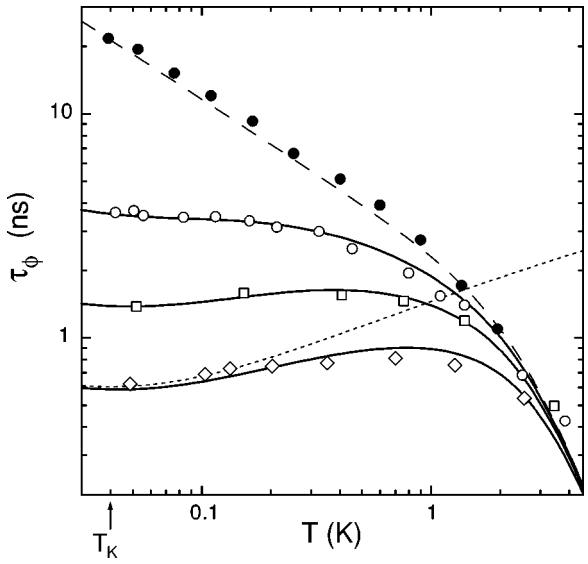

FIG. 5. Phase coherence time as function of temperature in several silver wires. Sample Ag(6N)c (●) is made of the purest silver source. Samples Ag(5N)b (○), Ag(5N)$c_{Mn0.3}$ (□), and Ag(5N)d_{Mn1} (◇) were evaporated simultaneously using our 5N silver source. Afterward, 0.3 ppm and 1 ppm of manganese was added by ion implantation respectively in samples Ag(5N)$c_{Mn0.3}$ and Ag(5N)d_{Mn1}. The presence of very dilute manganese atoms, a magnetic impurity of Kondo temperature $T_K = 40$ mK, reduces τ_ϕ leading to an apparent "saturation" at low temperature. Continuous lines are fits of $\tau_\phi(T)$ taking into account the contributions of electron–electron and electron–phonon interactions (dashed line) and spin–flip collisions using the concentration c_{mag} of magnetic impurity as a fit parameter (dotted line is τ_{sf} for $c_{mag} = 1$ ppm). Best fits are obtained using $c_{mag} = 0.13$, 0.39, and 0.96 ppm, respectively, for samples Ag(5N)b, Ag(5N)$c_{Mn0.3}$, and Ag(5N)d_{Mn1}, in close agreement with the concentrations implanted and consistent with the source material purity used.

A. Can dilute magnetic impurities account for a plateau in $\tau_\phi(T)$?

To answer this question experimentally, we fabricated simultaneously three silver samples Ag(5N)b, Ag(5N)$c_{Mn0.3}$, and Ag(5N)d_{Mn1}, and very dilute manganese atoms were introduced by ion implantation[28] in two of them. Manganese atoms form Kondo impurities in silver with a Kondo temperature $T_K \simeq 40$ mK.

The phase coherence times extracted from WL corrections are shown as symbols in Fig. 5. Samples Ag(6N)c, evaporated separately, is shown as a reference. At the time of this experiment only the 5N purity silver source was available. Sample Ag(5N)b, in which no manganese atoms were implanted, already shows very little temperature dependence of $\tau_\phi \sim 3.5$ ns below 0.3 K. Nevertheless, introducing more manganese reduces further the phase coherence time as illustrated with samples Ag(5N)$c_{Mn0.3}$ and Ag(5N)d_{Mn1} in which, respectively, 0.3 and 1 ppm of manganese were implanted. For instance, by adding 1 ppm of manganese, τ_ϕ was reduced by a factor of 6 while leaving τ_ϕ still nearly independent of temperature.

The effect of manganese on τ_ϕ is now compared with the existing theory of spin–flip scattering in the Kondo regime.

B. Comparison with the theory of spin–flip scattering

In the presence of spin–flip scattering the phase coherence time reads

$$\frac{1}{\tau_\phi} = \frac{1}{\tau_{ee}} + \frac{1}{\tau_{ph}} + \frac{1}{\tau_{sf}}, \tag{5}$$

where $1/\tau_{sf}$ is the spin–flip rate of electrons. This expression is valid when the spin–flip scattering time of the conduction electrons is longer than the spin relaxation time (τ_K for Korringa time) of the magnetic impurities themselves, i.e., $\tau_{sf} > \tau_K$.[29] This holds if

$$T \gtrsim \frac{c_{mag}}{\nu_F k_B}, \tag{6}$$

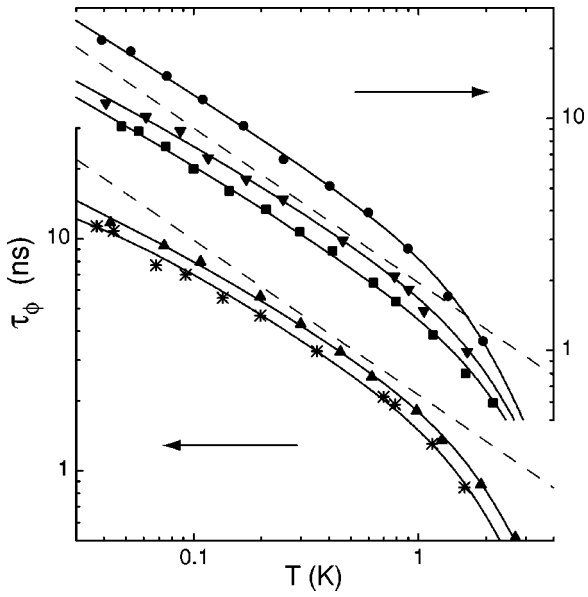

FIG. 6. Phase coherence time vs temperature measured on samples Ag(6N)a (■), Ag(6N)b (▼), Ag(6N)c (●), Ag(6N)d (▲), and Au(6N) (*). For clarity the graph has been split in two parts shifted vertically, as was done in Fig. 4. In contrast to Fig. 4, continuous lines are fits of the data to Eqs. (5) and (8), with the concentration of magnetic impurities as an additional fit parameter (see Table V). The quantitative prediction of Eq. (3) for electron–electron interactions in samples Ag(6N)b (top part) and Ag(6N)d (bottom part) are shown as dashed lines.

where $c_{\rm mag}$ is the concentration per unit volume of magnetic impurities. In silver, gold, and copper this criterion reads

$$T \gtrsim 40 \ \ {\rm mK} \times c_{\rm mag}({\rm ppm}), \tag{7}$$

in which $c_{\rm mag}$(ppm) is now written in parts per million atoms (ppm). In the opposite limit ($\tau_{\rm sf} < \tau_K$), the impact of spin flip scattering on τ_ϕ depends on the physical effect probed. For weak localization corrections with strong spin–orbit coupling, spin–flip scattering enters then as $2/\tau_{\rm sf}$ in Eq. (5).[20,29]

As long as $T \gtrsim T_K$, $\tau_{\rm sf}$ is well described by the Nagaoka-Suhl formula[30,31]

$$\frac{1}{\tau_{\rm sf}} = \frac{c_{\rm mag}}{\pi \hbar \nu_F} \frac{\pi^2 S(S+1)}{\pi^2 S(S+1) + \ln^2(T/T_K)}, \tag{8}$$

with S and T_K, respectively, the spin and Kondo temperature of the magnetic impurities.

Upon cooling down, $\tau_{\rm sf}$ decreases when T approaches T_K (dotted line in Fig. 5), whereas the electron–electron scattering time τ_{ee} increases. The combination of both contributions can result in a nearly constant phase coherence time above T_K, as shown by the solid lines in Fig. 5.

A quick way to estimate the concentration of magnetic impurities corresponding to a plateau in the phase coherence time is to compare $\tau_\phi^{\rm plateau}$ at the plateau to the prediction of Nagaoka-Suhl at $T = T_K$. In samples made of copper, gold and silver this gives

$$\tau_\phi^{\rm plateau} \simeq 0.6 \ \ {\rm ns}/c_{\rm mag}({\rm ppm}). \tag{9}$$

TABLE V. Fit parameters for $\tau_\phi(T)$ in silver and gold samples made of our 6N sources, taking into account, on top of the contributions of electron–electron and electron–phonon interactions, the additional contribution of dilute Kondo impurities of spin-1/2 as described by Eqs. (5) and (8). The corresponding fits are displayed as continuous lines in Fig. 6.

Sample	A ($A_{\rm thy}$) ($\rm ns^{-1}\,K^{-2/3}$)	B ($\rm ns^{-1}\,K^{-3}$)	$c_{\rm mag}$ (ppm)	T_K (K)
Ag(6N)a	0.68 (0.55)	0.051	0.009	0.04
Ag(6N)b	0.54 (0.51)	0.05	0.011	0.04
Ag(6N)c	0.35 (0.31)	0.051	0.0024	0.04
Ag(6N)d	0.50 (0.47)	0.054	0.012	0.04
Au(6N)	0.59 (0.40)	0.08	0.02	0.01

Continuous lines in Fig. 5 are fits of the measured $\tau_\phi(T)$ to Eq. (5) using Eq. (8), with magnetic impurities of Kondo temperature $T_K = 40$ mK as expected for manganese atoms. The parameters A and B in Eq. (4) could not be extracted independently for samples Ag(5N)b, $c_{\rm Mn0.3}$, and $d_{\rm Mn1}$. To avoid increasing unnecessarily the number of fit parameters, the values of A and B deduced from the fit of sample Ag(6N)c (dashed line) were used. Sample Ag(6N)c was chosen as a reference because its predicted electron–electron scattering rate is close to that of samples Ag(5N)b, Ag(5N)$c_{\rm Mn0.3}$, and Ag(5N)$d_{\rm Mn1}$. Following this procedure, the measurements could be reproduced accurately with[32] $S = 1/2$ and $c_{\rm mag} = 0.13$, 0.39, and 0.96 ppm, respectively, for samples Ag(5N)b, $c_{\rm Mn0.3}$, and $d_{\rm Mn1}$, in close agreement with implanted concentrations of manganese and compatible with the nominal purity of the Saclay 5N silver source. This confirms that the effect on τ_ϕ of the implantation of magnetic impurities with a low Kondo temperature is well understood, both qualitatively and quantitatively.

Looking back at the τ_ϕ data for samples Ag(6N)a, b, c, d and Au(6N) shown in Fig. 4, we note that the fits to those data would also improve with the addition of a very small quantity of magnetic impurities. We performed new fits to those data using Eqs. (5) and (8), with $c_{\rm mag}$ as an additional adjustable parameter. For the silver samples we kept $T_K = 40$ mK as for manganese impurity atoms, whereas for the gold sample Au(6N) we chose $T_K = 10$ mK as for chromium impurity atoms. The values of $c_{\rm mag}$ from the fits are 0.009, 0.011, 0.0024, 0.012, and 0.02 ppm, respectively, for samples Ag(6N)a, b, c, d, and Au(6N). The new fits are shown as continuous lines in Fig. 6 and the fit parameters are given in Table V. Note that these concentrations are about 100 times smaller than the nominal total impurity concentrations of the sources. As a striking example to show how small these numbers are, 0.01 ppm of impurities in sample Ag(6N)d corresponds to about 3 impurity atoms every micrometer in the wire. Such small concentrations of Kondo impurities are essentially undetectable by any means other than measuring the phase coherence time, especially in thin films. Moreover, no commercial provider can guarantee such a high purity for the source material.

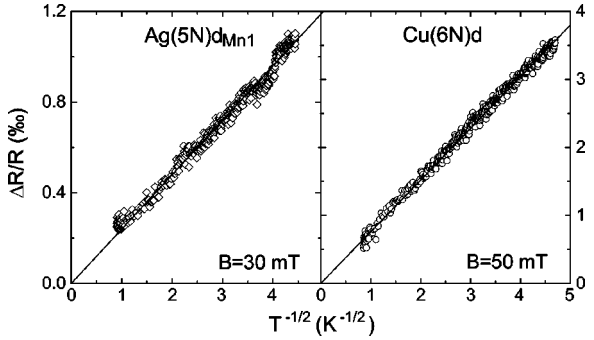

FIG. 7. Resistance of sample Ag(5N)d_{Mn1} ($\diamond$) and Cu(6N)d ($\circ$) plotted as function of $1/\sqrt{T}$. Continuous lines are fits using the functional form $\Delta R(T)/R = C/\sqrt{T}$, with $C = 2.4\times10^{-4}$ (left panel) and 7.6×10^{-4} $K^{1/2}$ (right panel), close to the predictions of Eq. (10) $C_{thy} = 1.8\times10^{-4}$ and 7.2×10^{-4} $K^{1/2}$, respectively. The logarithmic contribution to $R(T)$ from the Kondo effect is invisible in both samples, as it is masked by the much larger contribution from electron–electron interactions in the wires. From the comparison of Figs. 5 and 7, it appears clearly that the phase coherence time is a much more sensitive probe of very dilute magnetic impurities than the temperature dependence of the resistance.

C. Extremely dilute magnetic impurities and temperature dependence of the resistance

The temperature dependence of the resistance, $R(T)$, is often used as a probe of magnetic impurities, because of the well-known Kondo effect. Nevertheless, in thin wires, where the resistance also varies due to electron–electron interactions, it must be pointed out that $R(T)$ is not sensitive enough to detect small amounts of magnetic impurities. The contribution of electron–electron interactions,[15]

$$\frac{\Delta R(T)}{R} \simeq 3.126 \frac{R}{R_K}\frac{L_T}{L} \equiv \frac{C_{\rm thy}}{\sqrt{T}}, \tag{10}$$

with $L_T = \sqrt{\hbar D/k_B T}$ the thermal length, is much stronger and varies much more rapidly with temperature than the Kondo term, determined by $\Delta\rho_{\rm Kondo} \simeq -B_K \ln(T)$,[33] where $B_K \approx 0.2$ nΩ cm/ppm.[34] In our wires where the resistivity is about $\rho \sim 3$ $\mu\Omega$ cm, the corresponding relative variation of the resistance is about 10^{-5} per decade of temperature for 1 ppm of Kondo impurities. This is more than an order of magnitude smaller than the typical contribution of electron–electron interactions between 100 mK and 1 K.

This is illustrated in the left panel of Fig. 7 with sample Ag(5N)d_{Mn1} in which we implanted 1 ppm of manganese. The resistances are measured in a magnetic field $B \sim 20$–50 mT, large enough to suppress the WL corrections but small enough to avoid freezing out the spin–flip scattering of conduction electrons by magnetic impurities. We checked on several samples showing anomalous dephasing that $R(T)$ is independent of the applied magnetic field.

A striking conclusion is that the phase coherence time is a much more sensitive probe of very dilute magnetic impurities than the temperature dependence of the resistance, which is dominated by electron–electron interactions at low temperature.

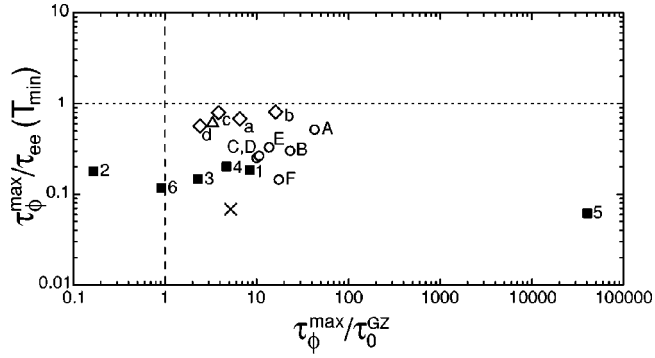

FIG. 8. Comparison between the predictive powers of the conventional theory of electron–electron interactions (Ref. 3), and of the theory of Golubev and Zaikin (Refs. 23,35). The X coordinate gives the ratio of the phase coherence time measured at the lowest temperature, $\tau_\phi^{\rm max}$, to $\tau_0^{\rm GZ}$, calculated from Eq. (11) with $b=1$. The Y coordinate is the ratio of $\tau_\phi^{\rm max}$ to $\tau_{ee}(T_{\rm min})$, the value calculated using the conventional theory [Eq. (3)] at the lowest temperature $T_{\rm min}$. Open symbols are data points for which the phase coherence time continues to increase at the lowest measurement temperature. Full symbols and $\times$ are data points for which the phase coherence time is nearly constant at low temperature. The conventional theory predicts that all data points lie on the horizontal dotted line if no extrinsic degrees of freedom, such as magnetic impurities, limit the phase coherence time. The GZ theory predicts that all data points lie on a vertical line if the phase coherence time already saturates, and to the left of that line if τ_ϕ still increases at low temperature. (The dashed line corresponds to the case $b=1$ in the GZ theory.)

VI. OTHER EXPLANATIONS OF ANOMALOUS DEPHASING

The evidence presented in the previous section shows that very dilute magnetic impurities could explain the anomalous dephasing frequently observed at low temperature. But are there other viable explanations?

A. Dephasing by high energy electromagnetic modes

Golubev and Zaikin (GZ) proposed[23,35] that zero temperature dephasing by high energy electromagnetic modes is responsible for the frequently observed saturation of τ_ϕ in metallic thin films. This theory, which is controversial,[36] predicts that the phase coherence time saturates at low temperature at $\tau_0^{\rm GZ}$ given by[35]

$$\frac{1}{\tau_0^{\rm GZ}} = \frac{\sqrt{2}\rho}{3R_K\pi\sqrt{D}}\left(\frac{b}{\tau_e}\right)^{3/2}, \tag{11}$$

where b is a constant numerical factor expected to be of order 1. It is interesting to point out that for a given material $\tau_0^{\rm GZ}$ is proportional to D^3 and is insensitive to the actual geometry of the sample.

Using this prediction, GZ were able to account for a subset of the experimental results published in Refs. 24,37 using the overall prefactor of the dephasing rate as an adjustable parameter.[35] Note that, as explained by GZ in their latest article,[35] the comparison with MJW data performed in Ref. 38 should be ignored because it was done using an expres-

sion for τ_0^{GZ} that does not apply to the experiment, but is valid only when the elastic mean free path exceeds the transverse dimensions of the wires.

Since the exact prefactor is unknown, it is not possible to rule out this theory by comparison with a single experiment. Instead, we propose here to compare the predictive power of the GZ theory with the conventional theory of electron–electron interactions for many samples. This is done in Fig. 8. This figure includes all gold, silver and gold–palladium samples for which it has not been shown that magnetic impurities are the main source of decoherence at low temperature, plus sample Cu(5N)a which was used by GZ for comparison of their theory with experiments.[35] (We do not show other copper samples or samples made from our 5N silver source, because they clearly contain magnetic impurities. See Sec. VII and Ref. 39.) The *X* coordinate in Fig. 8 gives the ratio of the phase coherence time measured at the lowest temperature, τ_ϕ^{max}, to τ_0^{GZ}, calculated from Eq. (11) with $b=1$. The *Y* coordinate is the ratio of τ_ϕ^{max} to $\tau_{ee}(T_{min})$, the value calculated using the conventional theory [Eq. (3)] at the lowest temperature T_{min}. Open symbols are samples for which τ_ϕ continues to increase at the lowest measurement temperature; upon cooling they move to the right. Full symbols are samples for which τ_ϕ is nearly constant at low temperature; they move downward when the temperature is reduced. As for theory, GZ predict that all full symbols should be aligned on a vertical line $\tau_\phi^{max}/\tau_0^{GZ}=b^{3/2}$, whereas open symbols would be located at $\tau_\phi^{max}/\tau_0^{GZ}<b^{3/2}$. In contrast, the conventional theory predicts that all data points should be aligned on the horizontal line $\tau_\phi^{max}/\tau_{ee}(T_{min})=1$. On this plot the data scatter in both directions. The most salient feature of the plot, however, is that the scatter in the horizontal direction extends over more than five orders of magnitude, whereas the scatter in the vertical direction extends over slightly more than one decade. The horizontal scatter indicates that GZ theory does not reproduce the dependence of τ_ϕ on sample parameters. In particular, the GZ prediction depends much too strongly on the diffusion coefficient, which varies considerably in MJW's six gold samples.

While no theory explains all of the experimental data without any additional parameters, it appears that the conventional theory does a better job than the GZ theory to predict the low temperature value of τ_ϕ.

B. Dephasing by two level systems

Two approaches to electron dephasing by two-level tunneling systems (TLS) have been proposed. The first, by Imry, Fukuyama, and Schwab,[21] requires a nonstandard distribution of TLS parameters. It was shown later that such a distribution would lead to large anomalies in the low-temperature specific heat, and in acoustic attenuation at very low temperature.[40] The second approach describes the coupling between the conduction electrons and the TLS via the two-channel Kondo effect.[22] In this model, the effect of TLS is very similar to that of magnetic impurities in the Kondo regime, at least at $T \gtrsim T_K$. The main criticism raised against this explanation is that, starting from any realistic model of a TLS, it may be impossible to reach the strong coupling regime where the Kondo temperature is larger than the tunneling level splitting.[41,42] From the experimental point of view, measurements of τ_ϕ from the weak localization contribution to the magnetoresistance cannot discriminate between magnetic impurities and TLS.

VII. TEST OF THE MAGNETIC IMPURITY HYPOTHESIS: PROBING $\tau_\phi(B)$

A definitive test of the role of spin-flip scattering for the saturation of τ_ϕ at low temperature is to probe how the dephasing time depends on magnetic field. It is expected that spin–flip scattering is suppressed when the dynamics of magnetic impurities is frozen by application of a sufficiently large magnetic field *B*. Indeed, if the Zeeman splitting is much larger than k_BT, magnetic impurities stay in their ground state. As a result spin–flip collisions vanish and τ_ϕ should climb up to the value expected from electron–electron interactions (independent of *B* as long as the cyclotron radius is much larger than the elastic mean free path). In the presence of spin-1/2 impurities, and neglecting Kondo effect, the spin–flip scattering rate of electrons vanishes at large field as (see Appendix C and Ref. 43)

$$\frac{\tau_{sf}(B=0)}{\tau_{sf}(B)}=\frac{g\mu B/k_BT}{\sinh(g\mu B/k_BT)}, \tag{12}$$

where *g* is the renormalized gyromagnetic factor of the magnetic impurities.

One possible method to detect a variation in τ_ϕ with magnetic field is to measure the average amplitude ΔG_{UCF} of universal conductance fluctuations in a metallic wire as a function of magnetic field. This method has two drawbacks. First $\Delta G_{UCF} \propto \tau_\phi^{1/4}$ depends only weakly on the phase coherence time. Second the large correlation field $\Delta B_{UCF} \simeq h/(ewL_\phi)$ of conductance fluctuations in mesoscopic wires makes it difficult to obtain accurate estimates of the averaged $\Delta G_{UCF}(B)$ at low temperature in the field range below the relevant magnetic field scale $g\mu B \sim k_BT$. For example, in Cu(6N)b, $\Delta B_{UCF} \simeq 25$ mT at 40 mK, whereas the characteristic field needed to freeze the magnetic impurities is as low as $k_BT/2\mu \simeq 55$ mT.

We have chosen instead to probe the magnetic field dependence of τ_ϕ by measuring the Aharonov-Bohm (AB) oscillations in the magnetoresistance of ring-shaped samples. For this purpose, we have fabricated two copper rings of radius $r=0.5$ and 0.75 μm, respectively, on the same chip as samples Cu(6N)c and Cu(6N)d. The ring perimeters are chosen to be larger than or similar to the phase coherence length at $B \approx 0$ in order to increase the sensitivity to variations of τ_ϕ. The averaged h/e AB oscillations amplitude ΔG_{AB} is related to the phase coherence time through[44]

$$\Delta G_{AB}=C\frac{e^2}{h}\frac{L_T}{\pi r}\sqrt{\frac{L_\phi}{\pi r}}\exp\left[-\frac{\pi r}{L_\phi}\right], \tag{13}$$

where *C* is a geometrical factor of order 1. The short period of AB oscillations with B (5.5 and 2.5 mT for $r=0.5$ and 0.75 μm, respectively) allows to estimate accurately the

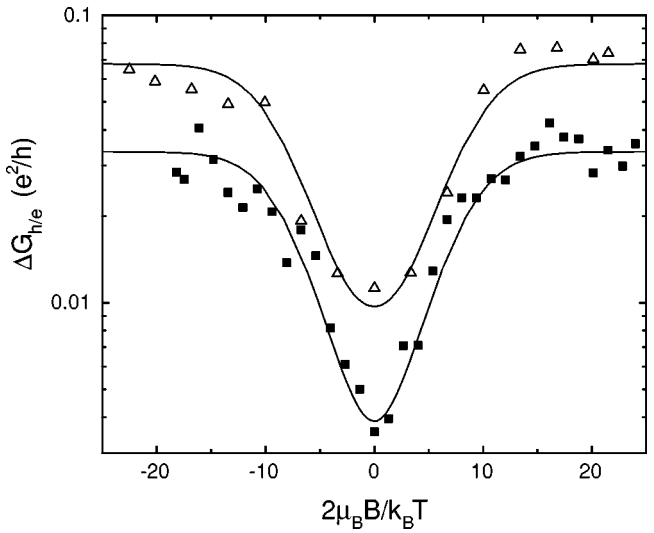

FIG. 9. Symbols: mean amplitude of the AB h/e oscillations ($\Delta G_{h/e}$) across the ring in sample Cu(6N)d at $T=40$ (△) and 100 mK (■), plotted in units of e^2/h as a function of the reduced magnetic field $2\mu_B B/k_B T$. Solid lines: fits to the two data sets using Eqs. (5), (12), and (13) with C and g as fit parameters. At 40 mK, the AB oscillations are unmeasurably small at B=0; the fit to those data includes the noise floor of the experiment.

magnetic field dependence of ΔG_{AB} on the much larger field scale needed to freeze the magnetic impurities.

This experiment was performed on copper samples because it is the material in which the presence of magnetic impurity was most questionable: no correlations were found between τ_ϕ and the copper source material purity; moreover, whereas in some samples τ_ϕ saturates at values as small as 0.2 ns [3 times smaller than in $\mathrm{Ag(5N)d_{Mn1}}$] we observed neither a nonmonotonic temperature dependence of $\tau_\phi(T)$, as in $\mathrm{Ag(5N)d_{Mn1}}$ (see Fig. 5), nor a Kondo contribution to $R(T)$.

Our experimental procedure and data analysis are detailed in Ref. 25. Figure 9 shows the amplitude of AB oscillations measured across the ring in sample Cu(6N)d at $T=40$ and 100 mK (symbols) as a function of reduced magnetic field $2\mu B/k_B T$. The data in Fig. 9 show that the amplitude of AB oscillations increases with magnetic field by a factor 8 at 100 mK and a factor 7 at 40 mK,[45] on a characteristic field scale proportional to T.

The solid lines in Fig. 9 are fits to the simple model represented by Eqs. (12) and (13), explained in Appendix C. We assumed that τ_ϕ at large B is limited only by electron–electron interactions and used the values given by theoretical prediction [Eq. (3)]: $\tau_\phi=5.4$ and 9.9 ns at 100 and 40 mK, respectively. The two remaining parameters, namely the gyromagnetic factor g and the geometrical constant[46] C, were adjusted to reproduce accurately our data. The best fit is obtained with $g=1.08$ and $C=0.17$. Note that a more rigorous approach to the magnetic-field dependence of AB oscillation amplitude has been published recently by Vavilov and Glazman.[47] Using their prediction [Eqs. (62) and (63) in Ref. 47] with a magnetic impurity spin[48] $S=1/2$ and $g=0.90$, we obtain a fit indistinguishable from the solid lines calculated with the simple model.

The impurity g-factors obtained from these fits, 1.08 and 0.90, are small, like the value $g=1.36$ found for electrons by neutron scattering in bulk CuO.[49]

This set of experiments confirms that spin–flip collisions are responsible for the apparent low temperature saturation of τ_ϕ we observe in copper samples.

VIII. COMPARISON WITH ENERGY EXCHANGE MEASUREMENTS

Parallel to this work, a systematic correlation was found between dephasing and energy exchange between electrons: all samples made of the same source material, using the same deposition system, either followed the theory of electron–electron interactions for both energy exchange and phase coherence, or displayed anomalous behaviors for both phenomena.[11,24,50,51] This correlation suggests that magnetic impurities could also be responsible for anomalous energy exchange. Such a possibility had not been considered until recently because, all spin states being degenerate at zero magnetic field, magnetic impurities do not contribute to energy exchange in first order. However, Kaminsky and Glazman have pointed out that energy exchange in the presence of magnetic impurities may take place with an appreciable efficiency by a second-order process.[52] The experimental proof that excess energy exchange observed in samples made of the 5N silver and copper sources results from dilute paramagnetic spins was obtained recently by measuring the dependence of energy exchange upon magnetic field.[39] Similarly to what was observed on the dephasing rate, the application of a large magnetic field on these samples reduces the rate of energy exchange. Note however that the amount of magnetic impurities needed to account for the measured energy exchange rates seems to be significantly larger than the estimations from $\tau_\phi(T)$; in the case of copper, the obtained g-factor $g=2.3$ is also different. More experiments are needed to clarify these issues.

IX. CONCLUSION

By measuring the phase coherence time as a function of temperature on wires made of silver, gold, and copper, from source materials of different purities, we have found that anomalous dephasing is correlated to source material purity in silver and gold samples, and systematic in copper samples. We showed experimentally that the presence of very dilute magnetic impurities with a low Kondo temperature in the host material can result in a broad plateau in $\tau_\phi(T)$ while being undetected in the temperature dependence of the resistance. Measurement of the magnetic field dependence of Aharonov-Bohm oscillations on relatively large copper rings revealed that the phase coherence time increases with B on a field scale proportional to the temperature. This confirms that an apparent ''saturation'' of τ_ϕ can be attributed to very dilute magnetic impurities.[53]

In the silver and gold samples discussed in this paper, we impute the presence of magnetic impurities to the purity of the material sources. We found that large coherence times at 40 mK could be obtained in samples fabricated with the

silver sources of the highest purity commercially available (6N). However, it is very difficult to rule out a small contamination during the evaporation process and eventually sample preparation. In the case of copper, the Kondo impurities probably originate from the copper oxide at the surface.[26]

ACKNOWLEDGMENTS

This work was supported by NSF Grants Nos. DMR-9801841 and 0104178, and by the Keck Microfabrication Facility supported by NSF DMR-9809688. We acknowledge the assistance of S. Gautrot, O. Kaitasov, and J. Chaumont at the CSNSM in Orsay University, who performed the ion implantation in samples $Ag(5N)c_{Mn0.3}$ and $Ag(5N)d_{Mn1}$. We are grateful to I. Aleiner, B.L. Altshuler, H. Bouchiat, M.H. Devoret, V.I. Fal'ko, L.I. Glazman, D. Natelson, M.G. Vavilov, and A.D. Zaikin for interesting discussions.

APPENDIX A: ELECTRON COOLING IN TRANSPORT MEASUREMENTS AT LOW TEMPERATURES

Joule heating is a concern when transport measurements are performed at low temperatures. Any current results in the production of heat, which can be either transferred directly to the phonons in the wire, or to the electrons in the contact pads, assumed to be much larger than the wire. At sub-Kelvin temperatures, the first process becomes very inefficient. The reason is that the phonon emission rate for an electron with an excess energy k_BT goes like[11] $\gamma \simeq 5\kappa_{\rm ph}(k_BT)^3$, with $\kappa_{\rm ph}\simeq 10\ {\rm ns}^{-1}\,{\rm meV}^{-3}$. The distance it will travel before losing its extra energy is then $\sqrt{D/\gamma} \simeq 18\ \mu{\rm m}\times(T/1\ {\rm K})^{-3/2}$ for a typical diffusion coefficient $D=100\ {\rm cm}^2/{\rm s}$. At $T=40$ mK, $\sqrt{D/\gamma}\simeq 2.2$ mm, a very macroscopic distance! Therefore one must take care that the electron's energy never gets so large at low temperature. Taken alone, the cooling by the contact pads through electronic heat transport results in a temperature profile in the wire

$$T_e(x)=\sqrt{T^2+\frac{3}{\pi^2}x(1-x)\left(\frac{eV}{k_B}\right)^2}, \qquad \text{(A1)}$$

with T_e the electron temperature in the contacts placed at the ends of the wire, assumed to be equal to the temperature of the phonons, x the relative position along the wire, and V the voltage across the wire. For $T=0$, the maximum temperature is $(\sqrt{3}/2\pi)(eV/k_B)\approx 3.2\ {\rm K}\times V/(1\ {\rm mV})$. By limiting the voltage across the sample to $eV=k_BT$, the maximal electron temperature is $T\sqrt{1+(3/4\pi^2)}\simeq 1.04\ T$. With such a low applied voltage, the phase coherence time, supposed to increase as $T_e^{-2/3}$ at low temperature, varies through the sample by $1-1.04^{-2/3}\simeq 2\%$, which is sufficiently small for most purposes. However, at very low temperature, a measurement of a voltage of order k_BT/e might become very time consuming if one considers that the input voltage noise for the best room-temperature commercial amplifiers is about 1 $\mathrm{nV}/\sqrt{\mathrm{Hz}}$ and that the weak localization correction to the conductance is about 10^{-3} of the total signal. For example at 10 mK, $10^{-3}k_BT/e\simeq 1$ nV, and an integration time of 100 s for each conductance measurement is needed to get a signal to noise ratio of 10. In fact, this estimation is often too pessimistic because cooling by phonons does play a role for long wires.[54] In order to evaluate this effect precisely, one has to solve the complete heat equation, which can be written in reduced units ($t_e(x)=T_e(x)/T$, $v=eV/k_BT$),

$$v^2+\frac{\pi^2}{6}\frac{d^2}{dx^2}t_e^2(x)-\left(\frac{T}{T_{\rm co}}\right)^3(t_e^5(x)-1)=0, \qquad \text{(A2)}$$

in which the first term describes Joule heating, the second the thermal conductivity of electrons, assuming Wiedemann-Franz law, and the last one the coupling to phonons.[11,55] We have defined a crossover temperature

$$T_{\rm co}=(\Sigma\rho L^2(e/k_B)^2)^{-1/3}, \qquad \text{(A3)}$$

with L the length of the wire, ρ its resistivity, Σ the electron–phonon coupling constant[56] (typically $\Sigma \sim 1-10\ {\rm nW}/\mu{\rm m}^3/{\rm K}^5$ in metallic thin films on Si substrate). The resulting temperature profile is shown in Fig. 10 for typical values: we consider a silver wire ($\Sigma \simeq 3\ {\rm nW}/\mu{\rm m}^3/{\rm K}^5$ from Table III) with $D=100\ {\rm cm}^2/{\rm s}$, $L=0.2$ mm, at $T=100$ and 200 mK, for $eV/k_BT=3$. The dotted line indicates the solution without phonons, the dashed line the solution without electronic heat transport. For this set of parameters, the crossover temperature is $T_{\rm co}\simeq 120$ mK. Hence, at 200 mK phonons reduce significantly the maximum electron temperature, which does not exceed the bath temperature by more than 16%. At 100 mK, cooling by phonon emission is inefficient, and the maximum electron temperature is 27% above T.

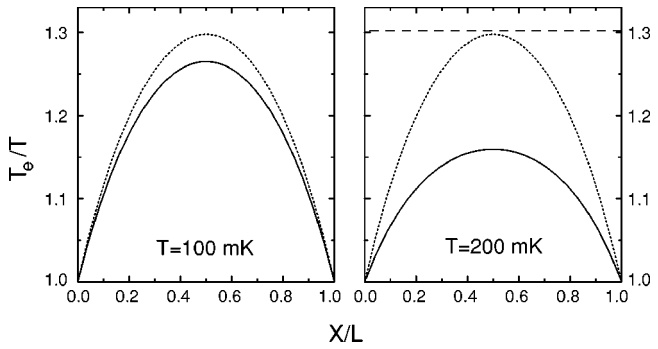

FIG. 10. Electrons heating in a typical silver wire (see text) of length $L=0.2$ mm, biased with a dc voltage V such that $eV/k_BT=3$ and for phonon temperatures $T=100$ and 200 mK, respectively, in the left and right panel. Continuous lines: ratio of electron temperature T_e with phonon temperature as function of the reduced position X/L in the wire, taking into account electron–phonon interactions [see Eq. (A2)]. Dotted lines: electron temperature as function of position neglecting phonons [see Eq. (A1)]. Dashed line in the right panel: electron temperature neglecting electronic heat transport (in the left panel this line would stand at $T_e/T=1.87$).

The analysis of the exact solutions of this equation allows to distinguish two opposite regimes: for $T\ll T_{\rm co}$, electrons are decoupled from phonons (cooling by phonons will become active only if the applied voltage is so high that the maximal temperature is above $T_{\rm co}$), and temperature is given

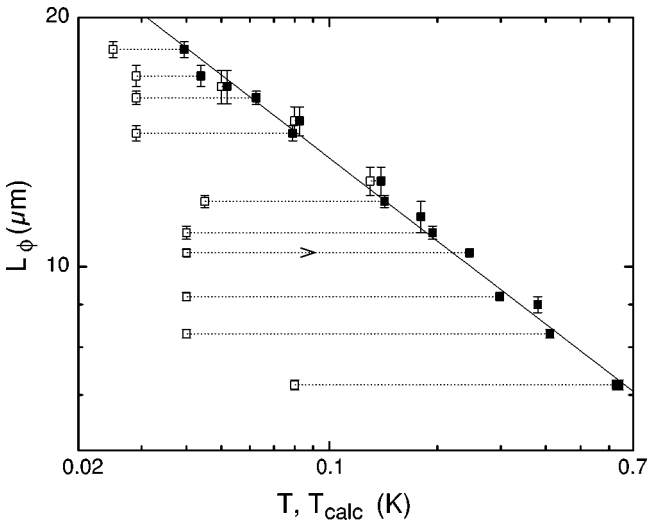

FIG. 11. Full symbols: phase coherence length measured on a 6N silver sample as a function of the electronic temperature $T_{\rm calc}$ calculated using Eq. (A2) for a cryostat temperature T represented by the attached open symbol. The continuous line represents the theoretical prediction $L_\phi \propto T^{-1/3}$ of electron–electron interactions (data taken at Saclay).

by the electronic conductivity alone, see Eq. (A1). This is the difficult regime, where the maximal voltage is of the order of k_BT/e. In the opposite situation $T \gg T_{\rm co}$, heat transfer to the contacts can be neglected, and cooling by phonons rules the game. The temperature of the electrons is then nearly homogeneous, with $T_e/T \approx (1+(T_{\rm co}/T)^3 v^2)^{1/5}$ and for $(T_{\rm co}/T)^3 v^2 \ll 1$ the temperature does not exceed T excessively: $T_e \approx T + \frac{1}{5}[T_{\rm co}^3 (eV/k_B)^2/T^4]$. One should thus fabricate wires as long as possible, in order to have a small crossover temperature $T_{\rm co}$ which allows to work at larger voltages.

In order to test the validity of this calculation, we performed a control experiment in which electrons were intentionally heated by applying ac currents. The sample, similar to the others presented in this review, consists of a 1.79-mm-long, 150-nm-wide, and 45-nm-thick wire made out of a 6N purity silver source. The diffusion coefficient $D = 139\ {\rm cm}^2/{\rm s}$ results in a crossover temperature $T_{\rm co} = 30$ mK. We extracted the phase coherence length L_ϕ from the magnetoresistance. For each magnetoresistance trace we show in Fig. 11 two symbols, one open and one full, at a *Y*-coordinate given by the corresponding value of L_ϕ. Open symbols are at the *X*-coordinate given by the cryostat temperature T at which the measurement was performed, whereas full symbols are at the *X*-coordinate given by the calculated electron temperature $T_{\rm calc}$. Since the magnetoresistance is given by $L_\phi \propto T^{-1/3}$, $T_{\rm calc}$ was calculated from the time- and position-average of $T_e^{-1/3}$, using temperature profiles obtained with Eq. (A2). For example, the pair of data points at $L_\phi \simeq 10.4\ \mu$m corresponds to $T = 40$ mK, $V_{\rm ac} = 0.86$ mV rms, leading to $T_{\rm calc} = 245$ mK. The data points with large heating ($T_{\rm calc} \gg T$) as well as those with little heating ($T_{\rm calc} \simeq T$) fall close to a single line $L_\phi \propto T^{-1/3}$, indicating that the electron temperature is correctly modeled.

APPENDIX B: DEPHASING BY ELECTRON–ELECTRON INTERACTIONS

Assuming that we can restrict ourself to two body interactions, the dephasing rate, or inverse lifetime, $1/\tau_{\rm in}(E,T)$ of an electron at energy E coupled only to the electronic fluid at temperature T results from all collision processes allowed by the Pauli exclusion principle,

$$\tau_{\rm in}^{-1}(E,T) \simeq \int_{|\varepsilon| \gtrsim \hbar/\tau_\phi} d\varepsilon \;\; K(\varepsilon)(1-f_T(E-\varepsilon))h(\varepsilon,T), \tag{B1}$$

where $f_T(E)$ is the Fermi function at temperature T, $K(\varepsilon)$ is the interaction ''Kernel'' of the screened Coulomb interaction, proportional to the modulus square of the interaction matrix element for an exchanged energy ε, and

$$h(\varepsilon,T) = \int_{-\infty}^{\infty} dE' f_T(E')(1-f_T(E'+\varepsilon))$$

$$= \frac{\varepsilon}{1-\exp(-\varepsilon/k_BT)}. \tag{B2}$$

The low energy cut-off $|\varepsilon| \gtrsim \hbar/\tau_\phi$ in Eq. (B1) is introduced because fluctuations on time scales longer than the electron's lifetime can be considered as static.[4]

The interaction kernel $K(\varepsilon)$ depends only on ε since the energies of interacting electrons are close to the Fermi energy E_F and $\varepsilon \lesssim k_BT \ll E_F$. Our samples are quasi-1D because the width and thickness of the wires are smaller than the length $L_\varepsilon = \sqrt{\hbar D/\varepsilon}$ for the probed energy exchanged. For quasi-1D samples the interaction kernel reads[57]

$$K(\varepsilon) = \kappa |\varepsilon|^{-3/2}, \tag{B3}$$

with

$$\kappa^{-1} = \hbar \sqrt{\frac{\pi \nu_F SL}{4} \frac{R_K}{R}}. \tag{B4}$$

The dephasing rate $1/\tau_{ee}(T)$ is the inverse lifetime averaged over thermal excitations

$$1/\tau_{ee}(T) = \int dE \frac{f_T(E)(1-f_T(E))}{k_BT} \tau_{\rm in}^{-1}(E,T). \tag{B5}$$

Injecting Eqs. (B1) and (B3) into Eq. (B5) we obtain[58]

$$1/\tau_{ee}(T) \simeq \int_{\hbar/\tau_{ee}}^{\infty} d\varepsilon \frac{\kappa\sqrt{\varepsilon}}{k_BT} \frac{\exp(\varepsilon/k_BT)}{(1-\exp(\varepsilon/k_BT))^2}. \tag{B6}$$

This expression shows that the effect of electron–electron interactions on quantum coherence in mesoscopic wires is dominated by processes with a small exchanged energy $\varepsilon \approx \hbar/\tau_\phi$. It is interesting to point out that this implies that a sample is quasi-1D with respect to decoherence as long as the phase coherence length $L_\phi = \sqrt{D\tau_\phi}$ is large compared to its transverse dimensions and small compared to its length.

This is not true for energy exchange, for which the dimensionality is determined by the length associated with the largest exchanged energy.

In order to obtain an analytical expression for $\tau_{ee}(T)$ we make the following approximation:

$$\frac{\exp(\varepsilon/k_BT)}{(1-\exp(\varepsilon/k_BT))^2}\simeq\frac{1}{(\varepsilon/k_BT)^2}. \tag{B7}$$

This approximation is justified since the integral is dominated by small energy exchanges. This leads to

$$\tau_{ee}\simeq\hbar\left[\frac{(\pi/16)(R_K/R)\nu_F SL}{(k_BT)^2}\right]^{1/3}, \tag{B8}$$

where we used Eq. (B4) for the interaction kernel.

The calculation of τ_ϕ described above makes use of a low energy cut-off, therefore the prefactor in Eq. (B8) is not reliable. To solve this technical difficulty, Altshuler, Aronov, and Khmelnitsky[3] calculated the effect of electron–electron interactions through the interaction of one electron with the fluctuating electromagnetic field resulting from other electrons at thermal equilibrium. Within this approach it is possible to calculate directly the conductivity taking into account electron–electron interactions. The dephasing rate is then obtained without reference to the energy decay rate. Neglecting spin–orbit coupling, this calculation yields[15]

$$\frac{\Delta R}{R}(B,T)=-\frac{2R}{R_K}\frac{\sqrt{D\tau_N}}{L}\frac{\mathrm{Ai}(\tau_N/\tau_H)}{\mathrm{Ai}'(\tau_N/\tau_H)}, \tag{B9}$$

with

$$\tau_N=\hbar\left[\frac{(R_K/R)\nu_F SL}{2\pi(k_BT)^2}\right]^{1/3},$$

$$\tau_H=\frac{3\nu e^2RS}{L}\left(\frac{\phi_0}{2\pi wB}\right)^2,$$

where $\phi_0=h/e\simeq4.1\times10^{-15}\ \mathrm{T\,m^2}$ is the flux quantum, $\mathrm{Ai}(x)$ is the Airy function and $\mathrm{Ai}'(x)$ its derivative. The time τ_N is often called Nyquist time in reference to the fluctuation-dissipation theorem used to evaluate the electromagnetic fluctuations for the calculation of weak localization corrections.

Since expression (B9) includes electron–electron interactions, it should be possible to deduce the contribution τ_{ee} of the screened Coulomb interaction on the phase coherence time. This can be done by pointing out that

$$\frac{\mathrm{Ai}(x)}{\mathrm{Ai}'(x)}=\frac{-1}{\sqrt{1/2+x}}(1+\epsilon(x)), \tag{B10}$$

where $|\epsilon(x)|<0.04$ for $x>0$. In practice, the experimental resolution is not sufficient to distinguish a relative discrepancy smaller than 4% of the amplitude of weak localization corrections, which are themselves smaller than 1% of the measured signal. Hence we can write

$$\frac{\Delta R}{R}(B,T)=\frac{2R}{R_KL}\sqrt{\frac{D}{1/2\tau_N+1/\tau_H}}. \tag{B11}$$

A comparison with Eq. (1) (neglecting spin–orbit coupling) allows us to extract the phase coherence time when it is limited by electron–electron interactions,

$$\tau_{ee}=\hbar\left[\frac{(4/\pi)(R_K/R)\nu_F SL}{(k_BT)^2}\right]^{1/3}$$

$$=2\tau_N. \tag{B12}$$

This expression of the phase coherence time τ_{ee} is larger by a factor $4/\pi^{2/3}\simeq1.9$ than the cut-off-dependent estimation in Eq. (B8).

APPENDIX C: MAGNETIC FIELD DEPENDENCE OF SPIN–FLIP SCATTERING

This appendix present a simple calculation of electron spin-flip scattering from magnetic impurities as a function of applied magnetic field B. The calculation is carried out at first order in spin–flip scattering, neglecting the Kondo effect. Moreover we consider here, for simplicity, magnetic impurities of spin-1/2.

The spin–flip rate $\tau_{\mathrm{sf}}^{-1}(E,B)$ of an electron at energy E is obtained from the Fermi Golden Rule,

$$\tau_{\mathrm{sf}}^{-1}(E,B)=c_{\mathrm{mag}}\lambda\{P_-(1-f_T(E-g\mu B))$$
$$+P_+(1-f_T(E+g\mu B))\}, \tag{C1}$$

where c_{mag} is the concentration of magnetic impurities, λ is proportional to the modulus square of the interaction potential electron-magnetic impurity, and $P_\pm$ is the probability to have the magnetic impurity in the up $(+)$ or down $(-)$ state relative to the magnetic field direction B. In absence of Kondo effect λ is approximated as independent of energy and magnetic field.

Since at thermal equilibrium $P_\pm=f_T(\pm g\mu B)$, we obtain

$$\tau_{\mathrm{sf}}^{-1}(E,B)=\frac{c_{\mathrm{mag}}\lambda(1+\exp(E/k_BT))/2}{\cosh(E/k_BT)+\cosh(g\mu B/k_BT)}. \tag{C2}$$

The spin–flip rate $\tau_{\mathrm{sf}}^{-1}(B)$ is averaged over electronic excitations

$$\tau_{\mathrm{sf}}^{-1}(B)=\int_{-\infty}^{+\infty}dE\frac{f_T(E)(1-f_T(E))}{k_BT}\tau_{\mathrm{sf}}^{-1}(E,B),$$

which gives

$$\frac{\tau_{\mathrm{sf}}(B=0)}{\tau_{\mathrm{sf}}(B)}=\frac{g\mu B/k_BT}{\sinh(g\mu B/k_BT)}. \tag{C3}$$

This result, also given in Ref. 43, is a finite-temperature generalization of the expression used by Benoit *et al.*[59] A rigorous theoretical calculation of the Aharonov-Bohm oscillation amplitude $\Delta G_{h/e}$ in presence of magnetic impurities

under a large externally applied magnetic field was first presented by Fal'ko.[60] A complete derivation of the magnetic field dependence of $\Delta G_{h/e}$ from first principles was finally published recently by Vavilov and Glazman.[47] As discussed in Sec. VII, the Vavilov-Glazman crossover function for $S=1/2$ is nearly indistinguishable from ours.

*Email address: fred.pierre@laposte.net. Permanent address after January 1, 2004: Laboratoire de Photonique et de Nanostructures (LPN)-CNRS, Route de Nozay, 91460 Marcoussis, France.

†Present address: Center for Advanced Nanotechnolgy, University of Toronto, Toronto, Ontario M5S 3E3, Canada.

[1] For a review, see *Mesoscopic Phenomena in Solids*, edited by B.L. Altshuler, P.A. Lee, and R.A. Webb (Elsevier, Amsterdam, 1991).

[2] A. Schmid, Z. Phys. **259**, 421 (1973).

[3] B.L. Altshuler, A.G. Aronov, and D.E. Khmelnitsky, J. Phys. C **15**, 7367 (1982).

[4] B.L. Altshuler and A.G. Aronov, in *Electron–Electron Interactions in Disordered Systems*, edited by A.L. Efros and M. Pollak (Elsevier Science, Amsterdam, 1985).

[5] S. Wind, M.J. Rooks, V. Chandrasekhar, and D.E. Prober, Phys. Rev. Lett. **57**, 633 (1986).

[6] P.M. Echternach, M.E. Gershenson, H.M. Bozler, A.L. Bogdanov, and B. Nilsson, Phys. Rev. B **48**, 11 516 (1993).

[7] P. Mohanty, E.M.Q. Jariwala, and R.A. Webb, Phys. Rev. Lett. **78**, 3366 (1997).

[8] H. Pothier, S. Guéron, N.O. Birge, D. Esteve, and M.H. Devoret, Phys. Rev. Lett. **79**, 3490 (1997).

[9] Some of the measurements shown in this article have already been published elsewhere (Refs. 11,24,25,50). (A list of samples with cross-references to previous articles is given in Ref. 14.)

[10] We did not need to perform ion-etching of the surface (Ref. 7) or predeposition of another metallic layer to promote the adhesion of the films.

[11] F. Pierre, Ann. Phys. (Paris) **26**, No. 4 (2001).

[12] For most samples we first melt the source material, evaporate 10–20 nm with a shutter protecting the sample, and pump down the chamber again for about 15 mn before the actual deposition. This pre-evaporation covers the walls of the evaporator with a clean layer of metal and makes it possible to maintain the pressure below 10^{-6} mbar during material deposition. We did not notice a reproducible difference between samples for which we did or did not follow this procedure.

[13] G. Bergmann, Phys. Rep. **107**, 1 (1984); S. Chakravarty and A. Schmid, *ibid.* **140**, 19 (1986).

[14] Ag(6N)a is Ag in Ref. 24, and Ag1 in Ref. 11. Ag6N(b) is Ag2 in Ref. 11. Au(6N) is AuMSU in Refs. 11,50. Cu(6N)a to Cu(6N)d are Cu1 to Cu4 in Ref. 25. Cu(5N)a is Cu in Ref. 24, and Cu1 in Ref. 11. Cu(5N)b is Cu2 in Ref. 11.

[15] I.L. Aleiner, B.L. Altshuler, and M.E. Gershenson, Waves Random Media **9**, 201 (1999).

[16] B.L. Altshuler and A.G. Aronov, Pis'ma Zh. Eksp. Teor. Fiz. **33**, 515 (1981) [JETP Lett. **33**, 499 (1981)].

[17] Several explanations can account for the small difference, mostly observed on silver samples, between the width measured using an electronic microscope and the one used to make accurate fits of low field magnetoresistance with weak localization theory. Amongst them we point out the non-uniformity of our wires, our limited accuracy on the average width (about ± 5 nm), the fact we assume a rectangular section for the wires, and most likely the limit of the diffusive approximation in silver wires for which the elastic mean free path is not always very small compared to w and which exhibit visible grain structure.

[18] Samples made of our 4N gold source also display anomalous dephasing. However, we could detect in these samples the presence of about 50 ppm of magnetic impurities, probably iron, that explains the observed temperature dependence of τ_ϕ. For details, see Ref. 50.

[19] B.L. Altshuler, M.E. Gershenson, and I.L. Aleiner, Physica E (Amsterdam) **3**, 58 (1998).

[20] S. Hikami, A.I. Larkin, and Y. Nagaoka, Prog. Theor. Phys. **63**, 707 (1980).

[21] Y. Imry, H. Fukuyama, and P. Schwab, Europhys. Lett. **47**, 608 (1999).

[22] A. Zawadowski, J. von Delft, and D.C. Ralph, Phys. Rev. Lett. **83**, 2632 (1999).

[23] D.S. Golubev and A.D. Zaikin, Phys. Rev. Lett. **81**, 1074 (1998).

[24] A.B. Gougam, F. Pierre, H. Pothier, D. Esteve, and N.O. Birge, J. Low Temp. Phys. **118**, 447 (2000).

[25] F. Pierre and N.O. Birge, Phys. Rev. Lett. **89**, 206804 (2002); F. Pierre and N.O. Birge, J. Phys. Soc. Jpn. Suppl. A **72**, 19 (2003).

[26] J. Vranken, C. Van Haesendonck, and Y. Bruynseraede, Phys. Rev. B **37**, 8502 (1988).

[27] D.K. Wohlleben and B.R. Coles, *Magnetism*, edited by H. Suhl (Academic, New York, 1973), Vol. 5.

[28] The energy of the ions, 70 keV, was chosen to obtain an homogeneous concentration of manganese atoms in the thickness of the wires.

[29] V.I. Fal'ko, JETP Lett. **53**, 340 (1991).

[30] M.B. Maple, *Magnetism*, edited by H. Suhl (Academic, New York, 1973), Vol. 5.

[31] C. Van Haesendonck, J. Vranken, and Y. Bruynseraede, Phys. Rev. Lett. **58**, 1968 (1987).

[32] In vacuum, the magnetic moment of manganese atoms is $S=5/2$, but $S=5/2$ does not allow accurate fits of the measurements. It has been suggested that the random crystal field effectively reduces the degeneracy of the lowest-lying spin multiplet to a doublet, regardless of the actual spin of the magnetic impurity [L. Glazman (private communication)]. See also O. Ujsaghy, A. Zawadowski, and B.L. Gyorffy, Phys. Rev. Lett. **76**, 2378 (1996).

[33] A.C. Hewson, *The Kondo Problem to Heavy Fermions* (Cambridge University Press, Cambridge, 1993).

[34] The value of B_K for low concentrations of iron in gold can be found for instance in P. Mohanty and R.A. Webb, Phys. Rev. Lett. **84**, 4481 (2000). This parameter is expected to be similar for other Kondo impurities in silver and copper.

[35] D.S. Golubev, A.D. Zaikin, and G. Schön, J. Low Temp. Phys. **126**, 1355 (2002).

[36] See J. von Delft, cond-mat/0210644, and references therein.

[37] D. Natelson, R.L. Willett, K.W. West, and L.N. Pfeiffer, Phys. Rev. Lett. **86**, 1821 (2001). In their article, the quantity Natelson *et al.* refer to as τ_ϕ or τ_N is four times smaller than the phase

coherence time extracted from Eq. (1) [see Eq. (1) in Natelson *et al.*]. We took this correction into account in Fig. 8. Note that the diffusion coefficients used by Natelson *et al.* were obtained from the conductivity of co-evaporated thin films. Using the expected geometry and the measured resistance of the wires, as was done for all other samples, would give diffusion coefficients about twice smaller, which would move the open circles in Fig. 8 about one decade to the right, and slightly upward.

[38] D.S. Golubev and A.D. Zaikin, Phys. Rev. B **59**, 9195 (1999).

[39] A. Anthore, F. Pierre, H. Pothier, and D. Esteve, Phys. Rev. Lett. **90**, 076806 (2003); A. Anthore, F. Pierre, H. Pothier, D. Esteve, and M.H. Devoret, in *Electronic Correlations*: *From Meso- to Nano-Physics*, edited by T. Martin, G. Montambaux, and J. Trân Thanh Vân (EDP Sciences, New York, 2001); cond-mat/0109297.

[40] I.L. Aleiner, B.L. Altshuler, and Y.M. Galperin, Phys. Rev. B **63**, 201401 (2001).

[41] I.L. Aleiner, B.L. Altshuler, Y.M. Galperin, and T.A. Shutenko, Phys. Rev. Lett. **86**, 2629 (2001); I.L. Aleiner and D. Controzzi, Phys. Rev. B **66**, 045107 (2002).

[42] A. Zawadowski and G. Zarand, cond-mat/0009283; O. Ujsaghy, K. Vladar, G. Zarand, and A. Zawadowski, J. Low Temp. Phys. **126**, 1221 (2002).

[43] J.S. Meyer, V.I. Fal'ko, and B.L. Altshuler, *Strongly-Correlated Fermions and Bosons in Low-Dimensional Disordered Systems*, edited by I. Lerner, B.L. Altshuler, V.I. Fal'ko, and T. Giamarchi (Kluwer Academic, Dordrecht, 2002); cond-mat/0206024.

[44] A.G. Aronov and Y.V. Sharvin, Rev. Mod. Phys. **59**, 755 (1987); V. Chandrasekhar, Ph.D. thesis, Yale University, 1989. We neglect here the triplet contribution to AB oscillations since the spin–orbit length is much smaller than L_ϕ.

[45] At 40 mK and low magnetic field, our experimental noise floor dominates the amplitude of conductance fluctuations in the h/e frequency window. This explains the smaller relative increase of ΔG_{AB} at 40 mK compared to 100 mK.

[46] In principle, the constant C in Eq. (13) is calculable from the known sample geometry. In practice, the calculation is quite difficult in four-terminal measurement geometry [Thomas Ludwig (private communication)]. See, D.P. DiVincenzo and C.L. Kane, Phys. Rev. B **38**, 3006 (1988); C.L. Kane, P.A. Lee, and D.P. DiVincenzo, *ibid.* **38**, 2995 (1988).

[47] M.G. Vavilov and L.I. Glazman, Phys. Rev. B **67**, 115310 (2003).

[48] Although the magnetic field dependence of the Vavilov-Glazman prediction depends on the spin S of the magnetic impurity, the quality of the fit adjusting the parameter g hardly changes with S, indicating that the noise in the data is too large to permit a reliable determination of S in our samples.

[49] B.X. Yang, J.M. Tranquada, and G. Shirane, Phys. Rev. B **38**, 174 (1988).

[50] F. Pierre, H. Pothier, D. Esteve, M.H. Devoret, A. Gougam, and N.O. Birge, in *Kondo Effect and Dephasing in Low-Dimensional Metallic Systems*, edited by V. Chandrasekhar, C. Van Haesendonck, and A. Zawadowski (Kluwer, Dordrecht, 2001), p. 119; cond-mat/0012038.

[51] F. Pierre, H. Pothier, D. Esteve, and M.H. Devoret, J. Low Temp. Phys. **118**, 437 (2000).

[52] A. Kaminski and L.I. Glazman, Phys. Rev. Lett. **86**, 2400 (2001).

[53] It is not clear that the saturation of τ_ϕ observed in strongly disordered alloys, cf. J.J. Lin, Y.L. Zhong, and T.J. Li, Europhys. Lett. **57**, 872 (2002), can be explained along the same lines.

[54] M. Henny, H. Birk, R. Huber, C. Strunk, A. Bachtold, M. Krüger, and C. Schönenberger, Appl. Phys. Lett. **71**, 773 (1997).

[55] F.C. Wellstood, C. Urbina, and J. Clarke, Phys. Rev. B **49**, 5942 (1992).

[56] Three parameters describing effects of electron–phonon scattering are used in this review: B in Eq. (4), Σ and $\kappa_{\rm ph}$ in Appendix A. They are related by the relations (Ref. 11), $\Sigma = 24\zeta(5)\nu_F\kappa_{\rm ph}k_B^5$ and $B = 6\zeta(3)\kappa_{\rm ph}k_B^3$, with $\zeta(x)$ the Riemann zeta function: $\zeta(5) \simeq 1.04$ and $\zeta(3) \simeq 1.2$. Introducing the heat capacity coefficient γ, one has the relation $\Sigma \simeq 1.05\gamma B$.

[57] A. Kamenev and A. Andreev, Phys. Rev. B **60**, 2218 (1999).

[58] We replaced the cut-off at $\hbar/\tau_\phi(T)$ by $\hbar/\tau_{ee}(T)$ whereas, when another inelastic process such as electron–phonon scattering limits the quantum coherence, the integral should be cut-off at $\hbar/\tau_\phi$ ($>\hbar/\tau_{ee}$). We neglect this correction here since it applies only when the contribution of electron–electron interactions is already weak.

[59] A.D. Benoit, S. Washburn, R.A. Webb, D. Mailly, and L. Dumoulin, *Anderson Localization*, edited by T. Ando and H. Fukuyama (Springer, Berlin, 1988).

[60] V.I. Fal'ko, J. Phys.: Condens. Matter **4**, 3943 (1992).

6.3 Complement: Why are interactions between magnetic impurities negligible ?

Vavilov, Glazman and Larkin [3] have calculated the effect on the electronic properties of the RKKY interactions between magnetic impurities [4]. RKKY interactions lead to a transition of the spin system to a spin glass state at a temperature T_{sg} dependent on the impurity concentration and on Kondo temperature. As far as electrons are concerned, the prediction is that the interplay between the Kondo effect and the RKKY interaction may result in a non trivial temperature dependence of the resistivity and the phase coherence time. These effects have been investigated in [5] for gold samples in which the magnetic impurities, iron, were estimated to be present at concentrations larger than $15\ \text{ppm}$. In our silver samples with an impurity concentration smaller than $1\,\text{ppm}$, the spin-glass transition temperature is predicted to be below 1mK. We are thus in the limit of small concentrations $T_{sg} \ll T_K$. In the temperature range $T \geq T_K$, the RKKY interactions between magnetic impurities have no effect on the resistivity and phase coherence time in our samples.

6.4 Conclusion

For the samples presented in this chapter, electronic decoherence at low temperature is essentially due to electron-electron and electron-magnetic impurity scattering. In the “pure” samples, the concentration of magnetic impurities found from fits is compatible with the nominal purity of the source. In the implanted samples, this concentration is in close agreement with the amount of magnetic impurities implanted. Since such a small amount of magnetic impurities is almost impossible to rule out in any sample, scattering from undetermined magnetic impurities likely explains the saturation observed in many experiments.

References of chapter 6

[1] I.L. Aleiner, B.L Altshuler, M.E. Gershenson, Waves in Random Media **9**, 201 (1999).

[2] B.L. Altshuler, A.G. Aronov, D.E. Khmelnitsky, J. Phys. C **15**, 7367 (1982).

[3] M.G. Vavilov, L.I. Glazman, and A.I. Larkin, cond-Mat/0305240.

[4] M.A. Ruderman and C. Kittel, Phys. Rev. **96**, 99 (1954); T. Kasuya, Prog. Theor. Phys. **16**, 45 (1956); K. Yosida, Phys. Rev. **106**, 893 (1957).

[5] F. Schopfer, C. Bäuerle, W. Rabaud, and L. Saminadayar, Advances in Solid State Physics, Vol 43, edited by B. Kramer (Springer Verlag, Berlin 2003) (cond-mat/0306276).

Chapter 7 Energy exchange and Kondo effect: Kondo-Impurity-Mediated interaction

Before the beginning of this thesis, energy exchange between quasiparticles was investigated in the Quantronics group in order to precisely understand the scattering mechanisms that limit the phase coherence. Energy exchange rates were found higher than predicted by the theory of Coulomb electron-electron interaction, with furthermore an unexpected energy dependence, and sample to sample variations [1]. The aim of the experiments presented in this chapter was to determine if the mechanism proposed by Kaminski and Glazman [2] to explain these results, based on magnetic impurities, was relevant. By convenience, this interaction mechanism, in which Kondo effect plays a major role, will be nicknamed “KIM interaction” for Kondo-Impurity-Mediated-Interaction.

Even if at zero-magnetic field the spin states of magnetic impurities are degenerated, magnetic impurities can mediate energy exchange by a process at second order in the coupling between electrons and magnetic impurities (see Figure 1, top). According to Kaminski and Glazman [2], the rate $\gamma(E)$ at which an electronic state of energy E and filling factor $f(E)$ is populated due to the coupling of electrons with magnetic impurity at second order can be written as:

$$\gamma(E) = \int d\varepsilon \ \left(f(E+\varepsilon)\left(1-f(E)\right) - f(E)\left(1-f(E-\varepsilon)\right)\right) W(\varepsilon, E)$$

with

$$W(\varepsilon, E) = W(\varepsilon) = \mathrm{K}(\varepsilon) \int dE' f(E') \ \left(1-f(E'+\varepsilon)\right),$$

and

$$\mathrm{K}(\varepsilon) = \pi^2 \ \frac{c_{imp}}{h\nu_F} \ \mathrm{S(S+1)} \ \frac{(\nu_F J)^4}{\varepsilon^2} \equiv \frac{\kappa_2}{\varepsilon^2}, \qquad (1)$$

where c_{imp} is the concentration of magnetic impurities, S their spin. In this calculation, the coupling constant between electrons of spins $\hat{s}$ and a magnetic impurity of spin $\hat{S}$ is described by a hamiltonian $\mathrm{H}_c = J\,\hat{s}.\hat{S}$. The kernel function $\mathrm{K}(\varepsilon)$ contains all the information on the energy exchange mechanism (intensity and energy dependence). The energy dependence $\mathrm{K}(\varepsilon) \propto \varepsilon^{-2}$ is different from the one calculated for pure Coulomb interaction in diffusive wires: $\mathrm{K}(\varepsilon) \propto \varepsilon^{-3/2}$. Such a ε^{-2}-dependence of energy exchange was first inferred by Pothier *et al.* [3] from measurements in copper wires and later on in wires made of gold [1]. KIM interaction is therefore a candidate to explain this large set of experimental results.

To find out if KIM interaction is relevant in mesoscopic wires, we have measured energy exchange in presence of an applied magnetic field B because it is expected that the rate of the KIM interaction depends on B. Indeed, in a magnetic field, scattering of an electron on a magnetic impurity can be already inelastic at first order, with an energy transfer $\pm g\mu_B B$ (see Figure 1, bottom), where g is the gyromagnetic factor of the impurity and μ_B the Bohr magneton. Magnetic impurities then behave as two-level systems, and the rate of KIM interaction is expected to be higher than at zero magnetic field as long as $g\mu_B B$ is not too large. When $g\mu_B B$ becomes larger than the width of the electronic energy distribution function, given by eU in our experiment, magnetic impurities cannot be excited by the electronic bath. Then the rate of first order processes vanishes. The rate of the second order process (see Figure 1, top) proportional to $(\varepsilon - g\mu_B B)^{-2}$ becomes also so small when B increases, that the KIM interaction rate decreases. Since the Pauli constraint imposes that the energies ε that can be exchanged by this process are such as $\varepsilon \leq eU$, the magnetic field at which KIM interaction is suppressed is predicted to scale with U.

In the above presentation, Kondo physics is embedded in the coupling constant J. As explained in Chapter 5, Kondo effect leads to a renormalization of the bare coupling constant J_0 between electrons and magnetic impurities due to the collective effect of all the conduction electrons. In an out-of-equilibrium situation, the renormalization depends on the local electron energy distribution function. The complete calculation was developed by Göppert *et al.* [4] and is presented in Section 7.1.3.3.

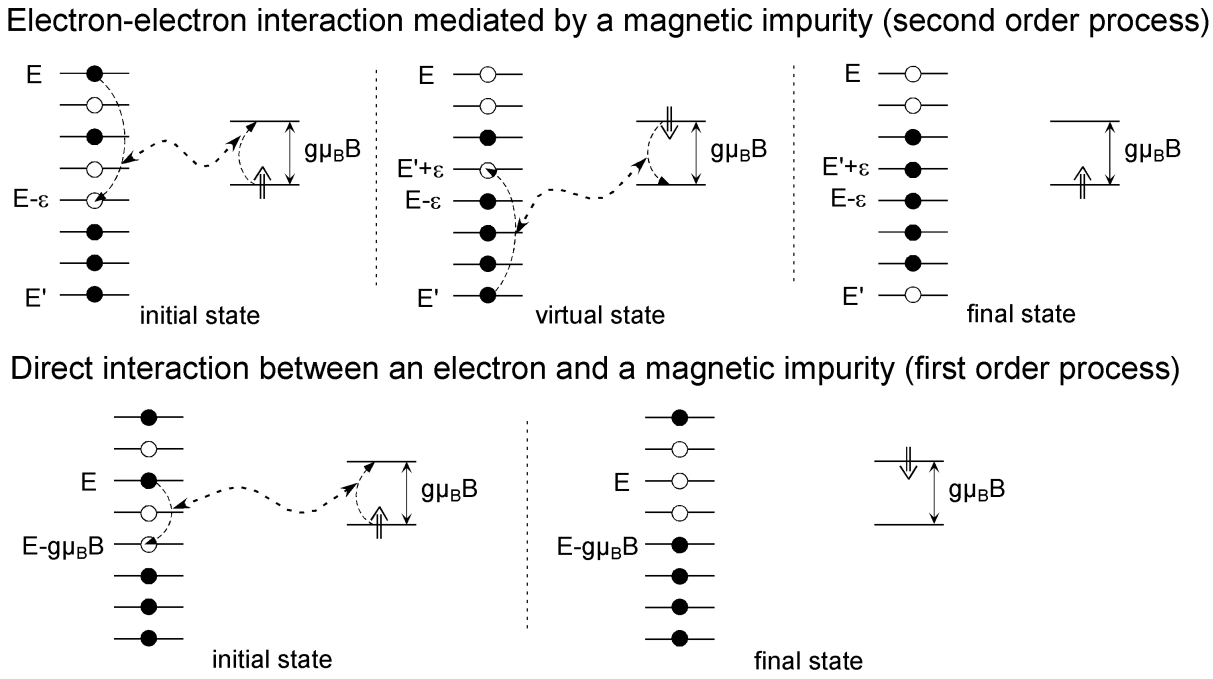

Figure 1: Description of the processes of energy redistribution between quasiparticles mediated by magnetic impurities. In each panel, the left ladder represents the energy spectrum of the electrons, and the two states on the right side represents the energy levels of the spin states of a magnetic impurity. Top: The second order process implies two electrons and a magnetic impurity. Bottom: The first order process directly exchanges $g\mu_B B$ between an electron and a magnetic impurity.

7.1 Energy exchange and quasiparticle energy distribution function

We first present how the energy exchange rate can be inferred from the quasiparticle energy distribution function.

7.1.1 Energy distribution function of quasiparticles in a voltage-biased wire

To access the energy exchange mechanisms between electrons, we prepare an out-of-equilibrium stationary situation by placing a diffusive metallic wire between two metal contacts biased at different potentials (see Figure 2). Energy exchange, which tends to establish a local equilibrium between electrons, and diffusion, which limits the dwell time of electrons in the wire, control the energy distribution of electrons.

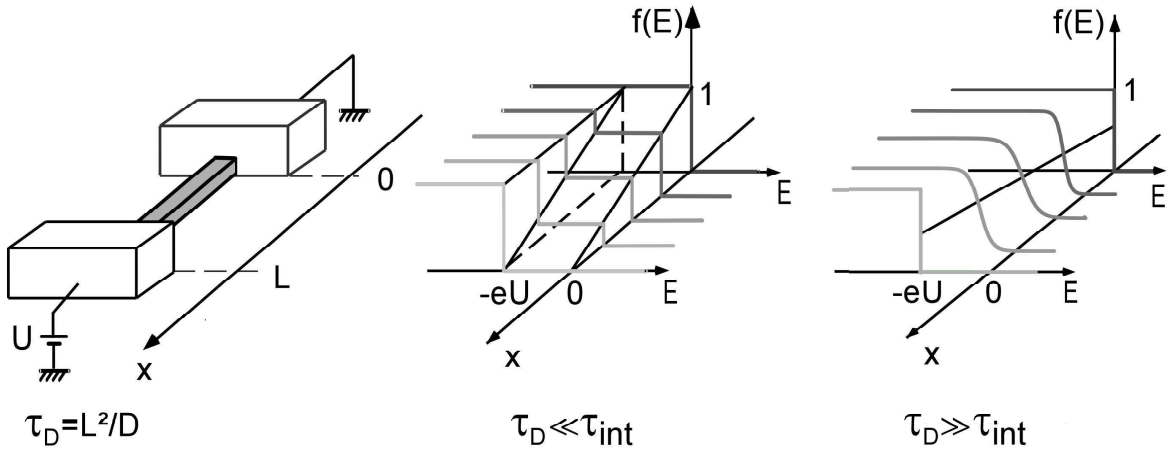

Figure 2: Schematic of the experiment: A wire of length L and electron diffusion coefficient D is connected to two reservoirs. A potential difference U is applied between the two reservoirs. The distribution functions of electrons in the reservoirs are Fermi functions shifted in energy by the electrochemical potential difference $eU \gg k_B T$. Distribution functions $f(x,E)$ are plotted for different positions along the wire in the limit of independent electrons (middle: $\tau_D << \tau_{\text{int}}$), and in the limit of strong electron-electron interaction (right: $\tau_D >> \tau_{\text{int}}$).

7.1.1.1 Independent electrons regime: $\tau_D \ll \tau_{\text{int}}$

If the typical time τ_D an electron spends in the diffusive wire is much smaller than the typical time of interactions between electrons τ_{int}, no inelastic scattering occurs while electrons travel through the wire, and the total energy of each electron is conserved during its motion. The energy distribution function $f(x,E)$, which reflects the probability to find an electron of energy E at position $x = x/L$, obeys the stationary quasiclassical Boltzmann equation [5]:

$$\frac{\partial^2 f(x,E)}{\partial x^2} = 0\,. \tag{2}$$

The distribution function thus interpolates linearly between the boundary distribution functions and reads:

$$f(x,E) = (1-x)\, f_T(E) + x\, f_T(E+eU)\,, \tag{3}$$

where $f_T(E) = \left(1+e^{E/k_BT}\right)^{-1}$ is the Fermi function at the temperature of the reservoir T. If $k_BT \ll eU$, the distribution function has a step at $f(x,E) = x$ for $-eU < E < 0$, as shown in Figure 2.

7.1.1.2 Thermalized electrons regime: $\tau_D \gg \tau_{\text{int}}$

If the typical time τ_D an electron spends in the diffusive wire is much larger than the typical time of interactions between electrons τ_{int}, numerous inelastic scattering events occur, and electrons thermalize locally (see Figure 2, right panel). At each position in the wire, the energy distribution function is a Fermi function, with a temperature $T_e(x)$ and an electrochemical potential eUx that depends on the position:

$$f(x,E) = f_{T_e(x)}(E - eUx)\,. \tag{4}$$

The temperature $T_e(x)$ obeys the heat equation [6,7,8]

$$\frac{\pi^2}{6}\frac{\partial^2 (k_B T_e)^2}{\partial x^2} + (eU)^2 = 0, \tag{5}$$

with the boundary conditions at the reservoirs $T_e(0) = T_e(1) = T$. The temperature along the wire is:

$$T_e(x) = \sqrt{T^2 + x(1-x)U^2/\mathbb{L}}\,, \tag{6}$$

where $\mathbb{L} = (\pi^2/3)(k_B/e)^2 \simeq 2.4\ \text{V}^2\ \text{K}^{-2}$ is the Lorenz number.

7.1.1.3 Intermediate regime: $\tau_D \simeq \tau_{\text{int}}$

In the intermediate regime, where $\tau_D \simeq \tau_{\text{int}}$, the energy distribution functions in the wire are rounded due to energy exchange between electrons. Yet, electrons are not thermalized, $f(x,E)$ is not a Fermi function, and the rate of energy exchange can be inferred

from the shape of $f(x,E)$ and its dependence on the voltage U. In our experiments, this intermediate regime is found for wire lengths of the order of 10 µm.

7.1.2 Calculation of the electron energy distribution function in presence of energy exchange

7.1.2.1 Boltzmann equation in the diffusive regime

Following Nagaev [9] and Kozub and Rudin [10], we use the Boltzmann equation to determine the electron energy distribution $f(x,E)$ in the wire. This equation reads in a stationary regime:

$$\frac{1}{\tau_D}\frac{\partial^2 f(x,E)}{\partial x^2} + I_{coll}\left(x,E,\{f\}\right) = 0, \tag{7}$$

where τ_D is the diffusion time of an electron in the wire and x the position in reduced units $x = x/L$, with L the wire length. The first term describes elastic collisions and $I_{coll}\left(x,E,\{f\}\right)$ accounts for the inelastic collisions.

The boundary conditions are imposed by the reservoirs:

$$f(0,E) = f_T(E)$$
$$f(1,E) = f_T(E+eU),$$

where $f_T(E)$ is the Fermi function at the temperature T of the electrodes.

7.1.2.2 Inelastic collisions responsible for energy exchange

The collision term can be written as the difference of two terms: an in-collision term, the rate at which particles are scattered in the state of energy E, and an out-collision term:

$$I_{coll}\left(x,E,\{f\}\right) = I_{coll}^{in}\left(x,E,\{f\}\right) - I_{coll}^{out}\left(x,E,\{f\}\right) \tag{8}$$

with

$$I_{coll}^{in}\left(x,E,\{f\}\right) = \int d\varepsilon\, f(x,E+\varepsilon)\,\left(1-f(x,E)\right)\,W(x,\varepsilon,E),$$

and

$$I_{coll}^{out}\left(x,E,\{f\}\right)=\int d\varepsilon\, f\left(x,E\right)\,\left(1-f\left(x,E-\varepsilon\right)\right)\,W\left(x,\varepsilon,E-\varepsilon\right).$$

The function $W\left(x,\varepsilon,E\right)$ describes the transition between two electron states with energies $E+\varepsilon$ and E at the position x. This transition is due to the Coulomb interaction with other electrons, coupling to phonons, or coupling to magnetic impurities [2].

7.1.2.3 Numerical solution

To calculate the electronic energy distribution function $f\left(x,E\right)$, Frederic Pierre has developed a C++ code based on a relaxation method. Starting from an initial distribution $f\left(x,E,t=0\right)$, it is let to evolve according to the non-stationary diffusive Boltzmann equation:

$$f\left(x,E,t+\delta t\right)=f\left(x,E,t\right)+\Lambda\left(\frac{1}{\tau_D}\frac{\partial^2 f\left(x,E,t\right)}{\partial x^2}+I_{coll}\left(x,E,\{f\},t\right)\right), \tag{9}$$

where Λ is a parameter optimized at each iteration to accelerate convergence. When the energy distribution function does not evolve any more, the obtained function is the solution of the stationary Boltzmann equation (7). In the collision term, inelastic processes, such as electron-electron interaction, electron-phonon interaction, electron-magnetic impurities interaction are included.

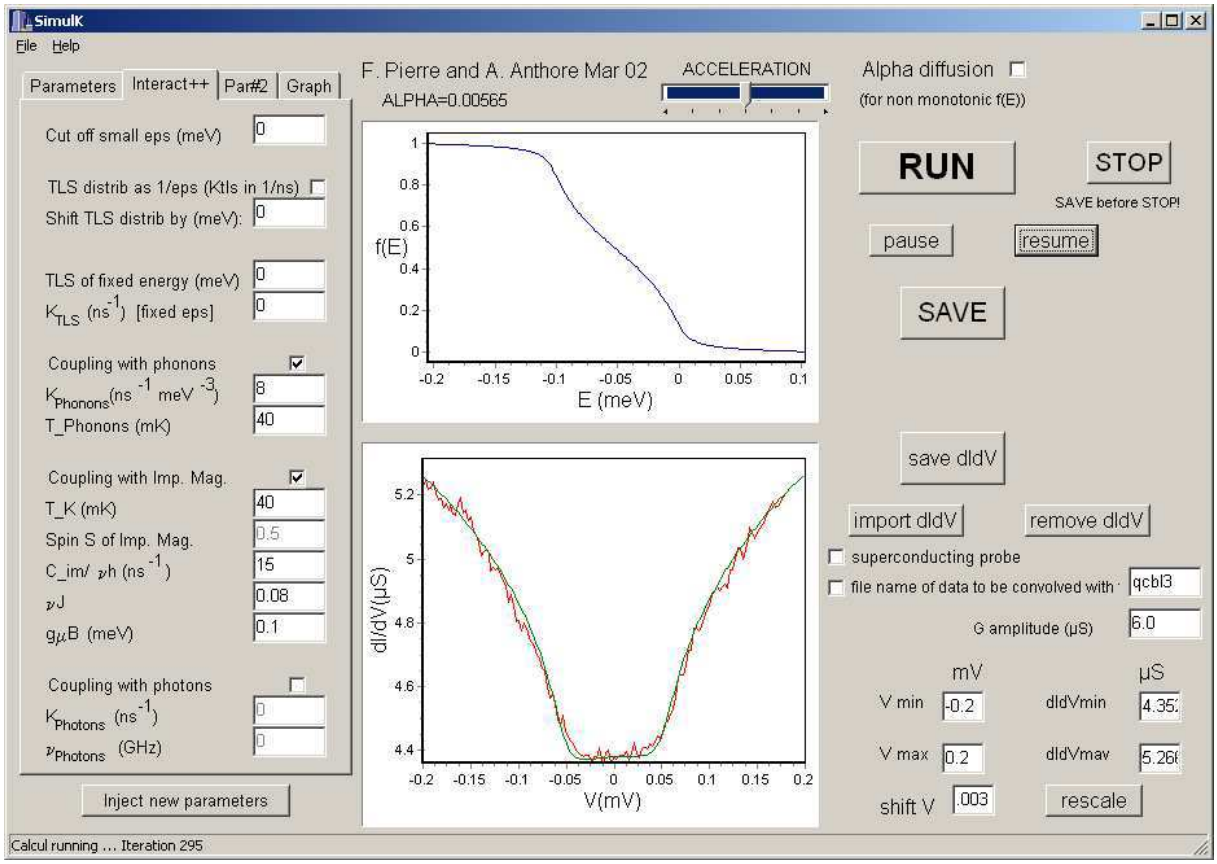

Figure 3: Graphic interface of the C++ code that calculates the distribution function of electrons $f(E)$ in a metallic wire connected at both ends to electrodes made of normal or superconducting metal. The calculation takes into account electron-electron interaction, electron-phonon interaction and coupling with magnetic impurities. We have added a routine to convolve $f(E)$ with any function to be able to compare calculation with measurements of the differential conductance of a tunnel junction formed between the out-of-equilibrium wire and a probe electrode.

7.1.3 Inelastic scattering mechanisms

In this part, we describe the theoretical predictions for the inelastic collision term of the Boltzmann equation associated with Coulomb electron-electron interaction, electron-phonon interaction and electron-magnetic impurity (KIM) interaction. The first two rates have been described in the thesis of S. Guéron [11] and F. Pierre [1]. For completion, we derive them again here, together with the KIM interaction rate.

7.1.3.1 Coulomb interaction between electrons

Altshuler *et al.* have calculated the energy exchange rate between electrons associated with Coulomb interaction [12]. They consider quasiparticles with a diffusive motion, which interact by Coulomb interaction screened by an effective medium constituted by all the electrons of the metal.

This leads to

$$W(x,\varepsilon,E) = W(\varepsilon) = \mathrm{K}(\varepsilon) \int dE' f(x,E') \left(1 - f(x,E'+\varepsilon)\right), \tag{10}$$

where the kernel of the electron-electron interaction $\mathrm{K}(\varepsilon)$ is, according to the Fermi Golden Rule:

$$\mathrm{K}(\varepsilon) = \frac{2\pi}{\hbar} \left(\frac{\nu_F}{2}\Omega\right)^3 \left\langle \left|M(\varepsilon)\right|^2 \right\rangle_{disorder}, \tag{11}$$

where $\langle\rangle_{disorder}$ is the average on the scatterers positions, Ω the sample volume, ν_F the density of states at the Fermi level and $\left|M(\varepsilon)\right|^2$ the average square of the matrix element for the interaction between electrons with energy transfer ε (see Figure 4).

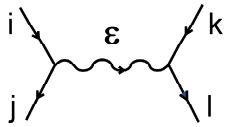

Figure 4: Diagram representing the exchange of an energy ε between two quasiparticles.

The matrix element writes:

$$\left|M(\varepsilon)\right|^2 = \left\langle \left|M_{ijkl}\right|^2 \right\rangle_{\substack{E_j - E_i = -\varepsilon \\ E_l - E_k = \varepsilon}},$$

with

$$\begin{aligned} M_{ijkl} = &\int d\boldsymbol{r} d\boldsymbol{r}' \Psi_i(\boldsymbol{r}) \Psi_j^*(\boldsymbol{r}) U_{\varepsilon/\hbar}(\boldsymbol{r}-\boldsymbol{r}') \Psi_k(\boldsymbol{r}') \Psi_l^*(\boldsymbol{r}') \\ &\pm \int d\boldsymbol{r} d\boldsymbol{r}' \Psi_i(\boldsymbol{r}) \Psi_j^*(\boldsymbol{r}') U_{\varepsilon/\hbar}(\boldsymbol{r}-\boldsymbol{r}') \Psi_k(\boldsymbol{r}') \Psi_l^*(\boldsymbol{r}) \end{aligned} \tag{12}$$

where the $\Psi(\boldsymbol{r})$ are the electronic wave functions in real space. Sign (+) corresponds to the antisymmetric spin state of the initial two-electron system, sign (-) to the symmetric spin state (The spin state of the final two-electron system remains the same as the initial one). The

potential $U_{\varepsilon/\hbar}(\boldsymbol{r}-\boldsymbol{r'})$ is the temporal Fourier transform of the microscopic interaction potential between electrons.

The squared of the matrix element $\left|M(\varepsilon)\right|^2$ has two types of contributions (see Figure 5). The first type (left of Figure 5), for which $i'=j$, $j'=i$, $k'=l$, and $l'=k$ always contributes. The second type (right of Figure 5), for which $i'=j$, $j'=k$, $k'=l$, and $l'=i$ and for which a phase associated with the scatterers position remains, contributes only for short range interaction and is neglected in the following[1] [13].

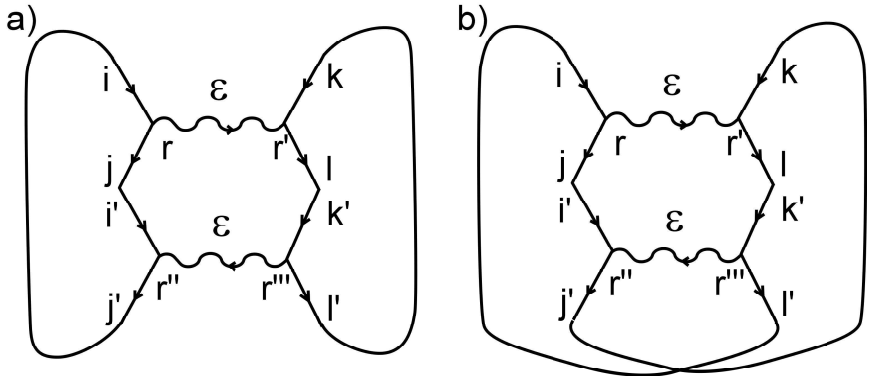

Figure 5: Diagrams that should contribute to the modulus squared of the disorder-averaged matrix element. The cross term b), which contributes for short range interaction is neglected in the following.

Therefore,

$$\mathrm{K}(\varepsilon)=\frac{2\pi}{\hbar}(\nu_F\Omega)^3\int d\boldsymbol{r}d\boldsymbol{r'}d\boldsymbol{r''}d\boldsymbol{r'''}U_{\varepsilon/\hbar}(\boldsymbol{r}-\boldsymbol{r'})\;U_{-\varepsilon/\hbar}(\boldsymbol{r''}-\boldsymbol{r'''})$$
$$\times\left\langle\left\langle\Psi_{\mathrm{i}}(\boldsymbol{r})\Psi_j^*(\boldsymbol{r})\Psi_j(\boldsymbol{r''})\Psi_i^*(\boldsymbol{r''})\Psi_{\mathrm{k}}(\boldsymbol{r'})\Psi_l^*(\boldsymbol{r'})\Psi_{\mathrm{l}}(\boldsymbol{r'''})\Psi_k^*(\boldsymbol{r'''})\right\rangle_{\substack{E_j-E_l=-\varepsilon\\E_l-E_k=\varepsilon}}\right\rangle_{\text{disorder}}. \tag{13}$$

In the diffusive regime, far from the metal-insulator transition, the disorder-averaged of $\left\langle\Psi_{\mathrm{i}}(\boldsymbol{r})\Psi_j^*(\boldsymbol{r})\Psi_{\mathrm{j}}(\boldsymbol{r''})\Psi_i^*(\boldsymbol{r''})\right\rangle_{E_j-E_l=\varepsilon}$ does not depend on the states *i* and *j* but on their energy difference and is equal to (see appendix 1):

$$\left\langle\left\langle\Psi_{\mathrm{i}}(\boldsymbol{r})\Psi_j^*(\boldsymbol{r})\Psi_{\mathrm{j}}(\boldsymbol{r''})\Psi_i^*(\boldsymbol{r''})\right\rangle_{E_j-E_l=\varepsilon}\right\rangle_{disorder}=\int\frac{d\boldsymbol{k}}{(2\pi)^3}\frac{\nu_F}{2\hbar N(E_F)^2\pi}\;\frac{D\boldsymbol{k}^2}{D^2\boldsymbol{k}^4+(\varepsilon/\hbar)^2}e^{i\boldsymbol{k}.(\boldsymbol{r}-\boldsymbol{r''})},$$

with $N(E_F)=\nu_F\Omega$, and D the electronic diffusion coefficient. It follows from (13):

[1] This term gives rise to an enhancement of the average of the squared matrix element with a prefactor dependent on the screening of the interaction. This prefactor, which depends on the nature of the material, has not been calculated for the one-dimension case.

$$\mathrm{K}(\varepsilon) = \frac{\nu_F}{4\pi^4\hbar^3}\int \mathrm{d}\boldsymbol{q}\left|\mathrm{U}_{\varepsilon/\hbar}(\boldsymbol{q})\right|^2 \left(\frac{D\boldsymbol{q}^2}{D^2\boldsymbol{q}^4+(\varepsilon/\hbar)^2}\right)^2. \tag{14}$$

The screened Coulomb interaction $U_{\varepsilon/\hbar}(\boldsymbol{q})$ is expressed in terms of the bare Coulomb interaction $U_0(\boldsymbol{q})$ and of the polarizability $\Pi(\boldsymbol{q},\varepsilon)$ of the electronic fluid:

$$U_{\varepsilon/\hbar}(\boldsymbol{q}) = \frac{U_0(\boldsymbol{q})}{1+\Pi(\boldsymbol{q},\varepsilon/\hbar)U_0(\boldsymbol{q})}, \tag{15}$$

with

$$\Pi(\boldsymbol{q},\varepsilon/\hbar) = \nu_F \frac{D\boldsymbol{q}^2}{D\boldsymbol{q}^2 - i\varepsilon/\hbar}.$$

In a metal, the density of states ν_F is of the order of 10^{47} J^{-1} m^{-3} and $\Pi(\boldsymbol{q},\varepsilon/\hbar)U_0(\boldsymbol{q}) \sim \nu_F S_e e^2/\varepsilon_0 \sim 10^6 \gg 1$ (S_e is the wire cross-section) so that the screened Coulomb potential simplifies to:

$$U_{\varepsilon/\hbar}(\boldsymbol{q}) = \frac{1}{\Pi(\boldsymbol{q},\varepsilon/\hbar)}.$$

It follows:

$$\mathrm{K}(\varepsilon) = \frac{1}{4\pi^4\nu_F\hbar^3}\int \frac{d\boldsymbol{q}}{D^2\boldsymbol{q}^4+(\varepsilon/\hbar)^2}. \tag{16}$$

In a metallic wire of width w and thickness t for energies ε smaller than $\hbar D/\max(w^2,t^2)$, only the uniform modes in the transverse dimensions contribute to $\mathrm{K}(\varepsilon)$, leading to:

$$\mathrm{K}(\varepsilon) = \left(\sqrt{2D}\ \pi\ \hbar^{3/2}\ \nu_F\ S_e\right)^{-1}\ \varepsilon^{-3/2}, \tag{17}$$

where $S_e = wt$ is the wire cross-section.

For a reason that we could not trace out, this derivation gives a prefactor for $\mathrm{K}(\varepsilon)$ smaller by a factor 2 than the result of Kamenev and Andreev [14]. In the following, we will refer to their result:

$$\mathrm{K}(\varepsilon) = \left(\sqrt{D/2}\ \pi\ \hbar^{3/2}\ \nu_F\ S_e\right)^{-1}\ \varepsilon^{-3/2}. \tag{18}$$

7.1.3.2 Electron-phonon interaction

The theoretical assumptions [1] made to calculate the electron-phonon interaction are the following:

(i) the phonon temperature T_p is small compared to the Debye temperature θ_D. Then only the acoustic branch of the phonons has to be taken into account and the dispersion relation between the energy and the wave vector q of a phonon is $\varepsilon_q = \hbar s q$, where s is the sound velocity;

(ii) the electronic wave functions are plane wave ones and not the diffusive wave functions used in the calculation of electron-electron interaction. This approximation is justified by the fact that phonons only play a role for large energies, which correspond, through the dispersion relation, to lengths of the same order or smaller than the electronic mean free path in the considered wire.

(iii) finite size effects for phonons are neglected because the phonons of the wire are coupled to phonons of the substrate, leading to a continuous energy spectrum.

(iv) coupling between electrons and phonons is described by a scalar deformation potential. Thus, only the longitudinal phonon mode is coupled to electrons and the square of the matrix element for the electron-phonon interaction is $\left|M(q)\right|^2 = \left|M_0\right|^2 q/\Omega$, where $\left|M_0\right|^2$ does not depend on the geometry [15]. This approximation is valid when the Fermi surface is spherical, which is a good approximation in copper, silver and gold.

According to the Fermi Golden Rule, the transition rate $\Gamma_{kk'}$ between two electronic states of wave vector k and k' is:

$$\begin{aligned}\Gamma_{kk'} = \frac{2\pi}{\hbar}\frac{\left|M_0\right|^2\left|\mathrm{k}-\mathrm{k}'\right|}{\Omega}\Big\{&\delta\left(E_k - E_{k'} + \varepsilon_{|k-k'|}\right)\left(1 - f\left(E_{k'} + \varepsilon_{|k-k'|}\right)\right)\eta_{ph}\left(\varepsilon_{|k-k'|}\right)\\ &+\delta\left(E_k - E_{k'} - \varepsilon_{|k-k'|}\right)\left(1 - f\left(E_{k'} - \varepsilon_{|k-k'|}\right)\right)\left(\eta_{ph}\left(\varepsilon_{|k-k'|}\right)+1\right)\Big\},\end{aligned} \tag{19}$$

where $\eta_{ph}(\varepsilon)$ is the Bose energy distribution function of the phonons.

To obtain the rate $\Gamma_k(\varepsilon)$ at which an electron with a wave vector k emits (ε>0) or absorbs

($\varepsilon < 0$) a phonon of energy ε, the previous equation has to be summed over the states *k'* with ε fixed. This leads to:

$$\Gamma_k(\varepsilon) = \frac{\varepsilon^2}{2\pi\hbar^5 s^3 v_F} |M_0|^2 \left(1 - f(E_k - \varepsilon)\right)\left(\eta_{ph}(|\varepsilon|) + \theta(\varepsilon)\right), \quad (20)$$

where $\theta(\varepsilon)$ is the Heaviside function.

The electron-phonon interaction rate is then written:

$$W(x,\varepsilon,E) = W(\varepsilon) = \kappa_{ph}\ \varepsilon^2\ \left(\eta_{ph}(|\varepsilon|) + \theta(\varepsilon)\right), \quad (21)$$

where $\kappa_{ph} = |M_0|^2 / (2\pi\hbar^5 s^3 v_F)$ is a constant that can be estimated from the temperature dependence of the phase coherence time. In our experimental conditions, the effect of electron-phonon coupling is a small correction to the distribution function calculated with direct interaction between electrons.

7.1.3.3 KIM interaction

In order to properly describe the collision term due to coupling of electrons with magnetic impurities, it is necessary to go beyond the perturbation theory given in the introduction. The complication arises from the fact that the renormalization of the coupling between electrons and magnetic impurities depends on the non-equilibrium electronic energy distribution function. The calculation developed in [16], presented below, is valid either at equilibrium well above Kondo temperature, or out-of-equilibrium for sufficiently smeared distribution functions, in presence or not of a magnetic field.

We now present briefly this calculation, which gives the collision integral for spin *S=½* impurities. Magnetic impurities are assumed to have a density c_{imp} small enough so that they do not interact one with another, and so that an electron is only coupled to one impurity at a time.

The explicit form of $W(x,\varepsilon,E)$ is the following:

$$W(x,\varepsilon,E) = \frac{c_{imp}}{v_F \hbar} \left(\frac{v_F J(x,\varepsilon,E)}{2}\right)^2 C(x,\varepsilon,E)\ , \quad (22)$$

where $J(x,\varepsilon,E)$ is the renormalized coupling constant between electrons and a magnetic

impurity, ν_F is the metal density of state, and $C(x,\varepsilon,E)$ is the Fourier transform of a spin-spin correlation function, which can be split as

$$C(x,t)=\frac{C_+(x,t)+C_-(x,t)}{2}+C_z(x,t), \tag{23}$$

where

$$C_\pm(x,t)=\left\langle S^\pm(t)S^\mp(0)\right\rangle$$
$$C_z(x,t)=\left\langle S^z(t)S^z(0)\right\rangle.$$

The averages are performed on the electron spin-states and energies weighted with the non-equilibrium distribution function determined self-consistently.

If the coupling between electrons and magnetic impurity is weak, these correlators only result from the spin relaxation and are equal to:

$$C_\pm(\varepsilon)=2\pi\ P_\pm\delta(\varepsilon\mp E_H)$$
$$C_z(\varepsilon)=\pi\delta(\varepsilon)/2,$$

where $P_\pm$ is the occupation probability for impurity spin-up or spin-down states, and E_H is the Zeeman splitting between these two states. These probabilities are determined by a master equation:

$$\frac{dP_\pm}{dt}=-\Gamma_\pm P_\pm+\Gamma_\mp P_\mp$$
$$P_+ + P_- =1, \tag{24}$$

where $\Gamma_\pm$ are the inverse life times of the spin-up and spin-down states.

If the coupling between electrons and magnetic impurity is strong, the time evolution of *C(t)* is governed by the Hamiltonian of the electrons-magnetic impurity system, which reads $H=H_0+H_c$ where $H_0=\sum_{k\sigma}\varepsilon_{k\sigma}c^+_{k\sigma}c_{k\sigma}-E_HS^z$ describes free electrons and an independent magnetic impurity. Here, operators $c^+_{k\sigma}$ and $c_{k\sigma}$ respectively creates and annihilates an electron in a given state k, with spin σ. The energy of this state is $\varepsilon_{k\sigma}$. The second term $-E_HS^z$ describes a spin ½ impurity with Zeeman splitting $E_H=g\mu_BB$, where g is the gyromagnetic factor of the magnetic impurity and $\mu_B=e\hbar/(2m_e)=0.058$ meV T^{-1} is the Bohr magneton (m_e is the electron weight). The interaction Hamiltonian

$\mathrm{H}_c = \sum_{k,k'} \left(\left(J_+^z c_{k\uparrow}^+ c_{k\uparrow} - J_-^z c_{k\downarrow}^+ c_{k\downarrow} \right) S^z + J^+ c_{k\downarrow}^+ c_{k\uparrow} S^+ + J^- c_{k\uparrow}^+ c_{k\downarrow} S^- \right)$ couples electrons to the impurity system with renormalized coupling constants J_+^z, J_-^z, J^+ or J^- that are different for all spin-components. The renormalization takes into account the distribution functions in the wire:

$$J_\pm^z(x,\varepsilon) = \frac{J_0}{\sqrt{\left|1-\left(\pi\nu_F J_0\right)^2 S(S+1)/4 - \nu_F J_0 g\left(x,\varepsilon \mp E_H\right)\right|^2 + \left(\pi\nu_F J_0\right)^2 S(S+1)}}$$

$$J^\pm(x,\varepsilon) = \frac{J_0}{\sqrt{\left|1-\left(\pi\nu_F J_0\right)^2 S(S+1)/4 - \nu_F J_0 \left(g\left(x,\varepsilon\right)+g\left(x,\varepsilon \pm E_H\right)\right)/2\right|^2 + \left(\pi\nu_F J_0\right)^2 S(S+1)}} \quad (25)$$

with $g\left(x,\varepsilon\right) = \int_{-\mathrm{D}}^{\mathrm{D}} \mathrm{d}\varepsilon' \, \frac{f\left(x,\varepsilon'\right)-0.5}{\varepsilon-\varepsilon'+i\delta}$,

where D is here the bandwidth of the conduction electrons.

The spin-spin correlators must be calculated using the renormalized constant and the projectors:

$$\begin{aligned} C_z\left(x,\omega\right) &= \frac{1}{2}\frac{\nu_z\left(x,\omega\right)}{\omega^2+\nu_z\left(x,\omega\right)^2} \\ C_\pm\left(x,\omega\right) &= \frac{2P_\pm\nu_\pm\left(x,\omega\right)}{\left(x,\omega\mp E_H\right)^2+\nu_\pm\left(x,\omega\right)^2}, \end{aligned} \quad (26)$$

where $\nu_{z,\pm}$ are the Korringa widths, *i. e.* the inverse lifetimes of the spin states, equal to

$$\begin{aligned} \nu_z\left(x,\omega\right) &= \pi\nu_F{}^2\left\{P_+\varsigma_+\left(x,\omega-E_H\right)+P_-\varsigma_-\left(x,\omega+E_H\right)\right\} \\ \nu_\pm\left(x,\omega\right) &= \frac{\pi}{4}\nu_F{}^2\left\{\varsigma_z\left(x,\omega\mp E_H\right)+\varsigma_\mp\left(x,\omega\right)/P_\pm\right\}, \end{aligned} \quad (27)$$

with

$$\begin{aligned} \varsigma_z\left(x,\omega\right) &= \int d\varepsilon' \left(J_+^z\left(x,\varepsilon'\right)J_+^z\left(x,\varepsilon'+\omega\right)+J_-^z\left(\varepsilon'\right)J_-^z\left(\varepsilon'+\omega\right)\right)\times f\left(x,\varepsilon'\right)\left(1-f\left(x,\varepsilon'+\omega\right)\right) \\ \varsigma_\pm\left(x,\omega\right) &= \int d\varepsilon' J^\mp\left(x,\varepsilon'\right)J^\pm\left(x,\varepsilon'+\omega\right)\times f\left(x,\varepsilon'\right)\left(1-f\left(x,\varepsilon'+\omega\right)\right), \end{aligned} \quad (28)$$

and

$$\begin{aligned} P_+ &= \frac{\int d\varepsilon' \, f\left(x,\varepsilon'\right)\left(1-f\left(x,\varepsilon'-E_H\right)\right)}{\int d\varepsilon' f\left(x,\varepsilon'\right)\left(1-f\left(x,\varepsilon'-E_H\right)\right)\times\int d\varepsilon' f(x,\varepsilon')\left(1-f\left(x,\varepsilon'+E_H\right)\right)} \\ P_- &= 1-P_+, \end{aligned} \quad (29)$$

the probabilities for spin-up or spin-down states calculated neglecting the Korringa width.

7.2 Experimental realization

7.2.1 Accessing the energy distribution functions with a tunnel probe electrode

As explained in Chapter 2, tunnel spectroscopy allows to obtain the electron energy distribution function. We have designed a long and narrow superconducting probe that forms a tunnel junction with the wire (see Figure 6). At zero magnetic field, we use the non-linearity of the differential conductance of the normal-superconducting tunnel junction to obtain $f(E)$. In a magnetic field larger than $0.1\mathrm{T}$, the probe electrode is no more superconducting but presents a resistance of about $1\,\mathrm{k}\Omega$, and we then take advantage of the Coulomb blockade of tunneling through the junction in series with this resistance.

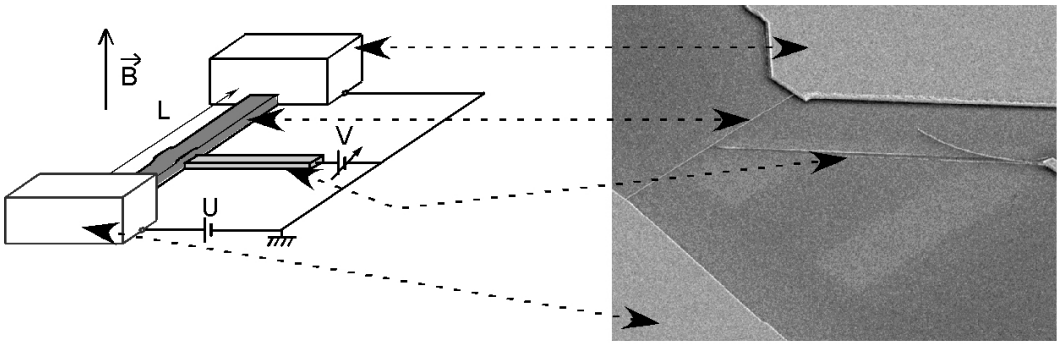

Figure 6: Left: Schematic of the circuit. A diffusive wire of length L is connected to two reservoirs biased at different potentials 0 and U. A long and narrow superconducting probe electrode forms a tunnel junction with the wire in its middle. Right: Micrograph of a sample seen at an angle with arrows related to the corresponding elements on the schematic.

In both cases, the differential conductance $dI/dV(V)$ of the tunnel junction can be written:

$$R_T \frac{dI}{dV}(V) = 1 + q * f(eV), \tag{30}$$

with R_T, the resistance of the tunnel junction and $q(E)$ a function dependent on the junction and environment characteristics (see Chapter 2 for details on the determination of $q(E)$).

When the probe electrode is superconducting, $q(E) = \partial n_s / \partial E$ with n_s the reduced density of states in the superconducting probe, and the energy distribution function $f(E)$ is obtained by

numerical deconvolution of $dI/dV(V)$ using Eq. (30). When the probe electrode is normal, $q(E)=\int_{-\infty}^{+\infty} d\varepsilon\ P(\varepsilon,T)\left(\partial\left(f_R(E+\varepsilon)-f_R(E-\varepsilon)\right)/\partial E\right)$ with $P(\varepsilon)$ a function that depends only on the tunnel junction environment and $f_R(E)$ the Fermi distribution at the refrigerator temperature. In this case, the deconvolution procedure could not be applied. The reason is that the Coulomb singularity is not as sharp as the BCS singularity so that the signal to noise ratio in $dI/dV(V)$ is too small to avoid additional numerical noise during deconvolution. We have then chosen to fit directly the measured differential conductance with Eq. (30) using the function $q(E)$ as determined in a calibration step and functions $f(E)$ calculated from a model. The differential conductance of such a junction shows a broad single dip when electron interactions are strong and lead to electronic thermalization, and a double dip when only little interaction occurs while electrons travel through the wire (see Figure 7).

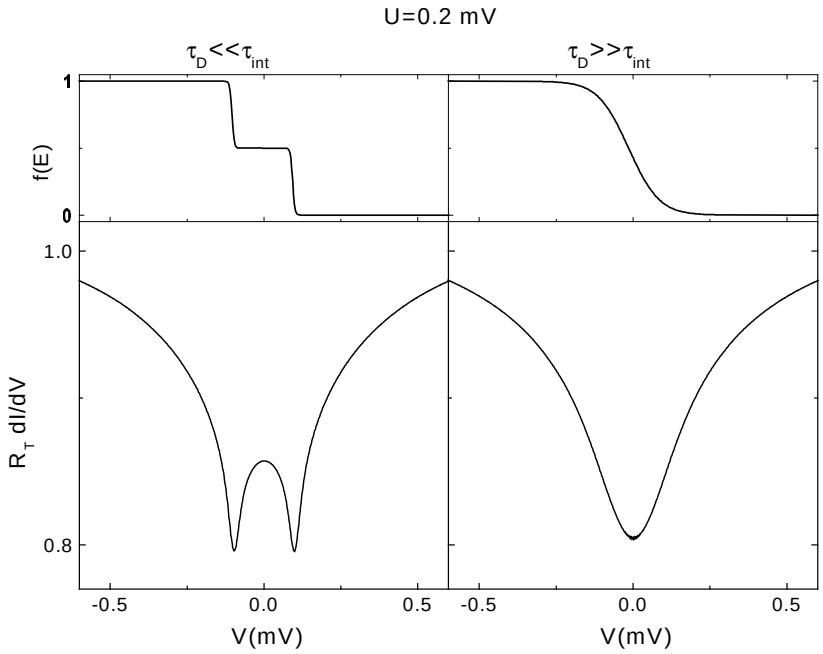

Figure 7: Top: Calculated distribution functions in the middle of an out-of-equilibrium wire in two extreme cases: $\tau_D \ll \tau_{int}$ (left) and $\tau_D \gg \tau_{int}$ (right). Bottom: Corresponding calculated differential conductance dI/dV of a tunnel junction formed between the wire and a resistive probe. The curve dI/dV shows a double dip when only little interaction occurs while electrons travel through the wire, and a broad single dip when electrons thermalize.

7.2.2 Geometrical and electrical characteristics of the measured samples

The fabrication process of the samples is detailed in Chapter 3. Measurements of energy exchange in a magnetic field have been performed on different metallic wires made of aluminum, silver, copper or gold. The electrical and geometrical characteristics of the main samples measured during this thesis are summarized in Table 1. Additional results on other silver samples are presented in Appendix 3.

Sample	Source	$L\,(\mu m)$	w (nm)	t (nm)	R (Ω)	D ($cm^2\ s^{-1}$)	l_e (nm)	τ_D (ns)
Al5	Al5N	5.05	110	45	28.6	64.8	9.5	3.9
Ag_{6N}I20	Ag6N	21.7	100	45	84.9	215	46.5	21.9
Ag_{5N}IV20	Ag5N	20.0	108	45	79.6	196	42.5	20.4
Au5	Au4N	5.1	85	45	42	109	23.5	2.4
Cu5	Cu5N	5.0	105	45	29.5	91	17	2.8

Table 1: Geometrical and electrical characteristics of the measured samples. The length is written L, the width w, the thickness t, the wire resistance R, the diffusion coefficient D, the electronic elastic mean free path l_e and the diffusion time $\tau_D = L^2 / D$.

The diffusion coefficient is obtained from Einstein' s relation $\sigma = \nu_F e^2 D$ where $\sigma = L/(Rwt)$ is the wire conductivity. The electronic elastic mean free path, given as an indication, is obtained from $D = 1/3\, v_F l_e$ with v_F the Fermi velocity. The value of ν_F and v_F used for aluminum, silver, copper, and gold are summarized in Table 2 [17].

	ν_F ($J^{-1}\ m^{-3}$)	v_F ($m\ s^{-1}$)
silver	1.03×10^{47}	1.39×10^{6}
copper	1.56×10^{47}	1.57×10^{6}
gold	1.14×10^{47}	1.39×10^{6}
aluminum	2.15×10^{47}	2.03×10^{6}

Table 2: Density of states at the Fermi level ν_F and Fermi velocity v_F in silver, copper, gold, and aluminum [17].

7.3 Measurements of energy exchange and comparison with theoretical predictions

7.3.1 Energy exchange in silver, copper and gold wires

Measurements of energy exchange were performed in silver, copper, and gold wires, which are known to behave differently [1]. Part of the results obtained for the silver wires were published in Phys. Rev. Lett. **90**, 076806 (2003). This article is reproduced in Appendix 2. The sample named Sample 1 in the article corresponds to $Ag_{5N}IV20$ and Sample 2 to $Ag_{6N}I20$. The results obtained for the copper wire were partly published in [18].

7.3.1.1 Energy exchange at zero magnetic field

7.3.1.1.1 Silver samples

The energy distribution functions measured at the middle of the two 20-µm silver wires are shown in Figure 8 for $U = 0.1,\ 0.2$ and $0.3\,\mathrm{mV}$. The two samples were obtained from silver sources with different purity ($Ag_{6N}I20$: 99.9999%-pure; $Ag_{5N}IV20$: 99.999%-pure). Though the diffusion times are very similar in both samples, the energy distribution functions differ strongly: in $Ag_{6N}I20$, the energy distribution functions display double steps, indicating that little interaction occurs; on the contrary in $Ag_{5N}IV20$, the energy distribution functions are rounded, indicating that interactions are strong. The data are fit with Eq. (7), taking into account for the collision term electron-electron interaction with the kernel $\mathrm{K}(\varepsilon) = \kappa_{3/2} / \varepsilon^{3/2}$ (see Eq. (18)), and electron-phonon interaction with the kernel described by Eq. (21). For the whole dataset of each sample, the single fit parameter is $\kappa_{3/2}$, $\kappa_{ph} = 8\ \mathrm{ns}^{-1}$ being obtained from the phase coherence time measurements [1]. The parameters $\kappa_{3/2}$ are found to be $0.1\ \mathrm{ns}^{-1}\ \mathrm{meV}^{-1/2}$ for $Ag_{6N}I20$ and $2.0\ \mathrm{ns}^{-1}\ \mathrm{meV}^{-1/2}$ for $Ag_{5N}IV20$. The calculated theoretical values using the geometrical and electrical characteristics of the samples (Table 1) are respectively $0.08\ \mathrm{ns}^{-1}\ \mathrm{meV}^{-1/2}$ and $0.075\ \mathrm{ns}^{-1}\ \mathrm{meV}^{-1/2}$. Whereas the intensity of the interaction in $Ag_{6N}I20$ is in close agreement with the predictions for Coulomb interaction, it is in $Ag_{5N}IV20$ much larger, indicating that extra interactions occur in this sample. The fact that

these extra interactions can be accounted for by a Kernel proportional to $1/\varepsilon^{3/2}$ is not significant because the data are so close to Fermi functions that equally good fits could be performed with other energy dependences.

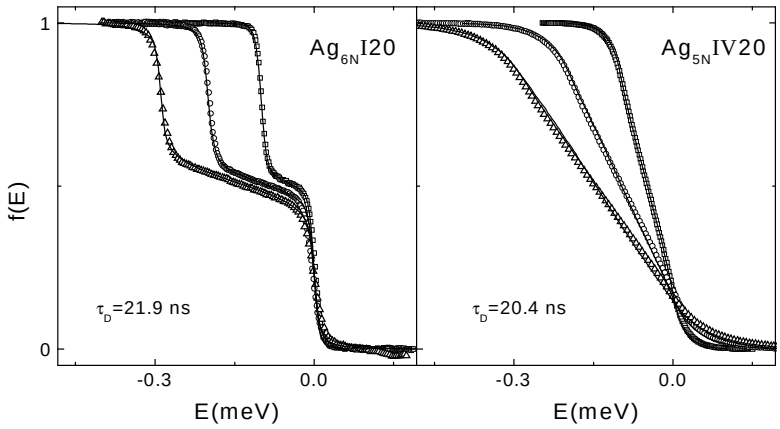

Figure 8: Symbols: Distribution functions measured in the middle of silver wires made from a 99.9999%-pure source (left panel) and from a 99.999%-pure source (right panel) for the applied voltages $U = 0.1, 0.2$ and $0.3\,\mathrm{mV}$. Solid lines: Calculated distribution functions with an interaction kernel $\mathrm{K}(\varepsilon) = \kappa_{3/2}\varepsilon^{-3/2}$ with $\kappa_{3/2} = 0.1\ \mathrm{ns^{-1}\,meV^{-1/2}}$ for $\mathrm{Ag_{6N}I20}$ and $\kappa_{3/2} = 2\ \mathrm{ns^{-1}\,meV^{-1/2}}$ for $\mathrm{Ag_{5N}IV20}$.

The results obtained on other wires from the three different silver sources we have used are presented in Appendix 3.

7.3.1.1.2 Gold and copper samples

The energy distribution functions in the middle of the 5-µm-long copper and gold wires are shown in Figure 9. These distribution functions are very similar. Like for the silver wires, we tried fits with Eq. (7) and with $\mathrm{K}(\varepsilon) = \kappa_{3/2}/\varepsilon^{3/2}$. The fit parameter $\kappa_{3/2}$ is chosen to account for the measurements at $U = 0.1\,\mathrm{mV}$. We obtain $\kappa_{3/2} = 2.7\ \mathrm{ns^{-1}\ meV^{-1/2}}$ for Cu5 and $\kappa_{3/2} = 3.5\ \mathrm{ns^{-1}\ meV^{-1/2}}$ for Au5. When comparing with the experimental data the energy distribution functions calculated at $U = 0.2$ and $0.3\,\mathrm{mV}$ using these values of $\kappa_{3/2}$, it is found that the discrepancy increases with the applied voltage. Moreover, the calculated theoretical values using the geometrical and electrical characteristics of the samples are respectively $0.115\ \mathrm{ns^{-1}\ meV^{-1/2}}$ and $0.075\ \mathrm{ns^{-1}\ meV^{-1/2}}$.

From these data, it is therefore possible to conclude not only that the intensity of energy exchange is larger than predicted for Coulomb interaction, but also that the energy dependence of the interaction kernel is not the one of Coulomb electron-electron interaction.

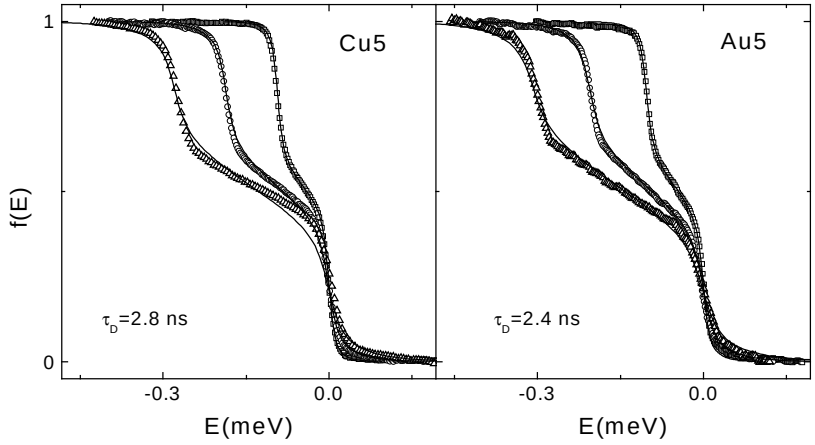

Figure 9: Symbols: Distribution functions measured in the middle of a copper wire (left panel) and of a gold wire (right panel) for the applied voltages $U = 0.1,\ 0.2$ and $0.3\,\mathrm{mV}$. Solid lines: Calculated distribution functions with an interaction kernel $\mathrm{K}(\varepsilon) = \kappa_{3/2}\varepsilon^{-3/2}$ where the parameter $\kappa_{3/2}$ is chosen to account for the measurements at $U = 0.1\,\mathrm{mV}$. The discrepancy between the measured and calculated distribution functions increases with the applied voltage.

7.3.1.1.3 Conclusion on the zero-magnetic-field measurements

Like in [1], we find that the intensity and energy dependence of interactions vary from sample to sample. The presence of magnetic impurities is the best candidate to explain extra interactions. Indeed, the zero-magnetic field data can be fit using the collision term calculated in section 7.1.3.3. Yet, the set of fit parameters is not single. It is thus not a proof that magnetic impurities are really responsible for the extra interactions. In order to perform a more stringent test, we have measured energy exchange in all these samples as a function of magnetic field.

7.3.1.2 Energy exchange in presence of magnetic field

7.3.1.2.1 Qualitative behavior

As explained before, energy exchange in a magnetic field affects the differential conductance $dI/dV(V)$ of the tunnel junction formed between the wire and the resistive probe electrode. The measured $dI/dV(V)$ in $Ag_{6N}I20$ and $Ag_{5N}IV20$ for different magnetic field B, and for the applied voltage $U = 0.1\,\text{mV}$ are shown in Figure 10. The behavior of both samples is once again different: In $Ag_{6N}I20$, dI/dV does not depend on the applied magnetic field, proving that the shape of $f(E)$ is not dependent on KIM interaction. In $Ag_{5N}IV20$, the broad peak at low magnetic field in dI/dV is progressively split in two peaks as the magnetic field increases, as expected from KIM interaction.

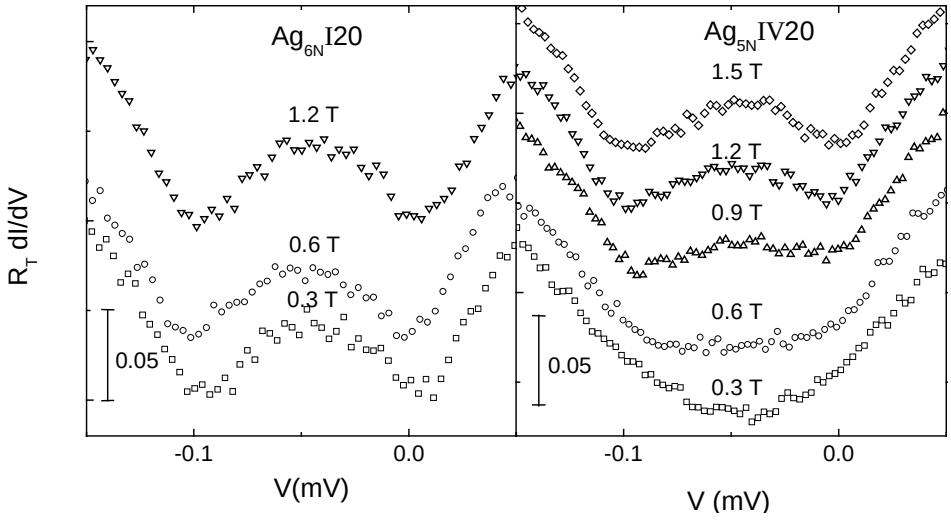

Figure 10: Measured differential conductance dI/dV for different applied magnetic field B in samples $Ag_{6N}I20$ and $Ag_{5N}IV20$ for $U = 0.1\,\text{mV}$. In $Ag_{6N}I20$, dI/dV does not depend on the magnetic field, proving the absence of KIM interaction. In $Ag_{5N}IV20$, the broad peak at low magnetic field in dI/dV is split in two peaks, proving that KIM interaction is reduced. The curves are offset vertically for clarity.

The same measurements were performed on Cu5 and Au5. The measured $dI/dV(V)$ in Cu5 and Au5 as a function of the magnetic field B for $U = 0.2\,\text{mV}$ are shown in Figure 11. Because of the shorter diffusion time τ_D in these samples, a double dip is always found at low field (at $B = 0$, $f(E)$ also presents sharp steps). In Cu5, this double dip is first slightly smeared out, then gets more pronounced as the magnetic field increases. This variation is

predicted for KIM interaction: the rate of KIM energy exchange first increases when first order processes become inelastic before being reduced when they vanish together with higher order processes. In Au5, the double dip in dI/dV becomes slightly more pronounced as the magnetic field increases, indicating that KIM interaction is also of importance.

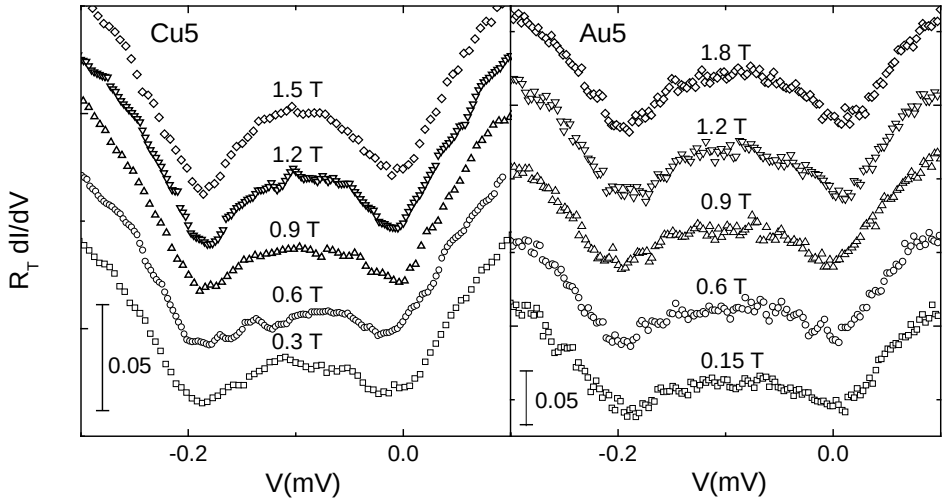

Figure 11: Measured differential conductance dI/dV for different applied magnetic field B in samples Cu5 and Au5 for $U = 0.2$ mV. In Cu5, the double dip in dI/dV is first slightly smeared out, then gets more pronounced as the magnetic field increases, reflecting the non-monotonous evolution of KIM interaction. In Au5, the double dip in dI/dV becomes slightly more pronounced as the magnetic field increases, proving that KIM interaction plays a role. The curves are offset vertically for clarity.

The extra-interactions observed at zero magnetic field in Ag_{5N}IV20, Cu5 and Au5 can therefore be attributed to Kondo impurities. The most probable low-Kondo-temperature magnetic impurity miscible in silver is manganese ($T_K = 40$ mK). In copper, magnetic impurities are not well identified but there is experimental evidence that copper oxide, which develops at the surface, contributes [19]. In gold, magnetic impurities could be iron ($T_K = 300$ mK), chromium ($T_K = 10$ mK), or manganese ($T_K < 10$ mK).

7.3.1.2.2 Quantitative comparison

In Ag_{6N}I20, the differential conductance dI/dV does not depend on magnetic field. It can be compared with the differential conductance calculated by convolution of the energy distribution function measured in absence of magnetic field with the *q*-function deduced from the dI/dV at equilibrium (see Eq. (30) and Chapter 2). This comparison is shown in Figure

12. There appears a discrepancy between the measured curve and the calculated one at the position of the dips, which increases with the voltage. Since this discrepancy does not depend on magnetic field, we attribute it to a heating of the electrons of the probe electrode (see discussion in Section 7.4.3.3). This heating associated with the current flowing through the probe electrode depends on the ratio between the probe electrode resistance R_p and the tunnel resistance R_T. When the probe electrode is superconducting, this effect is not significant because its superconducting properties are not affected by temperature as long as it remains much smaller than the critical temperature ($T_C \approx 1\,\mathrm{K}$).

Measurements of the differential conductance at finite magnetic field suggest that KIM interaction occurs in $\mathrm{Ag_{5N}IV20}$, Cu5 and Au5. We can now compare the data with the theoretical predictions of Section 7.1.2, by including for the calculation of $f(E)$ using Eq. (7) the collision term due to Coulomb electron-electron interaction, electron-phonon interaction and electron-magnetic impurity interaction.

The intensity of the Coulomb interaction $\kappa_{3/2}$ is obtained from the best fit of the large field B, low U data, where the B-dependent interaction has essentially vanished. For silver samples, which are the longest, a term of lesser importance is added to account for electron-phonon interaction. The intensity κ_{ph} of this interaction is fixed to $8\ \mathrm{ns^{-1}\ meV^{-3}}$, a value deduced from the phase coherence time measurements. The remaining part of energy exchange was fit with the KIM interaction. In the theory of KIM interaction, several parameters enter: the Kondo temperature T_K, the bare coupling constant between electrons and magnetic impurities J_0, the gyromagnetic factor of magnetic impurities g and the concentration of impurities c_{imp}. Yet, some of these parameters are known. The Kondo temperatures were fixed at the values deduced from the fit of phase coherence time measurements (see Chapter 6). These values are $T_K = 40$ mK for $\mathrm{Ag_{5N}IV20}$ (corresponding to manganese) and $T_K = 300$ mK for Au5 (corresponding to iron). For copper, equally good fits can be found for phase coherence time measurements for T_K between 0.1 [1] and 0.3 K with c_{imp} from 0.1 to 0.2 ppm. We have found that the best fits of the energy exchange measurements were obtained for $T_K = 300$ mK. The problem of a fine determination of the Kondo temperature of impurities in copper arises because the nature of magnetic impurities is

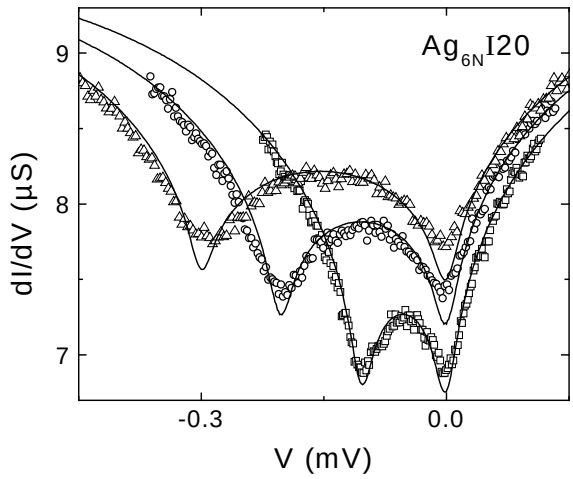

Figure 12: Symbols: Measured differential conductance in $Ag_{6N}I20$ at $B = 0.6$ T for applied voltages $U = 0.1$, 0.2 and 0.3 mV. Solid line: Calculated differential conductance by convolving the measured distribution function at $B = 0$ with the function q deduced from the Coulomb blockade signal at equilibrium. The discrepancy between the measured curve and the calculated one at the position of the dips increases with the voltage and is attributed to a heating of the probe electrode (see discussion in Section 7.4.3.3).

unknown. The coupling constant between electrons and magnetic impurities is related to the Kondo temperature by $k_B T_K = \mathrm{D} e^{-1/\nu_F J_0}$ where $\mathrm{D} \sim 1$ eV is the characteristic bandwidth of the conduction electrons and is fixed. Therefore only two fit parameters g and c_{imp} remain for KIM interaction.

The results of this procedure for $Ag_{5N}IV20$ and Cu5 are presented on Figure 13 and Figure 14. For both samples, the whole voltage and magnetic field dependence can be described with three significant fits parameters (summarized in Table 3). The corresponding energy distribution functions are also shown.

For Au5 the agreement on the whole voltage and magnetic field dependence is not so good (see Figure 15). This might be due to the fact that magnetic impurities are correlated due to the tendency of clustering of iron in gold [20].

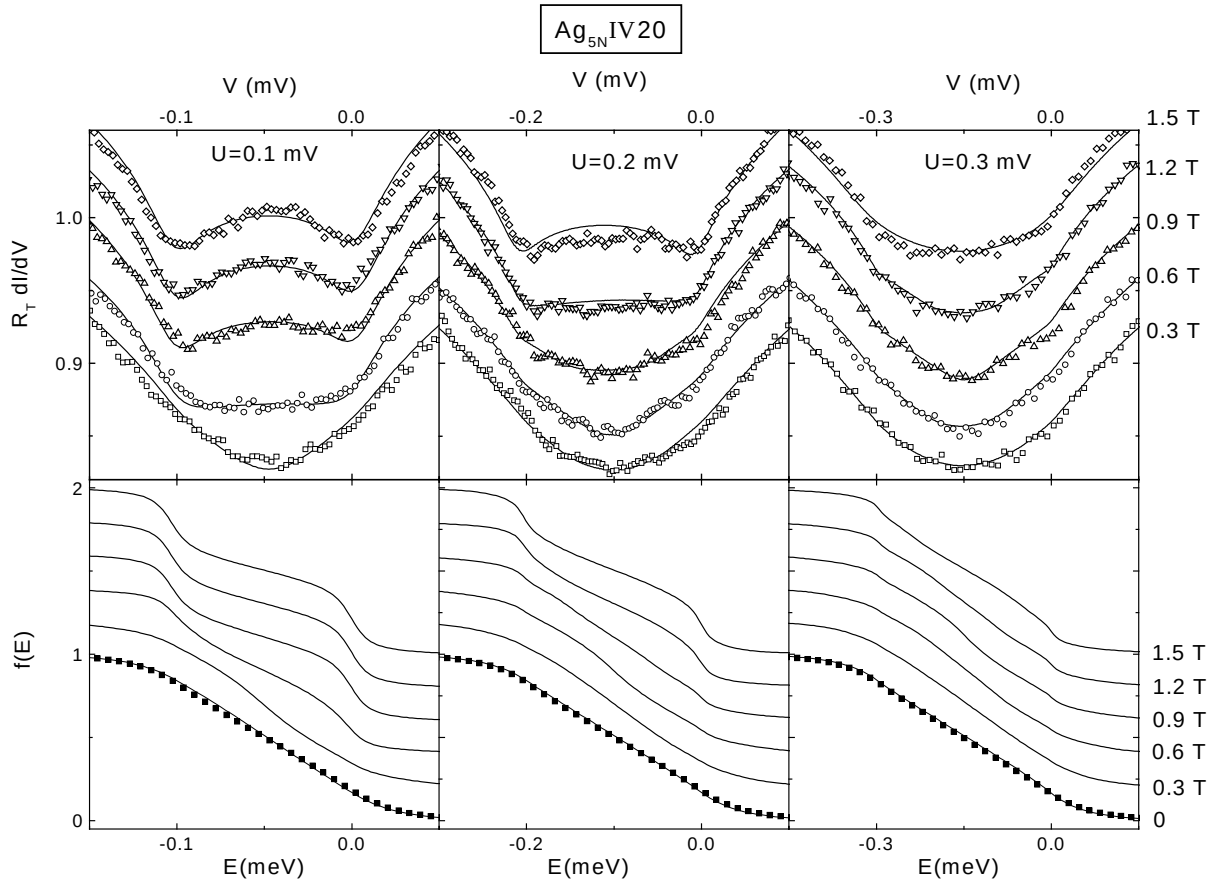

Figure 13: Top: Symbols: Measured differential conductance in $Ag_{5N}IV20$ for different applied magnetic field for the applied voltage $U = 0.1, 0.2, 0.3$ mV. The curves have been vertically offset by steps of 0.033, for clarity. Solid lines: Fits with theory including electron-electron interaction, electron-phonon interaction and KIM interaction. The fit parameters are $\kappa_{3/2} = 0.5$ ns^{-1}meV$^{-1/2}$, $c_{imp} = 17$ ppm and $g = 2.9$. Other parameters were fixed: $T_K = 40$ mK, $\nu_F J_0 = 0.08$, $\kappa_{ph} = 8$ ns^{-1} meV^{-3} and $T_{ph} = 40$ mK. Bottom: Symbols: Measured energy distribution functions at $B = 0$. Solid lines: Calculated energy distribution functions with the parameters listed above. The curves have been vertically offset by steps of 0.2, for clarity.

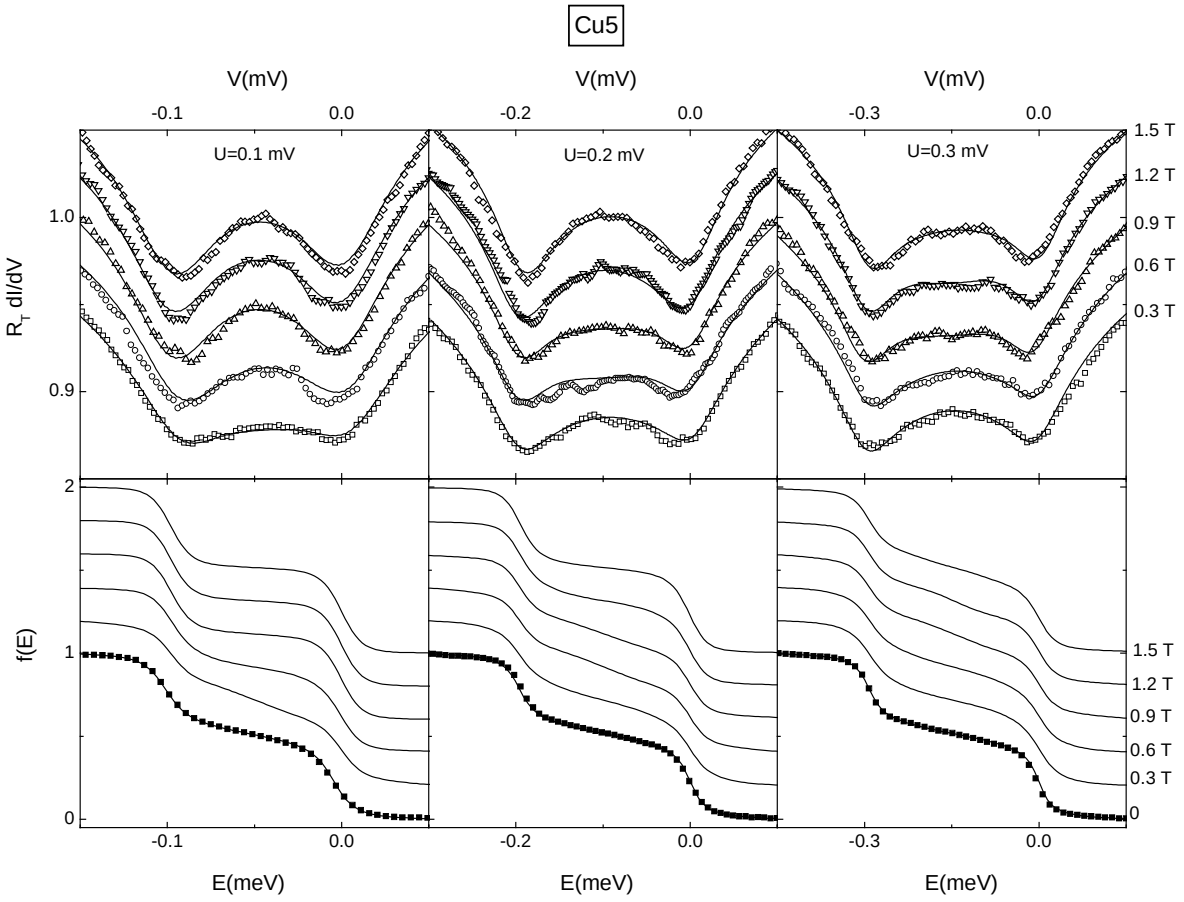

Figure 14: Top: Symbols: Measured differential conductance in Cu5 for different applied magnetic field for the applied voltage $U = 0.1$, 0.2, 0.3 mV . The curves have been vertically offset by steps of 0.033, for clarity. The curves are not symmetric because the probe electrode position is slightly different from $x = 1/2$: $x = 0.485$. Solid lines: Fits with theory including electron-electron interaction, electron-phonon interaction and KIM interaction. The fit parameters are $\kappa_{3/2} = 0.4$ ns^{-1}meV$^{-1/2}$, $c_{imp} = 4.8$ ppm and $g = 2.3$. Other parameters were fixed: $T_K = 300$ mK and $\nu_F J_0 = 0.1$. Bottom: Symbols: Measured energy distribution functions at $B = 0$. Solid lines: Calculated energy distribution functions with the parameters listed above. The curves have been vertically offset by steps of 0.2, for clarity.

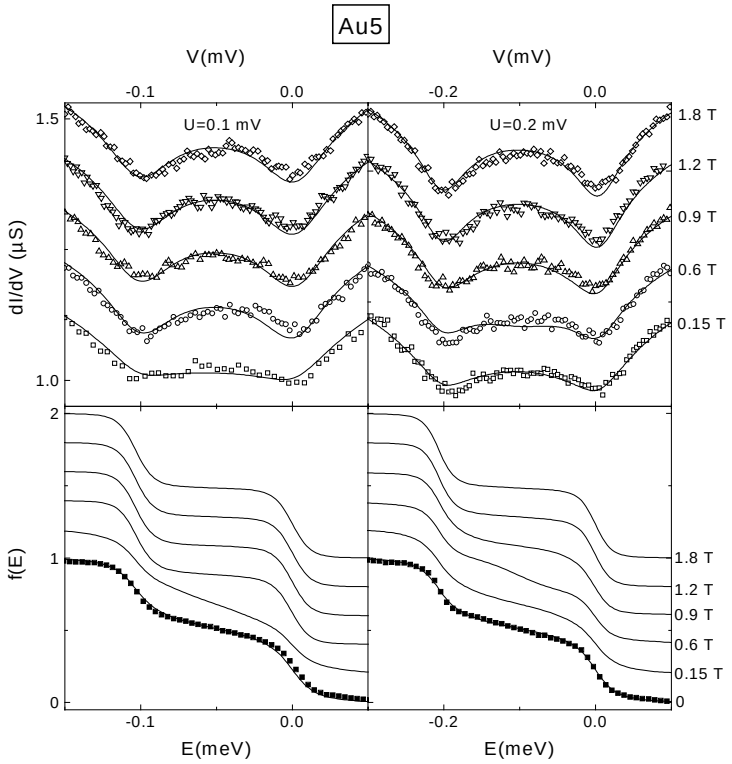

Figure 15: Top: Symbols: Measured differential conductance in Au5 for different applied magnetic field for the applied voltage $U = 0.1, 0.2$ mV. The curves have been vertically offset by steps of 0.033, for clarity. Solid lines: Fits with theory including electron-electron interaction, electron-phonon interaction and KIM interaction. The fit parameters are $\kappa_{3/2} = 0.4$ ns^{-1}meV$^{-1/2}$, $c_{imp} = 8$ ppm and $g = 3.4$. Other parameters were fixed: $T = 300$ mK and $\nu_F J_0 = 0.1$. Bottom: Symbols: Measured energy distribution functions at $B = 0$. Solid lines: Calculated energy distribution functions with the parameters listed above. The curves have been vertically offset by steps of 0.2, for clarity

7.3.1.2.3 Discussion

The fit parameters used to account for the data are summarized in Table 3 as well as the predicted intensity of Coulomb interaction $\kappa_{3/2}^{th}$.

			e-e interaction $\kappa_{3/2}\,(\mathrm{ns^{-1}meV^{-1/2}})$		e-ph interaction	KIM interactions			
Sample	$D\ (\mathrm{cm^2\ s^{-1}})$	$S_e\ (\times 10^{-3}\mu\mathrm{m^2})$	$\kappa_{3/2}^{th}$	$\kappa_{3/2}$	$\kappa_{ph}\,(\mathrm{ns^{-1}})$	$T_K\,(\mathrm{mK})$	$\nu_F J$	$c_{imp}\,(\mathrm{ppm})$	g
Al5	64.8	4.95	0.06	**0.06 ± 0.02**	**4**	–	–	–	–
$Ag_{6N}I20$	215	4.5	0.08	**0.1 ± 0.02**	8	–	–	–	–
$Ag_{5N}IV20$	196	4.86	0.075	**0.5 ± 0.1**	8	40	0.08	**17**	**2.9**
Au5	109	3.825	0.12	**0.4 ± 0.2**	–	300	0.1	**8**	**3.4**
Cu5	91	4.725	0.075	**0.4 ± 0.2**	–	**300**	0.1	**4.8**	**2.3**

Table 3: Parameters and fit parameters (**bold** characters) used to account for the measured energy distribution functions and differential conductance when electron-electron, electron–phonon and KIM interactions are included.

Coulomb electron-electron interaction

In $Ag_{6N}I20$, $\kappa_{3/2}$ is close to $\kappa_{3/2}^{th}$. In contrast in the three other samples, $\kappa_{3/2}$ is larger than predicted, even if the uncertainty on $\kappa_{3/2}$ in these samples displaying KIM interaction is larger because fits are made only on low-voltage high magnetic field curves. The accessible magnetic field was not high enough to reach the Coulomb-interaction-dominated regime at large voltage.

KIM interaction

Increased interactions at intermediate fields

In $Ag_{5N}IV20$, the measurement is not sensitive to the expected increase of the KIM interaction rate for intermediate fields because $f(E)$ is already close to a Fermi function at $B = 0$.

Renormalization effect

In order to evaluate the renormalization effect on J_0, we have calculated the collision term in Eq. (1) ($\mathrm{K}(\varepsilon) = \kappa_2/\varepsilon^2$) with the parameters c_{imp} and J_0 found to fit the data of $Ag_{5N}IV20$, assuming $S = 1/2$: $\kappa_2 = 0.004\ \mathrm{ns^{-1}}$. The result for $f(E)$ is shown for $U = 0.1\ \mathrm{mV}$ together with the calculated distribution function using renormalization and the same parameters on Figure 16. One clearly sees that the bare interaction leads to much less rounding than the

renormalized one.

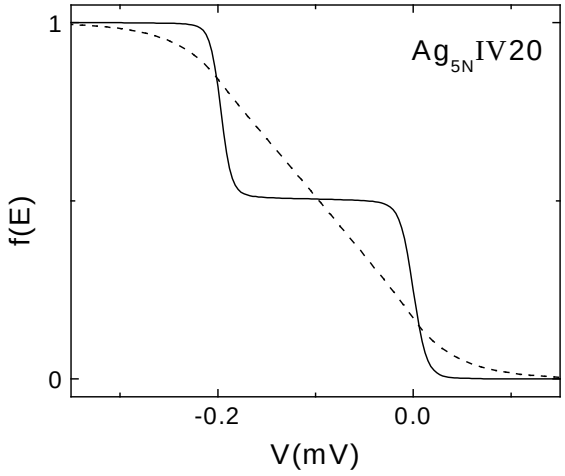

Figure 16: Solid line: Calculated energy distribution function taking only into account the second order in coupling between electrons and magnetic impurities with the parameters of Table 3 using Eq. (1). Dashed line: Calculated distribution function in $Ag_{5N}IV20$ for $U = 0.2$ mV taking into account the renormalization of the coupling between electrons and magnetic impurities. It is seen that the renormalization of the coupling constant by Kondo effect considerably enhances the interactions.

Concentrations of magnetic impurities

Source	c_{imp} (ppm)	c_{τ_ϕ} (ppm)
Ag6N	< 0.1	0.0024
Ag5N	17	0.13
Cu5N	4.8	0.15

Table 4: Fit concentrations deduced from energy exchange measurements c_{imp} and from phase coherence time measurements c_{τ_ϕ} on samples made of the same source. For sources of Ag5N and Cu5N, the concentration c_{imp} is found larger than c_{τ_ϕ}, suggesting that either pollution arises in the fabrication process of energy exchange samples, or the theory for KIM interaction is not sufficient.

The fit concentrations c_{imp} must be compared with c_{τ_ϕ}, the concentrations obtained from the fits of the measurements of the phase coherence time in long wires fabricated with the same source materials. The values are summarized in Table 4. The concentration c_{imp} is found systematically larger than c_{τ_ϕ} by at least one order of magnitude, suggesting that either

pollution arises in the fabrication process of energy exchange samples, or the effect of magnetic impurities is not well described by theory. In order to solve this problem, experiments in which c_{imp} can be controlled are essential.

Effect of the spin value of the magnetic impurities

The concentration c_{imp} is not correctly evaluated in the fits because the magnetic impurity spin is assumed to be ½, which might be incorrect. According to Ref. [2,16] the product $S(S+1)c_{imp}$ enters as a prefactor for the rate. However, this result does not take into account the spin dependence of the renormalized constant. The complete calculation was performed recently in [21] and the authors conclude that increasing the value of the spin *S* in the calculation does not lead to an increased rate.

Sensitivity to the Kondo temperature

The sensitivity of the calculated dI/dV curves on the Kondo temperature is exemplified on Figure 17 for parameters fitting Cu5: $c_{imp}/(\nu_F h)=5$, $g=2.3$ and $\mathrm{D}=1\ \mathrm{eV}$ and for two Kondo temperatures: $T_K=100\ \mathrm{mK}$ and $T_K=300\ \mathrm{mK}$. The $U=0.1\ \mathrm{mV}$ curves are nearly insensitive to T_K. At higher voltages, slight differences can be seen, but the result is clearly not very sensitive to T_K.

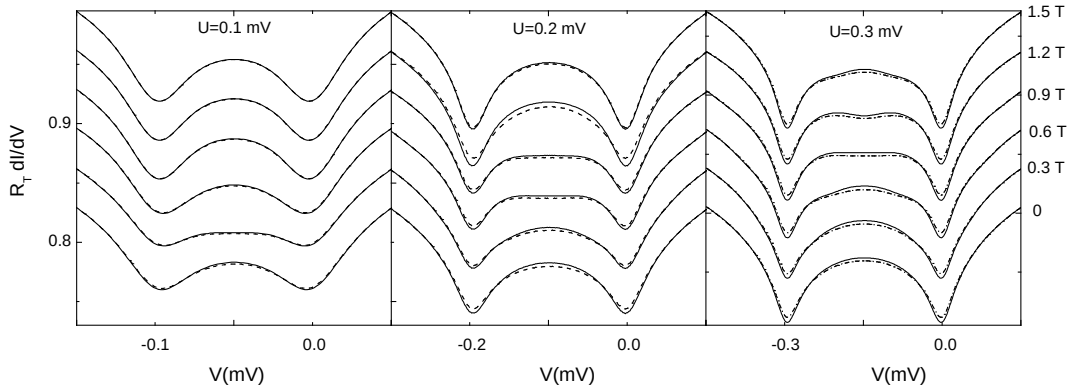

Figure 17: Calculated differential conductance dI/dV for different applied magnetic field with the fixed parameters for KIM interaction: $c_{imp}/(\nu_F h)=5$, $g=2.3$ and $\mathrm{D}=1\ \mathrm{eV}$ and the different couple of parameters $(T_K,\nu_F J_0)=(100\ \mathrm{mK},0.08)$ for the solid lines and $(T_K,\nu_F J_0)=(300\ \mathrm{mK},0.1)$ for the dashed lines. The curves have been vertically offset for clarity.

Gyromagnetic factor of magnetic impurities

The value of the gyromagnetic factor of magnetic impurities depends on many parameters: the spin-orbit coupling, the crystalline field [22] … For diluted manganese impurities in different matrices, it is however predicted that $g \sim 2$. Yet, the magnetic field at the position of the samples is not measured but calculated from the characteristics of the superconducting coil. A 10 % error on the value of B due to the evaluation of the exact position of the sample cannot be excluded, and corresponds to a 10% error on the *g*-factor. This does not account for the whole discrepancy.

In parallel with this work, F. Pierre and N.O. Birge have measured the Aharonov-Bohm oscillations in copper rings as a function of the magnetic field [23]. Aharonov-Bohm oscillations are recovered at large magnetic field demonstrating that magnetic impurities are also present, and that electronic coherence increases when magnetic impurities are polarized. To account for their data they need to introduce the gyromagnetic factor of the impurity: it is found equal to 0.9. The impurities are also believed to be associated with copper oxide, but the discrepancy in the *g*-factor between this experiment and energy exchange measurements is not understood.

7.3.2 Energy exchange in an aluminum wire

Measurements of energy exchange in an aluminum wire in its normal state should provide information on the electron-phonon coupling, which we naively expected to be large since it is responsible for the phase transition to a superconductive state. Such energy exchange measurements had never been performed before because they were previously based on superconductivity in aluminum. In our new set-up using Coulomb blockade where both the probe electrode and the wire are in the normal states, measurements on aluminum can be performed. Information on electron-phonon interaction was already inferred in aluminum from analysis of the resistivity and electron dephasing rate in the temperature range 1-300 K [24]. The theoretical predictions for electron-phonon interaction in aluminum are performed like for other metals [25] (see section 7.1.3.2).

The sample Al5 consists of a 5-µm long aluminum wire (see parameters in Tables 1 to 6). Measurements of the conductance of the probe junction as a function of bias voltage and magnetic field are shown in Figure 18. The differential conductance does not depend on the magnetic field, proving that KIM interaction is not relevant in this sample. This is indeed expected because the Kondo temperatures T_K of magnetic impurities in aluminum are higher than in silver, copper or gold: T_K varies exponentially with ν_F which is roughly twice as large in aluminum as in other metals. For the energies probed in this experiment, nothing is therefore magnetic.

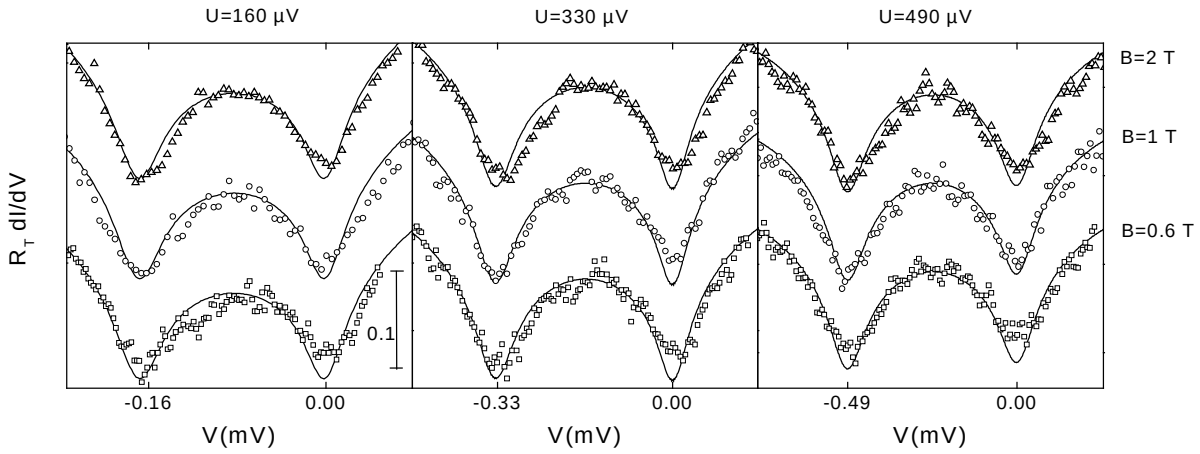

Figure 18: Symbols: Differential conductance dI/dV of a tunnel junction between a resistive probe electrode and an aluminum wire as a function of the bias voltage U across the wire and the applied magnetic field B. The curves have been vertically offset for clarity. At all the voltages, dI/dV does not depend on the magnetic field, proving the absence of KIM interaction. Solid lines: Fit with the parameters of Table 3, which are the same for all values of the magnetic field.

To test electron-phonon interaction, the bias voltage U of the wire was increased to large values for which the electron-phonon interaction contributes significantly to energy exchange (see Figure 19). The results are shown on Figure 20.

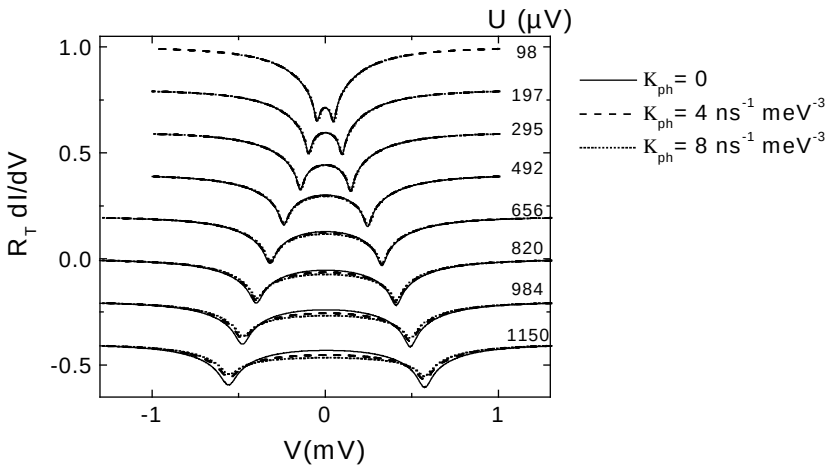

Figure 19: Influence of the electron-phonon interaction on the differential conductance dI/dV of the tunnel junction of the sample Al5 for different wire bias voltage U. Solid lines: $\kappa_{nh} = 0$. Dashed lines: $\kappa_{ph} = 0.4\,\text{ns}^{-1}\ \text{meV}^{-3}$. Dotted lines: $\kappa_{ph} = 0.8\,\text{ns}^{-1}\ \text{meV}^{-3}$ (see other parameters in Table 3). Electron-phonon interaction has a non-negligible effect only for the larger wire bias voltage.

The data are perfectly fit using for the electron-phonon interaction an inelastic collision term of the form of section 7.1.3.2. The amplitude of this term is found to be $\kappa_{ph} = 4\ \text{ns}^{-1}\ \text{meV}^{-3}$. The value in aluminum can be compared with the one deduced from phase coherence time measurements. The dephasing rate due to electron-phonon interaction is written BT^3 where $B = 6\xi(3)\kappa_{ph}k_B^3$ with $\xi(3) \simeq 1.2$, the Rieman zeta function (see Chapter 6). In [26], it was found $B_{\text{exp}} \simeq 0.9\ \text{ns}^{-1}\ \text{K}^{-3}$, leading to $\kappa_{ph} = 2\ \text{ns}^{-1}\ \text{meV}^{-3}$, which is of the same order of magnitude as our experimental value. Surprisingly, the amplitude of this term, $\kappa_{ph} = 4\ \text{ns}^{-1}\ \text{meV}^{-3}$, is in fact smaller than the one found in silver wire ($\kappa_{ph} = 8\ \text{ns}^{-1}\ \text{meV}^{-3}$). According to [24] the value of B in silver is such as $B_{\text{aluminum}} \sim B_{\text{silver}}$. This non-intuitive result provides from the difference between the sound velocity, the density of states and solid density of both metals.

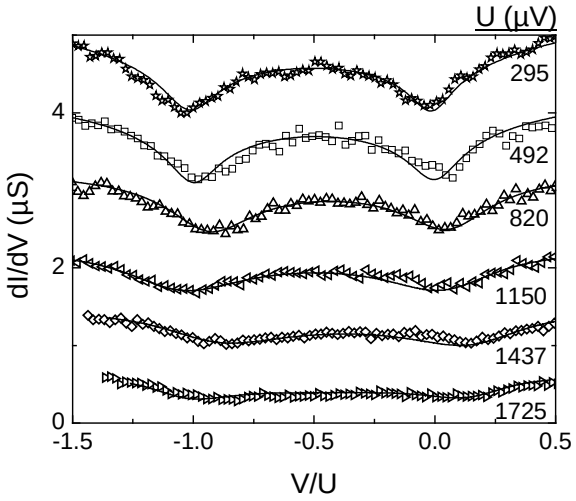

Figure 20: Symbols: Measured bias voltage U dependence of the differential conductance of a tunnel junction between a normal resistive tunnel junction and an aluminum wire in an applied magnetic field $B = 2$ T. The data have been vertically offset and V normalized to U for clarity. Lines: Fits with the parameters summarized in Table 3.

7.4 Experimental control

7.4.1 Reservoir heating

When a voltage U is applied between the reservoirs, the power $P = U^2/2R$ is dissipated in each reservoir. Although these reservoirs are thick to minimize heating, heating effects are observed when the wire resistance is small [27]. The heating effects were evaluated by F. Pierre in [1]. The reservoir temperature can be written:

$$T_r = \sqrt{T_0^2 + (\beta U)^2},$$

with T_0 the base temperature and β a coefficient dependent on the wire resistance, on the geometry of the reservoirs and on the nature of the metal. Typically for our experiments, it is found that $\beta^2 R \sim 10\ \Omega\ \mathrm{K}^2\ \mathrm{mV}^{-2}$. The coefficients β were fit parameters for experimental data but their influence is mostly visible in short wires on the sharpest part of the large voltage

curves. The values of β used for the different samples are summarized in Table 5. The geometry of the two reservoirs being slightly different, two different values are used: β_g for the ground reservoir and β_U for the other one.

Sample	β_g (K mV^{-1})	β_U (K mV^{-1})
Al5	0.13	0.16
Ag_{6N}I20	0	0
Ag_{5N}IV20	0	0
Au5	0.5	0.5
Cu5	0.5	0.5

Table 5: Heating coefficient due to the injected power in the ground reservoir β_g and the biased reservoir β_U for all the measured samples. The less resistive the wire, the larger the injected power and the higher β. For some samples, $\beta_g < \beta_U$ because of the small difference in the reservoirs geometry.

The effect of reservoirs heating is exemplified on Figure 21 for the sample Cu5. Heating effects are visible at the dips of the differential conductance curves, which correspond to the step positions of the distribution functions.

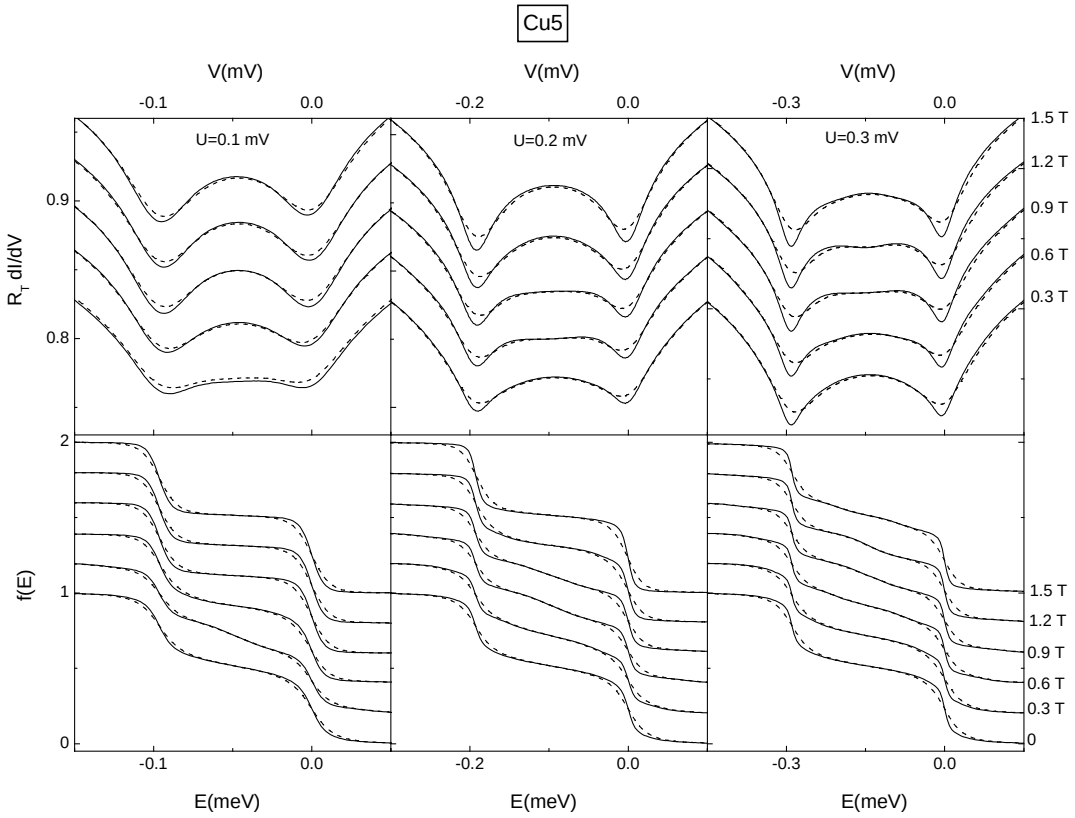

Figure 21: Calculated differential conductance dI/dV and energy distribution functions $f(E)$ with the parameters found to account for the data of Cu5 (see Table 3) taking into account heating of the reservoirs (dashed line) or neglecting it (solid lines).

7.4.2 Measurements with a superconducting probe

Measurements with superconducting probes have been performed for a few years in the Quantronics group. The deconvolution procedure of dI/dV and experimental controls are described in [11] and [1].

Here, a complication arises from the fact that the probe electrode was designed long and narrow and presents a non-negligible impedance, even in its superconducting state, compared to the resistance quantum R_K. This results in corrections to dI/dV due to dynamical Coulomb blockade of tunneling. At frequencies smaller than $2\Delta/h$, an aluminum wire behaves like a pure inductor. Its kinetic inductance is equal to $\hbar R_l/(\pi\Delta)$, where R_l is the wire resistance per unit length in the normal state. At frequencies above $2\Delta/h$, Cooper pairs can be broken into two quasiparticles and the aluminum probe electrode becomes dissipative. The admittance $Y(\omega)$ per unit length of a diffusive superconducting wire has been calculated within the framework of the BCS theory [28]. At zero temperature, the real and imaginary parts of $Y(\omega)$ are given by:

$$Y_1(\omega)=\frac{1}{R_p}\left\{\left(1+\frac{2\Delta}{\hbar\omega}\right)E(k(\omega))-\frac{4\Delta}{\hbar\omega}E(k(\omega))\right\} \text{ for } \hbar\omega\geq 2\Delta, \tag{31}$$

$$Y_2(\omega)=-\frac{1}{R_p}\left\{\frac{1}{2}\left(1+\frac{2\Delta}{\hbar\omega}\right)E(k'(\omega))-\frac{1}{2}\left(1-\frac{2\Delta}{\hbar\omega}\right)K(k'(\omega))\right\}, \tag{32}$$

where $k(\omega)=\left|(2\Delta-\hbar\omega)/(2\Delta+\hbar\omega)\right|$, $k'(\omega)=\left(1-k(\omega)^2\right)^{1/2}$, E and K are complete elliptic integrals, and R_p is the superconducting wire resistance in its normal state. In the superconducting state, the environment impedance of the junction of capacitance C is then:

$$Z_{env}^{S}(\omega)=\frac{1}{Y_1(\omega)+iY_2(\omega)+iC\omega}. \tag{33}$$

At zero temperature, the differential conductance $dI_{env}/dV(V)$ of the tunnel junction in presence of an electromagnetic environment is just the convolution of the differential conductance $dI/dV(V)$ of the tunnel junction without any environment with the probability $P(E)$ that a part of the energy is released to the environment of impedance Z_{env}^{S} [29,30] (see also appendix of Chapter 2).

The function $P(E)$ presents two parts: a delta function at zero energy corresponding to elastic tunneling, and an inelastic part for energies larger than 2Δ. The weight of the zero energy peak, which is 100 % in absence of Coulomb blockade, is in this case:

$$W_{el} = \exp\left(-2\int_0^{+\infty} \frac{\mathrm{Re}\left(Z_{env}^{S}(\omega)\right)}{R_K} \frac{d\omega}{\omega} \right). \tag{34}$$

The inelastic contribution to the differential conductance is non zero only for voltages larger than $3\Delta/e$ since the inelastic part of $P(E/e)$ is non-zero only for voltages larger than $2\Delta/e$, and since $dI/dV(V)$ of the normal-superconducting tunnel junction is non-zero only for voltages larger than Δ/e. Therefore, for $V < 3\Delta/e$, $dI_{env}/dV(V)$ is simply renormalized:

$$dI_{env}/dV(V) = W_{el}\, dI/dV(V), \tag{35}$$

an effect that can be interpreted as a renormalization of the tunnel conductance. As an example, $dI_{env}/dV(V)$ of the sample Cu5 is presented in Figure 22. A rounded step appears in the curve at $V = 3\Delta/e$. Without any environment, $dI/dV(V)$ is predicted to be proportional to the convolution of the BCS density of states in the superconducting electrode with the derivative of the Fermi function at the fridge temperature (see Chapter 2). The proportionality factor is the tunnel conductance of the junction. The curve below voltage $3\Delta/e$ is perfectly fit using a BCS function with $\Delta = 240\,\mu\mathrm{V}$ and a tunnel conductance of $20.8\,\mu\mathrm{S}$. At voltage larger than $3\Delta/e$, the tunnel conductance is found to be $23.3\,\mu\mathrm{S}$. The ratio of conductances corresponds to a factor $W_{el} = 0.89$. Conversely, the resistance R_p of the probe electrode and the junction capacitance C can be inferred from the Coulomb blockade signal in a magnetic field, when the probe electrode is in its normal state (see Chapter 2). The weight of the elastic peak W_{el} can then be calculated with Eqs. (34) using for Z_{env}^{S} Eqs (31), (32), and (33) and is found to be $W_{el} = 0.89$, in agreement with the weight deduced from experiments at $B = 0$.

A practical drawback of Coulomb blockade effect is that we cannot access the energy distribution functions for $|U| > 2\Delta$. The reason is that the structure in the dI/dV resulting from the convolution of $f(E)$ with a double step, of width eU, with the BCS density of states, of width 2Δ, extends down to voltages smaller than $-3\Delta/e$. The effect of Coulomb

blockade for these voltages is no more trivial. In practice, we have deconvolved $dI/dV(V)$ within the voltage range $|V| < 3\Delta$.

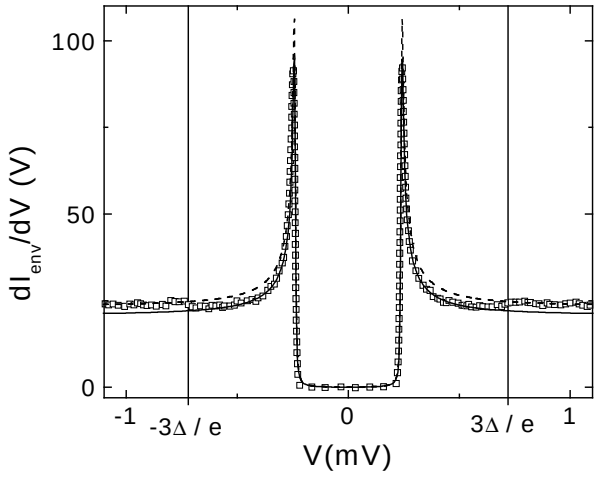

Figure 22: Symbols: Differential conductance $dI_{env}/dV(V)$ of a normal-superconducting tunnel junction embedded in a superconducting environment. Due to Coulomb blockade of tunneling of quasiparticles, a rounded step appears at the voltages $\pm 3\Delta/e$. Between these voltages, the curve is fit using a BCS density of states in the superconducting probe (dashed line) with a renormalized tunnel conductance (solid line).

7.4.3 Measurement with a normal resistive probe

7.4.3.1 Determination of the *q*-function

For each sample, we have checked that the differential conductance of the tunnel junction when the wire is at equilibrium ($U = 0$) does not depend on magnetic field (see Figure 23). The environmental characteristics were deduced from the fit of this signal to Coulomb blockade (see Chapter 2). The parameters for the effective environment impedances are summarized in Table 6.

Sample	R_p (kΩ)	T (mK)	C (f F)	R_T (kΩ)	Δ (μeV)	W_{el}
Al5	2.06	40	0.92	185	–	–
Ag_{6N}I20	1.65	35	0.9	102	237	0.89
Ag_{5N}IV20	1.34	31	0.8	167	240	0.88
Au5	1.68	48	0.95	704	245	0.88
Cu5	1.08	68	0.8	43	240	0.89

Table 6: Environmental characteristics of the tunnel junction in the measured samples. The resistance of the probe electrode is written R_p, its electronic temperature T, the capacitance of the tunnel junction C, its tunnel resistance R_T, and the gap and the resulting reduction factor when the probe electrode is in its superconducting state Δ and W.

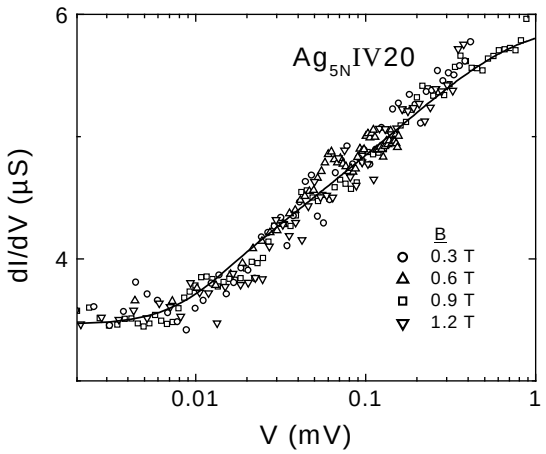

Figure 23: Symbols: Measured Coulomb blockade signal, for the sample Ag_{5N}IV20 when the wire is at equilibrium for different applied magnetic fields. Solid line: Fit of the data using Coulomb blockade theory and the parameters summarized in Table 6. The magnetic field has no visible effect.

7.4.3.2 Modelisation of the environment

The critical point in the calibration process of the junction and the environment characteristic is the choice of a model for the environment. As explained in Chapter 2, we just model the environment as the parallel combination of the probe electrode resistance and the

junction capacitance. To check the validity of this model, we have measured the Coulomb blockade singularity when the wire is at equilibrium as a function of the refrigerator temperature T_{fridge}. The results are shown on Figure 24 for a tunnel junction of resistance $R_T = 167\ \text{k}\Omega$ between a 5-µm long silver wire and a resistive probe electrode $R_p = 0.67\ \text{k}\Omega$ (sample $\text{Ag}_{5\text{N}}$III5 in appendix 3). The data are perfectly fit just by changing the temperature of the probe electrode T_{fit}. The fit temperature T_{fit} differs from the fridge temperature T_{fridge} only at the lowest temperature. This is attributed to spurious electromagnetic noise.

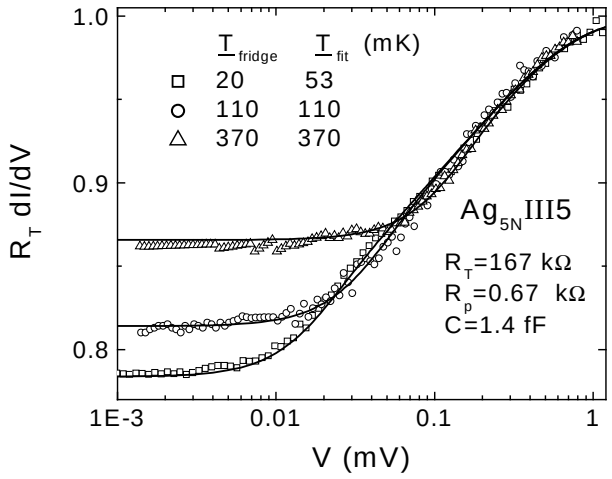

Figure 24: Symbols: Normalized differential conductance of a tunnel junction between a normal wire at equilibrium and a normal resistive probe electrode as a function of the fridge temperature. Solid lines: Fit using the Coulomb blockade theory. The environment of the junction is modeled by the parallel combination of its capacitance C and of the resistance of the probe electrode R_p. When the refrigerator temperature T_{fridge} increases the electronic temperatures in the wire and in the probe electrode T_{fit} follow. At the lowest temperature, the discrepancy between T_{fridge} and T_{fit} is attributed to spurious electromagnetic noise.

7.4.3.3 Heating of the probe electrode

The electronic temperature in the probe electrode enters in the calculation of the Coulomb blockade signal, and of the function q (see Chapter 2). When electrons of the probe electrode in its resistive state are heated up, coupling to the phonons is not efficient to thermalize them at the refrigerator temperature because this process is scarce and the probe electrode volume small. Assuming that the electrons in the reservoir at the end of the probe

electrode are at the fridge temperature T_0 (see Figure 25), one obtains the electronic temperature at the position of the tunnel junction by solving a heat equation with a source term:

$$T(V) = \sqrt{T_0^2 + \frac{R_p}{R_T} V^2 / \mathbb{L}}\,, \tag{36}$$

where $\mathbb{L}$ is the Lorenz number, R_p the probe electrode resistance and R_T the tunnel resistance.

For example, for $Ag_{6N}I20$, where $R_p = 1.65\ \text{k}\Omega$ and $R_T = 102\ \text{k}\Omega$, the temperature T at the junction position dependence on the applied voltage V is shown on Figure 25.

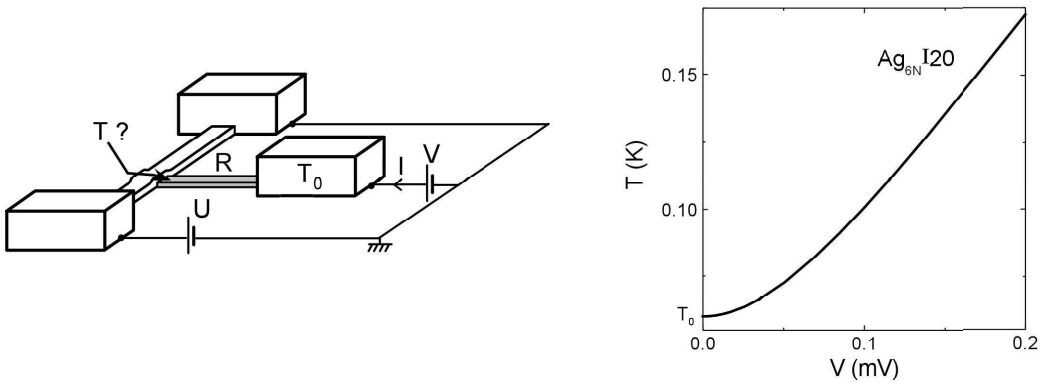

Figure 25: Left: Schematic of the circuit measurement. Electrons of the probe electrode are heated up by the measurement current only by their diffusive flow to the contact at T_0. Right: Electronic temperature T in the probe electrode at the junction position dependence on the voltage V for the Sample $Ag_{6N}I20$ where $R_p = 1.65\,\text{k}\Omega$ and $R_T = 103\ \text{k}\Omega$.

When the wire is biased out-of-equilibrium by an applied voltage U, the energy distribution function presents a double step and the differential conductance dI/dV of the tunnel junction two dips at $V = -U/2$ and $V = U/2$ (see Figure 2 and Figure 7). At these voltages, dI/dV is very sharp and is therefore very sensitive to the temperature. For $U = 0.1,\ 0.2$ and 0.3 mV, the respective electronic temperatures in the probe electrode at the position of the tunnel junction are $T = 75, 100$ and 135 mK. We have then calculated the function q using these different temperatures and convolved them with the measured distribution functions at $B = 0$. The

results are shown on Figure 26 together with the measured differential conductance at $B = 0.6$ T. The discrepancies observed on Figure 12 are suppressed, proving that electronic heating of the probe electrode was responsible for the differences.

For the other samples, in which dI/dV is not as sharp, the heating of the probe electrode has a negligible effect.

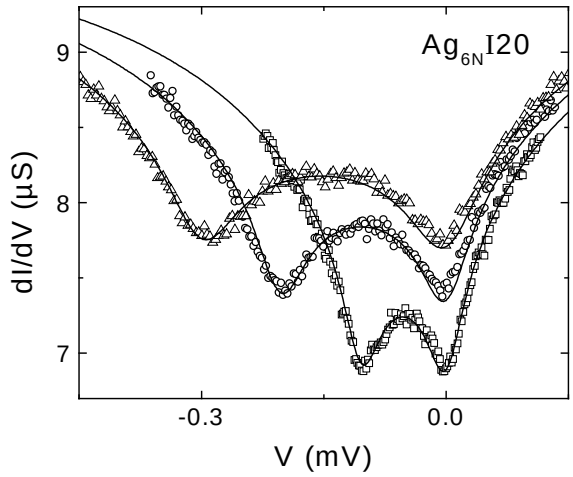

Figure 26: Symbols: Measured differential conductance in $Ag_{6N}I20$ at $B = 0.6$ T for applied voltages $U = 0.1$, 0.2 and 0.3 mV. Solid line: Calculated differential conductance by convolving the measured distribution function at $B = 0$ with a function q calculated with an electronic temperature T dependent on U and the parameters R_p, C deduced from the fit of the Coulomb blockade signal at equilibrium. The electronic temperatures were respectively $T = 75, 100$ and 135 mK for $U = 0.1,\ 0.2$ and 0.3 mV. In contrast to Figure 12, the experimental and calculated curves coincide for all applied voltages.

Appendix 1: Derivation of the kernel K(ε) of Coulomb electron-electron interaction from fluctuation-dissipation theorem

In the following, another derivation of the Kernel of interactions between electrons is developed using the fluctuation-dissipation theorem. A mesoscopic wire is treated as a system of fermions weakly coupled to a reservoir of bosons (the electrodynamics modes corresponding to currents and voltages propagating along the wire).

A fermionic system S and a bosonic reservoir R weakly coupled by a local interaction in space are considered. The Hamiltonian of this system in second quantification is then:

$$\begin{aligned} H &= H_s + H_R + H_I \\ H_s &= \sum_l \varepsilon_l \, a_l^+ a_l \\ H_R &= \sum_m \hbar\omega_m \, b_m^+ b_m \\ H_I &= e\int \rho(x) v(x) dx, \\ &= e\int \Psi^+(x)\Psi(x) V(x) dx \end{aligned} \tag{37}$$

where $\Psi(x) = \sum_l \Psi_l(x)\, a_l$ and $V(x) = \sum_m V_m(x)\, b_m^+ + V_m^*(x)\, b_m$.

The fermionic operators a_l^+ and a_l respectively creates and annihilates an electron in a given state *l*. The energy of this state is ε_l. The bosonic operators b_m^+ and b_m respectively creates and annihilates a photon in a given state *m*. The energy of this state is $\hbar\omega_m$. The field $V(x)$ is the local voltage in the fermionic system with a gauge such that $\vec{A} = 0$.

By application of the Fermi Golden Rule, the rate at which fermionic states *l* and *p*, respectively occupied and empty decays into *l* and *p* being empty and occupied while the bosonic environment decays from state *R* to *Q* is:

$$\begin{aligned} \Gamma_{l\bar{p},R\to\bar{l}p,Q} &= \frac{2\pi}{\hbar} e^2 \sum_R \sum_Q p_R \left| \int \Psi_l(x)\Psi_p^*(x) \left\langle R \middle| V(x) \middle| Q \right\rangle dx \right|^2 \delta(\varepsilon_{lp} + E_R - E_Q) \\ &= \frac{e^2}{\hbar^2} \int dx dy dt \left\langle V(x,t)V(y,0) \right\rangle e^{-i\varepsilon_{lp}\frac{t}{\hbar}} \Psi_l(x)\Psi_p^*(x)\Psi_l^*(y)\Psi_p(y), \end{aligned} \tag{38}$$

where p_R is the probability for the environment to be in the state R, l denotes an occupied state, $\bar{l}$ the same state but empty, and $\varepsilon_{lp} = \varepsilon_l - \varepsilon_p$.

Since the fermionic states taken into account are near the Fermi surface, $\Psi_l(x)\Psi_p^*(x)\Psi_l^*(y)\Psi_p(y)$ only depends on ε_{lp} and x, y and is called $M\left(x,y,\varepsilon_{lp}\right)$. The average quantity $\left\langle V(x,t)V(y,0)\right\rangle$ only depends on $x-y$ and t and is called $S_V\left(x-y,t\right)$. Then,

$$\Gamma_{\bar{p},R\to\bar{p},Q}=\frac{e^2}{\hbar^2}\Omega\int\frac{dk}{2\pi}\,S_V(-k,\frac{\varepsilon_{lp}}{\hbar})\,M(k,\varepsilon_{lp}). \tag{39}$$

The rate per unit of volume at which electrons lose the energy $\hbar\omega$, taking into account the spin conservation between respectively states p and $\bar{p}$, and l and $\bar{l}$, is:

$$p(\omega)=\frac{N(E_F)^2e^2}{4\pi\hbar}\int dk\;S_V(-k,\omega)\;M(k,\hbar\omega)\int dE\,f(E)\;(1-f(E-\hbar\omega)), \tag{40}$$

where $N\left(E_F\right)$ is the number of states per unit of energy at the Fermi level.

When a stationary voltage wave $V(x,t)=V_0\;\cos(\omega_0 t)\;\cos(k_0 x)$ is applied, its spectral density is $V_0^2\pi^2\;[\delta(k-k_0)+\delta(k+k_0)][\delta(\omega-\omega_0)+\delta(\omega+\omega_0)]$. The electromagnetic field associated to this voltage is $E\left(x,t\right)=k_0V_0\cos\left(\omega_0t\right)\sin\left(k_0x\right)$ and the current density in a complex notation: $j\left(x,t\right)=\sigma E\left(x,t\right)/\left(1+ik_0^2D/\omega_0\right)$ where σ is the dc-conductivity. The total absorbed power by electrons in the wire of section S_e per unit length is then:

$$P=\left\langle\frac{1}{2}\mathrm{Re}\left(j^*.\,E\right)\right\rangle=\frac{\sigma S_e\omega_0^2}{\omega_0^2+D^2k_0^4}\frac{k_0^2V_0^2}{4}, \tag{41}$$

where $\langle\ \rangle$ denotes the average on x.

By identification with $P=[-p(\omega_0)+p(-\omega_0)]\,\hbar\omega_0 S$, knowing that:

$$\int dE\,f(E)\;(1-f(E-\hbar\omega_0))=\frac{\hbar\omega_0}{e^{\beta\hbar\omega_0}-1},$$

one finds:

$$M(k,\omega)=\frac{\nu_F}{2\hbar N(E_F)^2\pi}\;\frac{Dk^2}{D^2k^4+\omega^2}, \tag{42}$$

where $\nu_F=N(E_F)/\Omega$ is the density of states per unit of energy and of volume at the Fermi level. This result for $M\left(k,\omega\right)$ is also available for $M\left(\boldsymbol{k},\omega\right)$ and was used in this chapter for the precedent derivation of the Kernel of electron-electron interaction.

If only Johnson-Nyquist noise is assumed to take place in the wire, by the fluctuation-

dissipation theorem, one finds that:

$$S_V(k,\omega) = \frac{2\rho}{S_e k^2} \; \frac{\hbar\omega}{1-e^{-\beta\hbar\omega}} = \frac{2\rho}{S_e k^2} \; \int dE' \, f(E') \; (1-f(E'+\hbar\omega)). \tag{43}$$

Then, by substitution in (40) and by identification with:

$$p(\omega) = \hbar v_F \mathrm{K}(\omega) \int dE' \, f(E') \; (1-f(E'+\hbar\omega)) \int dE \, f(E) \; (1-f(E-\hbar\omega)), \tag{44}$$

one obtains

$$\mathrm{K}(\varepsilon) = (\sqrt{2D} \; \pi \; \hbar^{3/2} \; v_F \; S_e)^{-1} \; \varepsilon^{-3/2}. \tag{45}$$

This calculation gives the same results as our first derivation. When comparing to the experiment, we nevertheless use a factor twice as large that corresponds to the result of Kamenev and Andreev [14].

Appendix 2: Article reporting measurements on the silver wires

We reproduce here the paper published in Phys. Rev. Lett. **90**, 076806 (2003).

Magnetic-Field-Dependent Quasiparticle Energy Relaxation in Mesoscopic Wires

A. Anthore, F. Pierre, H. Pothier, and D. Esteve

Service de Physique de l'Etat Condensé, Direction des Sciences de la Matière, CEA-Saclay, 91191 Gif-sur-Yvette, France

(Received 5 August 2002; published 20 February 2003)

In order to find out if magnetic impurities can mediate interactions between quasiparticles in metals, we have measured the effect of a magnetic field B on the energy distribution function $f(E)$ of quasiparticles in two silver wires driven out of equilibrium by a bias voltage U. In a sample showing sharp distributions at $B = 0$, no magnetic field effect is found, whereas, in the other sample, rounded distributions at low magnetic field get sharper as B is increased, with a characteristic field proportional to U. Comparison is made with recent calculations of the effect of magnetic-impurities-mediated interactions taking into account Kondo physics.

DOI: 10.1103/PhysRevLett.90.076806 PACS numbers: 73.23.–b, 71.10.Ay, 72.10.–d, 72.15.Qm

The understanding of the phenomena which, at low temperature, limit the extent of quantum coherence in electronic transport and allow the quasiparticles to exchange energy is presently an important issue in mesoscopic physics. There is indeed a discrepancy between the theory [1], which predicts that Coulomb interactions provide the dominant mechanism for decoherence and for energy exchange, and measurements of the coherence time [2,3] or of energy exchange rates [4–7] in numerous metallic samples. This discrepancy has been attributed either to a flaw in the theory [2], or to the presence in these samples of other mechanisms involving the scattering of electrons by undetected two-level systems or magnetic impurities. It has been indeed recently predicted that even a minute concentration of such scatterers would result in sizable energy exchange if the Kondo effect occurs [8–10]. Whereas the limitation of quantum coherence by the Kondo effect is widely known [11], its efficiency for mediating energy exchange between quasiparticles had not been anticipated. In the case of magnetic impurities, a significant weakening of this effective electron-electron interaction is furthermore predicted when a large magnetic field is applied [12]. In order to test these new predictions and more generally to understand inelastic processes in mesoscopic conductors, we have investigated the magnetic field dependence of the energy exchange rate in mesoscopic wires.

The samples are wires connected to reservoirs biased at potentials 0 and U (see Fig. 1). The energy distribution function in the middle of the wire, $f(E)$, depends on the ratio of the typical interaction time τ_{int} and the diffusion time of quasiparticles $\tau_D = L^2/D$. If $\tau_{\text{int}} \gg \tau_D$, interactions can be neglected and $f(E)$ is the average of the Fermi functions in both reservoirs, which have electrochemical potentials shifted by eU. In the experimental situation where $k_B T \ll eU$, $f(E)$ is then a two-step function. In the opposite limit $\tau_{\text{int}} \ll \tau_D$, local equilibrium is achieved at each coordinate along the wire, and $f(E)$ is a Fermi function at a temperature given by the balance between Joule heating and electronic heat conductivity to the reservoirs: This is the "hot-electron" regime [13]. The intermediate regime is of interest for experiments because the precise shape of $f(E)$ and its dependence on U are characteristic of the interaction rate and of its energy dependence [4].

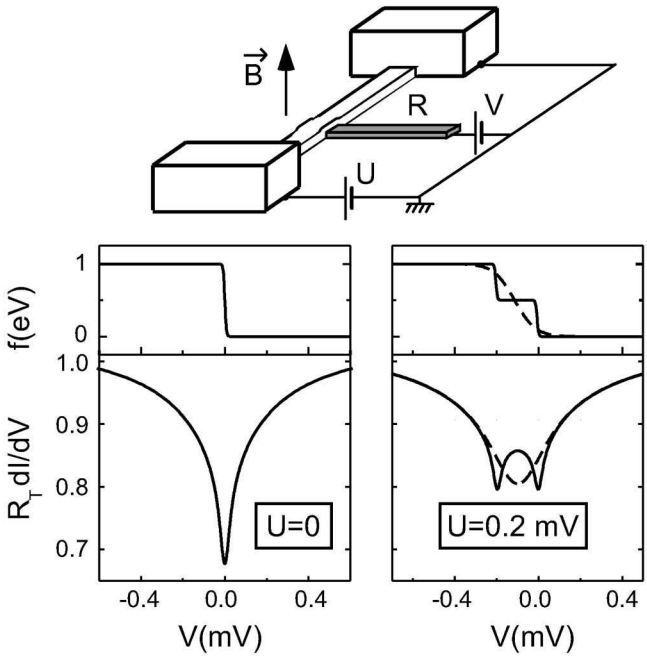

FIG. 1. Top: Layout of the experiment: A wire is connected to two large electrodes biased at potentials 0 and U. A resistive probe electrode (in grey) forms a tunnel junction with the wire. At equilibrium ($U = 0$), the differential conductance $dI/dV(V)$ of this junction displays a dip at zero bias, due to Coulomb blockade of tunneling (left). When the quasiparticles of the wire are driven out of equilibrium by a finite voltage U (right), their energy distribution function $f(E)$ depends on the interaction rate between quasiparticles. In the absence of interactions, $f(E)$ is a two-step function and $dI/dV(V)$ presents two dips (solid lines). With strong interactions, $f(E)$ is rounded, and $dI/dV(V)$ presents a broad dip (dashed lines).

 © 2003 The American Physical Society

At zero magnetic field, the distribution function $f(E)$ can be inferred from the differential conductance $dI/dV(V)$ of a tunnel junction between the central part of the wire and a superconducting (aluminum) probe electrode biased at potential V [4]. In magnetic fields larger than the critical field $B_c \sim 0.1$ T of the superconducting electrode, another method is required. Here, we have taken advantage of the nonlinearity of the current-voltage characteristic of a tunnel junction placed in series with a resistance R. When both electrodes of the junction are in the normal state and at thermal equilibrium, the differential conductance $dI/dV(V)$ displays a dip at $V = 0$ (see Fig. 1), due to the Coulomb blockade of tunneling [14]. Assuming that the two electrodes have different distribution functions f and f_{ref}, the differential conductance reads

$$\frac{dI}{dV}(V) = \frac{1}{R_{\mathrm{T}}}\int dE f(E)\int d\varepsilon P(\varepsilon) \times \frac{\partial}{\partial E}[f_{\mathrm{ref}}(E + eV + \varepsilon) - f_{\mathrm{ref}}(E + eV - \varepsilon)], \quad (1)$$

where R_{T} is the tunnel resistance of the junction, and $P(\varepsilon) = \int \frac{dt}{2\pi\hbar} e^{J(t)+i\varepsilon t/\hbar}$ the probability for an electron to tunnel through the barrier while releasing to the environment an energy ε, $J(t) = \int \frac{d\omega}{\omega}(\{2\mathrm{Re}[Z(\omega)]\}/R_K)[(e^{-i\omega t} - 1)/(1 - e^{-\hbar\omega/k_B T})]$ with $Z(\omega) = 1/(1/R + jC\omega)$, C the junction capacitance, $R_K = h/e^2 \approx 25.8\ \mathrm{k}\Omega$ the resistance quantum, and T the environment temperature. In the case where the distribution function $f(E)$ presents two steps, as in Fig. 1, and f_{ref} is a Fermi function at temperature T, one obtains, by linearity, two dips in $dI/dV(V)$ at $V = 0$ and $V = -U$. In contrast, in the hot electron regime, $dI/dV(V)$ displays a broad dip centered at $V = -U/2$ (see Fig. 1). In the experiments, a large series impedance at the relevant frequencies (up to about 50 GHz) was obtained by designing the probe electrode as a long, narrow, and thin aluminum electrode ($25\ \mu\mathrm{m} \times 150\ \mathrm{nm} \times 12\ \mathrm{nm}$), which presents a resistance $R \sim 1.5\ \mathrm{k}\Omega$ in the normal state.

We present here the results obtained on two silver samples in which the distribution functions found at $B = 0$ were extremely different. The samples were obtained from nominally five-nines purity (99.999%, sample No. 1) and six-nines purity (99.9999%, sample No. 2) source material. For both wires, the length and cross-section area are $L = 20\ \mu\mathrm{m}$, $S = 100\ \mathrm{nm} \times 48\ \mathrm{nm}$. The diffusion constants $D = 196$ and $215\ \mathrm{cm}^2/\mathrm{s}$, respectively, were deduced from the low temperature resistance. The tunnel resistances R_{T} (167 and 102 kΩ) and the capacitances C (0.8 and 0.9 fF) of the junctions, as well as the environment resistances R (1.34 and 1.65 kΩ), were obtained from fits with Eq. (1) of $dI/dV(V)$ measured at $B = 0.3$ T and $U = 0$. We have checked that these curves do not change with B when $B > B_c$.

At low magnetic field and low temperature, the probe electrode is superconducting. Its impedance is purely imaginary at frequencies lower than $2\Delta/h$ [15]. It results that for $eV \in [-3\Delta + U, 3\Delta]$ Coulomb blockade leads only to a reduction of the differential conductance, which is multiplied by a factor $\exp(-\int_0^\infty \frac{d\omega}{\omega}\{2\,\mathrm{Re}[Z(\omega)]/R_K\}) \sim 0.9$. Numerical deconvolution of $dI/dV(V)$ is therefore possible, and the distribution functions obtained at $U = 0.15$ mV are presented in the top of Fig. 2 for both samples. Whereas $f(E)$ is close to a double-step function in sample No. 2, it is much more rounded in sample No. 1, indicating that the energy exchange rate is much larger in the latter, since the diffusion times are very similar ($\tau_D = L^2/D \simeq 20$ ns). In the bottom of Fig. 2, we plot the calculated $R_T dI/dV(V)$ using formula (1) with $f(E)$ the distribution function measured at $B = 0$ (dashed curves), and present the measured curves for $B = 0.3$ T and $B = 1.2$ T (symbols) [16]. In sample No. 2, the magnetic field has no visible effect. Note, however, that the distribution functions are so close to a double step that the experiment is not sensitive enough to detect a possible slight reduction of the energy exchange rate with B. In contrast, in sample No. 1, the rounded dip at zero field is replaced at 1.2 T by a double dip, showing that the energy exchange rate has been reduced. Figure 3 shows the evolution of $dI/dV(V)$ with magnetic field, from 0.3 to 1.5 T by steps of 0.3 T, for $U = 0.1$, 0.2, and 0.3 mV. A similar behavior is observed at all values of U: The low-field broad conductance dip at $B = 0.3$ T tends to be

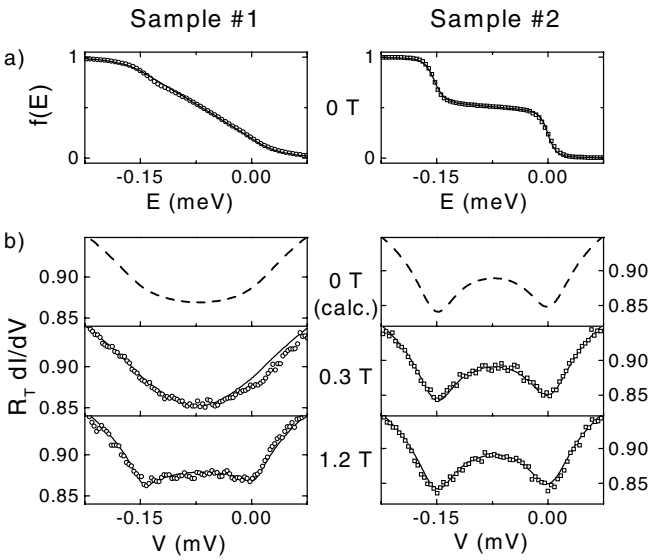

FIG. 2. (a) Symbols: Distribution functions $f(E)$ at $U = 0.15$ mV and zero magnetic field in samples No. 1 and No. 2, obtained by deconvolution of $dI/dV(V)$ with the probe electrode in the superconducting state. Solid lines: Fits with theory including the effect of Kondo impurities (see text). (b) Dashed line: Calculated Coulomb blockade signal $dI/dV(V)$ using the measured $f(E)$ at $B = 0$. Symbols: Measured $dI/dV(V)$ at $U = 0.15$ mV, with $B = 0.3$ and 1.2 T, the probe electrode being in the resistive state. Solid line: Fits with theory.

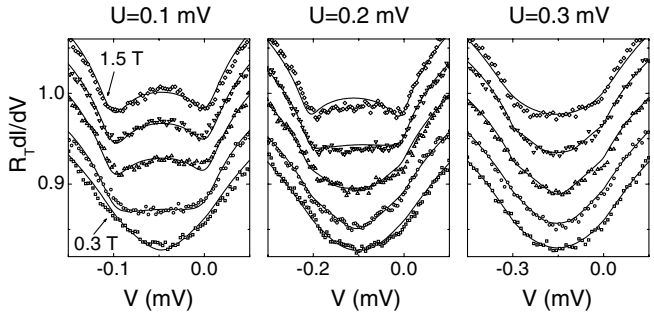

FIG. 3. Magnetic field effect in sample No. 1: differential conductance $dI/dV(V)$ at $U = 0.1$, 0.2 and 0.3 mV, for B ranging (from bottom to top) from 0.3 to 1.5 T by steps of 0.3 T. Successive curves have been vertically offset by steps of 0.033, for clarity.

replaced at large fields by a double-dip structure. In particular, the crossover field at which $dI/dV(V)$ is nearly constant over a broad voltage range is 0.6 T at $U = 0.1$ mV, 0.9 T at $U = 0.15$ mV (not shown), 1.2 T at $U = 0.2$mV, and 1.5 T at $U = 0.25$ mV (not shown), hence, presenting a linear increase with U. The comparison of the raw data on sample No. 1 and sample No. 2 in Fig. 2 already allows one to conclude that sample No. 1 presents an extra interaction which can be strongly reduced by applying a magnetic field.

We now compare the experimental data with theoretical predictions. The distribution function is calculated by solving the stationary Boltzmann equation in the diffusive regime [18,19]:

$$\frac{1}{\tau_D}\frac{\partial^2 f(x,E)}{\partial x^2} = -\mathcal{I}^{\text{in}}_{\text{coll}}(x,E,\{f\}) + \mathcal{I}^{\text{out}}_{\text{coll}}(x,E,\{f\}), \quad (2)$$

where $\mathcal{I}^{\text{in}}_{\text{coll}}$ and $\mathcal{I}^{\text{out}}_{\text{coll}}$ are the rates at which quasiparticles are scattered in and out of a state at energy E by inelastic processes. Assuming that the dominant inelastic process is a two-quasiparticle interaction which is local on the scale of variations of the distribution function,

$$\mathcal{I}^{\text{in}}_{\text{coll}} = \int d\varepsilon dE' K(\varepsilon) f^x_{E+\varepsilon}(1 - f^x_E) f^x_{E'}(1 - f^x_{E'-\varepsilon}), \quad (3)$$

where the shorthand f^x_E stands for $f(x,E)$. The out-collision term $\mathcal{I}^{\text{out}}_{\text{coll}}$ has a similar form. The kernel function $K(\varepsilon)$ is proportional to the averaged squared interaction between two quasiparticles exchanging an energy ε. Coulomb interactions lead, in diffusive wires, to $K(\varepsilon) = \kappa/\varepsilon^{3/2}$ [1], where $\kappa = (\pi\sqrt{D/2}\hbar^{3/2}\nu_F S)^{-1}$ with ν_F the density of states at the Fermi level [20]. The $B = 0$ data for sample No. 2 can be well fit using this term with $\kappa = 0.12\ \text{ns}^{-1}\,\text{meV}^{-1/2}$, of the same order of magnitude as the theoretical value $0.07\ \text{ns}^{-1}\,\text{meV}^{-1/2}$ [21], and a term of lesser importance describing phonon emission [22]. The $B = 0$ data for sample No. 1 can be fit similarly, with $\kappa = 2.4\ \text{ns}^{-1}\,\text{meV}^{-1/2}$; however, the reduction of the energy exchange rate with B indicates that an extra process is present at $B = 0$. We have in the following fixed κ to the best fit value obtained for the large field, low U data, where the B dependent interaction has essentially vanished: $\kappa = 0.5\ \text{ns}^{-1}\,\text{meV}^{-1/2}$ [21]. The remaining part of the energy exchange rate was fit with the theory of Göppert *et al.* [12,23], which accounts for the effective interaction in the presence of a concentration c of spin-$\frac{1}{2}$ impurities, with Kondo temperature T_K, gyromagnetic factor g, and coupling constant J between quasiparticles and magnetic impurities. The Kondo effect is included in this calculation, under the assumption that the distribution functions are not too sharp, leading to a renormalization of J depending on the distribution function itself. The corresponding inelastic integral can also be written in the form of Eq. (3), but with a $K(\varepsilon)$ function depending on the energies E and E' and on f. At zero magnetic field, the effect of this term on $f(E)$ is similar to that of a phenomenological kernel $K(\varepsilon) \propto 1/\varepsilon^2$ as found in [4]. For compatibility with phase-coherence time measurements (see below), the Kondo temperature was fixed at $T_K = 40$ mK, which is the Kondo temperature of Mn in Ag. As shown by solid lines in Figs. 2 and 3, the data can be accurately reproduced using $c = 17$ ppm, $g = 2.9$, and $\nu J = 0.08$ [24]. Note, however, that according to material analysis of the silver batch used to fabricate sample No. 1, no magnetic impurity was present in the source at the level of 1 ppm. Since in some samples made out of the same batch the intensity of the energy exchange rate measured at $B = 0$ was found to be up to 4 times smaller, pollution of the sample during fabrication might, at least partly, explain this large impurity concentration.

The impurity concentration deduced from the fits of $f(E)$ must be further compared with the one obtained from the analysis of measurements of the phase-coherence time in long wires fabricated previously with the same source materials. We have extracted the phase-coherence time τ_φ from the magnetoresistance of wires much longer than the phase-coherence length, using the weak localization theory. In samples made of 6N purity Ag, $\tau_\varphi(T) = A^{-1}T^{-2/3}$ from 1 K down to 40 mK, with $A = 0.36\ \text{ns}^{-1}\,\text{K}^{-2/3}$, in reasonable agreement with the theory of Coulomb interactions in disordered wires ($A_{\text{theory}} = 0.31\ \text{ns}^{-1}\,\text{K}^{-2/3}$). At $T = 40$ mK, $\tau_\varphi = 21$ ns. In samples made of 5N silver, $\tau_\varphi(T)$ does not vary between $T = 200$ mK and 40 mK, where we find $\tau_\varphi = 3.5$ ns. This behavior can be attributed to the presence of magnetic impurities, with concentration c, spin s, and Kondo temperature T_K, which lead to a spin-flip rate described by [11,25] $\gamma_{sf}(T) = (c/\pi\hbar\nu)\pi^2 s(s+1)/[\pi^2 s(s+1) + \ln^2(T/T_K)]$. The resulting phase-coherence time $\tau_\varphi(T) = 1/[AT^{2/3} + \gamma_{sf}(T)]$ shows very little variation between 40 and 200 mK and describes precisely the experimental data for $c = 0.13$ ppm, $T_K = 40$ mK, $s = 1/2$ and $A = A_{\text{theory}} = 0.4\ \text{ns}^{-1}\,\text{K}^{-2/3}$. This value of c, compatible with the nominal source purity, is smaller by 2 orders of magnitude than the value obtained from the fits of energy exchange data on sample No. 1. A similar set of results was also obtained with Cu samples, a

material in which the oxide at the surface of the films was found to cause dephasing at low temperature [26]. Data on energy exchange [17] could also be fit with the theory of Göppert *et al.* [12], using $T_K = 300$ mK, $c = 4.8$ ppm, $g = 2.3$, $\nu J = 0.1$, on top of a Coulombic term with intensity $\kappa = 0.5\ \mathrm{ns}^{-1}\,\mathrm{meV}^{-1/2}$ [23]. This result gives evidence that the anomalous interactions observed in many Cu wires at $B = 0$ [4,7] are also due to magnetic impurities. Here also, measurements of the phase-coherence time [7] are explained by significantly smaller impurity concentrations (~ 0.3 ppm). This repeated discrepancy on the concentrations deduced from the two types of measurements remains an open problem. From an experimental point of view, a more quantitative test of theory could be obtained in samples with added, identified magnetic impurities at a known concentration [27].

In conclusion, we have found that anomalous energy exchange rates between quasiparticles were strongly reduced by the application of a magnetic field. Moreover, the energy and magnetic field dependence of the exchange rate can be accurately accounted for by the presence of a small concentration of Kondo magnetic impurities [12]. It is worthwhile to compare this result with recent measurements on Aharonov-Bohm rings, which show that the small phase-coherence times found at $B = 0$ were increased in a finite magnetic field [28]. All these measurements indicate that the presence of very dilute magnetic impurities is a very plausible candidate to explain both extra dephasing and extra energy exchange observed in many mesoscopic samples.

We acknowledge the technical help of P. Orfila, fruitful discussions and correspondence with G. Göppert, H. Grabert, and N. Birge, and permanent input from M. Devoret, P. Joyez, C. Urbina, and D. Vion.

[1] For a review, see B. L. Altshuler and A. G. Aronov, in *Electron-Electron Interactions in Disordered Systems*, edited by A. L. Efros and M. Pollak (Elsevier, Amsterdam, 1985).
[2] P. Mohanty, E. M. Q. Jariwala, and R. A. Webb, Phys. Rev. Lett. **78**, 3366 (1997).
[3] For a review, see J. J. Lin and J. P. Bird, J. Phys. Condens. Matter **14**, R501 (2002).
[4] H. Pothier *et al.*, Phys. Rev. Lett. **79**, 3490 (1997).
[5] F. Pierre *et al.*, J. Low Temp. Phys. **118**, 437 (2000).
[6] F. Pierre *et al.*, in *Kondo Effect and Dephasing in Low-Dimensional Metallic Systems*, edited by V. Chandrasekhar, C. Van Haesendonck, and A. Zawadowski (Kluwer, Dordrecht, 2001), p. 119.
[7] F. Pierre, Ann. Phys. (Paris) **26**, No. 4 (2001).
[8] A. Kaminski and L. I. Glazman, Phys. Rev. Lett. **86**, 2400 (2001).
[9] G. Göppert and H. Grabert, Phys. Rev. B **64**, 033301 (2001).
[10] J. Kroha and A. Zawadowski, Phys. Rev. Lett. **88**, 176803 (2002).
[11] C. Van Haesendonck, J. Vranken, and Y. Bruynseraede, Phys. Rev. Lett. **58**, 1968 (1987).
[12] G. Göppert *et al.*, Phys. Rev. B **66**, 195328 (2002).
[13] A. H. Steinbach, J. M. Martinis, and M. H. Devoret, Phys. Rev. Lett. **76**, 3806 (1996).
[14] For a review, see G.-L. Ingold and Yu. Nazarov, in *Single Charge Tunneling*, edited by H. Grabert and M. H. Devoret (Plenum, New York, 1992).
[15] M. Tinkham, in *Introduction to Superconductivity* (McGraw-Hill, New York, 1985), Sect. 2-10.5.
[16] Because the signal to noise ratio is not large enough, numerical deconvolution of the $dI/dV(V)$ curves proved to be unreliable. In particular, the preliminary $f(E)$ curves in [17] and in [12] were artificially rounded. We prefer to present here raw data.
[17] A. Anthore *et al.*, in *Electronic Correlations: From Meso- to Nano-Physics*, edited by T. Martin, G. Montambaux, and J. Trân Thanh Vân (EDP Sciences, Les Ulis, 2001).
[18] V. I. Kozub and A. M. Rudin, Phys. Rev. B **52**, 7853 (1995).
[19] K. E. Nagaev, Phys. Lett. A **169**, 103 (1992); Phys. Rev. B **52**, 4740 (1995).
[20] A. Kamenev and A. Andreev, Phys. Rev. B **60**, 2218 (1999).
[21] In other experiments with silver wires [5], the fit value of κ was found to be between 3 and 10 times the theoretical one [7]. This scatter in the intensity of the interaction is presently not understood.
[22] F. Pierre *et al.*, Phys. Rev. Lett. **86**, 1078 (2001). The amplitude of the electron-phonon interactions is set to a value deduced from weak localization data: $\kappa_{ph} = 8\ \mathrm{ns}^{-1}\,\mathrm{meV}^{-3}$. When taking this term into account, the data of [5] are well fit by Coulomb interactions (see [7]). A slight heating of the environment with U was also taken into account in the fits.
[23] In Ref. [12], the agreement with experiment was poor for two reasons: First, the deconvolved data are artificially rounded; second, the effect of usual Coulombic interactions have not been taken into account in the calculation.
[24] The $dI/dV(V)$ are slightly asymmetric because the measuring probe is out of the center of the wire by $0.01L$. Note that the increase of the interaction rate at intermediate magnetic fields [17], when the Zeeman splitting of the impurity states is smaller than eU, is not visible because $f(E)$ is already close to a Fermi distribution at $B = 0$. This experiment is much more sensitive to the decrease of the exchange rate, which leads to a sharper structure in $f(E)$.
[25] M. B. Maple, *Magnetism*, edited by H. Suhl (Academic, New York, 1973), Vol. 5.
[26] J. Vranken, C. Van Haesendonck, and Y. Bruynseraede, Phys. Rev. B **37**, 8502 (1988).
[27] In practice, we have found that tunnel junctions with a silver electrode evolve, at room temperature, to an open circuit within a few hours, hence forbidding implantation of magnetic impurities.
[28] F. Pierre and N. O. Birge, Phys. Rev. Lett. **89**, 206804 (2002).

Appendix 3: Measurements on other silver wires

During this thesis, we have measured other silver samples made of 3 different sources (5N, 6N and 6N'). The two samples presented in the main body of this chapter were obtained from the source 5N and 6N.

The electrical and geometrical characteristics of the other samples are summarized in Table 7.

Sample	Source	$L\,(\mu m)$	$w\ (nm)$	$t\ (nm)$	$R\ (\Omega)$	$D\ (cm^2\ s^{-1})$	$\tau_D\ (ns)$
$Ag_{5N}I5$	Ag5N	5.45	117	45	17	230	1.3
$Ag_{5N}II5$	Ag5N	5.15	101	45	24	178	1.5
$Ag_{5N}III5$	Ag5N	5.27	120	45	20	184	1.5
$Ag_{6N'}II10$	Ag6N'	9.55	124	45	30.7	210	4.3
$Ag_{6N'}III40$	Ag6N'	38.4	185	45	–	~ 200	~ 80

Table 7: Geometrical and electrical characteristics of the measured samples. The length is L, the width w, the thickness t, the wire resistance R, the diffusion coefficient D, and the diffusion time from one end to the other τ_D.

To label the samples, we used the notation described in Figure 27. The samples $Ag_{6N'}II10$ and $Ag_{6N'}III40$ were the only ones made using the two-step process (see Chapter 3).

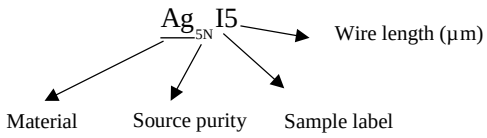

Figure 27: System used to label the samples.

The measured distribution functions and fits to the theory taking into account electron-phonon interaction and electron-electron interaction are presented in Figure 28. The electron-phonon interaction is included with $\kappa_{ph} = 8\,ns^{-1}\,meV^{-3}$ and $T_{ph} = 40\,mK$. The single fit parameter is the intensity of electron-electron interaction $\kappa_{3/2}$. We have measured the interaction in a magnetic field to know whether KIM interaction occurs in these samples.

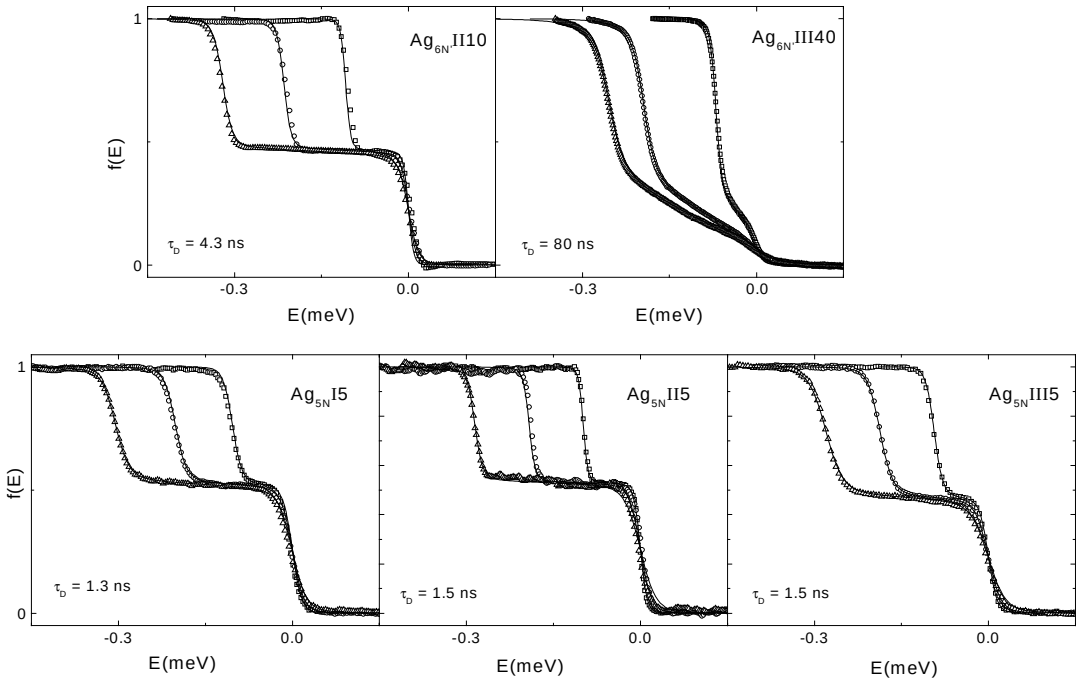

Figure 28: Symbols: Energy distribution functions for $U = 0.1$, 0.2 and 0.3 mV in five silver wires of different diffusion time τ_D. Top: The samples made using a 6N-pure silver source can be fit using the Kernel of Coulomb interaction only (Solid lines: Fits with $\kappa_{3/2} = 0.09$ ns^{-1} meV$^{-1/2}$ for Ag_{6N},II10 and $\kappa_{3/2} = 0.17$ ns^{-1} meV$^{-1/2}$ for Ag_{6N},III40). Bottom: Samples made using a 5N-pure source; The curves are fit using Coulomb interaction kernel (Solid lines: Predictions with $\kappa_{3/2} = 0.6$ ns^{-1} meV$^{-1/2}$, $\kappa_{3/2} = 0.3$ ns^{-1} meV$^{-1/2}$ and $\kappa_{3/2} = 0.6$ ns^{-1} meV$^{-1/2}$ for Ag_{5N}I5, Ag_{5N}II5 and Ag_{5N}III5 respectively).

The results for Ag_{6N},II10 and Ag_{5N}I5 are presented on Figure 29. For all the samples, the differential conductance of the tunnel junction does not depend on the magnetic field, and is close to the one inferred from the $B = 0$ measurements (heating effects as described in Section 7.4.3.3 are included). The small effect of B observed at the lowest bias voltage for Ag_{5N}I5 is not significant compared to the measurement precision.

The results for the samples made of the 5N-source are in sharp contrast with the results found for Ag_{5N}IV20: in this sample, energy exchange was dominated by KIM interaction up to large magnetic field, and the fit impurity concentration was 17 ppm. We have checked that in the samples presented in this appendix, we would have been able to detect impurity concentration larger than 2 ppm. These results suggest that the impurities in Ag_{5N}IV20 come from a pollution during the fabrication process.

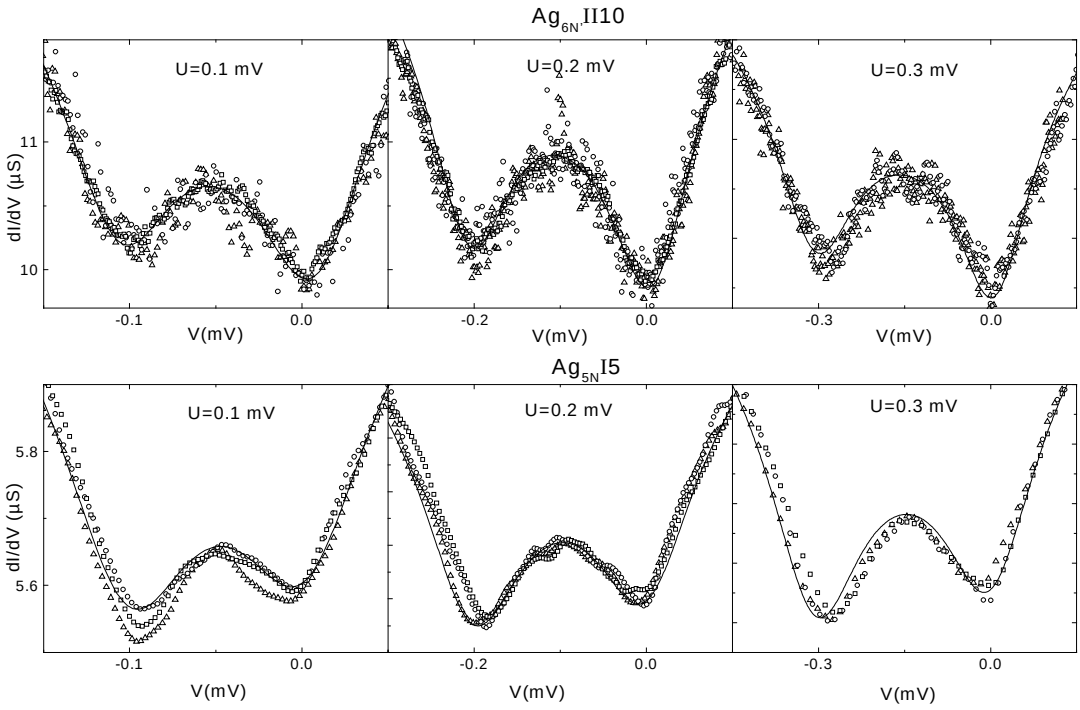

Figure 29: Symbols: Measured Coulomb blockade signal in $Ag_{6N'}II10$ and Ag5βI for $U = 0.1$, 0.2, and 0.3 mV and three different applied magnetic field ($B = 0.45$, 0.7, and 0.9 T for $Ag_{6N'}II10$ and $B = 0.15$, 0.6 and 1.2 T for Ag5βI). The curves do not depend on the magnetic field. KIM interaction are negligible in these samples compared to electron-electron interaction. Solid lines: Calculated Coulomb blockade signal using the samples characteristics and the measured energy distribution function at $B = 0$.

References of chapter 7

[1] F. Pierre, Ann. Phys. (Paris) **26**, No 4 (2001).

[2] A. Kaminski and L. I. Glazman, Phys. Rev. Lett. **86**, 2400 (2001).

[3] H. Pothier, S. Guéron, N.O. Birge, D. Esteve, and M.H. Devoret, Phys. Rev. Lett. **79**, 3490 (1997).

[4] G. Göppert, Y.M. Galperin, B.L. Altshuler, and H. Grabert, Phys. Rev. B **66**, 195328 (2002).

[5] B.L. Altshuler, A.G. Aronov, and D.E. Khmelnitskii, J. Phys. **C15**, 7367 (1982).

[6] M.J.M. de Jong, C.W.J. Beenakker, Physica A **230**, 219 (1996).

[7] D.E. Prober, M.N. Wybourne, M. Kansakar, Phys. Rev. Lett. **75**, 3964 (1995).

[8] A. Steinbach, J. Martinis, M.H. Devoret, Phys. Rev. Lett. **76**, 3806 (1996).

[9] K. E. Nagaev, Phys. Lett. A **169**, 103 (1992), Phys. Rev. B **52**, 4740 (1995).

[10] V. I. Kozub and A. M. Rudin, Phys. Rev. B **52**, 7853 (1995).

[11] S. Guéron, PhD thesis, University of Paris VI (October 1997).

[12] B.L. Altshuler and A.G. Aronov in *Electron-Electron Interactions in Disordered Systems*, edited by A.L. Efros and M. Pollak, (Elsevier Science Publishers B.V., 1985).

[13] B.N. Narozhny, G. Zala and I.L. Aleiner, Phys. Rev. B **65**, 180202 (2002).

[14] A. Kamenev and A. Andreev, Phys. Rev. B **60**, 2218 (1999).

[15] J.M. Ziman, *Principles of the Theory of Solids*, (Cambridge University Press, Cambridge, 1979).

[16] G. Göppert and H. Grabert, Phys. Rev. B **64**, 033301 (2001); G. Göppert, Y. M. Galperin, B. L. Altshuler, and H. Grabert , Phys. Rev. B **66**, 195328 (2002).

[17] H. Ibach, I. Luth, *Solid-State Physics, an Introduction to Principles of Material Science* (Springer, Berlin, 1966). The volumic density of states at the Fermi level ν_F is inferred from the experimental value of the calorific capacity $C = \gamma T$, related to ν_F through the equation $\gamma = \left(\pi^2/3\right) k_B^2 \nu_F$.

[18] A. Anthore, F. Pierre, H. Pothier, D. Esteve and M.H. Devoret, *Electronic Correlations: From Meso- to Nano-physics* edited by T. Martin, G. Montambaux, and J. Trân Thanh Vân (EDP Sciences, les Ulis, 2001), cond-mat/ 0109297.

[19] J. Vranken, C. Van Haesendonck, and Y. Bruynseraede, Phys. Rev. B **37**, 8502 (1988).

[20] H. Bouchiat, private communication.

[21] G. Göppert and H. Grabert, cond-mat/0305341.

[22] A. Abragam and B. Bleaney, *Electron Paramagnetic Resonance of Transition Ions* (Clarendon, Oxford, 1970), p.413.

[23] F. Pierre and N.O. Birge, Phys. Rev. Lett. **89**, 206804 (2002).

[24] N.G. Ptitsina, G.M. Chulkova, K.S. Il'in, A.V. Sergeev, F.S. Pochinkov, E.M. Gershenzon, and M.E. Gershenson, Phys. Rev. B **56**, 10089 (1997).

[25] W.E. Lawrence and A.B. Meador, Phys. Rev. B **18**, 1154 (1998).

[26] P. Santhanam and D.E. Prober, Phys. Rev. B **29**, 3733 (1984).

[27] M. Henny, S. Oberholtzer, C. Strunk, and C. Schönenberger, Phys. Rev. B **59**, 2871 (1999).

[28] M. Tinkham, *Introduction to Superconductivity*, (McGraw-Hill, New York, 1996) Sec. 3.9 and 3.10.

[29] G.L. Ingold and Yu. V. Nazarov in *Single Charge Tunneling*, edited by H. Grabert and M.H. Devoret (Plenum Press, New York, 1992), p 21.

[30] G. Falci, V. Bubanja, and G. Schön, Europhys. Lett. **14**, 109 (1991); Z. Phys. B **85**, 451 (1991).

Chapter 8 Summary: Inelastic scattering mechanisms in diffusive metallic wires

The results of the phase coherence time and energy exchange measurements presented in Chapter 6 and 7 bring evidence that at low temperature, two mechanisms dominate inelastic scattering: Coulomb electron-electron interaction and electron-magnetic impurities (KIM) interaction.

In energy exchange measurements, the presence of magnetic impurities is suggested by an anomalous energy dependence of the interaction at zero-magnetic field, and revealed by the magnetic field dependence of the electron energy distribution functions. In phase coherence time (τ_ϕ) measurements, the signature of magnetic impurities is the "saturation" of τ_ϕ. In the following, we compare quantitatively the theoretical predictions and experimental observations for both inelastic scattering mechanisms in the two types of experiments.

8.1 Coulomb electron-electron interaction

8.1.1 Coulomb electron-electron interaction and energy exchange

The predicted kernel for Coulomb electron-electron interactions is written in diffusive wires [1]:

$$\mathrm{K}(\varepsilon) = \frac{\kappa_{3/2}}{\varepsilon^{3/2}}, \tag{1}$$

with $\kappa_{3/2} = \left(\sqrt{D/2}\ \pi\ \hbar^{3/2}\ \nu_F\ \mathrm{S_e}\right)^{-1}$ [2]. The parameter $\kappa_{3/2}$ was the main fit parameter for the

samples in which energy exchange does not change with magnetic field. For the samples displaying a magnetic field dependence, $\kappa_{3/2}$ was determined by fitting the low-voltage high-magnetic field curves for which the Coulomb interaction dominates, but this determination is less accurate. The experimental values of $\kappa_{3/2}$ are summarized in Table 1 (samples measured during this thesis) and Table 2 (samples measured by F. Pierre [3][1]).

Sample	L (μm)	w (nm)	D ($cm^2\ s^{-1}$)	τ_D (ns)	$\kappa_{3/2}$ ($ns^{-1}\ meV^{-1/2}$)	$\kappa_{3/2}^{th}$ ($ns^{-1}\ meV^{-1/2}$)	B -dependent	c_{imp} (ppm)
Ag_{6N}I20	21.7	100	215	21.9	0.1±0.02	0.08	No	< 0.1
$Ag_{6N'}$II10	9.55	124	210	4.3	0.09±.01	0.06	No	< 0.5
$Ag_{6N'}$III40	38.4	185	200	80	0.17±0.02	0.05	?	?
Ag_{5N}I5	5.45	117	230	1.3	0.6±0.1	0.06	No	< 2
Ag_{5N}II5	5.15	101	178	1.5	0.3±0.05	0.085	No	< 2
Ag_{5N}III5	5.27	120	184	1.5	0.6±0.1	0.07	No	< 2
Ag_{5N}IV20	20.0	108	196	20.4	0.5±0.1	0.075	Yes	17
Al5	5.05	110	64.8	3.9	0.06±0.02	0.06	No	< 0.1
Au5	5.1	85	109	2.5	0.4±0.2	0.12	Yes	8
Cu5	5.0	105	91	2.8	0.4±0.2	0.075	Yes	4.8

Table 1: Summary of sample characteristics and Coulomb interaction intensity $\kappa_{3/2}$ deduced from energy exchange measurements in this thesis. The expected theoretical value $\kappa_{3/2}^{th}$ is also indicated.

Sample	L (μm)	w (nm)	D ($cm^2\ s^{-1}$)	τ (ns)	$\kappa_{3/2}$ ($ns^{-1}\ meV^{-1/2}$)	$\kappa_{3/2}$ ($ns^{-1}\ meV^{-1/2}$)
AgI5	5.0	90	115	2.2	1.2±0.2	0.13
AgII5	5.2	65	150	1.8	0.45±0.2	0.15
AgII10	10.3	65	165	6.4	0.55±0.15	0.15
AgIII20	19.6	160	230	16.7	0.5±0.05	0.05
AgIV20α	19.7	95	205	19.0	0.4±0.05	0.09
AgIV20β	19.9	100	185	21.0	0.4±0.1	0.09

Table 2: Summary of sample characteristics and Coulomb interaction intensity deduced from energy exchange measurements in the silver samples, made from the 6N source (same as Ag_{6N}I20), measured by F. Pierre [3] previous to this work. No test of KIM interaction was performed, but fits with Coulomb interaction only were excellent.

The experimental value $\kappa_{3/2}$ is always found larger (from 1 to 10 times) than the theoretical

[1] The process to measure energy exchange in presence of a magnetic field has only been developed during this thesis work, this is why the B-dependence of energy exchange in samples of Table 2 was not tested.

one $\kappa_{3/2}^{th}$. Variations from sample to sample are not correlated with the sample characteristics: width, length, thickness, or diffusion coefficient. The dispersion of the experimental values of $\kappa_{3/2}$ is illustrated in Figure 1 on which $\kappa_{3/2}$ is plotted as a function of $\kappa_{3/2}^{th}$.

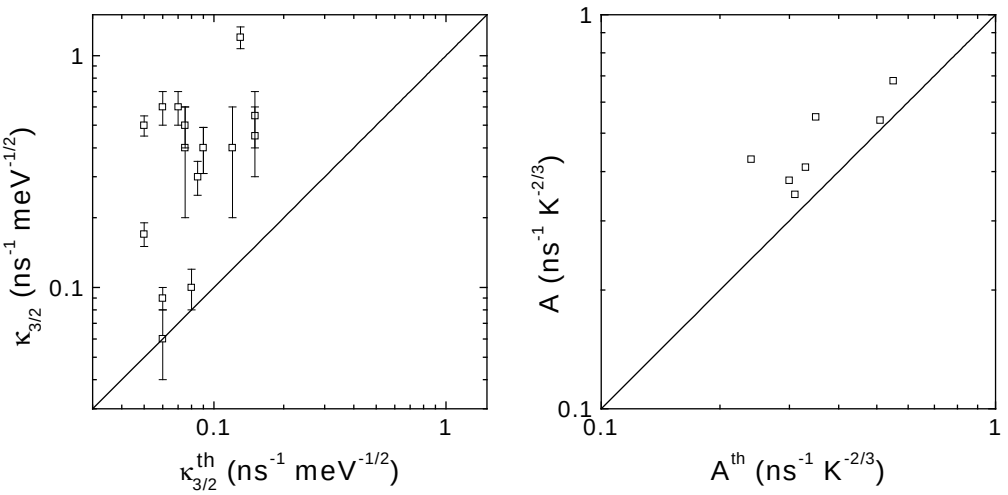

Figure 1: Left Panel: Symbols: Experimental value of the intensity of Coulomb interaction $\kappa_{3/2}$ deduced from fits of energy exchange measurements as a function of the value $\kappa_{3/2}^{th}$ calculated from samples characteristics. Right panel: Symbols: Experimental value of the intensity of Coulomb interaction A deduced from fits of phase coherence time measurements as a function of the value A_{th} calculated from samples characteristics. In both panels, the disagreement with theory is the distance to the solid line of slope 1.

8.1.2 Electron-electron interaction and electronic phase coherence

From phase coherence time measurements, the intensity and energy dependence of Coulomb interactions can also be inferred. It is predicted that the electronic decoherence rate dependence on temperature due to Coulomb interaction is written [4,5]:

$$\tau_{\phi}^{-1} = AT^{2/3}, \tag{2}$$

with $A = \left(2\sqrt{2D}\ \hbar^2 / k_B\ \nu_F\ S_e\right)^{-2/3}$. The dependence in $T^{2/3}$ is consistent with the kernel (1) dependence in $\varepsilon^{-3/2}$. The parameters A and $\kappa_{3/2}$ depend on the same combination of the sample characteristics and one can identify: $A = \left(4/\pi\ \sqrt{\hbar}/\left(k_B \kappa_{3/2}\right)\right)^{-2/3}$.

Measurements of phase coherence time dependence on temperature were performed on samples made from the same sources (Ag6N, Ag6N' , Ag5N, and Cu5N) asthe samples used

to measure energy exchange. In the samples displaying no saturation, the experimental value of A was the only fit parameter at low temperature. In the samples displaying saturation, the Coulomb interaction was never dominant on KIM interaction on the explored temperature range and the determination of A was less accurate, or even not possible. The experimental values are summarized in Table 3 (samples measured at Michigan State University by F. Pierre and N.O. Birge) and Table 4 (samples that we have measured).

The experimental values of A are of the same order of magnitude as the predicted value A_{th}. In silver the difference between the two values is at worse 25 %. The dispersion of A illustrated in Figure 1 is smaller than the dispersion of $\kappa_{3/2}$.

Sample	L (μm)	t (nm)	w (nm)	D ($cm^2\ s^{-1}$)	A ($ns^{-1}\ K^{-2/3}$)	A_{th} ($ns^{-1}\ K^{-2/3}$)	saturation	c_{τ_ϕ} (ppm)
Ag(6N)a	135	45	65	115	0.68	0.55	No	0.009
Ag(6N)b	270	45	100	70	0.54	0.51	No	0.011
Ag(6N)c	400	55	105	185	0.35	0.31	No	0.0024
Ag(5N)a	135	65	108	105	0.41	0.33	Yes	0.17
Ag(5N)b	270	65	90	135	0.35	0.31	Yes	0.13
Cu(5N)a	270	45	110	70	0.55	0.35	Yes	0.15
Cu(5N)b	270	45	100	160	–	0.29	Yes	0.75

Table 3: Summary of sample characteristics and Coulomb interaction intensity deduced from phase coherence time measurements in samples made from our 6N-, and 5N-sources. These measurements were performed by F. Pierre and N.O. Birge at Michigan State University.

Sample	L (μm)	t (nm)	w (nm)	D ($cm^2\ s^{-1}$)	A ($ns^{-1}\ K^{-2/3}$)	A_{th} ($ns^{-1}\ K^{-2/3}$)	saturation	c_{τ_ϕ} (ppm)
Ag(6N')	1790	45	150	139	0.38	0.30	No	0.05
Ag(5N)c	895	45	150	280	0.51	0.24	Yes	0.12

Table 4: Summary of sample characteristics and Coulomb interaction intensity deduced from phase coherence time measurements in silver samples, made from the 6Nb source (same as $Ag_{6N}I20$) and 5N-source (the sample Ag(5N)c was made after the sample of energy exchange measurement $Ag_{5N}IV20$). The measurements were performed at Saclay.

8.1.3 Conclusion on electron-electron interaction

Although theoretical predictions for energy exchange and decoherence rate due to electron-electron Coulomb interactions are performed using the same formalism, experimental

consistency with theoretical predictions differs strongly between the two types of measurements.

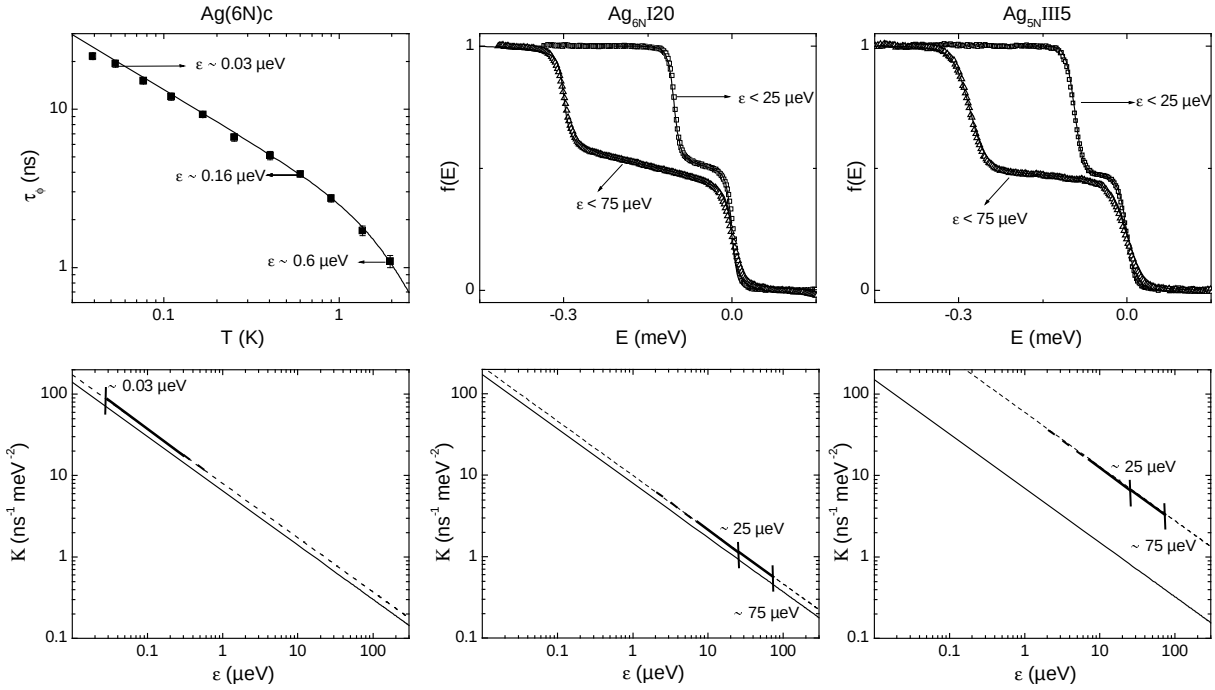

Figure 2: Scale of energies probed in phase coherence time measurements (exemplified for (Ag6N)c) and energy exchange measurements (exemplified for Ag_{6N}I20 and Ag_{5N}III5). Top: Measured curves and fits to Coulomb interaction theory. The probed energy limit ε is indicated . Bottom: Log-log representation of the Coulomb interaction Kernel using $\kappa_{3/2}^{th}$ (solid lines), and $\kappa_{3/2}$ (dashed lines) The bold lines indicate the range of probed energies.

The major difference between the two manifestations of Coulomb interaction is the probed energy range. Quasi-elastic scattering dominates decoherence, whereas processes at energies between 0 and roughly $eU/4$ determine the shape of the energy distribution function $f(E)$ (see Figure 2). In term of interaction time, this means that phase coherence time is sensitive to long-time interaction, whereas energy exchange is sensitive to short-time interaction. In our experiments, the diffusion coefficient is inferred from resistance measurement which is also sensitive to long-time dynamics. If in the experiments, the electron dynamics was not diffusive at all scales with the same diffusion coefficient, for example because of the granular structure or surface-dominated scattering (see Figure 3), the evaluation of D from the resistance would only be valid for phase coherence time measurements and not for energy

exchange measurements. This would explain the large discrepancy between the experimental values of $\kappa_{3/2}$ compared to the theoretical values and also the samples to samples variations, since the grain structure is different for each sample.

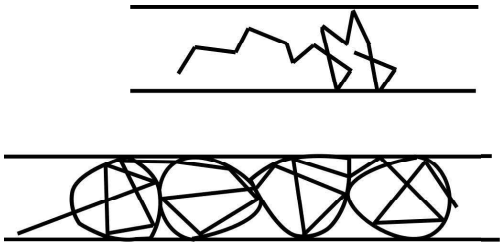

Figure 3: Top: Model of a wire and diffusive electron trajectory: the dispersion of times between two collisions is small. Bottom: Model of a wire and pseudo-diffusive trajectory: two typical times between collisions exist. The shorter one is probed in energy exchange measurements and the longer one in resistivity and phase coherence time measurements.

8.2 KIM interaction

We have demonstrated with our energy exchange measurements that in several samples KIM interaction dominates Coulomb interaction on a large range of temperature, as recently predicted [6]. KIM interaction manifests itself on phase coherence time measurements for all the samples made of 5N-copper and 5N-silver, and on energy exchange measurements for one of the samples made of 5N-silver and for the sample made of 5N-copper. Yet, a large discrepancy remains between the fit concentrations for both measurements (see Table 5).

Source	c_{imp} (ppm)	c_{τ_ϕ} (ppm)
Ag6N	< 0.1	0.0024, 0.009, 0.011
Ag5N	< 2, 17	0.13, 0.17
Ag6N'	< 0.5	0.05
Cu5N	4.8	0.15, 0.75

Table 5: Fit concentrations of energy exchange measurements c_{imp} and phase coherence time measurements c_{τ_ϕ} on samples made of the same source. For sources of Ag5N and Cu5N, the concentration c_{imp} is found larger than c_{τ_ϕ}, suggesting that either pollution arises in the fabrication process of energy exchange samples, or that the theory for KIM interaction is not sufficient.

Measurements on 5N-silver indicate that the discrepancy can be partly attributed to pollution

during fabrication: $Ag_{5N}IV20$ is the single 5N-silver sample to present more than 2 ppm of impurities whereas the sample Ag(5N)c made later from the same source only displays 0.1 ppm of impurities, according to weak localization measurements. Yet, fit concentrations on copper wires display also a discrepancy between phase coherence time and energy exchange measurements. A quantitative test of the theory of KIM interactions must be done by measuring energy exchange in samples made with very pure metal, in which controlled concentrations of magnetic impurities are implanted. A quantitative test was made on silver samples for phase coherence time measurements and proved that the fit concentrations are well estimated in this type of measurements [7]. To definitely settle out the concentration problem, a new fabrication process is presently being developed to allow measurements of phase coherence time and energy exchange on co-evaporated and co-implanted samples.

References of chapter 8

[1] B.L. Altshuler and A.G. Aronov, in *Electron-Electron Interactions in Disordered Systems*, edited by A.L. Efros and M. Pollak, (Elsevier Science Publishers B.V., 1985).

[2] A. Kamenev and A. Andreev, Phys. Rev. B **60**, 2218 (1999).

[3] F. Pierre, Ann. Phys. (Paris) **26**, No 4 (2001).

[4] I.L. Aleiner, B.L Altshuler, and M.E. Gershenson, Waves Random Media **9**, 201 (1999).

[5] B.L. Altshuler, A.G. Aronov, and D.E. Khmelnitsky, J. Phys. C **15**, 7367 (1982).

[6] A. Kaminski and L.I Glazman, Phys. Rev. Lett. **86**, 2400 (2001).

[7] F. Pierre, A.B. Gougam, A. Anthore, H. Pothier, D. Esteve and N.O. Birge, Phys. Rev. B. **68**, 085413 (2003).

PART 3

MESOSCOPIC SUPERCONDUCTIVITY

Chapter 9 Theoretical description of non-equilibrium superconductivity and proximity effect

The BCS theory of superconductivity [1] deals with equilibrium thermodynamical properties of superconductors. To predict out-of-equilibrium properties, this theory has been reformulated using Green functions in the Keldish formalism [2], leading to the general theory of non-equilibrium superconductivity. This formalism applies to situations in which superconducting properties are not homogeneous, it is therefore very powerful to deal with proximity effect, a phenomenon which occurs when normal (non-superconducting) and superconducting metals are in contact. In this chapter, the general starting points of non-equilibrium superconductivity and the derivation of Usadel equations are presented. Usadel equations are at the basis of the description of diffusive systems like ours. Starting from the Dyson equation, two usual approximations are made: quasiclassical approximation and diffusive limit [3]. For practical purposes, the Green functions are parameterized with two complex numbers, corresponding to a pairing angle and a superconducting phase.

9.1 Derivation of the Usadel equations

9.1.1 Out-of-equilibrium Green functions: Keldish formalism

9.1.1.1 Generality

Thanks to Green functions, the description of a complex electronic system can be achieved starting from the description of a simpler one, for example free and independent

electrons, on which an Hamiltonian describing impurity scattering or electron-electron interaction, or coupling with phonons, is adiabatically branched between the times $t = -\infty$ and $t = 0$.

The exact Green function of the system can be expressed with the Dyson equation from the free Green function G_0:

$$G = \frac{G_0}{1 - G_0 \Sigma}, \tag{1}$$

where Σ is the self-energy. The self-energy is a summation of an infinite number of distinct diagrams describing interactions [4]. Green functions are only useful if one can perform a perturbative development and approximates the self-energy by the lowest order terms in the series.

Starting from a fundamental state describing the system at $t = -\infty$, each perturbation term consists of the mean value of operators that act one after another in time. The state of the system at $t = +\infty$ has then to be known. At equilibrium, the final state is identical, modulus a phase, to the fundamental one. Out-of-equilibrium, the final state is unknown. Keldish' s trick is to make time return to the past at $t = -\infty$, by ordering time in the complex plan (see Figure 1).

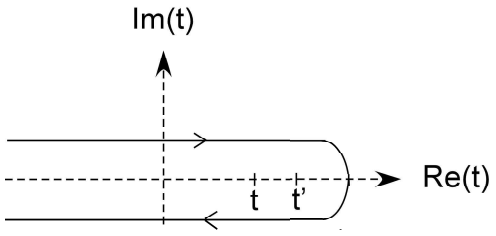

Figure 1 : Keldish contour in the complex plan. The arrows indicate the ordering of time.

The out-of-equilibrium formalism uses therefore the Green functions at equilibrium. Time has a positive or negative imaginary part and Green functions are 2×2 matrices expressed in term of G^R, G^A and G^K, the retarded, advanced and Keldish Green' s functions as:

$$G = \begin{pmatrix} G^R & G^K \\ 0 & G^A \end{pmatrix}, \tag{2}$$

where

$$
\begin{aligned}
G^R &= -i\theta(t-t')\left\langle\{\psi(r,t),\psi^+(r',t')\}\right\rangle \\
G^A &= i\theta(t'-t)\left\langle\{\psi(r,t),\psi^+(r',t')\}\right\rangle \\
G^K &= -i\left\langle[\psi(r,t),\psi^+(r',t')]\right\rangle,
\end{aligned}
\tag{3}
$$

with $\psi^+(r,t)$ the creation operator of a particle at the position r at time t. Here $\{\ \}$ stands for anticommutators, $[\ ]$stands for commutators and $\langle\ \rangle$ stands for an average on the dynamic state of the system. The functions G^R and G^A describe the equilibrium states of the system and G^K describes the occupation of these states.

9.1.1.2 Application to superconductivity

The Green functions formalism, adapted to superconductivity, describes a system of interacting electrons in terms of correlation functions $G^>$ and $G^<$, defined as the matrices:

$$
\begin{aligned}
\hat{G}^>(x,t,x',t') &= -i\left\langle\begin{pmatrix} c_\uparrow(x,t)c_\uparrow^\dagger(x',t') & c_\uparrow(x,t)c_\downarrow(x',t') \\ -c_\downarrow^\dagger(x,t)c_\uparrow^\dagger(x',t') & -c_\downarrow^\dagger(x,t)c_\downarrow(x',t')\end{pmatrix}\right\rangle \\
\hat{G}^<(x,t,x',t') &= i\left\langle\begin{pmatrix} c_\uparrow^\dagger(x',t')c_\uparrow(x,t) & c_\downarrow(x',t')c_\uparrow(x,t) \\ -c_\uparrow^\dagger(x',t')c_\downarrow^\dagger(x,t) & -c_\downarrow(x',t')c_\downarrow^\dagger(x,t)\end{pmatrix}\right\rangle,
\end{aligned}
\tag{4}
$$

where the fermionic operators $c_{\uparrow,\downarrow}^\dagger$ and $c_{\uparrow,\downarrow}$ respectively create and annihilate an electron of spin up or down and $\langle\ \rangle$ stands for an average on the dynamic state of the system for each matrix element. This theory, which contains the "anomalous" components $c_\uparrow(x,t)c_\downarrow(x',t')$ and $c_\downarrow^\dagger(x,t)c_\uparrow^\dagger(x',t')$, corresponding to the annihilation and creation of an electronic pair, treats the normal-like and superconducting-like correlations all at once. The retarded, advanced and Keldish Green' s functions are2×2 matrix, noted $\hat{G}^R$, $\hat{G}^A$ and $\hat{G}^K$, with

$$
\begin{aligned}
\hat{G}^R &= \theta(t-t')\left(\hat{G}^< - \hat{G}^>\right) \\
\hat{G}^A &= -\theta(t'-t)\left(\hat{G}^< - \hat{G}^>\right) \\
\hat{G}^K &= \hat{G}^< + \hat{G}^>.
\end{aligned}
\tag{5}
$$

The correlation functions obey the Dyson equation:

$$
\int dx''dt''\left(\breve{G}_0^{-1}(x'',t'',x',t') - \Sigma(x'',t'',x',t')\right)\breve{G}(x,t,x'',t'') = \breve{I}\,\delta(x'-x)\delta(t-t'),
\tag{6}
$$

where

$$\breve{G} = \begin{pmatrix} \hat{G}^R & \hat{G}^K \\ 0 & \hat{G}^A \end{pmatrix},$$

and

$$\Sigma = \begin{pmatrix} \Sigma^R & \Sigma^K \\ 0 & \Sigma^A \end{pmatrix},$$

the generalized self-energy, dependent on the Hamiltonian of the system, including the pairing hamiltonian of the BCS theory [1], electron-phonon scattering and elastic scattering on impurities. The function $\breve{G}_0$ is the free-electron Green's function, which reads:

$$\breve{G}_0^{-1}(\boldsymbol{x},t,\boldsymbol{x}',t') = \left(i\hbar\breve{\tau}_z\partial_t + \frac{1}{2m}\breve{\nabla}_{\boldsymbol{x}}^2 - \left(e\Phi(\boldsymbol{x}) + \mu\right)\breve{\tau}_0 \right)\delta(t-t'),$$

where the covariant spatial derivative and the Pauli matrices are defined as:

$$\breve{\nabla}_{\boldsymbol{x}} = \breve{\tau}_0\nabla_{\boldsymbol{x}} - \breve{\tau}_z\frac{ie\boldsymbol{A}(\boldsymbol{x})}{\hbar},$$
$$\breve{\tau}_i = \begin{pmatrix} \hat{\tau}_i & 0 \\ 0 & \hat{\tau}_i \end{pmatrix},\ \hat{\tau}_0 = \begin{pmatrix} 1 & 0 \\ 0 & 1 \end{pmatrix},$$
$$\hat{\tau}_x = \begin{pmatrix} 0 & 1 \\ 1 & 0 \end{pmatrix},\ \hat{\tau}_y = \begin{pmatrix} 0 & -i \\ i & 0 \end{pmatrix},\ \hat{\tau}_z = \begin{pmatrix} 1 & 0 \\ 0 & -1 \end{pmatrix},$$

with $\Phi(\boldsymbol{x}), \boldsymbol{A}(\boldsymbol{x})$ and μ respectively the scalar, vector and chemical potential, with the gauge convention $\nabla_{\boldsymbol{x}}\boldsymbol{A}(\boldsymbol{x}) = 0$.

When substracting the Dyson equation to its conjugate, Eq. (6) leads to:

$$\int d\boldsymbol{x}''dt''\left[\breve{G}_0^{-1}(\boldsymbol{x}'',t'',\boldsymbol{x}',t') - \Sigma(\boldsymbol{x}'',t'',\boldsymbol{x}',t'), \breve{G}(\boldsymbol{x},t,\boldsymbol{x}'',t'')\right] = 0.$$

This equation is the Gorkov equation [5]. The expression of the self-energy will be given below.

9.1.2 Quasiclassical approximation

The quasiclassical approximation consists of a perturbative development of the Dyson equation using a small parameter. In the case of superconductivity, this parameter is the ratio

Δ/E_F, with Δ the superconducting gap and E_F the energy at the Fermi level. In typical superconductor $\Delta / E_F = 10^{-3}$. The perturbative development aims at integrating out all physical quantities on scales smaller than ξ_0, the characteristic size of Cooper pairs. Physically, Cooper pairs are large enough compared to the Fermi length to be considered as having a quasiclassical motion. Since Cooper pairs are correlations of two electrons, knowing the phase of the two-electron wave function is sufficient in most cases. This wave function only depends on the center of mass coordinate and it is possible to integrate out the dependence on the relative coordinate in the Gorkov equation.

A Fourier transform to the momentum energy space leads then to the quasiclassical Green function

$$\breve{g}(\boldsymbol{x},t,\hat{\boldsymbol{p}},\varepsilon)=\begin{pmatrix}\hat{g}^R(\boldsymbol{x},t,\hat{\boldsymbol{p}},\varepsilon) & \hat{g}^K(\boldsymbol{x},t,\hat{\boldsymbol{p}},\varepsilon)\\ 0 & \hat{g}^A(\boldsymbol{x},t,\hat{\boldsymbol{p}},\varepsilon)\end{pmatrix}=\frac{i}{\pi}\int d\zeta_p \breve{G}(\boldsymbol{x},t,\hat{\boldsymbol{p}},\varepsilon),$$

where $\hat{\boldsymbol{p}}$ is a vector on the unit sphere and $\zeta_p = p^2/2m-\mu$.

The quasiclassical Green function obeys the equation

$$\left[\breve{g}_0^{-1}(\boldsymbol{x},t,\hat{\boldsymbol{p}},\varepsilon)-\sigma(\boldsymbol{x},t,\hat{\boldsymbol{p}},\varepsilon),\breve{g}(\boldsymbol{x},t,\hat{\boldsymbol{p}},\varepsilon)\right]=0, \tag{7}$$

with

$$\breve{g}_0^{-1}(\boldsymbol{x},t,\hat{\boldsymbol{p}},\varepsilon)=\hbar\breve{\tau}_z\partial_t-\varepsilon\breve{\tau}_z+\hbar v_F\hat{\boldsymbol{p}}.\breve{\nabla}_{\boldsymbol{x}},$$

where v_F is the Fermi velocity and with

$$\sigma(\boldsymbol{x},t,\hat{\boldsymbol{p}},\varepsilon)=\begin{pmatrix}\hat{\sigma}^R(\boldsymbol{x},t,\hat{\boldsymbol{p}},\varepsilon) & \hat{\sigma}^K(\boldsymbol{x},t,\hat{\boldsymbol{p}},\varepsilon)\\ 0 & \hat{\sigma}^A(\boldsymbol{x},t,\hat{\boldsymbol{p}},\varepsilon)\end{pmatrix},$$

the full quasiclassical self-energy. This equation, called the Eilenberger equation for superconductivity [6], is the central equation of the quasiclassical theory.

$\breve{g}$ also obeys a normalization condition: $\breve{g}^2(\boldsymbol{x},t,\hat{\boldsymbol{p}},\varepsilon)=\breve{\tau}_0$.

9.1.3 Diffusive limit: Usadel equations

9.1.3.1 Diffusive limit

In superconductivity, the diffusive limit applies when the mean free path is shorter than the superconductivity coherence length $\xi_0 = \hbar v_F / \Delta$ with v_F the velocity at the Fermi level and Δ the superconducting gap. In this limit, scattering on non-magnetic impurities, lattice defects or sample boundaries occur frequently on a trajectory of length ξ_0, and the full quasiclassical self-energy, associated to elastic scattering, can be written in the Born approximation:

$$\sigma_{el}(\boldsymbol{x},t,\hat{\boldsymbol{p}},\varepsilon) = \frac{\pi}{2\tau}\left\langle \hat{g}(\boldsymbol{x},t,\hat{\boldsymbol{p}},\varepsilon)\right\rangle,$$

where $\langle ... \rangle$ is the average value on the angles, justified because of the fast direction memory loss of electrons, and $1/2\tau = 2\pi n_i \nu_F \left\langle |U|^2 \right\rangle$. The concentration of impurities is n_i, ν_F is the density of states at the Fermi level and U is the Fourier transform of the impurities scattering potential. When the number of scatterers is large enough, this self-energy term dominates and the Green function is almost isotropic. Then, an expansion in spherical harmonics keeping only the s- and p- wave parts is performed:

$$\begin{aligned}\breve{g}(\boldsymbol{x},t,\hat{\boldsymbol{p}},\varepsilon) &\simeq \breve{g}_S(\boldsymbol{x},t,\varepsilon) + \hat{\boldsymbol{p}}.\breve{\boldsymbol{g}}_p(\boldsymbol{x},t,\varepsilon)\\ \sigma(\boldsymbol{x},t,\hat{\boldsymbol{p}},\varepsilon) &\simeq \sigma_S(\boldsymbol{x},t,\varepsilon) + \hat{\boldsymbol{p}}.\boldsymbol{\sigma}_p(\boldsymbol{x},t,\varepsilon),\end{aligned}$$

where $\hat{\boldsymbol{p}}.\breve{\boldsymbol{g}}_p \ll \breve{g}_S$ and $\hat{\boldsymbol{p}}.\boldsymbol{\sigma}_p \ll \sigma_S$.

Splitting Eq. (7) into an even and odd part with respect to $\hat{\boldsymbol{p}}$ yields to:

$$\begin{aligned}&\breve{g}_p = -l_e \breve{g}_S \left[\breve{\nabla}_{\boldsymbol{x}}, \breve{g}_S\right]\\ &\left[\hbar D \breve{\nabla}_{\boldsymbol{x}} \breve{g}_S \breve{\nabla}_{\boldsymbol{x}} - \breve{g}_{0S}^{-1} - i\sigma_S^{'}, \breve{g}_S\right] = 0,\end{aligned} \tag{8}$$

where $D = 1/3\, v_F l$ is the diffusion constant, $\sigma_S^{'}$ the quasiclassical self-energy in which the elastic collision term σ_{el} has been removed, and $\breve{g}_{0S}^{-1} = \hbar \breve{\tau}_z \partial_t - i\varepsilon\breve{\tau}_z$.

Eq. (8) are called Usadel equations [7]. They are the general starting point to calculate non-equilibrium effects in diffusive superconductors.

9.1.3.2 Usadel equations

In BCS theory, superconductivity is due to electron-phonon interaction. A pairing potential is then included in the self energy:

$$\sigma_{pair}^{e-ph} = i\begin{pmatrix} \hat{\Delta} & 0 \\ 0 & \hat{\Delta} \end{pmatrix},\ \hat{\Delta} = \begin{pmatrix} 0 & \Delta \\ \Delta^* & 0 \end{pmatrix},$$

where Δ is the superconducting order parameter:

$$\Delta = \frac{\nu_F V_{eff}}{8i}\int_{-\hbar\omega_D}^{\hbar\omega_D} d\varepsilon\ Tr\left(\left(\hat{\tau}_x - i\hat{\tau}_y\right)\hat{g}_S^K\right), \tag{9}$$

with V_{eff} the pairing interaction strength and ω_D the Debye pulsation as defined in the BCS theory of superconductivity [1].

The spin-flip scattering rate $1/\tau_{sf}$ contribution σ_{sf} to the self energy is:

$$\sigma_{sf} = -\frac{-i\hbar}{2\tau_{sf}}\breve{\tau}_z\breve{g}_s\breve{\tau}_z.$$

Using $\sigma'_S = \sigma_{pair}^{e-ph} + \sigma_{sf}$ yields in Eq. (7) to equation:

$$\left[\hbar D\breve{\nabla}_x\breve{g}_S\breve{\nabla}_x + i\breve{H}_0 - \frac{\hbar}{2\tau_{sf}}\breve{\tau}_z\breve{g}_S\breve{\tau}_z, \breve{g}_S\right] = 0, \tag{10}$$

with $\breve{H}_0 = \begin{pmatrix} \hat{H}_0 & 0 \\ 0 & \hat{H}_0 \end{pmatrix},\ \hat{H}_0 = \begin{pmatrix} \varepsilon & i\Delta \\ i\Delta^* & -\varepsilon \end{pmatrix}$.

Equation (10) is equivalent for the advanced, retarded and Keldish Green function to:

$$\begin{aligned}
&\left[\hbar D\hat{\nabla}_x\hat{g}_S^R\hat{\nabla}_x + i\hat{H}_0 - \frac{\hbar}{2\tau_{sf}}\hat{\tau}_z\hat{g}_S^R\hat{\tau}_z, \hat{g}_S^R\right] = 0 \\
&\left[\hbar D\hat{\nabla}_x\hat{g}_S^A\hat{\nabla}_x + i\hat{H}_0 - \frac{\hbar}{2\tau_{sf}}\hat{\tau}_z\hat{g}_S^A\hat{\tau}_z, \hat{g}_S^A\right] = 0 \\
&\hbar D\left(\left[\hat{\nabla}_x\hat{g}_S^R\hat{\nabla}_x, \hat{g}_S^K\right] + \left[\hat{\nabla}_x\hat{g}_S^K\hat{\nabla}_x, \hat{g}_S^A\right]\right) \\
&+i\left[\hat{H}_0, \hat{g}_S^K\right] - \frac{\hbar}{2\tau_{sf}}\left(\hat{\tau}_z\hat{g}_S^R\hat{\tau}_z\hat{g}_S^K - \hat{g}_S^R\hat{\tau}_z\hat{g}_S^K\hat{\tau}_z + \hat{\tau}_z\hat{g}_S^K\hat{\tau}_z\hat{g}_S^A - \hat{g}_S^K\hat{\tau}_z\hat{g}_S^A\hat{\tau}_z\right) = 0.
\end{aligned} \tag{11}$$

Equations (11) are the detailed Usadel equations. The projection on the s- wave of $\breve{g}$ obeys the same normalization condition as $\breve{g}$: $\breve{g}_S^2(\boldsymbol{x},\varepsilon) = \breve{\tau}_0$,

which is equivalent to

$$\hat{g}_S^R \hat{g}_S^R = \hat{\tau}_0, \ \hat{g}_S^A \hat{g}_S^A = \hat{\tau}_0$$
$$\hat{g}_S^R \hat{g}_S^K + \hat{g}_S^K \hat{g}_S^A = 0.$$

Eq. (8) is equivalent to the conservation of the current. The spectral density of current is defined as:

$$J(\varepsilon, \boldsymbol{x}) = \sigma(\boldsymbol{x}) \breve{g}_S \breve{\nabla}_{\boldsymbol{x}} \breve{g}_S,$$

where $\sigma(\boldsymbol{x})$ is the normal-state conductivity. This leads to the current density:

$$J(\boldsymbol{x}) = -\frac{\sigma}{8e} \int d\varepsilon Tr\left[\hat{\tau}_z (\hat{g}_S^R \hat{\nabla}_{\boldsymbol{x}} \hat{g}_S^K + \hat{g}_S^K \hat{\nabla}_{\boldsymbol{x}} \hat{g}_S^A) \right].$$

The density of quasiparticle states is given by :

$$N(\boldsymbol{x}, \varepsilon) = \frac{\nu_F}{2} \mathrm{Re}\left(Tr\left(\hat{g}^R(\boldsymbol{x}, \varepsilon) \hat{\tau}_z \right) \right).$$

9.2 Parameterization of the Usadel equations

9.2.1 Definition of the pairing angle and of the complex phase

The normalized condition $\hat{g}_S^R \hat{g}_S^R = \hat{\tau}_0$, and the fact that $Tr\left(\hat{g}_S^R\right) = 0$, allows to parameterize $\hat{g}_S^R$ with two complex parameters $\theta(\boldsymbol{x}, \varepsilon)$ and $\varphi(\boldsymbol{x}, \varepsilon)$:

$$\begin{aligned} \hat{g}_S^R &= \cos\theta \ \hat{\tau}_z + \sin\theta \ \cos\varphi \ \hat{\tau}_x - \sin\theta \ \sin\varphi \ \hat{\tau}_y \\ &= \begin{pmatrix} \cos\theta & \sin\theta \ \mathrm{e}^{\mathrm{i}\varphi} \\ \sin\theta \ \mathrm{e}^{-\mathrm{i}\varphi} & -\cos\theta \end{pmatrix}. \end{aligned} \tag{12}$$

The advanced and retarded component of $\hat{g}_S^R$ are related by the equation:

$$\hat{g}_S^A = -\hat{\tau}_z \hat{g}_S^{R+} \hat{\tau}_z.$$

Hence,

$$\hat{g}_S^A = \begin{pmatrix} -\cos\theta^* & \sin\theta^* \ \mathrm{e}^{\mathrm{i}\varphi^*} \\ \sin\theta^* \ \mathrm{e}^{-\mathrm{i}\varphi^*} & \cos\theta^* \end{pmatrix}. \tag{13}$$

The last renormalization condition allows to write $\hat{g}_S^K$ as

$$\hat{g}_S^K = \hat{g}_S^R \hat{h} - \hat{h}\hat{g}_S^A. \tag{14}$$

The distribution matrix $\hat{h}$ (also called filling matrix) can be chosen as diagonal and is related to the distribution functions for electrons f_e and holes f_h:

$$\hat{h} = \begin{pmatrix} 1-2f_e & 0 \\ 0 & 2f_h\text{-}1 \end{pmatrix}, \tag{15}$$

where the energy is measured from the chemical potential of the superconductor.

For convenience, $\hat{h}$ is also written

$$\hat{h} = f_{od}\hat{\tau}_0 + f_{ev}\hat{\tau}_{z,} \tag{16}$$

with f_{od} and f_{ev} respectively odd and even functions of energy, related to the physical distribution functions of electrons through the expression:

$$f(\boldsymbol{x},\varepsilon) = \left(1 - f_{od}(\boldsymbol{x},\varepsilon) - f_{ev}(\boldsymbol{x},\varepsilon)\right)/2. \tag{17}$$

For example, in a reservoir at potential V and at thermal equilibrium *T*,

$$\hat{h}_{eq} = \begin{pmatrix} \tanh\dfrac{\varepsilon + eV}{2k_BT} & 0 \\ 0 & \tanh\dfrac{\varepsilon + eV}{2k_BT} \end{pmatrix}, \tag{18}$$

and

$$\begin{aligned} f_{od} &= \frac{1}{2}\left(\tanh\frac{\varepsilon + eV}{2k_BT} + \tanh\frac{\varepsilon - eV}{2k_BT}\right) \\ f_{ev} &= \frac{1}{2}\left(\tanh\frac{\varepsilon + eV}{2k_BT} - \tanh\frac{\varepsilon - eV}{2k_BT}\right). \end{aligned} \tag{19}$$

The odd and even functions are represented in Figure 2.

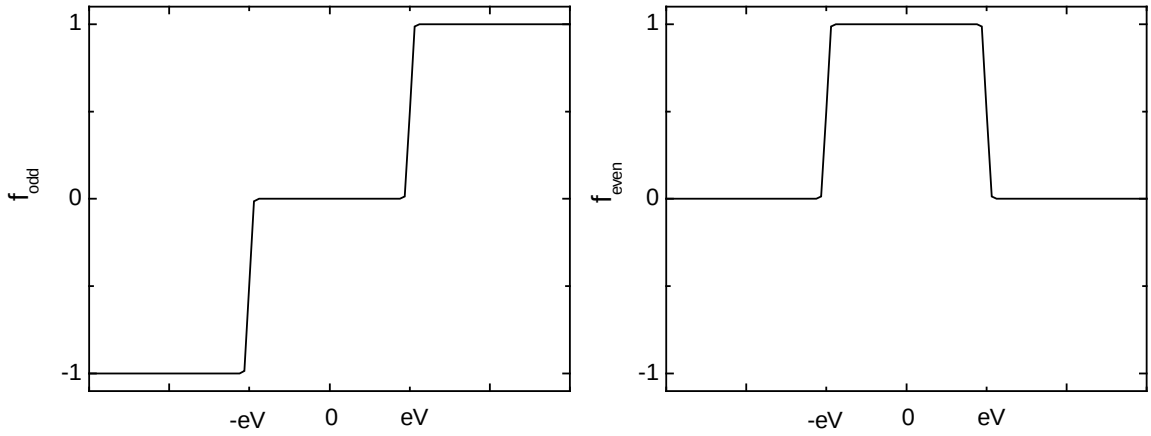

Figure 2: Odd and even part of the energy distribution function used in the theory of non-equilibrium superconductivity, in the case where the system is a reservoir at a potential V.

9.2.2 Equations for the pairing angle θ and the phase φ

The parameterization in θ and φ of the Usadel equations leads to the following equations.

9.2.2.1 Order parameter equation

In the general case, with the previous definition, the order parameter reads:

$$\Delta(\boldsymbol{x}) = \frac{\nu_F V_{eff}}{4i} \int_{-\hbar\omega_D}^{\hbar\omega_D} d\varepsilon \, f_{od} \left(\sin\theta \; e^{i\varphi} - \sin\theta^* \; e^{i\varphi^*} \right) - f_{ev} \left(\sin\theta \; e^{i\varphi} + \sin\theta^* \; e^{i\varphi^*} \right). \qquad (20)$$

At equilibrium, for a bulk superconductor, φ is real, $f_{ev} = 0$ and $f_{od} = \tanh(\varepsilon / 2k_B T)$, leading to

$$\Delta(\boldsymbol{x}) = \nu_F V_{eff} \int_0^{\hbar\omega_D} d\varepsilon \;\; \tanh\frac{\varepsilon}{2k_B T} \mathrm{Im}\left(\sin\theta\right) e^{i\varphi} \, .$$

9.2.2.2 Equilibrium Usadel equations

The part of equation concerning the advanced and retarded Green functions defines

equilibrium equations:

$$\begin{aligned}
&\frac{\hbar D}{2}\nabla^2\theta+\left(i\varepsilon-\left(\frac{\hbar}{\tau_{sf}}+\frac{\hbar D}{2}\left(\nabla\varphi-\frac{2e}{\hbar}\boldsymbol{A}\right)^2\right)\cos\theta\right)\sin\theta+\\
&\left(\frac{\Delta(\boldsymbol{x})e^{-i\varphi}+\Delta^*(\boldsymbol{x})e^{i\varphi}}{2}\right)\cos\theta=0\\
&\nabla\left(\left(\nabla\varphi-\frac{2e}{\hbar}\boldsymbol{A}\right)\sin^2\theta\right)=\frac{i\sin\theta}{\hbar D}\left(\Delta(\boldsymbol{x})e^{-i\varphi}-\Delta^*(\boldsymbol{x})e^{i\varphi}\right).
\end{aligned}\tag{21}$$

For a bulk superconductor, where φ is real, Eqs. (21) have simpler expressions:

$$\begin{aligned}
&\frac{\hbar D}{2}\nabla^2\theta+\left(i\varepsilon-\left(\frac{\hbar}{2\tau_{sf}}+\frac{\hbar D}{2}\left(\nabla\varphi-\frac{2e}{\hbar}\boldsymbol{A}(\boldsymbol{x})\right)^2\right)\cos\theta\right)\sin\theta+\Delta(\boldsymbol{x})e^{-i\varphi}\cos\theta=0\\
&\nabla\left(\left(\nabla\varphi-\frac{2e}{\hbar}\boldsymbol{A}(\boldsymbol{x})\right)\sin^2\theta\right)=0.
\end{aligned}\tag{22}$$

In a normal metal, the order parameter is zero and the equations describing a normal metal with only spin-flip scattering are found taking $\Delta=0$ in Eq. (21).

9.2.2.3 Density of states

The density of quasiparticle states is related to the pairing angle by:

$$N(\varepsilon,\boldsymbol{x})=\nu_F\,\mathrm{Re}(\cos\theta).\tag{23}$$

In bulk superconductors obeying BCS theory, the order parameter $\Delta=\Delta_{BCS}e^{i\varphi}$ is constant and Eq. (21) simply reduces to

$$\tan\theta=i\frac{\Delta_{BCS}}{\varepsilon},\tag{24}$$

or

$$\begin{aligned}
\theta_{BCS}(\varepsilon)&=\frac{\pi}{2}+i\ \mathrm{arctanh}\frac{\varepsilon}{\Delta_{BCS}} \qquad \text{if } |\varepsilon|<\Delta_{BCS}\\
&=i\ \mathrm{arctanh}\frac{\Delta_{BCS}}{\varepsilon} \qquad \text{if } |\varepsilon|>\Delta_{BCS}.
\end{aligned}\tag{25}$$

The energy dependence of the pairing angle in bulk superconductor is represented in Figure 3. From the definition (23), the density of states is found as

$$n(\varepsilon) = 0 \qquad \text{if } |\varepsilon| < \Delta_{BCS}$$
$$= \nu_F \frac{|\varepsilon|}{\sqrt{\varepsilon^2 - \Delta_{BCS}^2}} \qquad \text{if } |\varepsilon| > \Delta_{BCS},$$

in agreement with the BCS result.

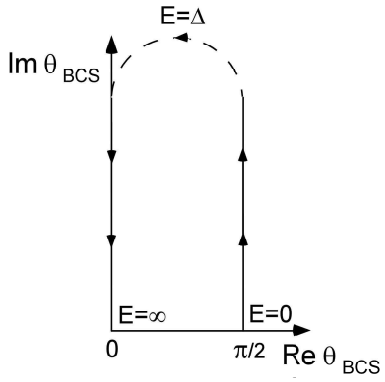

Figure 3: Energy dependence of the pairing angle in a homogeneous superconductor in the complex plane.

9.2.2.4 Out-of equilibrium Usadel equations

The equation on the Keldish Green function allows to calculate the filling factors. In the limit when $\tau_{sf} \to \infty$ and $A = 0$, the following two equations are obtained:

$$\nabla\left\{\left(1+|\cos\theta|^2-|\sin\theta|^2\cosh(2\varphi_2)\right)\nabla f_{od} - |\sin\theta|^2\sinh(2\varphi_2)\nabla f_{ev} + 2\,\mathrm{Im}\left(\sin^2\theta\,\nabla\varphi\right) f_{ev}\right\} = 0$$
$$\hbar D\,\nabla\left\{\left(1+|\cos\theta|^2+|\sin\theta|^2\cosh(2\varphi_2)\right)\nabla f_{ev} + |\sin\theta|^2\sinh(2\varphi_2)\nabla f_{od} + 2\,\mathrm{Im}\left(\sin^2\theta\,\nabla\varphi\right) f_{od}\right\} \quad (26)$$
$$= 2 f_{od}\,\mathrm{Re}\left(\sin\theta\,\left(\Delta(\boldsymbol{x})e^{-i\varphi} - \Delta^*(\boldsymbol{x})e^{i\varphi}\right)\right) - 2 f_{ev}\,\mathrm{Re}\left(\sin\theta\,\left(\Delta(\boldsymbol{x})e^{-i\varphi} + \Delta^*(\boldsymbol{x})e^{i\varphi}\right)\right),$$

where φ_1 and φ_2 denote the real, and imaginary parts of the complex phase φ, respectively.

For a bulk superconductor, where φ is real, Eqs. (26) read:

$$\nabla\left\{\cos^2\theta_1\nabla f_{od} + \mathrm{Im}\left(\sin^2\theta\,\nabla\varphi\right) f_{ev}\right\} = 0$$
$$\nabla\left\{\cosh^2\theta_2\nabla f_{ev} + \mathrm{Im}\left(\sin^2\theta\,\nabla\varphi\right) f_{od}\right\} = -2\delta f_{ev}\,\mathrm{Re}\left(\sin\theta\right), \quad (27)$$

where θ_1 and θ_2 denote the real and imaginary parts of the pairing angle θ, respectively and $\delta = \mathrm{Re}\left(\Delta(\boldsymbol{x})e^{-i\varphi}\right)$. Equations (27) generalize Boltzmann equations to situations where superconducting correlations are present. The “source” term in the second equation, related to the order parameter, is in a bulk superconductor proportional to

$$\mathrm{Re}\left(\sin\theta_{BCS}\right)=\frac{\Delta_{BCS}}{\sqrt{\Delta_{BCS}^2-\varepsilon^2}} \qquad \text{if } |\varepsilon|<\Delta_{BCS}$$
$$=0 \qquad \text{if } |\varepsilon|>\Delta_{BCS}.$$

This term represents the Andreev reflections of electrons into holes below the gap. It is of importance for the following to note that inelastic processes are not included in Eqs. (26).

9.2.2.5 Current density

The current density is related to the pairing angle and the complex phase by:

$$\begin{aligned}\boldsymbol{J}(\boldsymbol{x}) &= -\frac{\sigma}{e}\int_0^\infty d\varepsilon\, f_{od}\,\mathrm{Im}\left(\sin^2\theta\left(\nabla\varphi-\frac{2e}{\hbar}\boldsymbol{A}\right)\right)\\ &\quad -\frac{\sigma}{2e}\int_0^\infty d\varepsilon\left(\nabla f_{ev}\left(1+\left|\cos\theta\right|^2+\left|\sin\theta\right|^2\cosh\left(2\varphi_2\right)\right)+\nabla f_{od}\left|\sin\theta\right|^2\sinh\left(2\varphi_2\right)\right) \qquad (28)\\ &= \boldsymbol{J}_S\left(\boldsymbol{x}\right)+\boldsymbol{J}_N\left(\boldsymbol{x}\right).\end{aligned}$$

The first term corresponds to a supercurrent, proportional to the phase gradient. At equilibrium, when $f_{ev}=0$,

$$\boldsymbol{J}_S\left(\boldsymbol{x}\right)=\frac{\sigma}{e}\int_0^\infty d\varepsilon\tanh\frac{\varepsilon}{2k_BT}\mathrm{Im}\left(\sin^2\theta\left(\nabla\varphi-\frac{2e}{\hbar}\boldsymbol{A}\right)\right). \qquad (29)$$

The second term corresponds to a current of quasiparticles due to a gradient of occupation factors. When the phase is real, $\boldsymbol{J}_N$ is equal to

$$\boldsymbol{J}_N\left(\boldsymbol{x}\right)=\frac{\sigma}{e}\int_0^\infty d\varepsilon\cosh^2\theta_2\nabla f_{ev}\,. \qquad (30)$$

9.3 Proximity effect and boundary conditions

At an interface between a superconductor and a normal metal, the superconducting correlations are delocalized. The decay of the correlations can be handled with Usadel equations, the normal metal being described with $\Delta=0$. The boundary conditions determine the properties inside the electrodes. In the next section, the general boundary conditions at interfaces for Green functions are presented as well as their equivalences in term of pairing

angle and complex phase.

9.3.1 Continuity of Green functions and reservoirs

At a transparent interface, the advanced, retarded and Keldish Green functions are continuous. With the parameterization chosen in the previous section, this is equivalent to the continuity of θ, φ, f_{ev} and f_{od}. These values are well defined in reservoirs of bulk superconductor and normal metal and are listed below.

In a bulk superconductor, the phase φ is real, and the order parameter is equal to $\Delta = \Delta_{BCS} e^{i\varphi}$, leading to

$$\begin{aligned} \theta_{BCS}(\varepsilon) &= \frac{\pi}{2} + i \operatorname{arctanh} \frac{\varepsilon}{\Delta_{BCS}} \qquad \text{if } |\varepsilon| < \Delta_{BCS} \\ &= i \operatorname{arctanh} \frac{\Delta_{BCS}}{\varepsilon} \qquad \text{if } |\varepsilon| > \Delta_{BCS}. \end{aligned} \tag{31}$$

In a bulk normal metal, Eq. (21) leads to $\theta_N = 0$ and the phase φ is not defined.

In a normal reservoir at potential V, the distribution functions are given by:

$$\begin{aligned} f_{od} &= \frac{1}{2}\left\{ \tanh \frac{\varepsilon + eV}{2k_B T} + \tanh \frac{\varepsilon - eV}{2k_B T} \right\} \\ f_{ev} &= \frac{1}{2}\left\{ \tanh \frac{\varepsilon + eV}{2k_B T} - \tanh \frac{\varepsilon - eV}{2k_B T} \right\}. \end{aligned} \tag{32}$$

9.3.2 Spectral current conservation

In the quasiclassical approximation, the information on length scales of the order of Fermi wavelength has been integrated out. Consequently, effects of potential barriers or interfaces can not be accounted for on this level. It turns out from a full study of theory that these effects are equivalent to effective boundary conditions for the quasiclassical Green functions. These boundary conditions couple the classically transmitted and reflected trajectories and are equivalent to the conservation of the spectral current:

$$\sigma_l \breve{g}_l \breve{\nabla}_x \breve{g}_l = \sigma_r \breve{g}_r \breve{\nabla}_x \breve{g}_r = \frac{g_{\text{int}}}{2}\left[\breve{g}_l, \breve{g}_r\right], \tag{33}$$

where $\breve{g}_l, \breve{g}_r$ and g_{int} are respectively the Green functions of left and right parts and the conductance of the interface, σ_l and σ_r are the conductivity of left and right parts.

References of chapter 9

[1] J. Bardeen, L. N. Cooper, and J. R. Schrieffer, Phys. Rev. **108**, 1175 (1957).

[2] J. Rammer and H. Smith, Rev. Mod. Phys. **58**, 323 (1986).

[3] W. Belzig, F. K. Wilhelm, C. Bruder, G. Schon, and A. D. Zaikin, Superlattices and Microstructures, **25** No 5/6 (1999) (cond-mat/9812297).

[4] D. Mahan, *Many-Particle Physics* (Plenum Press, New York and London, 1993), p.109.

[5] A. I. Larkin and Yu.N. Ovchinikov, Zh. Eksp. Teor. Fiz. **55** 2262 (1968) [Sov. Phys. JETP **28**, 1200 (1969)].

[6] G. Eilenberger, Z. Phys. **214**, 195 (1968).

[7] K. D. Usadel, Phys. Rev. Lett. **25**, 507 (1970).

Chapter 10 Density of states in a superconductor carrying a supercurrent and exposed to a magnetic field

The superconducting order is based on pairing electronic states that transform into one another by time reversal. Superconducting order is modified by physical phenomena that break time reversal symmetry, such as a magnetic field, or that hinder the pairing of time-reversed electronic states, such as a supercurrent. In the early stages of the theory of superconductivity, it was predicted that in diffusive superconductors, in which the electron mean free path is short compared to the BCS coherence length ξ_0, and in homogeneous situations, the effect of all depairing mechanisms can be described by a single parameter, the depairing energy [1]. Later on, the theory of out-of-equilibrium superconductivity (see Chapter 9) extended this equivalence in the diffusive limit to inhomogeneous situations where the order parameter may vary in space.

Experimentally, measurements of the density of states (DOS) in a thin superconductor placed in an in-plane magnetic field were well accounted for by the concept of depairing energy [2]. On the other hand, the effect of a supercurrent was probed in a single experiment, focused on the reduction of the superconducting gap close to the critical temperature [3].

In order to test the predicted fundamental equivalence between the effect of a magnetic field and a supercurrent in a diffusive superconductor, we have measured the DOS in a superconducting wire carrying a supercurrent or exposed to a magnetic field (see Figure 1). The width and thickness of the wire were chosen smaller than the London length so that the current flow is homogeneous and the magnetic field penetrates uniformly. This situation is the simplest that allows to test quantitatively the theoretical predictions.

In this chapter, the theoretical predictions for the dependence of the DOS and of the superconducting order parameter on the depairing energy are first detailed. Then, the experimental realization is described. At the end, the obtained results are compared with theory.

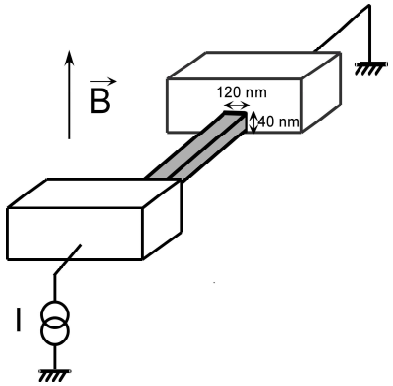

Figure 1: Layout of the experiment: A wire of width and thickness smaller than the London length $\lambda_L = 175$ nm can be current biased and exposed to a magnetic field.

10.1 Theoretical predictions for the density of states and order parameter in the wire

10.1.1 Usadel equations and superfluid velocity

We calculate the DOS in a superconducting wire in presence of a supercurrent or a magnetic field using the equilibrium Usadel equations. The superconducting order is parameterized with the complex pairing angle $\theta(\boldsymbol{x},\varepsilon)$ and phase $\varphi(\boldsymbol{x},\varepsilon)$ (see Chapter 9):

$$\frac{\hbar D}{2}\nabla^2\theta + \left(i\varepsilon - \left(\frac{\hbar}{2\tau_{sf}} + \frac{\hbar}{2D} V_S(\boldsymbol{x})^2 \right) \cos\theta \right) \sin\theta + \Delta(\boldsymbol{x}) e^{-i\varphi} \cos\theta = 0, \tag{1}$$

$$\nabla\left(V_S(\boldsymbol{x}) \sin^2\theta \right) = 0; \tag{2}$$

the order parameter equation (see Chapter 9):

$$\Delta(\boldsymbol{x}) = \nu_F V_{eff} \int_0^{\hbar\omega_D} d\varepsilon \ \tanh\frac{\varepsilon}{2k_B T} \mathrm{Im}\left(\sin\theta\right) e^{i\varphi}, \tag{3}$$

and the current phase relation (see Chapter 9):

$$j_S(\boldsymbol{x}) = \frac{\sigma}{eD}\int_0^\infty d\varepsilon \tanh\frac{\varepsilon}{2k_BT}\,\mathrm{Im}\left(\sin^2\theta\; V_S(\boldsymbol{x})\right), \tag{4}$$

where V_S is the superfluid velocity:

$$V_S(\boldsymbol{x}) = D\left(\nabla\varphi(\boldsymbol{x}) - \frac{2e}{\hbar}\boldsymbol{A}(\boldsymbol{x})\right). \tag{5}$$

The supercurrent and the magnetic field induce respectively a phase gradient $\nabla\varphi$ and a vector potential $\boldsymbol{A}(\boldsymbol{x})$ that appear in the combination $V_S(\boldsymbol{x})/D = \nabla\varphi(\boldsymbol{x}) - (2e/\hbar)\boldsymbol{A}(\boldsymbol{x})$ in the Usadel equations.

In the following, the set of self-consistent equations ((1)-(5)) are first solved for the simple situations where there are no magnetic field or supercurrent, and when the superfluid velocity is uniform in space. Then, the effects of the magnetic field and of the supercurrent in the experimental situation are described.

10.1.2 Density of states in absence of magnetic field and supercurrent

We focus first on the simple case without magnetic field or supercurrent. In the absence of magnetic field and supercurrent, $V_S = 0$ and the superconducting wire remains invariant by translation. No spatial dependence remains in Eq. (1), Eq. (2) and Eq. (3), which simplify to the two following equations:

$$\varepsilon + i\gamma\cos\theta = i\Delta\frac{\cos\theta}{\sin\theta}, \tag{6}$$

$$\Delta = \nu_F V_{eff}\int_0^{\hbar\omega_D} d\varepsilon\;\tanh\frac{\varepsilon}{2k_BT}\,\mathrm{Im}\left(\sin\theta\right), \tag{7}$$

with $\gamma = \hbar/\tau_{sf}$ the spin-flip rate.

In aluminum, the spin-flip rate is negligible and Eq. (6) leads to:

$$\tan\theta(\varepsilon) = \frac{i\Delta}{\varepsilon},$$

which is the BCS result, while Eq. (7) gives the BCS gap equation in the bulk:

$$\Delta_0 = \nu_F V_{eff} \int_0^{\hbar\omega_D} d\varepsilon \ \tanh\frac{\varepsilon}{2k_B T}\,\mathrm{Re}\frac{1}{\sqrt{\varepsilon^2-1}}.$$

In the following the spin-flip rate will be neglected.

10.1.3 Density of states in the case of an uniform superfluid velocity

When V_S is uniform in space, Eq. (1) and Eq. (2) also simplify to Eq. (6) with $\gamma = \hbar/(2D)\ V_S^2$.

Equation (6) has a non-trivial analytical solution for $\gamma \neq 0$:

$$\cos\theta(\varepsilon,\gamma,\Delta) = \frac{i\varepsilon}{2\gamma} + \frac{\sqrt{p+q}}{2\sqrt{3}\gamma} + \frac{1}{\sqrt{6}\gamma}\sqrt{p - \frac{q}{2} - \frac{3\sqrt{3}i\varepsilon}{\sqrt{p+q}}\left(\gamma^2+\Delta^2\right)}, \tag{8}$$

with $p = 2\gamma^2 - \varepsilon^2 - 2\Delta^2$, $q = \left(\alpha^2 + r^2\right)/r$, $r = \left(\alpha^3 - 2\beta^2 + 2\beta\sqrt{-\alpha^3+\beta^2}\right)^{1/3}$, and $\alpha = \Delta^2 - \gamma^2 - \varepsilon^2$, $\beta = 3\sqrt{3}\ \varepsilon\ \gamma\ \Delta$.

Eq. (8) is solved self-consistently with Eq. (7) to calculate the DOS in the wire and the order parameter when $\gamma \neq 0$.

The natural energy scale is the gap energy, which is the modulus of the order parameter Δ_0 when $\gamma = 0$. In Figure 2, the DOS $n_S(\varepsilon) = \mathrm{Re}\left(\cos\left(\theta(\varepsilon)\right)\right)$ is plotted versus ε/Δ_0 for several values of γ/Δ_0. When γ increases, the smearing of the peak gets more pronounced and the gap in the DOS is reduced. Increasing the superfluid velocity weakens the superconductivity by inducing more depairing in the wire. The previous resolution proves that depairing is accounted for in Usadel equations by a single quantity, denoted γ here, corresponding to an energy. The energy γ is called the depairing energy in the following.

In Figure 3, the reduction of the order parameter and the reduction of the spectral gap $\Omega_g(\gamma)$, *i.e.* the gap observed in the DOS, are plotted versus the depairing energy. These two quantities are related by:

$$\Omega_g(\gamma) = \Delta(\gamma)\left(1 - \left(\frac{\gamma}{\Delta(\gamma)}\right)^{2/3}\right)^{3/2}. \tag{9}$$

From Eq. (9), a superconductor is gapless, which means that the spectral gap is zero, when

$\gamma/\Delta(\gamma)=1$. This corresponds to values of depairing energy such as $0.45\Delta_0 \le \gamma$. Above a depairing energy of $0.5\Delta_0$, superconductivity is suppressed: $\Delta(\gamma)=0$.

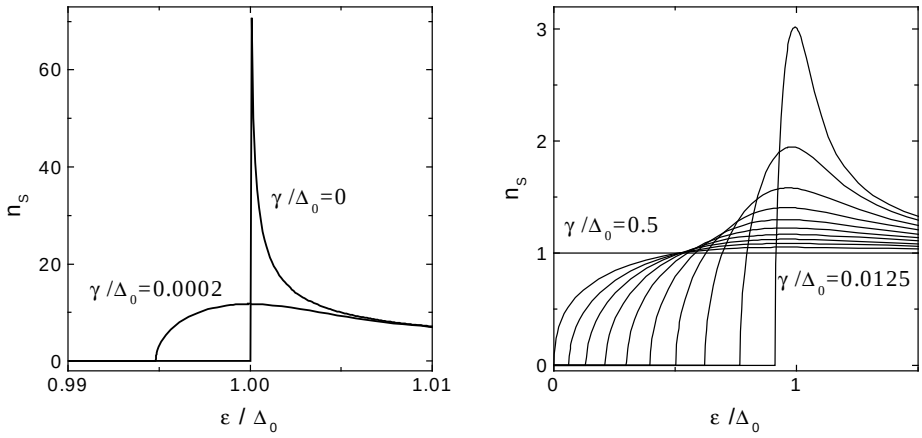

Figure 2: Theoretical predictions for the DOS in a superconductor versus reduced energy for several values of the depairing energy γ. Left panel: γ = 0 and 0.0002. Right panel: from right to left: γ = 0.0125, and 0.05 to 0.5 by steps of 0.05 in units of Δ_0, the order parameter when $\gamma = 0$.

The function $\Delta(\gamma)$ should depend on the superconductor nature since the pairing potential V_{eff} and the Debye pulsation ω_D are material dependent. However, it was found numerically that this reduction is similar within 5 parts in thousand for niobium, aluminum, and lead using the parameters given in Table 1 [4].

Superconductor	Δ_0 (meV)	$\hbar\omega_D$ (meV)
Aluminum	0.18	36.2
Lead	1.1	8.3
Niobium	1.4	23.8

Table 1: Bulk order parameter and Debye energies for different superconductors.

In the following, we focus on the case of the experiment, where a transverse magnetic field is applied and the wire is current biased. The corresponding vector potential and phase gradient have then to be determined to calculate the superfluid velocity, which is *a priori* dependent on

the position in the wire, the corresponding depairing energy and DOS.

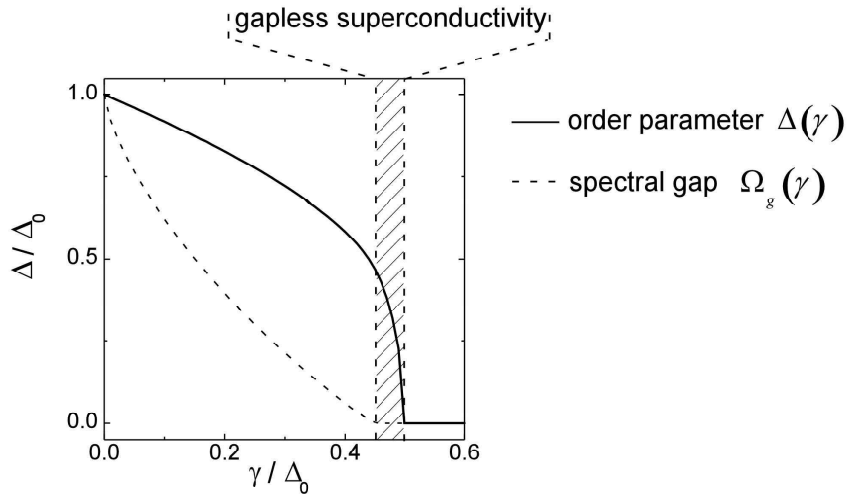

Figure 3: Order parameter $\Delta(\gamma)$ and spectral gap $\Omega_g(\gamma)$ in units of the order parameter Δ_0 at $B=0$ and $I_S=0$ versus depairing energy. When $0.45\Delta_0 \le \gamma \le 0.5\Delta_0$, gapless superconductivity occurs. When $\gamma \ge 0.5\,\Delta_0$, superconductivity is suppressed.

10.1.4 Depairing induced by a magnetic field

The width and thickness of the wire are smaller than the London length $\lambda_L = \sqrt{\hbar/(\mu_0 \pi \sigma \Delta_0)} = 175\,\text{nm}$, where σ is the conductivity of the wire in its normal state, $\mu_0 = 4\pi.10^{-7}$ H.m and Δ_0 is the gap of the bulk superconductor; it is then predicted that the magnetic field applied perpendicularly to the wire penetrates uniformly [5] (see Figure 4).

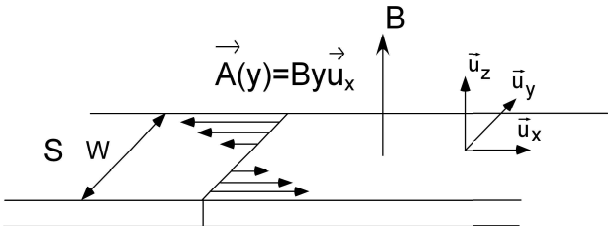

Figure 4: Sketch of a superconducting wire in a magnetic field B.

The vector potential in the wire corresponding to the applied magnetic field in the London

gauge can be written:

$$A(y) = By\vec{u}_x \tag{10}$$

where $\vec{u}_x$ is the unitary vector in the direction of the wire. The induced current density by the magnetic field is:

$$j_S(y) = -\frac{2\sigma}{\hbar} A_x(y) \int_0^\infty d\varepsilon \tanh\frac{\varepsilon}{2k_B T} \mathrm{Im}\left(\sin^2\theta\right). \tag{11}$$

These currents tend to screen the magnetic field. According to the laws of electromagnetism, these currents give rise to a magnetic field $\vec{B}$ with: $\mathrm{curl}\left(\vec{B}\right) = \mu_0 j_S \vec{u}_x$. The maximum value of $\int_0^\infty d\varepsilon \tanh\left(\varepsilon/2k_B T\right) \mathrm{Im}\left(\sin^2\theta\right)$ is $\Delta_0\pi/2$, a value reached when the density of states in the wire is a pure BCS one. Induced currents result then in a negligible correction factor $\simeq 1 - 1/60\left(w/\lambda_L\right)^2 \simeq 0.99$ for the magnetic field in the middle of the wire, justifying the assumption of uniform penetration of $\vec{B}$ in the wire.

The variations of the pairing angle along the transverse direction to the wire were numerically calculated using equilibrium Usadel equations and the boundary conditions $\nabla\theta = 0$. The densities of states in the middle and on the side of the wire for a magnetic field of 30 mT are plotted in Figure 5 for two situations: $w \simeq \xi_0$ (experimental situation) and $w = 2\,\xi_0$. It is found that, despite the transverse variation of A, θ is homogeneous for $w \simeq \xi_0$: the "rigidity length" of the order parameter, given by $\xi_0 = \sqrt{\hbar D/\Delta_0}$, is such that only an average effect of A is seen. In contrast, for $w = 2\,\xi_0$, variations of θ occur in the transverse y-direction, following the variation of A. For the experimental situation, we can thus use one-dimensional Usadel equations. The effect of the magnetic field is included in Eq. (6) by averaging A^2 over the width of the wire: $\left\langle A^2 \right\rangle_y = B^2 w^2/12$. The resulting depairing energy is then:

$$\gamma(B) = \frac{D}{6\hbar} e^2 B^2 w^2 . \tag{12}$$

The superfluid velocity V_S is constant, and the equations to calculate the DOS in presence of a magnetic field are the Eqs. (6) and (7) like in Section 10.1.3.

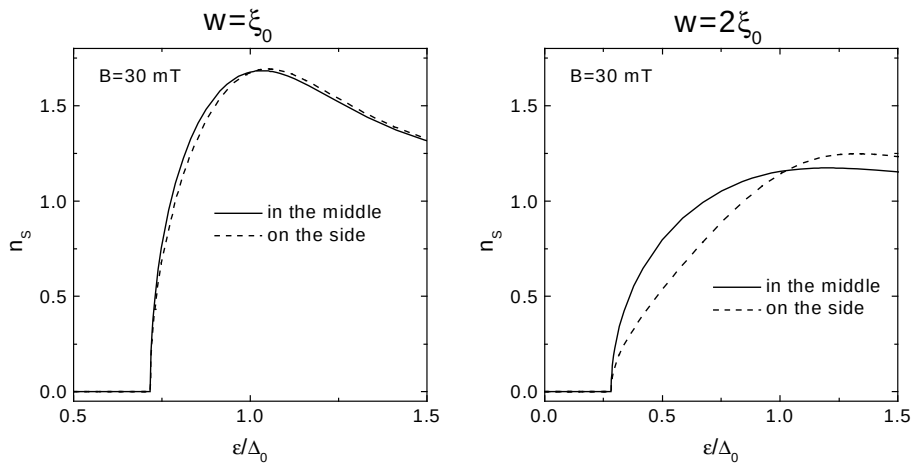

Figure 5: Density of states at two transverse positions in a wire of width w. The length $\xi_0 = \sqrt{\hbar D/\Delta_0}$ is the coherence length in the superconducting wire. The dotted line represents the DOS in the middle of the wire, the dashed line the DOS on the side of the wire. The experimental situation corresponds to $w = \xi_0$, where the differences between the two DOS are small.

10.1.5 Depairing induced by a supercurrent

The large reservoirs at the end of the wire are bulk superconductors with a real phase independent of energy. The difference in their phases is determined by the bias current. As a consequence, the phase gradient in the wire is also energy independent, so that the current density can be written as:

$$j_S = \frac{\sigma}{e}\nabla\varphi\int_0^\infty d\varepsilon \tanh\frac{\varepsilon}{2k_BT}\mathrm{Im}\left(\sin^2\theta\right), \tag{13}$$

leading to:

$$\nabla\varphi = \frac{eR}{L}\frac{I_S}{U_S(\theta)},$$

with:

$$U_S = \int_0^\infty d\varepsilon \tanh\frac{\varepsilon}{2k_BT}\mathrm{Im}\left(\sin^2\theta\right).$$

Since $\nabla\varphi$ is constant, the superfluid velocity V_S is uniform in space. The calculation of the DOS in presence of the supercurrent is then carried out using Eqs. (6) and (7) like in Section

10.1.3.

The depairing energy due to the supercurrent is equal to:

$$\gamma(I_S) = \frac{\hbar D}{2}\left(\frac{eR}{L}\right)^2\left(\frac{I_S}{U_S(\gamma)}\right)^2. \qquad (14)$$

A complication in the determination of the depairing energy arises from its self-consistent definition through Eq. (6), (7) and (13): the supercurrent density depends, on one hand on the depairing energy, and on the other hand on the density of states in the wire, which itself depends on the depairing energy. An approximate expression for the resulting $U_S(\gamma)/\Delta_0$, valid at $k_B T << \Delta$, for $\gamma/\Delta_0 \leq 0.3$ was found numerically (see Figure 6):

$$U_S(\gamma)/\Delta_0 \simeq \pi/2 - 1.8\,\gamma/\Delta_0 - 1.0\,(\gamma/\Delta_0)^2. \qquad (15)$$

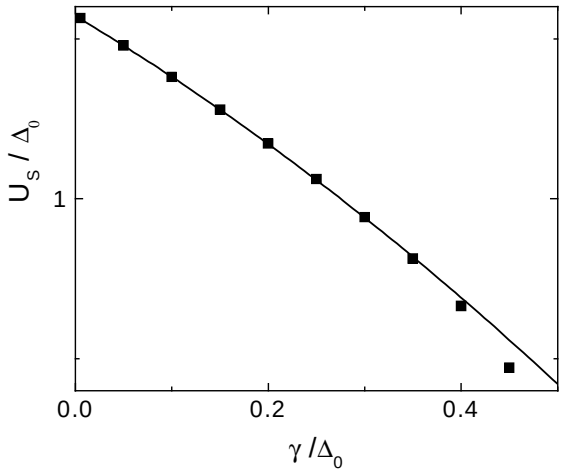

Figure 6: Symbols: Numerical calculation of the pair energy U_S in units of Δ_0 versus the depairing energy. Solid lines: Approximate expression $U_S(\gamma)/\Delta_0 \simeq \pi/2 - 1.8\,\gamma/\Delta_0 - 1.0\,(\gamma/\Delta_0)^2$.

A by-product of the Usadel equations is a calculation of the critical current. According to Eqs. (11) and (13), the supercurrent density in the wire can be written as a product of a density of charge in the superconducting state $\rho_S = e\nu_F U_S$ and of the superfluid velocity V_S. The density of charge in the superconducting state decreases with the depairing energy whereas the superfluid velocity increases. In zero magnetic field, the supercurrent versus the depairing

energy reaches a maximum corresponding to the critical current at $\gamma/\Delta_0 = 0.238$, leading to $I_C \simeq 0.75\,\Delta_0/\left(eR(\xi_0)\right)$ (see Figure 7.) Note that when the critical current is reached in such a wire, the density of states still presents a gap since $\gamma/\Delta_0 < 0.45$.

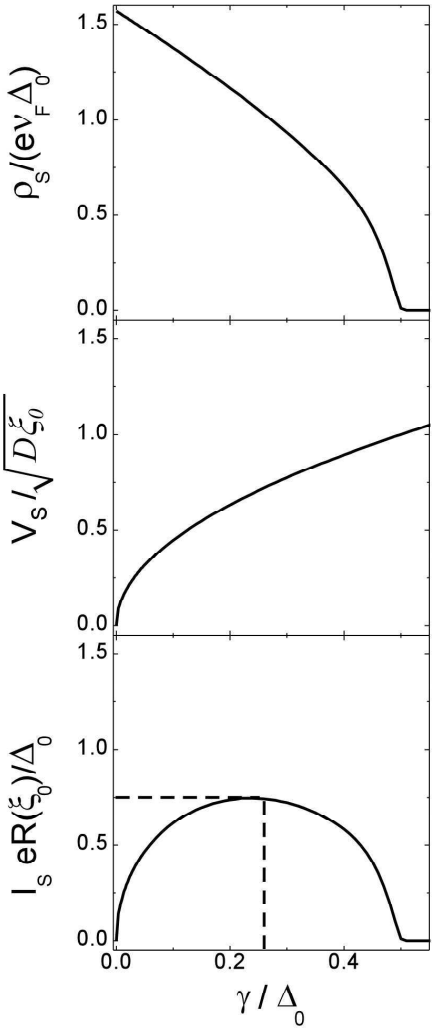

Figure 7: The normalized supercurrent (bottom panel) through a wire is proportional to a density of charge in the superconducting state ρ_s (upper panel) times the superfluid velocity V_s (middle panel). The supercurrent versus the depairing energy reaches a maximum corresponding to the critical current at $\gamma/\Delta_0 = 0.238$, leading to $I_C \simeq 0.75\,\Delta_0/\left(eR(\xi_0)\right)$.

This result has been obtained for a one-dimensional wire where U_S and therefore the current

density is homogeneous over the width of the wire. Such a simplification results from the negligible effect of the magnetic field created by the supercurrent in the experimental situation $w < \lambda_L$. This can be checked by calculating the vector potential created by the homogeneous current I_S. Assuming a cylindrical wire, the potential vector in the wire due to I_S is:

$$A_x(r) = \frac{\mu_0 I_S}{\pi w^2} r^2, \tag{16}$$

r being the distance from the center of the wire. The depairing energy due to this field is then on average:

$$\gamma_{ind} = \frac{e^2 D \mu_0^2 I_S^2}{40 \hbar \pi^2}, \tag{17}$$

whereas the direct depairing energy due to the supercurrent is equal to:

$$\gamma_{dir} = \frac{\hbar D}{2}\left(\frac{eR}{L}\right)^2\left(\frac{I_S}{U_S(\gamma)}\right)^2. \tag{18}$$

The ratio of the depairing energy due to the induced field and due to the supercurrent is $\approx (S/\lambda_L)^2 / 90 \approx 3.10^{-5}$ (we have used the fact that $U_S \simeq \Delta_0$). The effect of the induced magnetic field is thus negligible compared to the effect of the supercurrent for a wire of smaller width than λ_L.

For wider wires, the density of current is non-homogeneous and the superconducting velocity can be locally larger than the critical velocity [6]. The problem becomes non-local and non-linear. In this case, the critical current is equal to the current that results in the critical field on the side of the wire.

10.2 Experimental realization

10.2.1 Characteristics of the sample

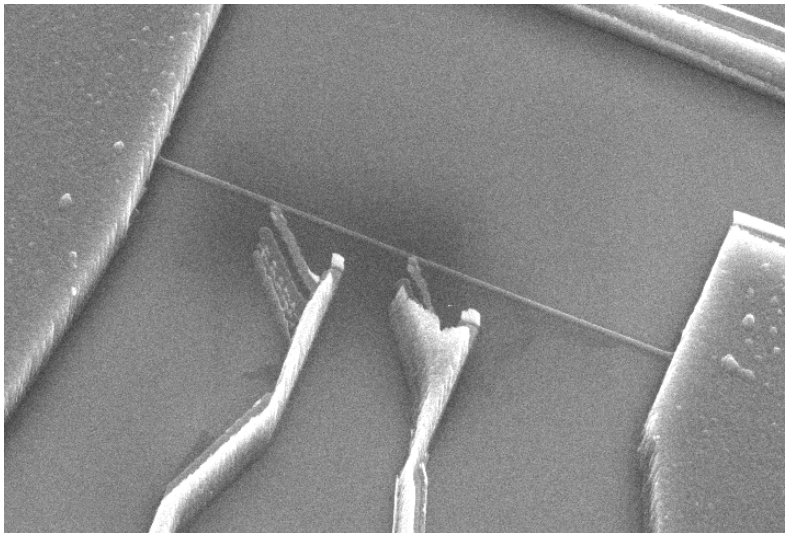

Figure 8: SEM micrograph of the sample viewed at an angle of 40°. The 120 nm-wide, 10 µm-long superconducting wire is connected to large superconducting thick pads. Two normal probes form tunnel junctions with the wire in order to measure the density of states in the superconducting wire.

A SEM micrograph of the measured sample is shown in Figure 8. The density of states in the wire was probed by two tunnel junctions. In chapter 2, we have shown that the differential conductance $dI/dV(V)$ of a Normal-Superconducting tunnel junction is at $T = 0$ directly proportional to the DOS in the superconducting wire neglecting charging effects. In the following, the contribution of charging and finite temperature effects are evaluated.

10.2.2 Contribution of the Coulomb blockade

In our experiment, it was found out that charging effects had a measurable effect. This is seen in Figure 9, which shows the differential conductance of the tunnel junction when superconductivity is suppressed by an applied magnetic field $B = 0.1$ mT . The conductance at zero voltage is reduced by $\simeq 8\%$.

Since this correction is small, a perturbative calculation in the impedance of the environment of the tunnel junction is sufficient (see Appendix of Chapter 2 and [7]). This impedance is modeled by the parallel combination of a resistance R_{eff} with a capacitance C_{eff}. In the perturbative theory, the probability to transfer a part ε of the available energy in the tunnel event to the environment $P(\varepsilon,T)$ does not depend on the temperature: $P(\varepsilon,T)=P(\varepsilon,0)$, and is equal at low energy to:

$$P(\varepsilon)\approx\frac{\alpha}{\varepsilon_0}\left(\frac{\varepsilon}{\varepsilon_0}\right)^{\alpha-1} \quad \text{for } 0<\varepsilon<<\varepsilon_0, \tag{19}$$

where $\alpha=2R_{eff}/R_K$, and $\varepsilon_0=e^2/(\pi\alpha C_{eff})$. The parameters α and ε_0 are deduced from the differential conductance when a magnetic field larger than the critical field of the superconductor is applied. The DOS in the wire is then constant and the differential conductance is given by:

$$\frac{dI}{dV}(V)=\frac{1}{R_T}\left|\frac{eV}{\varepsilon_0}\right|^{\alpha} \quad \text{for } eV<<\varepsilon_0. \tag{20}$$

In Figure 9, a fit of the differential conductance of the tunnel junction by the perturbative theory of Coulomb blockade is presented. The fit parameters for the environment are $R_{eff}=250\ \Omega$ and $C_{eff}=8$ fF.

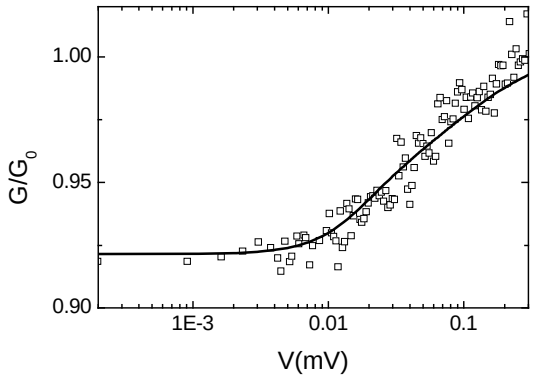

Figure 9: Differential conductance of the tunnel junction between the side probe electrode and the wire in its normal state, normalized to the conductance G_0 at large voltage. Due to Coulomb blockade, the conductance presents a dip at low voltage. The line is a fit using Coulomb blockade theory (Eqs. (19) and (20)) with an electromagnetic environment that consists of the parallel combination of $R_{eff}=250\ \Omega$ and $C_{eff}=8$ fF.

Using this expression of $P(\varepsilon,T)$, the differential conductance reads (see Chapter 2):

$$\frac{dI}{dV}(V)=\frac{1}{R_T}\int_0^{+\infty}dE\int_0^{+\infty}d\varepsilon\; n_S(E-\varepsilon)P(\varepsilon,T)\left(\frac{\partial f_N}{\partial E}(eV-E)+\frac{\partial f_N}{\partial E}(eV+E)\right), \qquad (21)$$

where n_S is the density of states in the superconducting wire and f_N the quasiparticles energy distribution according to a Fermi function.

In Figure 10, the corrections due to Coulomb blockade are exemplified by a fit of data with and without taking into account Coulomb blockade. The peak value in dI/dV is just reduced by a few percent when Coulomb blockade is included.

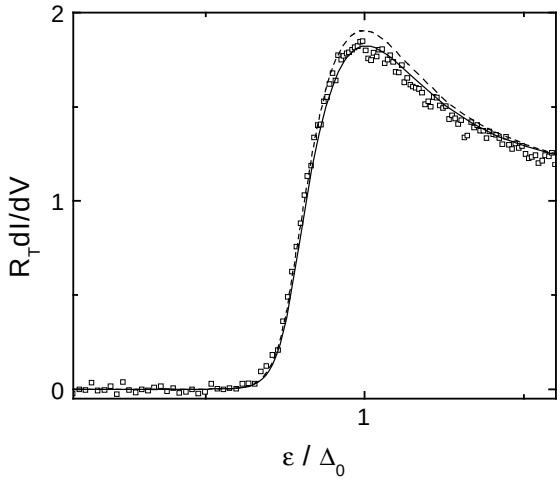

Figure 10: Symbol: Measured differential conductance of the tunnel junction between the normal slightly resistive probe electrode and the superconducting wire exposed to a magnetic field of $23\ \mathrm{mT}$. Dashed line: fit of the data without taking into account charging effect of the junctions. Solid line: Fit of the data taking into account Coulomb blockade of tunneling with an electromagnetic environment that consists of the parallel combination of $R_{eff}=250\ \Omega$ and $C_{eff}=8\,\mathrm{fF}$.

The finite temperature of the normal probe is now to be taken into account in f_N.

10.2.3 Finite temperature effects

In the experiment, the temperature of the probe electrodes is slightly dependent on V due to their geometry. Indeed, Joule heating is a concern at low temperature. Any current

results in production of heat (thermic energy), which can be transferred directly to the phonons in the wire or to electrons in the large pads. At sub-Kelvin temperatures, the first process is very inefficient because the phonon emission rate goes like $5\kappa_{ph}\left(k_B T_{ph}\right)^3$ with $\kappa_{ph} \simeq 10$ ns^{-1}meV^{-3} [8]. Moreover, in our experiment, the normal probe electrode is thermally isolated from the larger contact pad by superconducting connections due to the fabrication process, limiting the efficiency of the second process. Therefore, heat transport only takes place through electron-phonon coupling in the probe electrode and electron tunneling through the junction. Since the volume, in which the coupling to phonons can take place is small, this thermalization mechanism is all the more inefficient: an input power in the fW range can significantly rise the temperature. At bias voltages larger than the superconducting gap, heating of the normal part by the tunnel current has a sizeable effect on electron temperature. In contrast, at bias voltages slightly smaller than the gap voltage, only quasiparticles with a large energy can tunnel from the normal part (see Figure 11), resulting in an effective cooling of the normal part. The electronic temperature T is found by solving the heat equation [9] (see Equation (22)) taking into account the heat transfer to the phonon bath at temperature T_{ph} and the heat transfer through the junction:

$$\Sigma\Omega\left(T^5 - T_{ph}^5\right) + \int dE \frac{E}{e^2 R_T} n_S\left(E + eV\right)\left(1 - f_N\left(E,T\right)\right) - P_{in} = 0\,, \tag{22}$$

with Σ the electron-phonon coupling constant, Ω the volume of the isolated normal probe

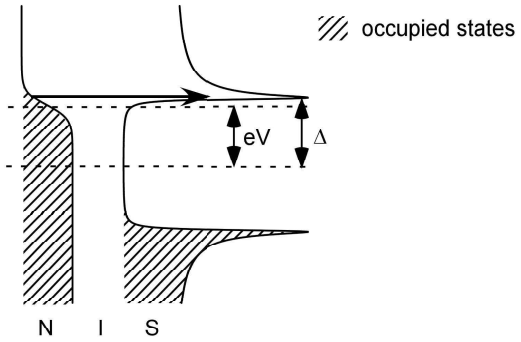

Figure 11: Principle of electron cooling effect in a normal superconducting tunnel junction. When the junction is biased just below the gap of the superconducting part, only hot quasiparticles from the normal part can tunnel, resulting in an effective cooling of the normal part.

and where P_{in} accounts for additional uncontrolled heat flow, which can be attributed to spurious electromagnetic noise. The electron-phonon coupling constant depends on the metal and is related to κ_{ph} by $\Sigma = 24\zeta(5)\nu_F \kappa_{ph} k_B^5$ with $\zeta(5) = 1.04$. In copper, $\Sigma \simeq 2$ nW μm^{-3} K^{-5}. In the experiment, the differential conductance of the probe tunnel junction at $B = 0$ and $I_S = 0$ was fit using Ω and P as fit parameters in Eq. (22) and including Eq. (21) with a BCS DOS for n_S, a Fermi function at an effective temperature dependent on V for f. The volume of the normal part is also a fit parameter because of the poorly defined geometry of the electrode. Coulomb blockade of tunneling was taken into account with the parameters determined above. The phonons were assumed to be thermalized at the refrigerator temperature $T_{ph} = 25$ mK. In Figure 12, the differential conductance calculated using the fit parameters $\Omega = 0.08\ \mu\text{m}^3$ and $P_{in} = 185$ aW is compared to the data. The corresponding

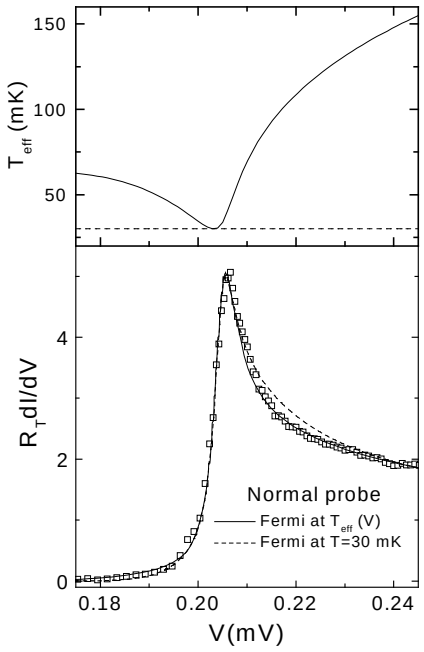

Figure 12: Bottom panel: Symbols: Measured differential conductance of the tunnel junction between the normal, thermally isolated, probe and the superconducting wire. Solid line is a fit using a BCS density in the superconducting part and assuming an energy distribution according to a Fermi function at $T_{eff}(V)$ plotted in the top panel. Dashed line is the calculated dI/dV using a BCS density in the superconducting part and assuming an energy distribution according to a Fermi function at $T = 30$ mK (corresponding to the dashed line in the top panel).

electronic temperature dependence on the bias voltage V is also plotted. The order of magnitude of Ω is in agreement with the geometry. The value of P_{in} leads, for bias voltages smaller than the gap, to an effective temperature of 65 mK.

10.3 Measurement of the density of states in a superconductor carrying a supercurrent or exposed to a magnetic field

10.3.1 DOS in the superconducting wire: experiment versus theory

The results of our paper published in Phys. Rev. Lett. **90**, 127001 (2003) are reproduced here. In Figure 13, the solid lines are fits taking into account Coulomb blockade of tunneling and temperature corrections.

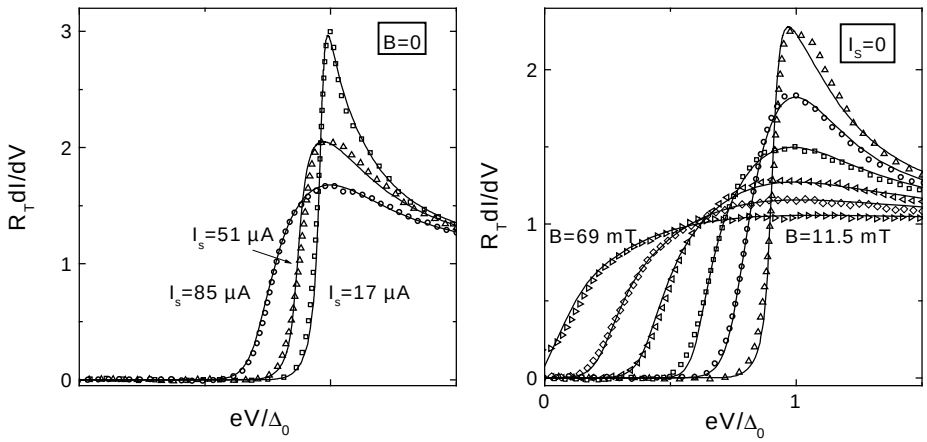

Figure 13: Normalized differential conductance of the probe tunnel junction: Left: at $B = 0$, as a function of the supercurrent I_S. Right: at $I_S = 0$, as a function of the magnetic field B. The solid lines are the best fits of the data.

As predicted by theory, the gapless regime obtained for $0.45\,\Delta_0 < \gamma < 0.5\,\Delta_0$ cannot be reached with a supercurrent, because the wire switches to the resistive branch for a depairing energy equal to $0.24\,\Delta_0$. The critical current was estimated to be $I_C = 106\,\mu\text{A}$. The values of

the fit parameters γ are given in Figure 14. By fitting $\gamma(I_S, B)/\Delta_0$ with the equation, deduced from Usadel equations:

$$\frac{\gamma}{\Delta_0} = \left(\frac{\Delta_0}{U_S(\gamma)} \frac{I_S}{I_\gamma} \right)^2 + \left(\frac{B}{B_\gamma} \right)^2, \tag{23}$$

and Eq. (15) , we find $I_\gamma = 240\,\mu\text{A}$ and $B_\gamma = 105\,\text{mT}$. The theoretical values assuming that the "electrical dimensions" of the wire are the geometrical ones are $I_\gamma = \sqrt{2}\Delta_0 e^{-1}\xi_0^{-1}(L/R) = 310\,\mu\text{A}$ and $B_\gamma = \hbar\sqrt{6}(\xi_0 ew)^{-1} = 105\,\text{mT}$. The depairing induced by the current is then larger than the predicted one. Knowing that $I_\gamma \propto \xi_0^{-1}$ and $B_\gamma \propto (w\xi_0)^{-1}$, the experimental values of I_γ and B_γ can be used to extract effective values $\xi_{0\text{eff}} = 162\,\text{nm}$ (instead of $125\,\text{nm}$) and $w_{\text{eff}} = 93\,\text{nm}$ (instead of $120\,\text{nm}$). This corresponds in turn to an increased value of the diffusive coefficient $D = 81\,\text{cm}^2\text{s}^{-1}$ and, through the expression of the resistance, to an effective thickness $t_{\text{eff}} = 31\,\text{nm}$ (instead of $40\,\text{nm}$). Reduced effective dimensions could be partly attributed to the surface oxidation of aluminum, which was exposed to air before measurement, and to surface roughness. Yet, the typical thickness of the oxide layer is about $2\,\text{nm}$ and surface roughness is usually estimated at about $3\,\text{nm}$. It can be argued that it is not enough to account for the reduced dimensions. Another explanation might be that the diffusion coefficient D is misestimated from the DC conductivity through the Einstein relation $\sigma = \nu_F e^2 D$.

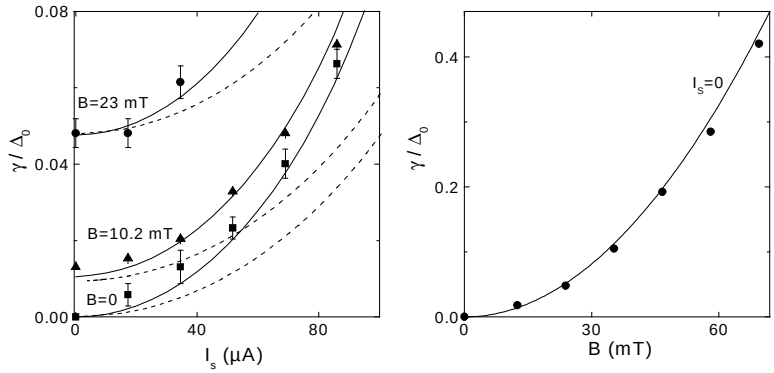

Figure 14: Depairing energy γ (in units of the gap Δ_0 at $B = 0$ and $I_S = 0$) for different currents and magnetic fields, deduced from the fits of the dI/dV . Solid lines are fits with theory leading to depairing current and magnetic field $I_\gamma = 240\,\mu\text{A}$ and $B_\gamma = 105\,\text{mT}$. Dashed lines: Theoretical predictions with the depairing current and magnetic field $I_\gamma = 310\,\mu\text{A}$ and $B_\gamma = 105\,\text{mT}$ calculated from the electrical and geometrical characteristics of the wire.

10.3.2 DOS at two different positions in the wire

In the paper, only the results obtained for the side junction are presented. The reduction of the gap and the smearing of the peaks when the magnetic field or the supercurrent increase are also observed at the position of the middle junction. Yet, the DOS in the wire at the two positions for a fixed supercurrent or a fixed magnetic field were different (see Figure 15). When comparing the DOS at the side position to the middle position, a given magnetic field induces more depairing, whereas a given supercurrent induces less depairing. This difference is attributed to a difference in the wire width w at the two junction positions. The depairing energy scales as w^2 in the case of a magnetic field and as $1/w^2$ in the case of a supercurrent. The difference estimated from the depairing energy gives $w_L / w_R = 1.2$, where w_L and w_R are the width of the wire at the side and middle positions, respectively. This ratio is in good agreement with the estimated one from SEM observation.

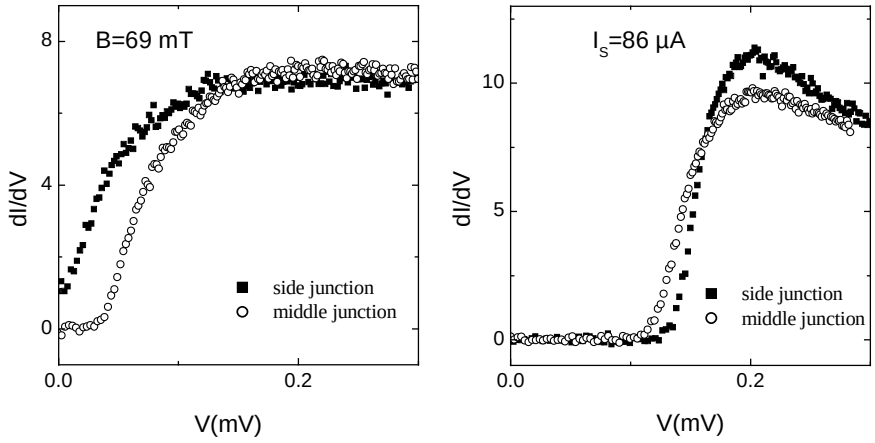

Figure 15: Comparison of differential conductances of the two probe tunnel junctions at $B = 69\,\mathrm{mT}$ and $I_S = 0$ (left panel) and $B = 0$ and $I_S = 86\,\mu\mathrm{A}$ (right panel). At the position of the side junction, the magnetic field induces more depairing whereas supercurrent induces less depairing than at the middle junction. This difference is explained by the different widths of the wire at the two junctions. At the position of the side junction, the wire is wider.

10.4 Conclusion

The effect on the superconducting order of a supercurrent I_S and of a magnetic field B has been probed by tunneling spectroscopy. As predicted by the theory of mesoscopic superconductivity in diffusive conductors, the overall effect solely depends on a single parameter, the depairing energy. For our narrow wire, the Usadel equations lead to a simple expression for this depairing energy as a function of I_S and B, which compares with the experimental determination of the depairing energy. Yet, the experimental values of the characteristics depairing current I_γ and magnetic field B_γ correspond to effective dimensions of the wire smaller than the geometrical dimensions measured on a SEM micrograph. This discrepancy, also observed on another sample, is partly attributed to surface roughness and surface oxidation but is not totally understood.

Appendix: Article reproducing results on the depairing in a superconductor

We reproduce here the article published in Phys. Rev. Lett. **90**, 127001 (2003).

Density of States in a Superconductor Carrying a Supercurrent

A. Anthore, H. Pothier, and D. Esteve

Service de Physique de l'Etat Condensé, Direction des Sciences de la Matière, CEA-Saclay, 91191 Gif-sur-Yvette, France

(Received 20 December 2002; published 24 March 2003)

We have measured the tunneling density of states (DOS) in a superconductor carrying a supercurrent or exposed to an external magnetic field. The pair correlations are weakened by the supercurrent, leading to a modification of the DOS and to a reduction of the gap. As predicted by the theory of superconductivity in diffusive metals, we find that this effect is similar to that of an external magnetic field.

DOI: 10.1103/PhysRevLett.90.127001 PACS numbers: 74.78.Na, 74.20.Fg, 74.25.Sv

How is the superconducting order modified by a supercurrent? The superconducting order is based on pairing electronic states which transform into one another by time reversal. The ground-state wave function corresponds to a coherent superposition of doubly empty and doubly occupied time-reversed states, in an energy range around the Fermi level given by the BCS gap energy. When an external magnetic field $\vec{B} = \mathrm{curl}\vec{A}$ is applied, time-reversed states are dephased differently, resulting in a weakening of superconductivity. In the presence of a supercurrent, the superconducting order no longer corresponds to the pairing of time-reversed states, which results in a kinetic energy cost, and again in a weakening of superconductivity. In the early stages of the theory of superconductivity, it was found that, in diffusive superconductors (in which the electron mean-free-path is short compared to the BCS coherence length) and in homogeneous situations, the modification of the superconducting order by a magnetic field, by a current, and by paramagnetic impurities can be described by a single parameter, the depairing energy Γ [1]. Later on, the reformulation of the theory by Usadel [2,3] in the diffusive limit extended this equivalence to inhomogeneous situations, where the modulus of the order parameter may vary in space. In the Usadel equations, all physical quantities involve only the intrinsic combination $\vec{\nabla}\varphi - (2e/\hbar)\vec{A}$, where the gradient $\vec{\nabla}\varphi$ in the phase of the superconducting order parameter is associated with the supercurrent, revealing the equivalence of a supercurrent and of an applied magnetic field. The Usadel equations are now at the basis of the understanding of mesoscopic superconductivity in diffusive conductors [4,5]. Experimentally, measurements of the density of states (DOS) in a thin superconductor placed in an in-plane magnetic field were well accounted for by the concept of depairing energy [6]. In contrast, the effect of a supercurrent has been partly addressed in a single experiment, focused on the reduction of the superconducting gap close to the critical temperature [7]. A complication of the experiments with a supercurrent is that, if the sample width exceeds the London penetration length λ_L, the current distribution given by the nonlocal equations of electrodynamics [8] is not homogeneous. In the experiment reported here, the superconductor is wire shaped, with thickness and width smaller than λ_L, so that the current flow is homogeneous and the magnetic field penetrates completely. Moreover, the effect of the magnetic field induced by the supercurrent is then negligible. This simple geometry allows one to test the fundamental equivalence between the effect of a magnetic field and of a supercurrent in a diffusive superconductor and to compare precisely with the predictions of the Usadel equations.

Our experiment was performed on a current-biased superconducting wire made of aluminum, placed in a perpendicular magnetic field B (see Fig. 1). The density of states in the wire was inferred from the differential conductance $dI/dV(V)$ of a tunnel junction formed

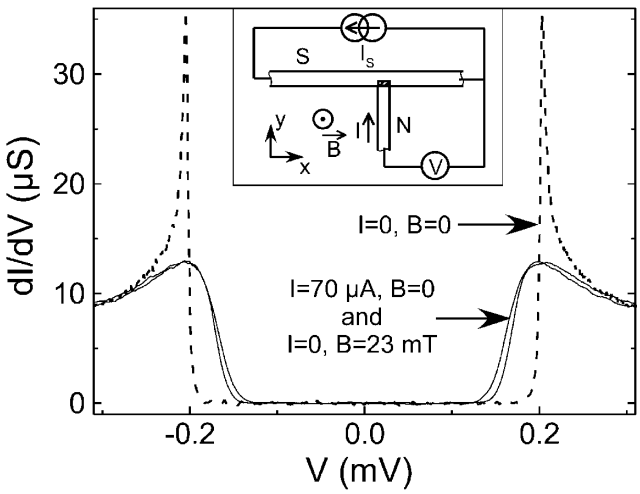

FIG. 1. Inset: layout of the experiment: a 10-μm-long, 120-nm-wide, and 40-nm-thick superconducting (aluminum) wire can be current biased at I_S or exposed to a magnetic field B. A normal probe electrode forms a tunnel junction (dashed area) with the wire. Main panel: measured $dI/dV(V)$ for different combinations of the bias current and magnetic field: dashed line: $I_S = 0$ and $B = 0$; solid lines: $I_S = 70$ μA and $B = 0$, and $I_S = 0$ and $B = 23$ mT. To a good approximation (see text), the differential conductance of the junction $dI/dV(V)$ is proportional to the DOS in the superconductor.

 © 2003 The American Physical Society

between a small section of the wire and a normal probe electrode made of copper. Disregarding Coulomb blockade and temperature effects (see below), $dI/dV(V)$ is proportional to the DOS $n(eV)$. The sample was fabricated in an electron-beam evaporator in a single pump-down, using the three-angle shadow-mask technique through a PMMA suspended mask patterned using e-beam lithography [9]. The substrate was thermally oxidized silicon. The 10-μm-long aluminum wire, with width $w = 120$ nm and thickness $t = 40$ nm was superficially oxidized in order to form a tunnel barrier with the copper probe electrode overlapping it on an area 150×60 nm^2. The sample was mounted in a copper box thermally anchored to the mixing chamber of a dilution refrigerator. Measurements were performed at 25 mK. From the low-temperature, high-magnetic-field wire resistance in the normal state, $R = 77\ \Omega$, the conductivity $\sigma = 27\ \Omega^{-1}\,\mu\text{m}^{-1}$ is inferred assuming that the electrical cross section of the wire is $S = wt$. The diffusion coefficient $D = 49\ \text{cm}^2\,\text{s}^{-1}$ is then deduced using Einstein's relation $\sigma = N(0)e^2D$, where $N(0) = 2.15 \times 10^{47}\ \text{J}^{-1}\,\text{m}^{-3}$ is the density of states at the Fermi level of aluminum and e is the electronic charge. The superconducting gap $\Delta_0 = 205\ \mu\text{eV}$ was deduced from the differential conductance-voltage characteristic $dI/dV(V)$ measured at $B = 0$, $I_S = 0$ (dashed line in Fig. 1). Using these parameters, we obtain the superconducting coherence length $\xi_0 = \sqrt{\hbar D/\Delta_0} \approx 125$ nm and the London length $\lambda_L = \sqrt{\hbar/(\mu_0 \pi \sigma \Delta_0)} \approx 175$ nm. Since $\lambda_L \gg w/2$, the current density is homogeneous when the wire is current biased, and a magnetic field penetrates uniformly in the wire. The measured critical current of the wire at $B = 0$ was $I_c = 106\ \mu\text{A}$.

In Fig. 1, two $dI/dV(V)$ curves are shown, respectively, measured at $I_s = 70\ \mu\text{A}$, zero field, and at zero current, $B = 23$ mT. The reduction of the gap and the smearing of the peak near the gap energy are similar in the two situations, bringing already evidence of the equivalent effect of I_S and B. Note that the magnetic field created by the supercurrent has a negligible effect: for $I_s = 70\ \mu\text{A}$ in the wire (see Fig. 1), $\mu_0 I_s/(2\pi w) \sim 0.15$ mT whereas the resulting DOS is recovered at $I_S = 0$ with $B = 23$ mT. A complete set of data is presented in Fig. 2, with $dI/dV(V)$ measured for $I_S = 17$, 51, and 85 μA at $B = 0$, and for $B = 11.5$ to 69 mT by steps of 11.5 mT, at $I_S = 0$. Note that when the wire is current biased, the superconducting state is metastable. In practice, for bias currents larger than 85 μA, the system switches to the resistive state during the recording of the $dI/dV(V)$ curve. The measured curve is then similar to that obtained in the normal state. In order to account quantitatively for the data, we use the Usadel theory [2,3]. In this theory, correlations between electrons of opposite spins and momenta are described by a complex function $\theta(\vec{r}, E)$, the pairing angle, which depends on both space and energy, and a local complex phase

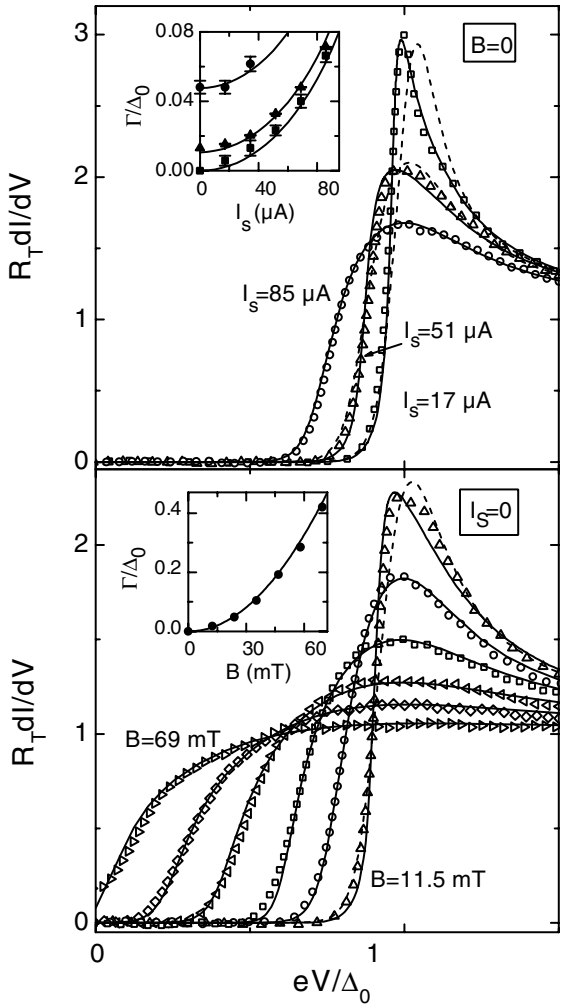

FIG. 2. Normalized differential conductance $dI/dV(V)$ of the probe tunnel junction: Top: at $B = 0$, as a function of the supercurrent I_S (from right to left: $I_S = 17$, 51, and 85 μA). Bottom: at $I_S = 0$, as a function of the magnetic field B (from 11.5 to 69 mT by steps of 11.5 mT). Solid lines are best fits with $dI/dV(V)$ calculated with an electronic temperature dependent on V (see text); dashed lines are the best fits with $dI/dV(V)$ calculated with a constant electronic temperature. Insets: depairing energy Γ (in units of the gap Δ_0 at $B = 0$ and $I_S = 0$) for different currents and magnetic fields, deduced from the fits of $dI/dV(V)$. In the top inset, square symbols correspond to the data in the main panel ($B = 0$), whereas triangles and disks were obtained from data taken at $B = 10.2$ mT and $B = 27$ mT, respectively. Solid lines: fits with theory, leading to depairing current and magnetic field $I_\Gamma = 240\ \mu\text{A}$ and $B_\Gamma = 105$ mT.

$\varphi(\vec{r}, E)$. The local density of states is given by $n(\vec{r}, E) = N(0)\text{Re}\{\cos[\theta(\vec{r}, E)]\}$. The pairing angle and the complex phase obey the Usadel equations:

$$\frac{\hbar D}{2}\nabla^2\theta + \left[iE - \frac{\hbar}{2D}\vec{v}_s^2\cos\theta\right]\sin\theta + \Delta\cos\theta = 0, \quad (1)$$

$$\vec{\nabla}(\vec{v}_s \sin^2\theta) = 0, \quad (2)$$

where we have introduced the superfluid velocity $\vec{v}_s = D[\vec{\nabla}\varphi - (2e/\hbar)\vec{A}]$. A term describing spin-flip scattering, which is found negligible in our experiment, has been omitted here. The pairing potential $\Delta(\vec{r})$ is determined self-consistently by

$$\Delta(\vec{r}) = N(0)V_{\text{eff}} \int_0^{\hbar\omega_D} dE \tanh\left(\frac{\beta E}{2}\right) \text{Im}(\sin\theta), \quad (3)$$

where V_{eff} is the pairing interaction strength, ω_D is the Debye pulsation, $\beta = (k_B T)^{-1}$, k_B is the Boltzmann constant, and T is the temperature of the superconductor.

The supercurrent density $\vec{j}$ is given by

$$\vec{j}(\vec{r}) = \frac{\sigma}{eD} \int_0^{\infty} dE \tanh\left(\frac{\beta E}{2}\right) \text{Im}(\sin^2\theta)\vec{v}_s. \quad (4)$$

In a situation such as ours where the system consists entirely of a single superconductor, $\vec{\nabla}\varphi$ does not depend on energy, and $\vec{j}$ can be written as a product of the density of charge in the superconducting state $\rho_S(\vec{r}) = eN(0)U_S(\vec{r})$, with $U_S(\vec{r}) = \int_0^{\infty} dE \tanh(\frac{\beta E}{2}) \text{Im}(\sin^2\theta)$.

We have first checked numerically that the dependence of θ on the directions transverse to the wire could be neglected because the width and thickness are smaller than the superconducting coherence length ξ_0, which is the characteristic length scale for the variations of θ. As a consequence, all the quantities can be replaced by their values averaged on the transverse directions. In the London gauge, the effect of the magnetic field is described by a vector potential parallel to the wire axis x, with an amplitude $A_x = By$, so that $\langle A_x \rangle = 0$ and $\sqrt{\langle A_x^2 \rangle} = Bw/(2\sqrt{3})$ [10]. The constant phase gradient $\partial\varphi/\partial x$ is given by the supercurrent $I_S = jS = U_S L/(eR)(\partial\varphi/\partial x)$. Since $\partial^2\varphi/\partial x^2 = 0$, Eq. (2) reduces to $\partial(\sin^2\theta)/\partial x = 0$. No spatial dependence remains in Eq. (1), and one recovers the generic equation given in Ref. [1]:

$$E + i\Gamma\cos\theta = i\Delta\frac{\cos\theta}{\sin\theta}, \quad (5)$$

where

$$\Gamma = \frac{\hbar}{2D}\langle \vec{v}_s^2 \rangle = \frac{\hbar D}{2}\left[\left(\frac{\partial\varphi}{\partial x}\right)^2 + \left(\frac{2e}{\hbar}\right)^2 \langle A_x^2 \rangle\right] \quad (6)$$

is the depairing energy, which contains the effect of both a phase gradient and a magnetic field. Note that since $\Gamma/\Delta_0 = \frac{1}{2}(\xi_0\partial\varphi/\partial x)^2 + \frac{1}{6}[\xi_0 wB/(\hbar/e)]^2$ the relevant parameters are the phase difference between two points of the wire distant by ξ_0 and the number of flux quanta in an area $w\xi_0$. The depairing energy is related to the external parameters I_s and B by the equation

$$\frac{\Gamma}{\Delta_0} = \left(\frac{\Delta_0}{U_S(\Gamma)}\frac{I_s}{I_\Gamma}\right)^2 + \left(\frac{B}{B_\Gamma}\right)^2, \quad (7)$$

where we have introduced the characteristic depairing current and magnetic field $I_\Gamma = \sqrt{2}\Delta_0/[eR(\xi_0)]$, with $R(\xi_0) = R\xi_0/L$ the resistance of the wire on a length ξ_0, and $B_\Gamma = \sqrt{6}(\hbar/e)/(w\xi_0)$. Since the transverse dimensions of the wire are smaller than the London length λ_L, the depairing energy due to the induced field is negligible (smaller by a factor $\sim 10^{-4}$ [11]) compared to the one due to the supercurrent. The DOS for a given depairing energy Γ is obtained from the self-consistent solution of Eqs. (3) and (5). For practical purposes, we give the approximate expressions for the resulting $\Delta(\Gamma)/\Delta_0$ and $U_s(\Gamma)/\Delta_0$, valid, at $k_B T \ll \Delta$, for $\Gamma/\Delta_0 \lesssim 0.3$:

$$\frac{\Delta(\Gamma)}{\Delta_0} \simeq 1 - 0.75\frac{\Gamma}{\Delta_0} - 0.54\left(\frac{\Gamma}{\Delta_0}\right)^2,$$
$$\frac{U_s(\Gamma)}{\Delta_0} \simeq \pi/2 - 1.8\frac{\Gamma}{\Delta_0} - 1.0\left(\frac{\Gamma}{\Delta_0}\right)^2. \quad (8)$$

The differential conductance measured in the experiments is not exactly proportional to the density of states $n(E)$ in the superconducting wire. Two effects must be taken into account in order to calculate $dI/dV(V)$ from $n(E)$: Coulomb blockade and the temperature of the probe electrode. Coulomb blockade results from the finite impedance of the electromagnetic environment of the tunnel junction [4]. The characteristics of the environment are found from the $dI/dV(V)$ characteristic of the circuit in the normal state, reached at $B > 0.1$ T, which presents a 10% logarithmic dip at zero voltage. The environment can be modeled by a capacitance $C = 8$ fF in parallel with a resistance $R = 250\ \Omega$. Coulomb blockade results in a convolution of the density of states with a function $P(E)$, the probability for the electromagnetic environment of the tunnel junction to absorb an energy E [12]:

$$\frac{dI}{dV}(V) = \frac{1}{R_t}\int_0^{eV} dE n(E) P(eV - E). \quad (9)$$

Here, $P(E) = \alpha/E_0(E/E_0)^{\alpha-1}$ for E smaller than $E_0 = e^2/\pi\alpha C$, with $\alpha = 2R/(h/e^2)$. The tunnel resistance of the junction was $R_t = 140\ \text{k}\Omega$. As a result of this correction, the peak value of $n(E)$ is reduced by a few percent in $dI/dV(V)$. Finite temperature in the normal probe results in a further convolution with the derivative of a Fermi function. In our experimental setup, this temperature is slightly voltage dependent, because the probe electrode is thermally isolated from the larger contact pads by superconducting connections. Heat transport occurs only by electron-phonon coupling and by electron tunneling through the junction. Since both mechanisms are very inefficient, even an input power $\mathcal{P}_{\text{in}}$ in the fW range can induce a significant temperature increase. At bias voltages large compared to the superconducting gap, heating by the tunneling current has a sizable effect. In contrast, at bias voltages V slightly below Δ/e, only quasiparticles at energies larger than $\Delta - eV$ can tunnel, resulting in

evaporative cooling [13]. The effective electron temperature T is obtained by solving the heat equation

$$\Sigma\Omega(T^5 - T_{\rm ph}^5) - \mathcal{P}_{\rm in} + \int dE \frac{E}{e^2 R_T} n(E + eV)(1 - f(E)) = 0. \quad (10)$$

The first term describes heat transfer to the phonon bath, with $\Sigma \simeq 2\ \mathrm{nW\,\mu m^{-3}\,K^{-5}}$ for Cu [9], $\Omega \simeq 0.08\ \mu\mathrm{m}^3$ is the volume of the normal region of the probe electrode, and $T_{\rm ph} = 25$ mK is the phonon temperature. The second term accounts for additional uncontrolled heat flow, which we attribute to spurious electromagnetic noise. The third term accounts for heat transfer through the junction, with $f(E)$ the Fermi function at temperature T. From the fit of the data at $B = 0$ and $I_s = 0$, we find $\mathcal{P}_{\rm in} = 185$ aW, corresponding to $T = 65$ mK at $eV \ll \Delta_0$. The maximum cooling effect is reached at $eV/\Delta_0 = 0.99$, where $T = 30$ mK; heating dominates for $eV/\Delta_0 > 1.02$, with $T = 210$ mK at $eV/\Delta_0 = 1.5$.

In Fig. 2, we present the best fits of the data by solid lines, taking into account both Coulomb blockade and temperature corrections. The values of the fit parameter Γ for each curve are given in the insets. For a comparison, fits with a constant electron temperature ($T = 60$ mK) are shown by dashed lines. The V-dependent temperature correction matters only for the sharpest curves. In turn, by fitting $\Gamma(I_s, B)/\Delta_0$ with Eqs. (7) and (8), we find $I_\Gamma = 240\ \mu$A and $B_\Gamma = 105$ mT. The theoretical values, assuming that the electrical dimensions of the wire are identical to the geometrical ones, are $I_\Gamma = 310\ \mu$A and $B_\Gamma = 105$ mT. Conversely, the experimental values of $I_\Gamma \propto \xi_0^{-1}$ and $B_\Gamma \propto (w\xi_0)^{-1}$ can be used to extract effective values $\xi_{0\rm eff} = 162$ nm (instead of 125 nm) and $w_{\rm eff} = 93$ nm (instead of 120 nm). This corresponds in turn to an increased value of the diffusive coefficient: $D = 81\ \mathrm{cm^2\,s^{-1}}$ and, through the resistance, to an effective thickness $t_{\rm eff} = 31$ nm (instead of 40 nm). Reduced effective dimensions for electrical transport could be attributed partly to the surface oxidation of the aluminum, which was exposed to air at atmospheric pressure before measurement, and to surface roughness.

A by-product of the Usadel equations is a straightforward calculation of the critical current. According to Eq. (4), $I_S \propto U_s(\Gamma)\partial\varphi/\partial x$. Since $U_s(\Gamma)$ decreases with Γ, I_s presents a maximum as a function of $\partial\varphi/\partial x$, which is the thermodynamic critical current. At $B = 0$ and $k_B T \ll \Delta_0$, the maximum occurs at $\xi_0\partial\varphi/\partial x \approx 0.69$ and corresponds, in agreement with [14], to $I_c \approx 0.75 S\Delta_0^{3/2}\sqrt{N(0)\sigma/\hbar} \approx 0.53 I_\Gamma = 125\ \mu$A (using the experimental determination of I_Γ). The difference with the measured $I_c = 106\ \mu$A might be due to the uncontrolled environment of the wire and to inhomogeneities in the wire cross section.

In conclusion, we have measured by tunneling spectroscopy on a superconducting wire the effect on the superconducting order of a supercurrent I_S and of an external magnetic field B. As predicted by the theory of superconductivity in diffusive conductors, the overall effect solely depends on a single parameter, the depairing energy Γ. For our narrow wire, the Usadel equations lead to a simple expression for this depairing energy as a function of I_S and B, which compares well with the experimental determination of Γ.

We thank C. Mitescu for the communication of his Ph.D. thesis and for correspondence and N. Birge for his comments on the manuscript. We acknowledge the technical help of P. Orfila and permanent input from M. Devoret, P. Joyez, F. Pierre, C. Urbina, and D. Vion.

[1] For a review, see K. Maki, in *Superconductivity*, edited by R. D. Parks (Marcel Dekker, New York, 1969), p. 1035.
[2] K. D. Usadel, Phys. Rev. Lett. **25**, 507 (1970).
[3] For a review, see W. Belzig, F. Wilhelm, C. Bruder, G. Schön, and A. D. Zaikin, Superlattices Microstruct. **25**, 1251 (1999).
[4] S. Gueron, H. Pothier, N. O. Birge, D. Esteve, and M. H. Devoret, Phys. Rev. Lett. **77**, 3025 (1996).
[5] B. Pannetier and H. Courtois, J. Low Temp. Phys. **188**, 599 (2000); H. Courtois, P. Charlat, Ph. Gandit, D. Mailly, and B. Pannetier, J. Low Temp. Phys. **116**, 187 (1999); P. Dubos, H. Courtois, B. Pannetier, F. K. Wilhelm, A. D. Zaikin, and G. Schön, Phys. Rev. B **63**, 064502 (2001).
[6] J. L. Levine, Phys. Rev. **155**, 373 (1967). In this work, the films were thick enough to ensure that the deparing effect was dominating the Zeeman effect.
[7] C. D. Mitescu, Ph.D. thesis, California Institute of Technology, Pasadena, 1966.
[8] M. Tinkham, *Introduction to Superconductivity* (McGraw-Hill, New York, 1985); J. Sánchez-Cañizares, J. Ferrer, and F. Sols, Phys. Rev. B **63**, 134504 (2001).
[9] F. Pierre, Ann. Phys. (Paris) **26**, No. 4 (2001).
[10] When taking into account the screening of the magnetic field inside the superconductor, we get a negligible correcting factor $\approx 1 - 1/60(w/\lambda_L)^2 \approx 0.99$.
[11] For a cylindrical wire with cross-area S, the ratio is $(S/\lambda_L^2)^2/90$.
[12] For a review, see G.-L. Ingold and Yu. Nazarov, in *Single Charge Tunneling*, edited by H. Grabert and M. H. Devoret (Plenum Press, New York, 1992).
[13] M. Nahum, T. M. Eiles, and J. M. Martinis, Appl. Phys. Lett. **65**, 3123 (1994).
[14] J. Romijn, T. M. Klapwijk, M. J. Renne, and J. E. Mooij, Phys. Rev. B **26**, 3648 (1982).

References of chapter 10

[1] For a review, see K. Maki in *Superconductivity*, edited by R. D. Parks (Marcel Dekker, New York, 1969), p. 1035.

[2] J. L. Levine, Phys. Rev. **155**, 373 (1967).

[3] C. D. Mitescu, PhD thesis, California Institute of Technology, Pasadena (1966).

[4] D.R.Lide, Handbook of Chemistry and Physics, 76th edition, p 12-64 (1995-96).

[5] M. Tinkham, *Introduction to superconductivity* (Mc Graw Hill, 1985).

[6] J. Sanchez-Canizares, J. Ferrer, and F. Sols, Phys. Rev. B **63**, 134504 (2001).

[7] G.-L. Ingold and Yu. Nazarov in *Single Charge Tunneling*, edited by H. Grabert and M. H. Devoret (Plenum Press, New York, 1992) .

[8] F. Pierre, Ann. Phys. (Paris) **26**, No 4 (2001)

[9] M. Nahum, T. M. Eiles, and J. M. Martinis, Appl. Phys. Lett. **65**, 3123 (1994).

Chapter 11 Proximity effect in an SNS structure

The modification of the properties of a normal metal electrode close to a contact with a superconducting one, a phenomenon called proximity effect, has been highlighted by experiments on mesoscopic devices [1]. Properties of proximity effect structures can be well understood using the concept of Andreev reflection: an Andreev reflection consists of the reflection of a quasielectron into a quasihole (or vice versa) at the N side of an NS interface, a process that transfers a Cooper pair into the superconductor. The pair made of the quasielectron and reflected quasihole is called Andreev pair. In diffusive systems, the Usadel equations allow the calculation of electronic properties such as the densities and filling of states, directly taking into account Andreev reflections. For example, in metallic proximity structures, equilibrium properties such as the density of states [2] or the conductivity [3] are well explained. In a diffusive short normal wire connected to superconducting pads, a supercurrent was measured [4]. A quantitative agreement was found with the predictions using Usadel equations. In [4], the focus was on the low voltage regime $eV < \varepsilon_T$ where $\varepsilon_T = \hbar D / L^2$ is the Thouless energy, L the length of the normal part and D the diffusion coefficient. In this regime close to equilibrium, the Andreev pairs remain coherent along the wire and carry the supercurrent. In the experiment presented in this chapter, the set-up, described in the first part, is similar: a normal diffusive wire is connected to two superconducting pads. A supercurrent and signatures of the minigap, which is predicted to open in the wire density of states when a supercurrent flows, were observed. Comparison of these observations and theoretical predictions are performed in the second part. We focus in the third part of this chapter on the large voltage regime where, even if Andreev pairs of large energy loose their coherence along the wire, signatures of Andreev reflections are still visible in the quasiparticles energy distribution function in the normal wire and in the current-voltage

characteristic.

11.1 Superconducting-Normal-Superconducting structure

11.1.1 Experimental realization

Two samples were fabricated. The SEM Micrographs of these samples are presented in Figure 1. In the first one, a 5-µm-long, 45-nm-thick silver wire extends at both ends into large contact pads, which are covered by a 300-nm-thick layer of aluminum. The reservoirs are thus made of an Ag/Al bilayer and have a gap reduced by proximity effect. In order to obtain a larger superconducting gap, a second sample in which the reservoirs have no underlying silver layer on an area of 300×500 nm^2 just at the ends of the wire was made. The scale of 500 nm is typically the distance on which proximity effect extends in aluminum, so that at the ends of the wire the superconducting layer is expected to have recovered its bulk property. Transport was probed by measuring current-voltage characteristic. Moreover, in both samples, two superconducting probe electrodes form tunnel junctions with the wire at $x=0.5$ (middle junction) and at $x=0.25$ (side junction) where x is expressed in reduced units of the wire

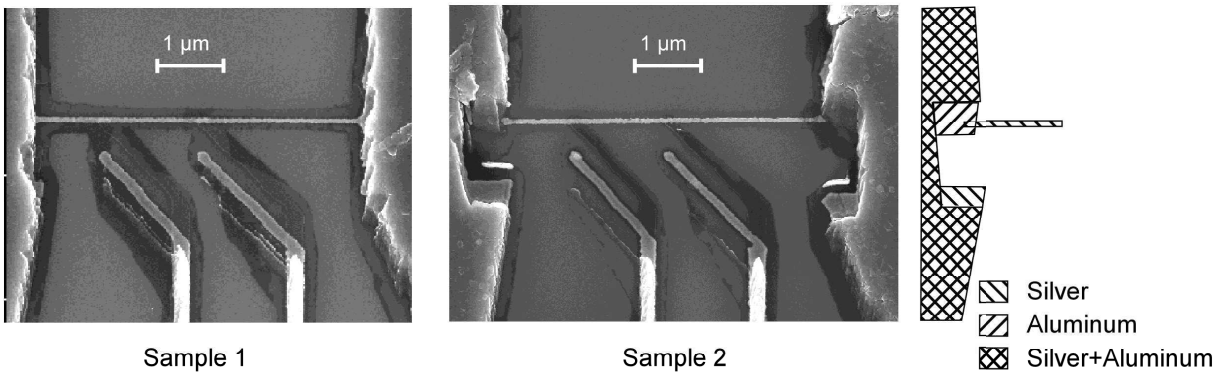

Figure 1: SEM micrographs of the samples used to investigate proximity effect. A normal 5-µm-long silver wire is connected to aluminum superconducting pads. Two superconducting probe electrodes form tunnel junctions with the wire. The quasiparticle energy distribution function in the wire is inferred from the differential conductance of the tunnel junctions. Left, the wire is connected to pads made of a bilayer silver-aluminum, leading to weakened superconductivity. Middle, the region of the pads where the wire is connected is only made of aluminum. Right: Schematic of the contact between the wire and the superconducting pads for sample 2.

length L. As shown in Chapter 2, these electrodes allow the tunnel spectroscopy of the quasiparticle energy distribution function in the wire if the modification of the density of states in the normal wire can be neglected. The geometrical and electrical characteristics of the samples are summarized in Table 1.

Sample	w (nm)	t (nm)	L (µm)	R (Ω)	D ($cm^2.s^{-1}$)	ε_T (µeV)	Δ (µeV)	R_T^S (kΩ)	R_T^M (kΩ)
1	80	45	5.15	38	140	0.35	115	132	46
2	70	45	5.6	58	116	0.25	130	192	247

Table 1: Geometrical and electrical characteristics of the measured samples: width w, thickness t, length L, resistance R, diffusion coefficient D, Thouless energy $\varepsilon_T = \hbar D / L^2$, gap energy in the superconducting reservoirs Δ, tunnel resistance of the side junction R_T^S, and of the middle one R_T^M.

11.1.2 Model

The model of the system is presented in Figure 2. The diffusive normal wire of length $L = 5\ \mu\text{m}$ is connected to two superconductors. The modulus of the parameter order in the superconductors is noted Δ. In the calculation, the wire is considered as one-dimensional since its width $(80\,\text{nm})$ and thickness $(45\,\text{nm})$ are smaller than the coherence length $\xi_0 = \sqrt{\hbar D / \Delta} \simeq 300\,\text{nm}$. The contacts between the superconducting pads and the normal wire are assumed to be perfectly transparent. The theoretical predictions are made for the experimental conditions of sample 1 at temperature $T = 14\,\text{mK}$:

$$\frac{\Delta}{\varepsilon_T} = 330,$$
$$\frac{k_B T}{\varepsilon_T} = 3.5.$$

In the equilibrium regime, detailed calculations were performed by P. Charlat [5,6] and Dubos [4,7] using the Usadel equations derived from the theory of non-equilibrium superconductivity (see Chapter 9).

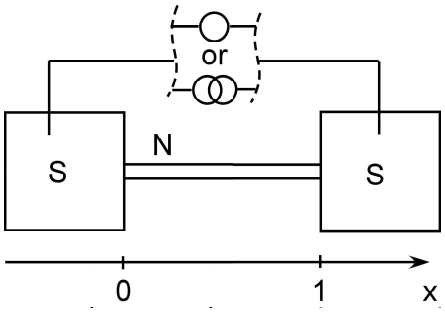

Figure 2: Layout of the experiment. The normal wire is connected to two superconductors. When the normal wire sustains a supercurrent, it is current biased. Otherwise the wire is voltage biased. The positions in the wire are given in reduced units $x = X / L$, with L the wire length.

11.2 Equilibrium regime

11.2.1 Theoretical predictions

We consider first the situation where the system is current-biased, assuming a static phase difference, *i.e.* with no voltage across the wire. The phase gradient between the superconducting reservoirs $\nabla\varphi$ and the supercurrent are related by:

$$j_s(x) = \frac{\sigma}{e}\int_0^\infty d\varepsilon \tanh\frac{\varepsilon}{2k_BT}\,\mathrm{Im}\left(\sin^2\theta\,\nabla\varphi\right). \tag{1}$$

The determination of the phase gradient from the supercurrent depends on the pairing angle $\theta(x,\varepsilon)$ in the wire. This leads, like in Chapter 10, to the self-consistent solution of the Usadel equations.

In order to discuss the density of states in the normal wire, the phase difference χ_0 between the superconducting reservoirs is taken as a parameter. This phase difference resulting from the supercurrent does not depend on energy. The equilibrium Usadel equations are then:

$$\begin{aligned}
&\frac{\hbar D}{2L^2}\frac{\partial^2\theta}{\partial x^2} + \left(i\varepsilon - \frac{\hbar D}{2L^2}\left(\frac{\partial\varphi}{\partial x}\right)^2\cos\theta\right)\sin\theta = 0 \\
&\frac{\partial}{\partial x}\left(\frac{\partial\varphi}{\partial x}\sin^2\theta\right) = 0,
\end{aligned} \tag{2}$$

with the boundary conditions for the superconducting reservoirs:

$$\theta(0,\varepsilon)=\theta(1,\varepsilon)=\theta_{BCS}(\varepsilon)=\arctan\left(\frac{i\Delta}{\varepsilon}\right)$$
$$\varphi(0,\varepsilon)-\varphi(1,\varepsilon)=\chi_0.$$

The modification of the pairing angle in the superconducting reservoirs due to proximity effect is neglected. We recall here the results obtained from these equations in [8] and [4]:

- A minigap appears in the density of states of the normal wire. The value of this gap does not depend on the position in the wire but just on the phase difference χ_0 between the two superconductors (see Figure 3). Its value E_g is of the order of the Thouless energy and is much smaller than the gap in the superconducting reservoirs.

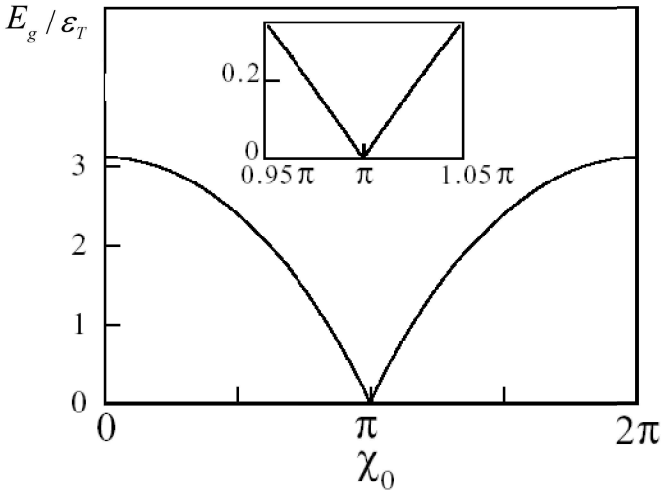

Figure 3: Energy gap E_g in units of the Thouless energy versus the phase difference χ_0 between the two superconducting contacts (from [5]). The inset shows the linear dependence of E_g near $\chi_0=\pi$.

The densities of states at various positions along the wire are presented in Figure 4 for $\chi_0=0$. In Figure 5, the average DOS on the sample length for different values of χ_0 is presented (from [6]).

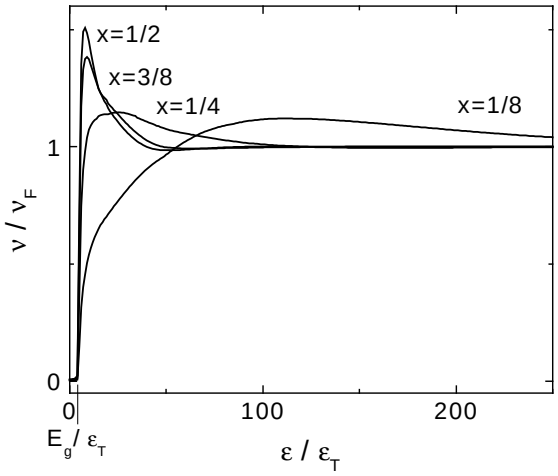

Figure 4: Density of states along a normal wire connected to two superconducting pads at the same phase. A minigap appears in the DOS. Its value does not depend on position.

- The maximum supercurrent that the wire can sustain was evaluated by Dubos et al [4]. This critical supercurrent I_C is predicted to be:

$$I_C = \alpha \frac{\varepsilon_T}{eR_N}, \tag{3}$$

where R_N is the wire resistance in its normal state and α a numerical constant dependent on Δ/ε_T and $k_B T/\varepsilon_T$. In the experimental conditions of sample 1, $\alpha \simeq 5$.

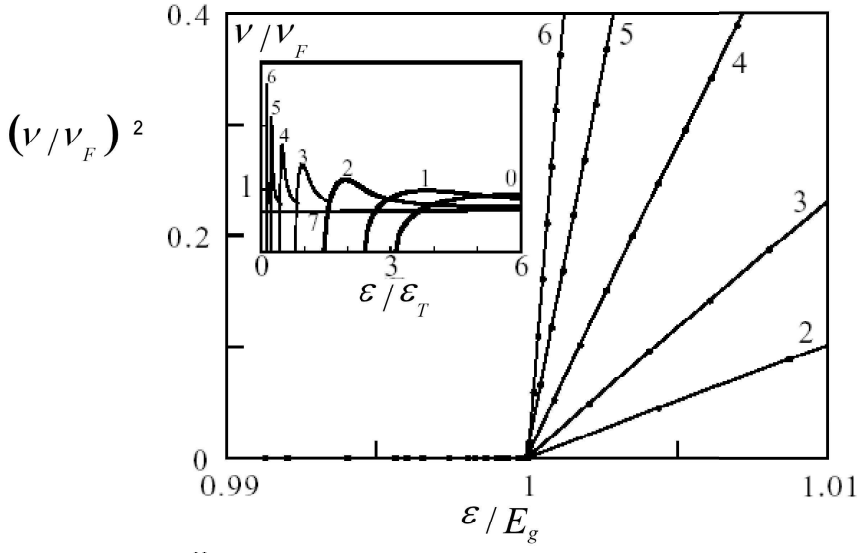

Figure 5: From [6]. Square power of the average density of states on the wire length versus reduced energy ε / E_g near the gap edge. Curves labeled 0, 1, 2, 3, 4, 5, 6, and 7 are for $\chi_0 = 0$, $\pi/2$, $3\pi/4$, $7\pi/8$, $15\pi/16$, $31\pi/32$, $63\pi/64$, and π. The insert shows the full density of states curves.

11.2.2 Supercurrent

The small-scale current-voltage characteristic of sample 1 is presented in Figure 6. A supercurrent branch is observed. Switching to a resistive state is found at I_S=39 nA , a value slightly smaller than the predicted critical current $I_C = 45$ nA from Eq. (3). This discrepancy could be due to thermal fluctuations that induce switching before I_C is reached or to the presence of vortices in the superconductors. This last hypothesis is reinforced by the observation of a hysteretic magnetic field dependence of I_S , with the maximum $I_S = 39$ nA at $B = 50\,\mathrm{G}$ (at $B = 0$, $I_S = 15$ nA).

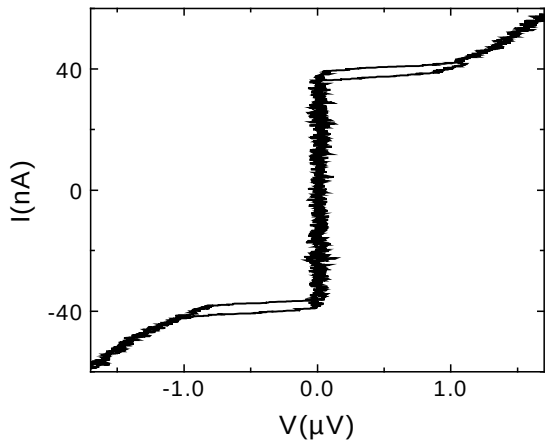

Figure 6: Current voltage characteristic of sample 1.

In sample 2, no supercurrent was found. The predicted critical current was 11 nA . Anticipating on distribution function measurements, the absence of supercurrent is attributed to a finite contact resistance between the wire and the superconducting pads: as explained in Figure 1, the two samples strongly differ in the geometry of this contact.

11.2.3 Signatures of a minigap in the density of states in presence of a supercurrent

When the wire sustains a supercurrent, a phase difference appears between the superconductors, leading to a change in the DOS $n(E)$ of the normal wire and in a change of the minigap energy E_g. This effect would be best probed with a tunnel junction to a normal electrode. In the experiment, the probe electrodes were superconducting because the main goal of the experiment was to probe the quasiparticles energy distribution function in the normal wire (see 11.3). Yet, signatures of the minigap in the density of states of the normal wire could be observed in the differential conductance curves $dI/dV(V)$ of the tunnel junctions. In Figure 7, we present an example of $dI/dV(V)$ for the side junction of sample 1 when the wire sustains a supercurrent of 9 nA.

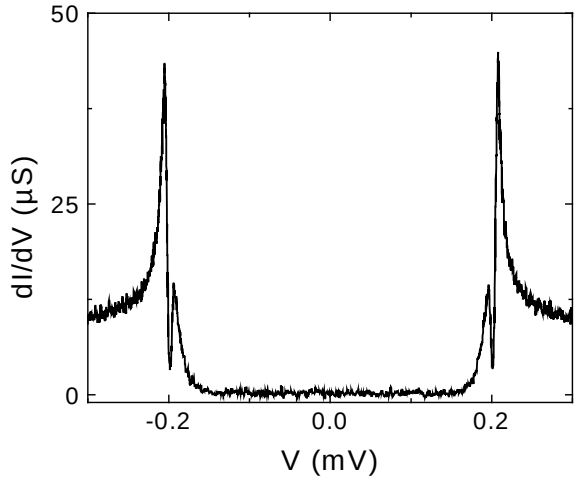

Figure 7: Differential conductance dI/dV of the side tunnel junction when the normal wire sustains a supercurrent $I_S = 9\,\text{nA}$. Additional structures appear near the gap of the probe electrode $\Delta_p = 200\,\mu\text{V}$.

Singularities are visible near $V = \pm 0.2$ mV. At zero temperature, it is known that the differential conductance of a tunnel junction between two electrodes with gaps Δ and Δ^* presents a gap at the value $\Delta + \Delta^*$ [9] (see Figure 8). Here a second peak appears at $\Delta - \Delta^*$ because Δ^* corresponds to the Thouless energy E_g, which is the typical energy scale of the minigap in the wire density of states, and which is of the same order as the electronic temperature in the normal wire [10]. This situation corresponds to the case 2) of Figure 8. The

analysis of this singularity allows to gain information on the minigap.

11.2.3.1 What does the superconducting electrode probe in the wire?

In the conditions of these measurements, the quasiparticle energy distribution function $f(E)$ in the wire is a Fermi function at a temperature close to the fridge temperature and the density of states $n(E)$ in the wire is unknown. The differential conductance of the probe junction between the superconducting probe and the normal wire is written:

$$\frac{dI}{dV}(V) = 1 + \int_{-\infty}^{+\infty} dE \frac{\partial n_S(E-eV)}{\partial E} n(E) f(E) + \int_{-\infty}^{eV} dE \frac{\partial n(E)}{\partial E} n_S(E-eV). \qquad (4)$$

This expression is not a simple convolution and the DOS $n(E)$ cannot be easily extracted from $dI/dV(V)$. Therefore, we compare directly the predicted $dI/dV(V)$ curves using a calculated $n(E)$ with the experimental measurements of $dI/dV(V)$.

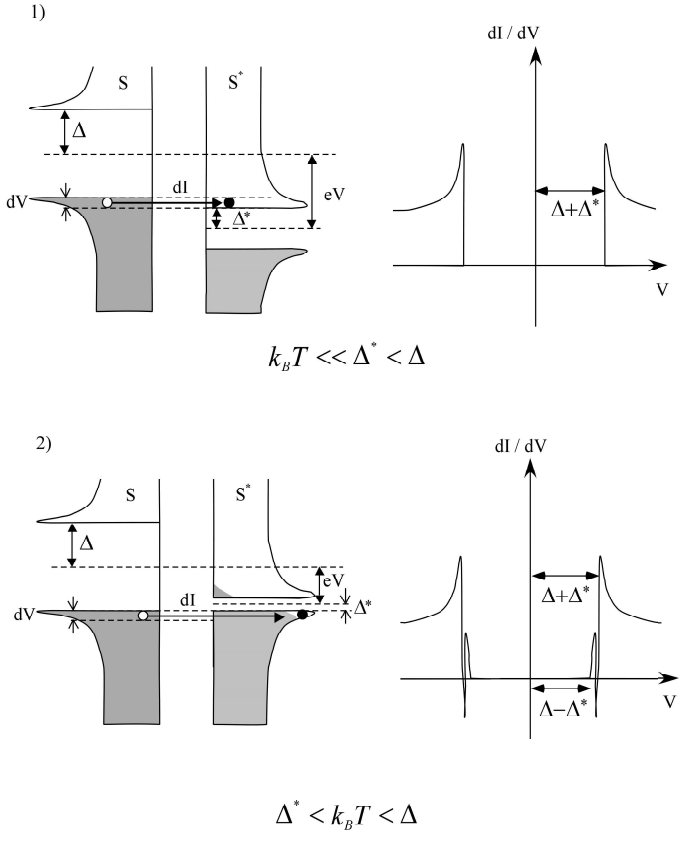

Figure 8: Differential conductance dI/dV of a tunnel junction between a superconductor of BCS density of states with a gap Δ and a modified superconductor with an unknown density of states with a gap Δ^*. The left part represents the occupied states (Gray) and the emptied states in both electrodes of the tunnel junction. 1) When the modified gap is much larger than temperature, $\Delta^* >> k_B T$, dI/dV presents a gap at $\Delta + \Delta^*$. 2) When the modified gap is smaller than temperature, $\Delta^* < k_B T < \Delta$, dI/dV presents a gap at about $\Delta + \Delta^*$ and a characteristic structure at $\Delta - \Delta^*$.

11.2.3.2 Minigap revealed by the tunnel junctions differential conductance

The results discussed here were obtained on sample 1 (the single one that presents a supercurrent).

11.2.3.2.1 Temperature dependence

We have investigated the temperature dependence of $dI/dV(V)$ at a fixed value of the supercurrent (9 nA). If the modification of the superconducting properties of the bulk pads with temperature can be neglected, only the filling factor of the states in the normal wire is modified. Figure 9 presents a comparison between the theoretical and experimental evolutions of dI/dV with temperature around $V = -0.2$ mV (data around $V = +0.2$ mV are identical). If the overall shape of the curves is correctly described by theory, the peak at -0.22 mV is found sharper in the experiment whereas the one near -0.19 mV is found more rounded. This discrepancy arises possibly from the wrong evaluation of the density of states in the normal wire, which neglects the effect of electron-electron interaction.

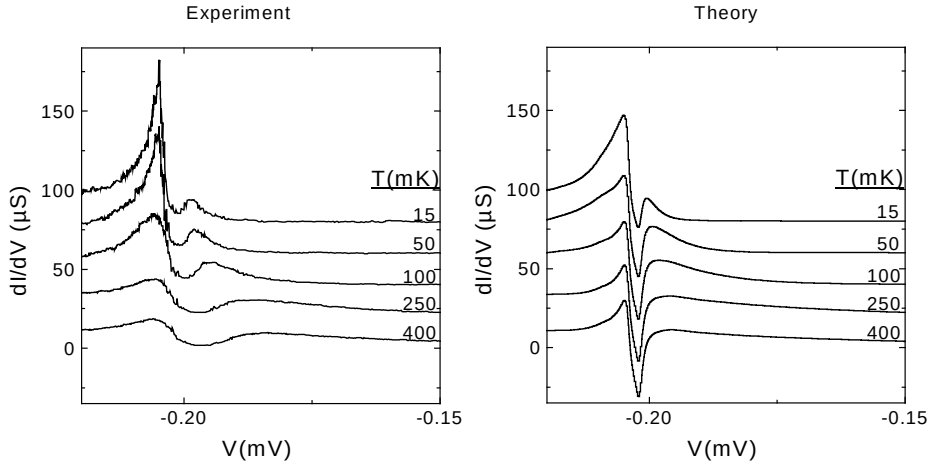

Figure 9: Measured and calculated differential conductance of the side tunnel junction as a function of the temperature when a supercurrent of 9 nA flows in the wire. Assuming that the superconducting pads are not modified, only the filling of the states in the normal wire is modified. When the temperature increases, the same evolution is found qualitatively.

11.2.3.2.2 Supercurrent dependence

The minigap and the density of states depend theoretically on the phase difference between the two superconductors (see Section 11.2.1), which is determined by the bias current (Eq. (1)). Experimentally, we observe an evolution of the $dI/dV(V)$ of the tunnel junction with the supercurrent, as shown in Figure 10 (the data were taken at $B=0$, where $I_S=15$ nA). To predict the density of states in the normal wire versus the supercurrent, Eq. (1) must be solved self-consistently with Eq. (2). Qualitatively, χ_0 is expected to evolve in a nearly sinusoidal way [7] from 0 to $\pi/2$ when I goes from 0 to I_C. The minigap energy is therefore expected to decrease to 0 for increasing values of I. The minigap can be directly inferred from the $dI/dV(V)$ curves: as exemplified on Figure 8, E_g/e is equal to half the distance in voltage $V_{p1}-V_{p2}$ between the two peaks. At $\chi_0=0$, $(V_{p1}-V_{p2})/2=2.4$ μV instead of the theoretical value $E_g \simeq 3.1\varepsilon_T \simeq 1.0$ μV. Instead of decreasing with I, V_1-V_2 increases (see Figure 10). We assume that this evolution is due to vortices in the pads that move with the current, as for the critical current dependence on magnetic field.

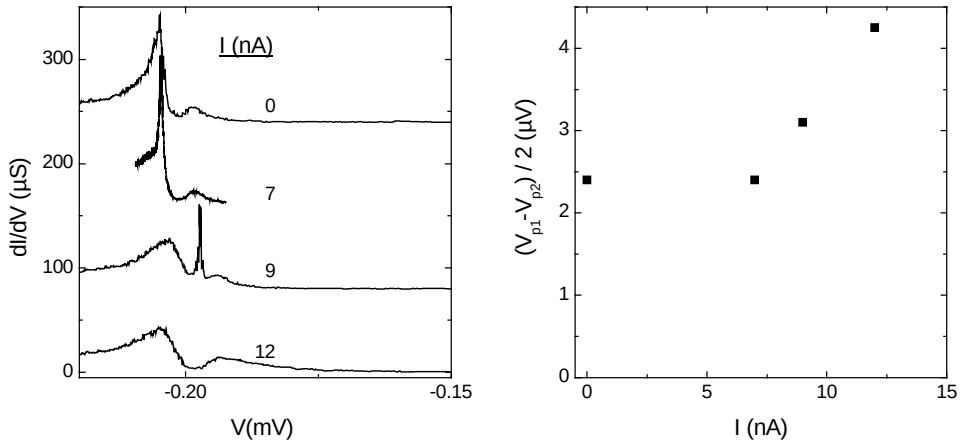

Figure 10: Left panel: Differential conductance of the side tunnel junction when the wire carries a supercurrent. A minigap opens in the wire density of states, leading to the peak near the gap edge of the superconducting electrode. Right panel: Difference between the positions $V_{p1}-V_{p2}$ of the peaks in the differential conductance versus the supercurrent.

11.2.3.2.3 Position dependence

All the data shown till here correspond to the side junction. For a given phase difference, theory predicts that the density of states in the wire varies with position (see Figure

4) but that the minigap is constant. In the experiment (see Figure 11), the density of states in the middle of the wire appears to be much rounded than at $x = 0.25$, an effect not predicted by theory. We attribute this discrepancy to the effect of electron-electron interaction in the normal wire.

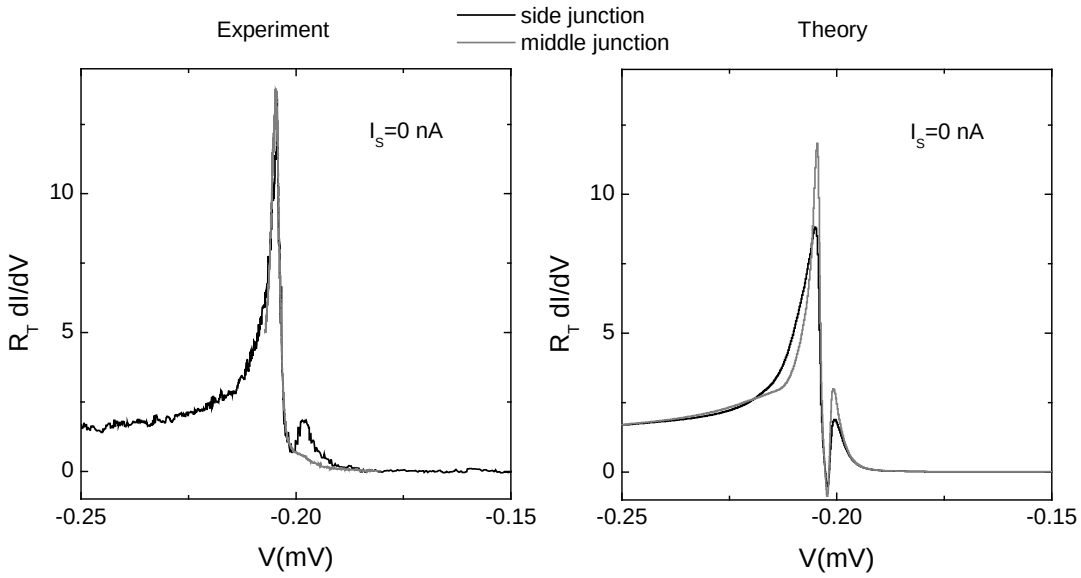

Figure 11: Left: Normalized differential conductance of the two tunnel junctions when the phase difference χ_0 between the two superconducting pads is zero. Right: Theoretical predictions using the DOS calculated in Section 11.2.1.

11.2.3.3 Conclusions on the minigap observation

This set of measurements brings evidence for the existence of a minigap in the density of states of a normal wire connected to two superconductors. The observed dependence of the DOS on the supercurrent and on position does not correspond to theory. Part of the discrepancy can be attributed to vortices in the superconductors. The fact that we neglect electron-electron interaction in theory is also probably another reason. More information would be gained in a dedicated experiment in which the probe electrode would be normal instead of superconducting.

11.3 Out-of-equilibrium regime

11.3.1 Quasiparticle energy distribution function in the out-of-equilibrium regime

In this section, our results published in Phys. Rev. Lett. **86**, 1078 (2001) are described and completed.

11.3.1.1 Theoretical predictions

The quasiparticle energy distribution function in the normal wire can be simply accounted for by the picture of Andreev reflections: at an NS interface, a quasielectron of energy ε smaller than the gap of the superconductor cannot enter the superconductor, and is reflected into a quasihole with energy $-\varepsilon$, while a Cooper pair enters the superconductor (see Figure 12). The energy reference is the chemical potential of the superconductor.

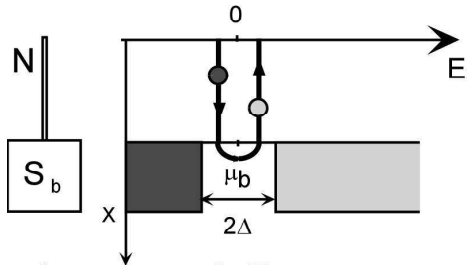

Figure 12: Left: A normal wire is connected to a superconductor. Middle: Representation in the energy (horizontal axis) and position (vertical axis) space of an Andreev reflection responsible for the current transport at an NS interface. The excitation spectrum of the superconductor has a gap 2Δ centered on its chemical electropotential μ_b, with quasielectrons states occupied at negative energies (dark area) and empty at positive energies (light gray area). A quasielectron from the normal part (dark disk) of energy smaller than the superconducting gap can not enter the superconductor and is reflected in a quasihole (light gray disk).

Due to proximity effect, the density of states in the normal metal is modified near the NS interface. The distance over which the normal metal is affected depends on energy. In absence of spin-flip scattering, this distance is predicted to be infinite at energy equal to the electrochemical potential of the S electrode. In experiments, this distance is limited by all decoherence phenomena in the normal wire, and is much smaller than the wire length. To a

first approximation, this modification is neglected and the SNS system can be modeled like in Figure 13. Electrons with a small energy bounce back and forth between the two superconducting reservoirs before exiting the wire. Within the diffusive approximation, the occupation factors of the quasiparticles states vary linearly between 0 and 1 along the paths between the reservoirs. The path length depends on bias voltage (see Figure 13). This representation allows to predict the energy distribution function of electrons anywhere in the wire.

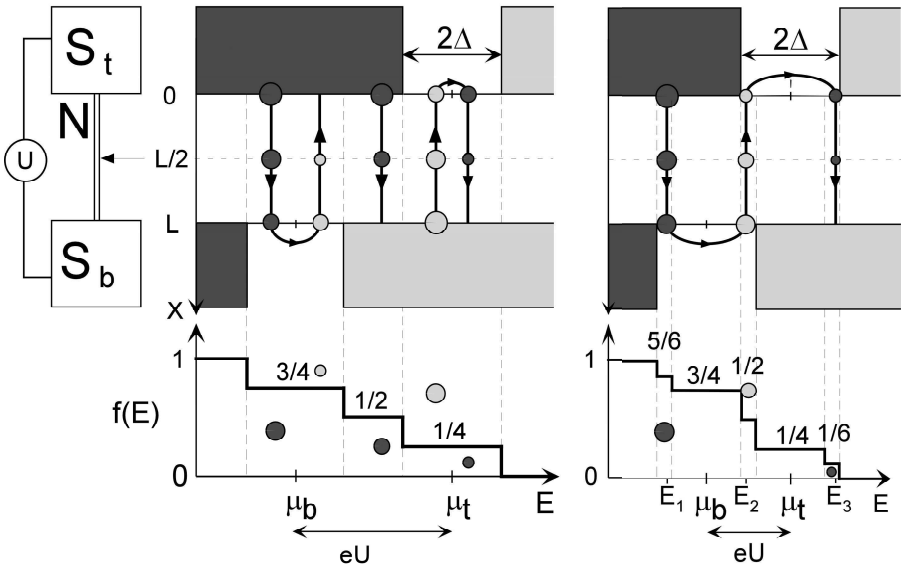

Figure 13: Left: Layout of the experiment: A voltage U is applied between two superconductors (S) connected through a normal wire (N) of length L. A superconducting probe, represented by an arrow, forms a tunnel junction with the central part of the wire. Top center and top right: Representation in the energy (horizontal axis) and position (vertical axis) space of the quasiparticle paths responsible for the current transport. The excitation spectrum of the top and bottom superconductors has a gap 2Δ centered on their electrochemical potentials μ_t and μ_b ($\mu_t - \mu_b = eU$), with quasielectron states occupied at negative energies (dark areas) and empty at positive energies (light gray areas). Quasiparticle paths consist of quasielectrons (dark disk) and quasiholes (light gray disk) trajectories at symmetric energies about μ_t and μ_b, connected by Andreev reflection. The area of the disk is proportional to the occupation factor of the quasiparticle state, which varies linearly along the path from 1 to 0. The bottom plots are the energy distribution predicted at the center of the wire, at $eU > 2\Delta$ (center) and $\Delta < eU < 2\Delta$ (right).

11.3.1.2 Bias-voltage dependence

The energy distribution functions obtained by deconvolution of the differential conductance of the middle junction in sample 1 as a function of U are presented in Figure 6. The predictions of the simplified model taking into account only Andreev reflections are also

presented: the energy gap in the superconducting aluminum reservoirs is a fit parameter equal to $115\,\mu eV$, which is smaller than the gap of bulk aluminum ($200\,\mu eV$), as expected for an NS bilayer. For the two larger bias voltages the position and the width of the steps are well accounted for by this theory. Yet, the measured steps are rounded. For the lower voltage, the predicted steps are washed out by the rounding.

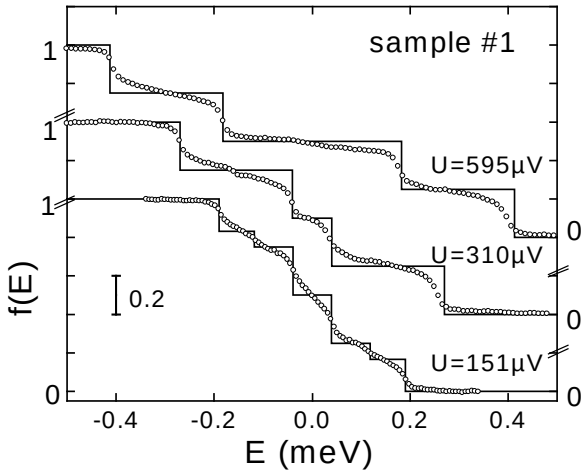

Figure 14: Energy distribution functions in the middle of the wire of sample 1, when the reservoirs are in the superconducting states and voltage biased at U. Symbols are experimental data; solid lines are the expectation of a simplified theory taking only into account multiple Andreev reflections.

The rounding of the steps is due to energy exchange between quasiparticles in the normal wire. The longer the quasiparticles stay in the wire, the more they interact, and the more rounded is the distribution function [11]. This effect is visible on the curve taken at $U = 595\,\mu V$, where the plateau centered at 0.5 corresponding to quasiparticles going through the wire once has a smaller slope than the ones at 0.25 and 0.75, which correspond to quasiparticles going through the wire twice.

To evaluate the rate of energy exchange in the normal wire, we have applied a magnetic field that turns the reservoirs normal, but keeps the probe electrode superconducting. Indeed, the bilayered Al-Ag reservoirs are less robust to magnetic field. It was then possible to measure the out-of-equilibrium energy distribution function of quasielectrons like in [11] and to

deduce the rate and energy dependence of energy exchange (see Figure 15). Afterwards, the deduced rate was included in a calculation of $f(E)$, (see [11] and Chapter 7 for more details):

$$D\frac{\partial^2 f}{\partial x^2} + I_{coll}(f) = 0. \tag{5}$$

Andreev reflections at the NS interfaces enter in the boundary conditions for $|E| < \Delta$:

$$f(\mu + E) = 1 - f(\mu - E) \tag{6}$$

$$\frac{\partial f}{\partial x}(\mu + E) = -\frac{\partial f}{\partial x}(\mu - E). \tag{7}$$

The condition (6) accounts for the equality of the occupancy of quasielectrons and quasiholes states at symmetric energies about the electrochemical potential μ of the superconductor. The condition (7) is the conservation of the quasiparticle current.

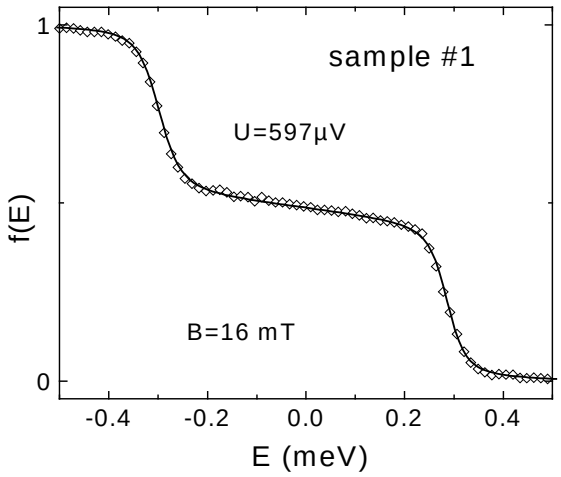

Figure 15: Energy distribution function in the middle of the wire of sample 1, when the reservoirs are in the normal state and voltage biased at $U = 597\ \mu V$.

The data in Figure 14 are well accounted for with a calculation including in $I_{coll}(f)$ electron-electron interaction and electron-phonon interaction (see Figure 16). The intensity of interactions were found to be $\kappa_{3/2} = 0.75\ \text{ns}^{-1}\ \text{meV}^{-1/2}$ and $\kappa_{ph} = 8\ \text{ns}^{-1}\ \text{meV}^{-3}$. The predicted

electron-electron interaction intensity is $\kappa_{3/2}^{th} = 0.12$ ns^{-1} meV$^{-1/2}$ (see Chapter 7).

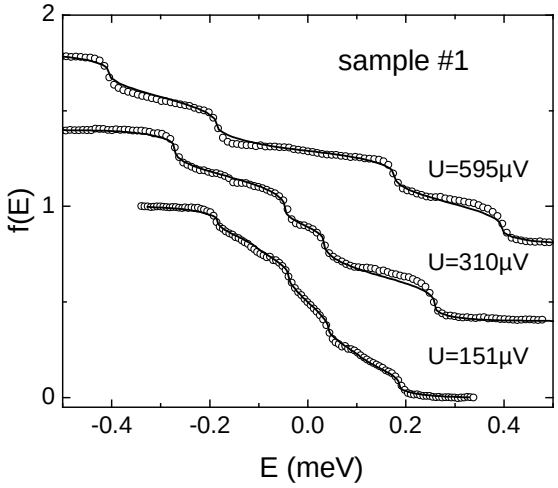

Figure 16: Energy distribution function in the middle of the wire of sample 1, when the reservoirs are in the superconducting state and voltage biased at U. Symbols are experimental data; solid lines are the solution of the Boltzmann equation taking into account multiple Andreev reflections and energy exchange.

11.3.1.3 Position dependence

In sample 1, at the position of the side junction, whatever the bias voltage, the energy distribution functions display strange features (see Figure 17 for $U = 0$ and $U = 595\,\mu\text{V}$). The reason is that at this position, the density of states in the normal wire is modified by proximity effect. The length over which this modification extends depends on the energy relatively to the electrochemical potential μ of the superconducting reservoir. At μ, this modification typically extends in the normal part over L_ϕ at the electronic temperature T_e. In our out-of-equilibrium situation, T_e must be replaced with the width of the energy distribution function $U + 2\Delta$: At $U = 595\ \mu\text{V}$, for example, $T_e \simeq 9\,\text{K}$ and $L_\varphi \simeq 1.5\,\mu\text{m}$ for 6N-silver (see Chapter 6). As a consequence, like in Section 11.2.3.1, $n(E)$ is modified at the position of the side junction, which is 1.25 μm away from the left superconductor and the deconvolution of the differential conductance of the tunnel junction does not give $f(E)$. The observation on Figure 17 that some extra peaks on the deconvolved data are at an energy equal to the chemical potential μ_L of the nearest superconducting reservoir whereas nothing is observed at

the other chemical potential μ_R buttresses the previous explanation.

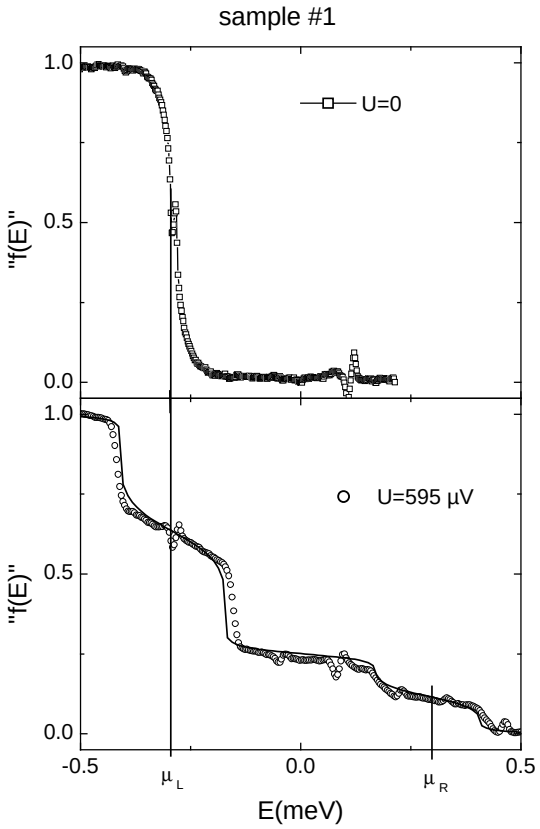

Figure 17: Symbols: Apparent energy distribution functions "$f(E)$" obtained by deconvolution of dI/dV measured at $x = 1/4$ for $U = 0$ and $U = 595\,\mu\mathrm{V}$. Bottom: Solid line is the calculated energy distribution function at $x = 1/4$ with the fit parameters that account for energy distribution functions in the middle of the wire (see Figure 16).

In sample 2, the measured distribution functions at two different positions along the wire are well accounted for by the simplified theory (see Figure 18), if one assumes that the positions of the junctions are $x = 0.58$ (instead of 0.5) and $x = 0.35$ (instead of 0.25). This shift is attributed to a significant contact resistance at the reservoirs in this sample, equivalent to an extra length of the wire. The effective positions of the probe junctions correspond to an effective lengthening of the left side of the wire by about $850\,\mathrm{nm}$. The existence of such a contact resistance was also inferred from the absence of supercurrent, and prevents from a modification of the density of states by proximity effect at the position of the side junction like in sample 1. This explains why the strange features of Figure 17 are absent on Figure 18. The widths of the side steps give slightly different gaps at both ends: $120\ \mu\mathrm{V}$ and $140\ \mu\mathrm{V}$.

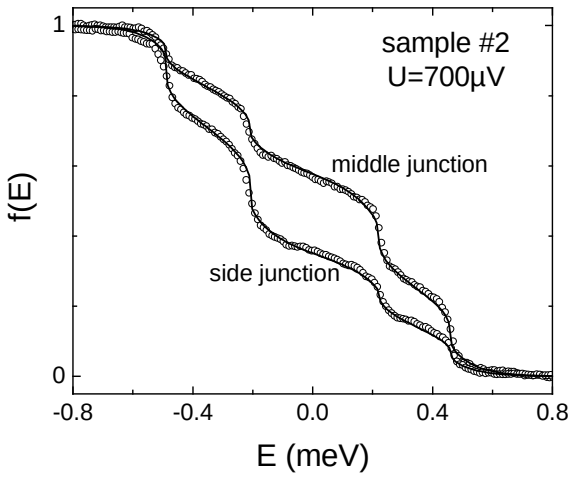

Figure 18: Distribution functions in sample 2 as measured by the middle and side junctions for $U = 700\ \mu\mathrm{V}$. Symbols: Experiment. Solid line: Solution of the Boltzmann equation accounting for the Andreev reflections at the reservoirs and electron-electron interaction within the wire for $x = X / L = 0.58$ and $x = X / L = 0.35$.

11.3.2 Current-voltage characteristic of the SNS structure

11.3.2.1 Experimental observation

For both samples, even if the current voltage characteristic looks linear at first glance, a subgap structure is revealed by differential conductance measurements (see Figure 19). Such a subgap structure, which was already observed by Hoss *et al.* [12] is not expected in the simplified picture of Andreev reflections. In order to describe the modification of the density of states near the NS interface, we have performed a calculation using the theory of non-equilibrium superconductivity.

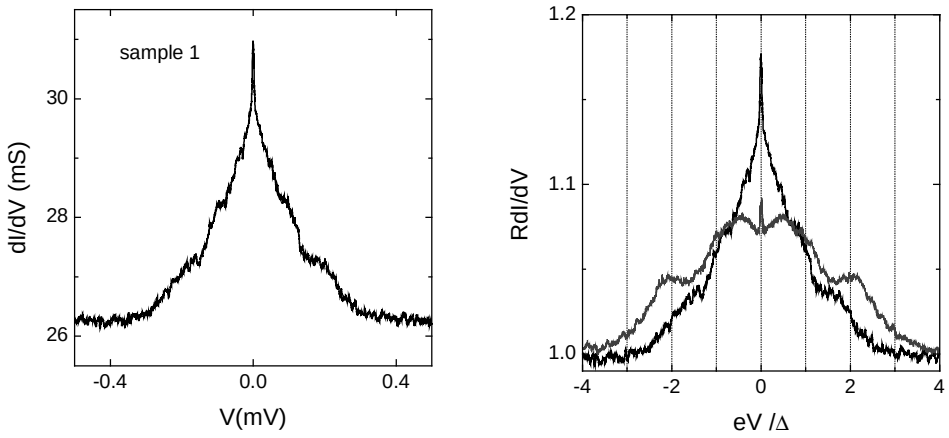

Figure 19: Left panel: Measured differential conductance dI/dV of the normal wire in sample 1. The conductance of the wire shows a step-like behavior as a function of the voltage. Right panel: Differential conductance, normalized to the conductance at large voltage $1/R$, versus voltage, normalized to the gap voltage of the superconducting pads Δ, for sample 1 (black line) and 2 (gray line).

11.3.2.2 Theoretical predictions

To calculate the current voltage characteristic of the SNS structure, we use the equilibrium and out-of-equilibrium Usadel equations. The current is derived from the quasiparticle energy distribution function in the wire.

11.3.2.2.1 Energy distribution function in the middle of the wire

In the finite voltage regime, proximity effect has two consequences: the modification of the density of states in the normal wire near the NS interface and the modification of the filling factors of the quasiparticles states in the normal wire as a whole. In presence of a finite voltage, the phase difference between the two superconducting pads depends on time. The theory of non-equilibrium superconductivity does not apply to such a non-stationary case. In order to circumvent this difficulty, we assume that the wire is long enough so that, in the middle, the wire is normal and the pairing angle equal to zero. The problem can then be solved by separating the wire into two systems made of a normal wire connected at one end to a single superconducting reservoir: A first one between $x=0$ and $x=1/2$, with a superconducting reservoir at $x=0$, a second one between $x=1/2$ and $x=1$, with a

superconducting reservoir at $x=1$. The equilibrium and out-of-equilibrium Usadel equations can then be used (see Chapter 9). Afterwards, both solutions are matched together by continuity. This model is solved in details in Appendix 1. An example of solutions is shown in Figure 20. This approach fails to account for the smoothing of the energy distribution function because electron-electron interaction is not included in the calculation. The positions of the steps are the same as those found with the approach of Andreev reflections. The sharp features, at energies equal to the electrochemical potential of the superconducting reservoirs, in the middle of the plateaus, are signatures of proximity effect. Note that at the position of the side junction of sample 1, the apparent energy distribution functions on Figure 17 present sharp feature at energy equal to the electrochemical potential of the nearest superconducting reservoir but for a different reason, as seen from their shape: by tunneling one obtains a contribution of the density of states as explained before.

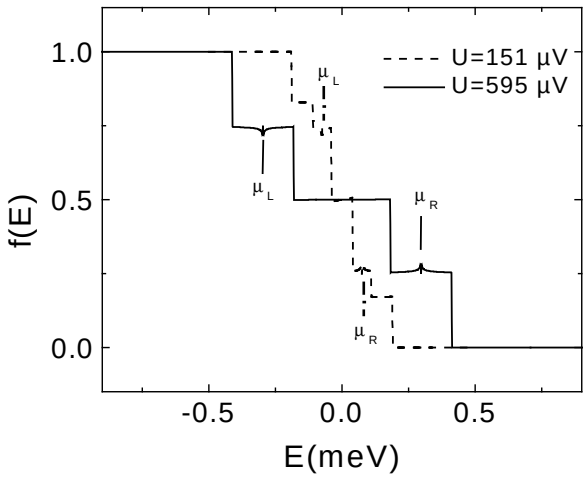

Figure 20: Calculated quasielectron energy distribution functions in the middle of a normal wire connected to two superconducting pads, of gap $\Delta=115\,\mu\mathrm{V}$, voltage biased at $U=151\,\mu\mathrm{V}$ and $595\mu\mathrm{V}$. The calculations are based on the Usadel equations. The modification of the pairing angle in the normal wire and in the superconducting pads near the NS interface due to proximity effect is taken into account and is responsible for the sharp feature on the steps at energies equal to the electrochemical potential of the superconducting reservoirs. The rounding of $f(E)$ is absent because electron-electron interaction is not included in the calculation.

11.3.2.2.2 Current-voltage characteristic

From the distribution function in the middle of the wire, the current-voltage characteristic is obtained by integrating out the following equation (see Chapter 9):

$$j_N = \frac{\sigma}{e}\int_0^{+\infty} d\varepsilon \left(\cos^2\theta_1 \frac{\partial f_{od}}{\partial x} + \cosh^2\theta_2 \frac{\partial f_{ev}}{\partial x} \right), \tag{8}$$

with σ the conductivity in the normal metal. This formula gives the normal wire resistance when $\theta = 0$. Since the current is conserved along the wire, it can be calculated in the middle where the wire is assumed to be normal, $\theta_1(1/2,\varepsilon) = \theta_2(1/2,\varepsilon) = 0$, so that Eq. (8) simplifies to:

$$j_N = \frac{\sigma}{e}\int_0^{+\infty} d\varepsilon \left(\frac{\partial f_{od}}{\partial x} + \frac{\partial f_{ev}}{\partial x} \right). \tag{9}$$

The differential conductance obtained from this calculation is presented in Figure 21. Peaks appear in the differential conductance at energies equal to submultiple of twice the gap $2\Delta/n$.

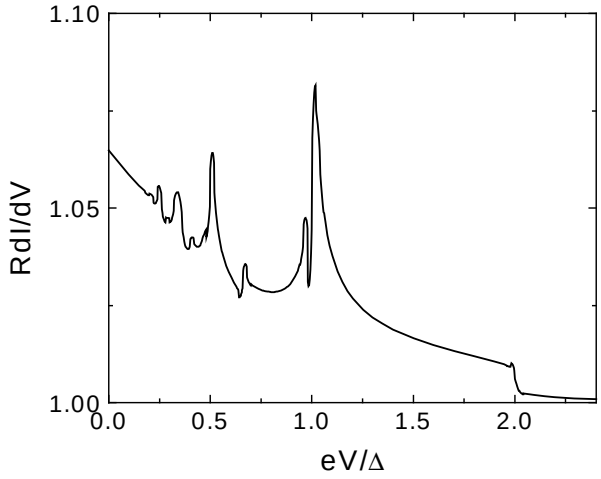

Figure 21: Predicted differential conductance of a normal wire connected to two superconducting reservoirs of gap Δ. The length of the normal wire is $9L_\Delta = 9\sqrt{\hbar D/\Delta}$ with D the diffusion constant of the normal wire. Peaks appear in the differential conductance at energies equal to submultiple of twice the gap.

Even if the experimental results show some similarities with this curve, they are much more rounded. Moreover, the order of magnitude of the predicted effect is smaller than the experimental one, proving that this model fails to capture the essential physics.

11.4 Conclusion

Two theoretical descriptions of proximity effect have been used to compare with experiments. The first one, based on Usadel equations, neglects the effect of Coulomb electron-electron interaction, but describes the propagation of pair correlation. We have adapted it to out-of-equilibrium situations in which two superconductors are biased at different potentials. The second theoretical framework is based on the Boltzmann equation and treats Coulomb interaction in details. Proximity effect is introduced as a boundary condition, which is an oversimplification. All the properties specific to pair correlation cannot be found from this second formalism: the supercurrent, the DOS, the voltage-dependent resistance are only expected from Usadel equations. It is however found that the agreement with this theory based on Usadel equations is rather poor, suggesting that Coulomb interaction does play an important role, too. A term that accounts for electron-electron interaction should be added in the earlier steps of the mesoscopic superconductivity theory in the self-energy expression (see Chapter 9 and [13]). For the energy distribution functions, the adapted Usadel equations only predict slight modification of $f(E)$, whereas the most salient modifications of $f(E)$ are due to Coulomb interaction. Boltzmann equation gives then the best description.

More experiments are needed in this field: for shorter wires, modifications of $f(E)$ by pair correlations should become measurable, and interactions should be less important. The simplest geometry would be a wire with one contact superconducting, the other one normal (SNN). Both normal and superconducting probe electrodes would allow for independent measurements of the density of states and energy distribution functions.

Appendix 1: Calculation with the Usadel equations of the energy distribution function in the middle of an SNS structure

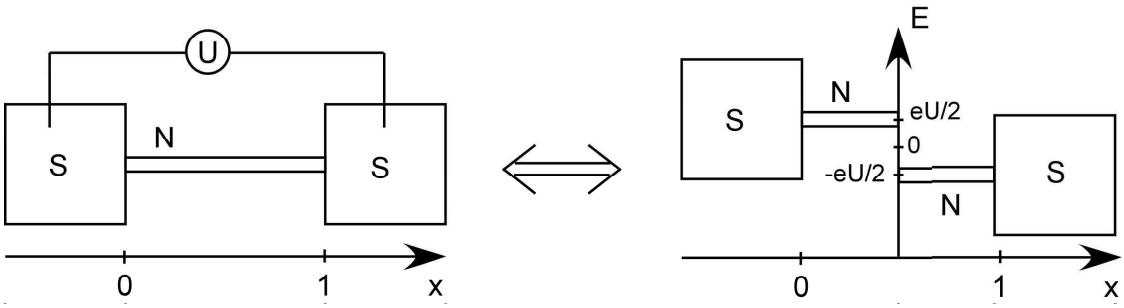

Figure 22: Left: Layout of the experiment. A normal wire is connected to two large superconducting voltage-biased electrodes. Right: To perform the calculation of the energy distribution function in the middle of the wire with Usadel equations, the density of states in the middle of the wire is assumed to be normal so that the wire can be modeled by two SN systems with different reference energies.

To calculate the energy distribution function in the middle of the normal wire, the system is modeled by two half systems made of a normal wire connected to only one superconducting reservoir (see Figure 22). The energies are expressed in units of Δ, the gap of the superconductor pads. The pairing angle θ and the filling factors f_{od} and f_{ev} are introduced.

Density of states in a normal wire connected at one end to a superconductor

The modifications of the density of states near the NS interface are taken into account on both side of the contact. When neglecting the spin-flip scattering, since $\nabla\varphi = 0$, the equilibrium Usadel equations can be simplified to:

$$\frac{\partial^2\theta}{\partial x^2} + 2i\varepsilon\sin\theta + 2\frac{\Delta(x)}{\Delta}\cos\theta = 0,$$

where $\Delta(x) = 0$ in the normal part and $\Delta(x) = \Delta$ far from the interface in the superconductor. The out-of-equilibrium equations in the normal wire can be written:

$$\nabla\left\{\cos^2\theta_1 \nabla f_{od}\right\} = 0$$
$$\nabla\left\{\cosh^2\theta_2 \nabla f_{ev}\right\} = 0.$$

The density of states at the end of the wire is assumed to be normal, so that:

$$\theta(1/2,\varepsilon)=0\,.$$

By symmetry, one also has:

$$\frac{\partial\theta}{\partial x}(1/2,\varepsilon)=0\,.$$

When integrating twice the equilibrium Usadel equation, one obtains for $x>0$:

$$\theta(x,\varepsilon)=4\arctan\left(\tan\frac{\theta(0,\varepsilon)}{4}e^{(i-1)\varepsilon x}\right).$$

Far inside the superconducting reservoir, bulk BCS properties are recovered. In practice, superconductivity is modified on a distance from the contact $\sim\sqrt{\hbar D/\Delta}<L$, so that we take:

$$\theta(\text{-}1,\varepsilon)=\theta_{BCS}(\varepsilon)$$
$$\frac{\partial\theta}{\partial x}(\text{-}1,\varepsilon)=0.$$

When integrating once the equilibrium Usadel equation, one obtains for $x<0$:

$$\left(\frac{\partial\theta}{\partial x}\right)^2-4i\varepsilon\cos\theta+4\sin\theta=4\sqrt{1-\varepsilon^2}\,.$$

The contact between the superconductor and the normal wire is assumed to be perfectly transparent, so that by continuity: $\sin\left(\theta(0,\varepsilon)\right)=i\varepsilon+\sqrt{1-\varepsilon^2}$.

For the out-of-equilibrium equations, the superconductor is assumed to be a reservoir at zero temperature so that:

$$f_{ev}(0,\varepsilon)=0$$
$$f_{od}(0,\varepsilon)=-1\quad\text{if}\quad\varepsilon<0$$
$$f_{od}(0,\varepsilon)=1\quad\text{if}\quad\varepsilon>0.$$

One obtains then:

$$f_{od}(x,\varepsilon)=f_{od}(0,\varepsilon)+a(\varepsilon)\int_0^x\frac{dX}{\cos^2\theta_1(X,\varepsilon)}$$
$$f_{ev}(x,\varepsilon)=b(\varepsilon)\int_0^x\frac{dX}{\cosh^2\theta_2(X,\varepsilon)},$$

with $a(\varepsilon)=0$ for $\varepsilon<1$.

Energy distribution function in the middle of the wire

A voltage U is applied between the two superconducting reservoirs. The energy reference is taken in the middle of the wire (see Figure 22).

Then the distribution function can be written for the left and right part:

$$f_{od}^{L}(x,E) = f_{od}(0, E+eU/2) + a(E+eU/2)\int_0^x \frac{dX}{\cos^2\theta_1(X,\varepsilon)}$$

$$f_{od}^{L}(x,E) = b(E+eU/2)\int_0^x \frac{dX}{\cosh^2\theta_2(X,\varepsilon)}$$

$$f_{od}^{R}(x',E) = f_{od}(0, E-eU/2) + a(E-eU/2)\int_0^{x'} \frac{dX}{\cos^2\theta_1(X,\varepsilon)}$$

$$f_{od}^{L}(x',E) = b(E-eU/2)\int_0^x \frac{dX}{\cosh^2\theta_2(X,\varepsilon)}.$$

Writing that the energy distribution function and the spectral current are continuous at $x = 1/2$, the following equation is obtained:

$$0 = \frac{f(E)-f(E+eU)}{i_2(E+eU/2)} + \frac{f(E)-f(E-eU)}{i_2(E-eU/2)}$$
$$+ \begin{cases} 0 & \text{if } |E+eU/2| < \Delta \\ \dfrac{f(E)+f(E+eU)-2\operatorname{sign}(E+eU/2)}{i_1(E+eU/2)} & \text{if } |E+eU/2| > \Delta \end{cases}$$
$$+ \begin{cases} 0 & \text{if } |E-eU/2| < \Delta \\ \dfrac{f(E)+f(E-eU)-2\operatorname{sign}(E-eU/2)}{i_1(E-eU/2)} & \text{if } |E-eU/2| > \Delta, \end{cases}$$

with

$$i_1(E) = \int_0^{L/2} \frac{dX}{\cos^2\theta_1(X,\varepsilon)}$$

$$i_2(E) = \int_0^{L/2} \frac{dX}{\cosh^2\theta_2(X,\varepsilon)}.$$

Appendix 2: Article reporting results on the energy distribution functions in an SNS structure

We reproduce here the paper published in Phys. Rev. Lett. **86**, 1078 (2001).

Multiple Andreev Reflections Revealed by the Energy Distribution of Quasiparticles

F. Pierre, A. Anthore, H. Pothier, C. Urbina, and D. Esteve

Service de Physique de l'Etat Condensé, Commissariat à l'Energie Atomique, Saclay, F-91191 Gif-sur-Yvette Cedex, France

(Received 13 October 2000)

We have performed the tunnel spectroscopy of the energy distribution function of quasiparticles in 5-μm-long silver wires connected to superconducting reservoirs biased at different potentials. The distribution function $f(E)$ presents several steps, which are manifestations of multiple Andreev reflections at the NS interfaces. The rounding of the steps is well explained by electron-electron interactions.

DOI: 10.1103/PhysRevLett.86.1078 PACS numbers: 74.50.+r, 72.10.–d, 73.23.–b

The modification of the properties of a normal (i.e., nonsuperconducting) metallic electrode when it is connected to a superconducting one, a phenomenon called "proximity effect," has been highlighted by experiments on mesoscopic devices [1]. In metallic nanostructures, equilibrium properties, such as the density of states [2], the conductivity [3], or the supercurrent [4], are now well explained. The propagation of the correlations between time-reversed states from a superconductor (S) into a diffusive normal metal (N) is described by the Usadel equations [5], which apply to situations where all superconductors are at the same potential. In this Letter, we address an out-of-equilibrium situation, in which two superconductors connected through a long ($L \simeq 5$ μm), diffusive normal wire are biased at different potentials (see Fig. 1). We have measured the energy distribution function of quasiparticles in the middle of the wire, which is expected to be strongly modified by the presence of superconductors at the ends, since quasiparticles can escape the wire only if their energy exceeds the energy gap Δ of the superconductor. Therefore, in the presence of a finite voltage across the wire, the quasiparticles in the wire are expected to be "heated" up to the gap energy [6]. A quantitative description follows from the concept of multiple Andreev reflections, which recently has been shown to describe in great detail the current-voltage characteristics [7], the noise [8], and the supercurrent [9] in atomic point contacts between superconductors. An Andreev reflection consists of the reflection of a quasielectron into a quasihole (or vice versa) at the N side of an NS interface, a process which transfers a Cooper pair into the superconductor. The energies of the two quasiparticles involved are symmetrical with regard to the electrochemical potential of the superconductor. When two superconductors are present, successive Andreev reflections at both superconductors lead to a progressive rise of the quasiparticle energies, till the superconducting gap is exceeded. At zero voltage, multiple Andreev reflections lead to the formation of bound states which carry the supercurrent [10]; at finite voltage, they result in nonlinearities in the current voltage characteristics [6,7]. Here, we focus on the fingerprint of multiple Andreev reflections in the shape of the energy distribution function $f(E)$ of the quasiparticles.

For simplicity, we first make the following assumptions: (i) electron-electron and electron-phonon interactions are neglected; (ii) the renormalization of the diffusion constant in the normal wire by proximity effect is neglected; (iii) the probability of Andreev reflection is taken equal to 1 for quasiparticle energies within the gap, and to 0 elsewhere. Under assumptions (i) and (ii), the distribution function varies linearly with the position X along the wire [11]. Because of Andreev reflection, the occupation factor for quasielectrons and quasiholes at symmetrical energies about the electrochemical potential μ of the superconductor is equal at the NS interfaces, as well as their gradients.

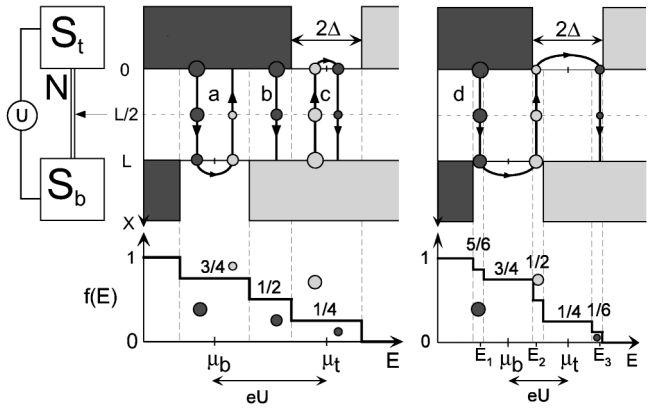

FIG. 1. Left: layout of the experiment: a voltage U is applied between two superconductors (S) connected through a normal wire (N) of length L. A superconducting probe electrode, represented by an arrow, forms a tunnel junction with the central part of the wire. Top center and top right: representation in the energy (horizontal axis) and position (vertical axis) space of the quasiparticle paths responsible for the current through the normal wire. The excitation spectrum of the top and bottom superconductors has a gap 2Δ centered on their electrochemical potentials μ_t and μ_b ($\mu_t - \mu_b = eU$), with quasielectron states occupied at negative energies (dark areas) and empty (light gray areas) at positive energies. Quasiparticle paths consist of quasielectron (dark disks) and quasihole (light gray disks) trajectories at symmetric energies about μ_t or μ_b, connected by Andreev reflection. The area of the disks is proportional to the occupation factor of the quasiparticle state, which varies linearly along the path from 1 to 0. The bottom plots are the energy distribution functions at the center of the wire, at $eU > 2\Delta$ (center) and $\Delta < eU < 2\Delta$ (right).

 0031-9007/01/86(6)/1078(4)$15.00 © 2001 The American Physical Society

One can therefore define quasiparticle paths in the energy-position space between occupied and empty quasiparticle states in the superconductors, along which both the nature of the quasiparticle and its energy change at each NS interface. The occupancy f of the quasiparticle state on this diffusive path varies continuously from 1 to 0 along the trajectory, with a gradient given by the inverse of the length of the trajectory. Hence, f is simply, at a given point of a trajectory, the remaining fraction of the path. The distribution function $f(E)$, which is defined for quasielectrons, is then equal to f at a point where the quasiparticle on the considered trajectory is a quasielectron, and to $1 - f$ where it is a quasihole. This allows one to determine the distribution function as a function of energy and position in the wire. Two examples are illustrated in Fig. 1. In the first one, the voltage $U = (\mu_t - \mu_b)/e$ is larger than $2\Delta/e$ (with μ_t and μ_b the electrochemical potentials of the two superconductors). The leftmost quasiparticle path in Fig. 1, labeled a, is emitted from a filled quasielectron state in the top superconductor at an energy E between $\mu_b - \Delta$ and $\mu_b + \Delta$. This quasielectron is then reflected as a quasihole at the bottom NS interface, at an energy symmetrical about μ_b. It is then absorbed in the top superconductor where quasihole states are unoccupied at the corresponding energy (since quasielectron states are filled), and the quasiparticle path has a total length $2L$. At the energy of the initial quasielectron, the position $X = L/2$ is reached when $3/4$ of the total path remains; therefore, $f(E) = 3/4$. The second path in Fig. 1, labeled b, has length L: quasielectrons from the top superconductor with an energy between $\mu_b + \Delta$ and $\mu_t - \Delta$ are absorbed in the bottom superconductor after one traversal of the wire. Therefore $f(E) = 1/2$ at $X = L/2$. The third path, labeled c, resembles path a, with an inversion of quasiholes and quasielectrons. One obtains thus $f(E) = 1 - 3/4 = 1/4$ at the middle of the wire. Altogether, the energy distribution function at $X = L/2$ presents three steps, at $3/4$ (width 2Δ), $1/2$ (width $eU - 2\Delta$), and $1/4$ (width 2Δ). The right diagram of Fig. 1 deals with the case $\Delta < eU < 2\Delta$. The steps of $f(E)$ at $3/4$ and $1/4$ are still present, since the paths of length $2L$ of the former diagram (not reproduced here) are still relevant for the energy intervals $[\mu_b + \Delta - eU; \mu_b - \Delta + eU]$ and $[\mu_t + \Delta - eU; \mu_t - \Delta + eU]$. In addition, a new type of path appears, labeled d, with length $3L$. One obtains then three extra steps in $f(E)$, at $5/6$, $1/2$, and $1/6$. More generally, multiple Andreev reflections lead to the appearance of steps in $f(E)$ at energies between $\mu_b - \Delta$ and $\mu_t + \Delta$. The number of steps is $2 \times \text{int}(\frac{2\Delta}{eU}) + 3$, and the sum of the widths of two successive steps is eU. In the limit $U \to 0$, $f(E)$ varies linearly from 1 at $E = -\Delta$ to 0 at $E = \Delta$. To conclude, this simple model predicts a staircase pattern in the energy distribution function, which directly reveals multiple Andreev reflections.

We report results obtained on two samples, fabricated by shadow mask evaporation in order to obtain the complete structure schematically described in Fig. 1. The normal metal 45-nm-thick wires are made of 99.9999% purity silver, as samples in which phase coherence lengths beyond 10 μm were found [12]. The wire length of sample No. 1 (sample No. 2) is $L = 5.15$ μm (5.6 μm), the width $w = 80$ nm (70 nm), and the normal state resistance, measured at large voltage, $R = 38\ \Omega$ (58 Ω). The length is chosen short enough for the energy redistribution among quasiparticles to be small [13], but long enough for the density of states at the middle of the wire to be almost energy independent [2]. In sample No. 1, the wire extends at both ends into large contact pads which are covered by a 300-nm-thick aluminum layer. The reservoirs are therefore bilayers of Ag and Al and have thus a reduced superconducting gap. In sample No. 2, the contact pads have no underlying silver layer on a rectangle of 300×500 nm^2 just at the ends of the wire, in order to obtain a larger superconducting gap. A tunnel junction is formed at the middle of the wire (and, on sample No. 2, also at 1.25 μm from the top electrode), with a 100-nm-wide aluminum probe electrode. The samples were mounted in a shielding copper box on a sample holder thermally anchored to the mixing chamber of a dilution refrigerator. All connecting lines to the samples are filtered at 4.2 K and at the sample temperature. The experiment consists of measuring the differential conductance $dI/dV(V)$ of the probe junction when a voltage U is applied across the wire. Under the assumptions that the density of states of the normal wire is constant at the position of the probe junction and that the temperature of the probe electrode remains negligible compared to the critical temperature of aluminum, the differential conductance of the junction is simply a convolution product of the derivative of the density of states of the superconductor and of the distribution function in the wire [11,14]. We deconvolve the data numerically, after determining the junction resistance and gap energy at equilibrium ($U = 0$) where $f(E)$ is expected to be a Fermi function. In Fig. 2, we present with open symbols the distribution functions measured on sample No. 1 at $U = 151$ μV, 310 μV, and 595 μV, and in Fig. 3 on sample No. 2 at $U = 700$ μV, for both positions. The energy reference was taken at the potential of the center of the wire ($\mu_t = eU/2$, $\mu_b = -eU/2$). As expected from the simplified description of multiple Andreev reflections presented above, the distribution function for sample No. 1 presents, at large voltages (310 and 595 μV in Fig. 2), three steps near $\frac{3}{4}$, $\frac{1}{2}$, and $\frac{1}{4}$ (dashed lines). The distance between the center of the side steps is well given by eU. Their width gives the value of the gap in the reservoirs: $\Delta = 115$ μeV, which is as expected smaller than the gap of aluminum (200 μeV). In contrast with the simplified model, the steps are not flat, and the slope of the side steps near $3/4$ and $1/4$ is larger than the slope at $1/2$. Moreover, the model predicts five steps in $f(E)$ when U is between Δ/e and $2\Delta/e$ (see Fig. 1), whereas the data taken at $U = 155$ μV display only slight inflections of $f(E)$ around the predicted values. At voltages below 100 μV,

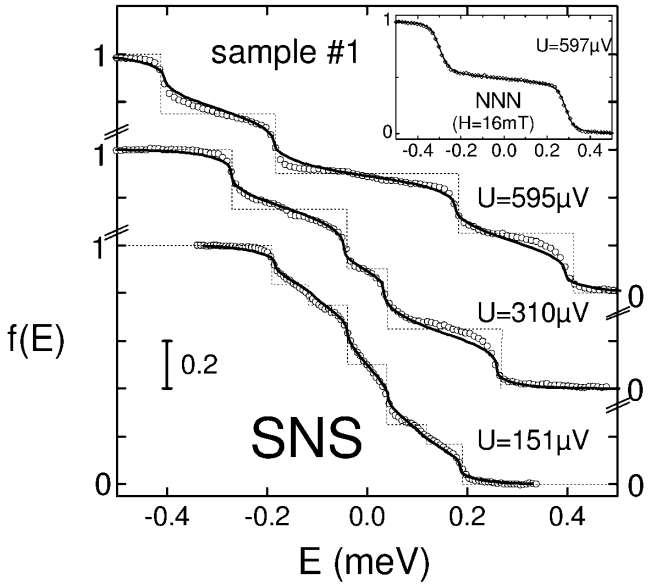

FIG. 2. Distribution functions at the middle of the wire of sample No. 1, when the reservoirs are in the superconducting state or in the normal state (inset), for different values of the bias voltage U. Symbols are experimental data, dotted lines are the expectations of the simplified theory with multiple Andreev reflections alone as in Fig. 1, and solid lines correspond to the solution of the Boltzmann equation with the Coulomb interaction term.

no structure can be seen in the distribution function, and irregularities appear in the deconvolved data, resulting from our neglection of the modification of the density of states in the wire at the scale of the Thouless energy $\hbar D/L^2$ [15] (data not shown). In sample No. 2, the evolution of the distribution function with position agrees qualitatively with the model. However, the exact position of the steps is slightly shifted from the expected values. We attribute this shift to the small size of the top NS contact, which introduces a significant contact resistance, accounted for by an extra length of the wire. The relative position of the probe junctions needed to explain the position of the steps in $f(E)$ turns out to be $X/L = 0.58$ (instead of 0.5) and $X/L = 0.35$ (instead of 0.25), which corresponds to an effective lengthening of the top end of the wire by about 850 nm. The widths of the side steps give slightly different gaps at both ends: 120 and 140 μeV.

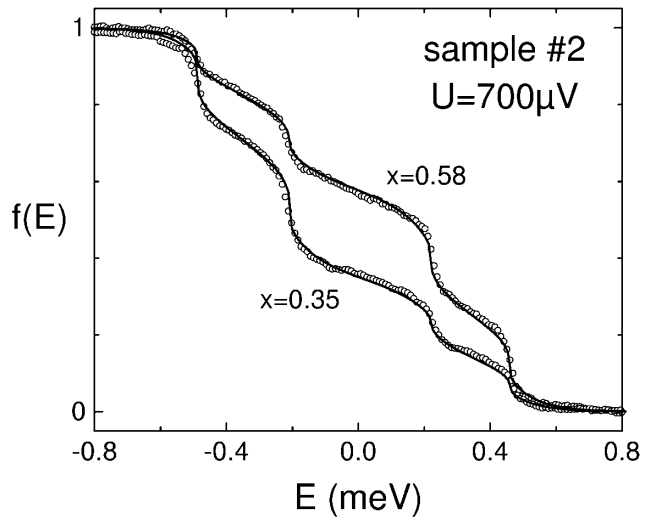

FIG. 3. Distribution functions on sample No. 2, at two positions ($x \equiv X/L = 0.58$ and $x = 0.35$), for $U = 700$ μV. Symbols: experiment. Solid lines: solution of the Boltzmann equation accounting for the Andreev reflections at the reservoirs and electron-electron interactions within the wire.

In order to account for the rounding of the steps, we now include in the analysis the effect of energy relaxation of quasiparticles, due to Coulomb electron-electron [13] and electron-phonon [16] interactions. These interactions contribute to the stationary Boltzmann equation which determines the variations of $f(E)$:

$$D\,\frac{\partial^2 f_E}{\partial X^2} + I_{\rm in}^{e\text{-}e}(f_E) + I_{\rm in}^{e\text{-ph}}(f_E) = 0$$

through the interaction collision integrals [11,13]

$$I_{\rm in}^{e\text{-}e}(f_E) = \int d\varepsilon\, dE'\, K_e(\varepsilon) \times \{f_E \overline{f_{E-\varepsilon}} f_{E'} \overline{f_{E'+\varepsilon}} - \overline{f_E} f_{E-\varepsilon} \overline{f_{E'}} f_{E'+\varepsilon}\},$$

$$I_{\rm in}^{e\text{-ph}}(f_E) = \int d\varepsilon\, K_{\rm ph}(\varepsilon) f_E \overline{f_{E-\varepsilon}},$$

where $K_e(\varepsilon) = \kappa_e/\varepsilon^{3/2}$, $K_{\rm ph}(\varepsilon) = \kappa_{\rm ph}\varepsilon^2$ [17], f_E stands for $f(E)$, and $\overline{f_E}$ stands for $1 - f(E)$. In order to determine the Coulomb interaction parameter κ_e, we have taken advantage in sample No. 1 of the weaker superconductivity in the reservoirs than in the probe finger, which allows one to turn just the reservoirs normal in a moderate magnetic field ($H = 16$ mT, applied perpendicular to the sample plane), while keeping the probe superconducting. The distribution function with normal reservoirs at $U = 595$ μV is displayed in the inset in Fig. 2, and has, as expected [11], only one step near $1/2$. From the fit of a set of such curves at different values of U, we have confirmed the ε dependence of $K(\varepsilon)$ and obtained [13] $\kappa_e = 0.75\ \mathrm{meV}^{-1/2}\,\mathrm{ns}^{-1}$. The coupling constant $\kappa_{\rm ph}$ between electrons and phonons was extracted from the temperature dependence of the phase coherence time on similarly fabricated silver samples [12]: $\kappa_{\rm ph} = 8\ \mathrm{meV}^{-3}\,\mathrm{ns}^{-1}$. When the reservoirs are superconducting, the same Boltzmann equation also allows one to compute numerically $f(E)$, with the following boundary conditions for $|E| < \Delta$: (a) $f(\mu + E) = 1 - f(\mu - E)$ accounts for the equality of the occupancy of quasielectron and quasihole states at symmetric energies about the electrochemical potential μ of the superconductor and (b) $\frac{\partial f}{\partial x}(\mu + E) = -\frac{\partial f}{\partial x}(\mu - E)$ is the conservation of the quasiparticle current. The results for $f(E)$, using the value of κ_e and $\kappa_{\rm ph}$ given above, are plotted with solid lines in Fig. 2. Note that the inclusion of the phonon term $I_{\rm in}^{e\text{-ph}}(f)$ changes only slightly $f(E)$. The side steps at $\frac{3}{4}$ and $\frac{1}{4}$ are more rounded than the step at $\frac{1}{2}$, as observed.

Indeed, they correspond to quasiparticles staying in the wire 4 times longer on average (path length $2L$), which are thus more likely to interact with other quasiparticles. The distribution function at $U = 151\ \mu$V is very rounded by interactions, as expected for quasiparticle paths with lengths $2L$ and $3L$. The overall agreement with the measurements indicates that this simple picture of multiple Andreev reflections [i.e., with assumptions (ii) and (iii)] together with Coulomb interactions captures the essential phenomena. In sample No. 2, a good fit of the data is found with $\kappa_e = 0.35\ \mathrm{meV}^{-1/2}\,\mathrm{ns}^{-1}$ at both measuring positions (see solid curves in Fig. 3).

We now discuss the influence of a more precise description of Andreev reflection, i.e., when relaxing assumptions (ii) and (iii). This can be achieved using the Usadel equations [5], assuming that the wire is long enough so that the superconducting correlations are completely lost in the middle of the wire [18], and neglecting electron-electron interactions. Qualitatively, in the example of trajectory a in Fig. 1, the time spent near the bottom NS interface is shortened by the renormalization of the diffusion constant at energies close to the electrochemical potential of the superconductors [3], which results in a shorter remaining length when $X = L/2$ and thus to a value for $f(E)$ smaller than $3/4$. However, in our experiment, where the length of the wire is 1 order of magnitude larger than the superconducting coherence length $\sqrt{\hbar D/\Delta}$, this effect on $f(E)$ turns out to be negligible.

To conclude, our measurements display clear signatures of multiple Andreev reflections in SNS junctions and demonstrate the importance for the proximity effect of electron-electron interactions, a contribution which is not taken into account in the standard Usadel formalism.

[1] B. Pannetier and H. Courtois, J. Low Temp. Phys. **188**, 599 (2000), and references therein.

[2] S. Guéron, H. Pothier, N. O. Birge, D. Esteve, and M. H. Devoret, Phys. Rev. Lett. **77**, 3025 (1996).

[3] H. Courtois, P. Charlat, Ph. Gandit, D. Mailly, and B. Pannetier, J. Low Temp. Phys. **116**, 187 (1999).

[4] P. Dubos, H. Courtois, B. Pannetier, F. K. Wilhelm, A. D. Zaikin, and G. Schön, cond-mat/0008146.

[5] A. Schmid, in *Nonequilibrium Superconductivity, Phonons, and Kapitza Boundaries,* edited by K. E. Gray (Plenum Press, New York, 1981), p. 423; J. Rammer and H. Smith, Rev. Mod. Phys. **58**, 323 (1986); A. I. Larkin and Yu. N. Ovchinikov, in *Nonequilibrium Superconductivity,* edited by D. N. Langenberg and A. I. Larkin (North-Holland, Amsterdam, 1986), p. 493; K. D. Usadel, Phys. Rev. Lett. **25**, 507 (1970).

[6] C. Strunk, T. Hoss, T. Nussbaumer, and C. Schönenberger, in *Quantum Physics at Mesoscopic Scale,* edited by C. Glattli, M. Sanquer, and J. Trân Thanh Vân, Series Moriond Condensed Matter Physics (Editions Frontières, Gif-sur-Yvette, France, 1999).

[7] E. Scheer, N. Agrait, J.-C. Cuevas, A. Levy Yeyati, B. Ludoph, A. Martin-Roderos, G. R. Bollinger, J. M. van-Ruitenbeek, and C. Urbina, Nature (London) **394**, 154 (1998).

[8] R. Cron, M. F. Goffman, D. Esteve, and C. Urbina (to be published).

[9] M. F. Goffman, R. Cron, A. Levy Yeyati, P. Joyez, M. H. Devoret, D. Esteve, and C. Urbina, Phys. Rev. Lett. **85**, 170 (2000).

[10] A. Furusaki and M. Tsukada, Solid State Commun. **78**, 299 (1991); C. W. J. Beenakker and H. van Houten, Phys. Rev. Lett. **66**, 3056 (1991).

[11] H. Pothier, S. Guéron, Norman O. Birge, D. Esteve, and M. H. Devoret, Phys. Rev. Lett. **79**, 3490 (1997).

[12] A. B. Gougam, F. Pierre, H. Pothier, D. Esteve, and N. O. Birge, J. Low Temp. Phys. **118**, 447 (2000).

[13] F. Pierre, H. Pothier, D. Esteve, and M. H. Devoret, J. Low Temp. Phys. **118**, 437 (2000).

[14] J. M. Rowell and D. C. Tsui, Phys. Rev. B **14**, 2456 (1976).

[15] When heating the sample, the conductance peak at Δ/e in the $dI/dV(V)$ characteristic taken at $U = 0$ split into two peaks, as expected from the presence of a minigap in the density of states in the wire [see W. Belzig, C. Bruder, and A. L. Fauchere, Phys. Rev. B **58**, 14 531 (1998); F. K. Wilhelm and A. A. Golubov, Phys. Rev. B **62**, 5353 (2000)].

[16] The collision term corresponding to phonon emission is important for data taken on long wires at large voltages. The addition of this term to the electron-electron collision term in the Boltzmann equation suffices to account for the measured distribution functions in silver wires, without any *ad hoc* assumption [13].

[17] The ε^2 dependence of the electron-phonon interaction kernel is equivalent to the T^3 dependence of the energy transfer rate between electrons and phonons reported, for example, in M. L. Roukes, M. R. Freeman, R. S. Germain, R. C. Richardson, and M. B. Ketchen, Phys. Rev. Lett. **55**, 422 (1985).

[18] E. V. Bezuglyi, E. N. Bratus', V. S. Shumeiko, G. Wendin, and H. Takayanagi, Phys. Rev. B **62**, 14 439 (2000).

References of chapter 11

[1] B. Pannetier and H. Courtois, J. Low Temp. Phys. **188**, 599 (2000); P. Dubos, H. Courtois, O. Buisson and B. Pannetier, Phys. Rev. Lett. 87, 206801 (2001).

[2] S. Guéron, H. Pothier, N. O. Birge, D. Esteve, and M. H. Devoret, Phys. Rev. Lett. **77**, 3025 (1996).

[3] H. Courtois, P. Charlat, Ph. Gandit, D. Mailly, and B. Pannetier, J. Low Temp. Phys. **116**, 187 (1999).

[4] P. Dubos, H. Courtois, B. Pannetier, F. K. Wilhelm, A. D. Zaikin, and G. Schön, Phys. Rev. B **63**, 064502 (2001).

[5] P. Charlat, PhD thesis, Université Joseph Fourier, Grenoble (1997).

[6] F. Zhou, P. Charlat, B. Spivak, B. Pannetier, J. Low Temp. Phys. **110**, 841 (1998). [cond-mat/9707056].

[7] P. Dubos, PhD thesis, Université Joseph Fourier, Grenoble (2000).

[8] D. A. Ivanov, R. von Roten, and G. Blatter, Phys. Rev. B **66**, 052507 (2002).

[9] M. Tinkham, *Introduction to superconductivity* (Mc Graw Hill, 1985).

[10] F.K. Wilhelm, and A.A. Golubov, Phys. Rev. B **62**, 5353 (2000).

[11] F. Pierre, Annales de Physique **26**, No 4 (2001).

[12] T. Hoss, C. Strunk, T. Nussbaumer, R. Huber, U. Staufer, and C. Schönenberger, Phys. Rev. B **62**, 4079-4085 (2000).

[13] J. Rammer and H. Smith, Rev. Mod. Phys. **58**, No 2 (1986).

Index

Tables

Articles